DYNAMICS OF LONG-TERM SEA-LEVEL CHANGE

AND VERTICAL MOTION OF CONTINENTS

Thesis by

Sonja Spasojevic

In Partial Fulfillment of the Requirements

for the Degree

of Doctor of Philosophy

California Institute of Technology

Pasadena, California

2011

(Defended November 11, 2010)

Acknowledgements

I want to first express the sincerest gratitude to my thesis advisor Prof. Michael Gurnis for his incredible guidance and vision during all stages of my research, his extraordinary enthusiasm and excitement for every problem we tackled, and above all his great understanding and confidence in me. He created a great working environment, which promotes research independence and creativity, and enables students to grow into researchers. I am sure knowledge and skills I gained during our collaboration will significantly shape my future career.

I am also very grateful to my co-advisor Prof. Rob Clayton for introducing me to crustal geophysics and for providing great help during our New Zealand receiver function research. Prof. Clayton taught me how to approach problems from the most practical and logical angle, enabling great research efficiency and productivity. I am also very grateful for his great academic and career advice, and being available any time I needed his help.

I want to extend my gratitude to my academic advisor Prof. Mark Simons for very insightful scientific discussions and help with various academic issues. I am also grateful to Prof. Woodward Fischer for accepting to be on my thesis committee at the very end of my PhD research, and to Prof. John Grotzinger for helpful advice during his tenure on my thesis committee.

My thesis research benefited greatly from a number of collaborations. I want to express special gratitude to Dr. Rupert Sutherland for introducing me to anomalous observations on New Zealand–Antarctica conjugate margins and global geoid lows, for being such an inspiring and efficient collaborator, and for his hospitality during my stay in New Zealand. I also enjoyed collaborating with Dr. Lijun Liu, and I learned a lot as we worked together on North America sea-level problems. I also benefited greatly from collaboration with Prof. Dietmar Müller and his EarthByte research group. I deeply appreciate discussions with Prof. Müller, and interesting ideas he shared with me. I am also very grateful to Statoil for providing financial support for my PhD research, and facilitating valuable discussion during Summits held in Oslo and Bergen.

I am also grateful to Dr. Lydia DiCaprio and Dr. Maria Seton for help with developing plate reconstructions and infrastructure within the GPlates framework. My special thanks goes to Mark Turner for always being willing to resolve any issue regarding GPlates infrastructure and making a special effort to create a fruitful collaboration between researchers and software developers. I also want to thank Prof. Michael Gurnis, Dr. Vlad Manea and Daniel Bower for fruitful collaboration during development of numerous generations of plate reconstructions. My work also greatly benefited from discussions with Dr. Lydia DiCaprio, Dr. Nathan Downey, Dr. Vlad Manea, Danier Bower, Laura Alisic and Dr. Lijun Liu. I also deeply appreciate the help of Dr. Zhimei Yan with receiver function processing and analysis.

Dr. Eh Tan and other staff at the Computational Infrastructure for Geodynamics always provided great help with resolving CitcomS computational issues. I also want to thank Michael Black, Scott Dungan, Jian (Ken) Ou and Naveed Near-Ansari for their help with computing-related issues. I am very thankful to Viola Carter, Donna Mireles, Sarah Gordon and Rosemary Miller for their smiling way of resolving any organizational or administrative issue.

I want to express a special appreciation to Michelle Selvans for her great friendship and support during my PhD studies. I really cannot imagine my Caltech experience without her contagious smile and the warmest hug, and I am very grateful to have her as my friend. I am also very grateful to YoungHee Kim for her willingness to help at any moment. I am extending my gratitude to my other SeismoLab and GPS classmates and officemates.

As I am finishing my PhD studies, I want to thank people and institutions that shaped my previous educational experience. Special thanks goes to Radisav Golubovic and Petnica Science Center for introducing me to the world of Geoscience; I will be forever grateful to the experience I had during my tenure in Petnica. I also want to thank my professors and teaching assistants from the College of Mining and Geology in Belgrade for providing me with such a great background for my future studies.

At the end I want to dedicate this thesis to my family; without their love and support this thesis or any other accomplishment wouldn't be possible and wouldn't have much meaning. Words really cannot express my love and gratitude for my parents,

Đurđa and Srđan, for being the best possible role models anyone can wish for, and my brother, Ognjen, for being my biggest supporter in good and bad times. My husband, Smiljan, is an endless source of love, support, encouragement and laughter, and I cannot imagine achieving this milestone without him. I also want to thank my mother-in-law, Slobodanka, and sister-in-law, Sanja, for their support, help and love, and for caring about how many research articles I published. Finally, birth of my daughters, Katarina and Mila, brought a great joy to my life, and I am truly thankful to them for providing a new purpose to everything I do. Хвала вам неизмјерно! Волим вас бескрајно!

Abstract

We formulate and apply dynamic models to better understand mantle processes and evolution, the vertical motion of continents, and regional and global sea-level change since 100 Ma. We show that evolving mid-to-upper mantle upwellings explain observed anomalously shallow bathymetry, the negative geoid, and the low seismic shear velocity anomalies in the Ross Sea region of Antarctica. These upwellings create a long-lived dynamic topography high, and the Campbell plateau of New Zealand experienced excess subsidence as it moved away from this upwelling. We then use instantaneous models globally to demonstrate that upper-to-mid mantle upwellings, located in the Indian Ocean, Ross Sea, northeast Pacific, and west Atlantic, are the primary cause of high-amplitude geoid minima that are localized within the longer wavelength geoid trough created by Mesozoic slabs. We propose that these upwellings constitute an unrecognized mode of mantle upwellings, potentially developed in response to the ancient subduction zones.

In an alternative approach, we apply inverse models to North America (NAM), and find that the vertical motion and relative sea level were controlled by Farallon slab subduction. The Farallon slab was flat-to-shallow lying in the Late Cretaceous and in turn controlled the marine inundation of the western NAM. During the Cenozoic, the Farallon slab sank into the lower mantle, while NAM moved westward in a mantle reference frame, resulting in the dynamic uplift of the western half and dynamic

subsidence of the eastern half of NAM. We then use dynamic models and hypsometric analysis to show that the proposed dynamic subsidence potentially explains discrepancies between low-amplitude of sea-level fall inferred from subsidence analysis of New Jersey boreholes compared to sea-level curves based on global data sets.

Finally, we formulate dynamic models based on a hybrid approach, accounting for long-term sea-level change factors self-consistently. We infer the relative importance of dynamic topography versus other factors in controlling regional sea level and relative large-scale vertical motions, and calculate a global sea-level curve. We find that the eustatic sea-level fall since the Late Cretaceous is driven by changes in the age of the ocean floor, but is partially offset by dynamic topography.

Contents

List of Figures

List of Tables

Chapter 1

Introduction

Mantle convection is one of the most important Earth processes, controling the thermal and geologic evolution of the earth, the distribution of land and ocean on geologic time scales, and motion of tectonic plates, while also influencing a range of other processes and phenomena, such as Earth's climate system, glaciation cycles, and formation of mineral and hydrocarbon resources, just to name few [*Schubert et al.*, 2001]. Recent advances in seismic tomography (e.g., *Grand* [2002]; *Li et al.* [2008]; *Ren et al.* [2007]; *Ritsema et al.* [2004]) enable a better definition of present-day mantle structure at intermediate and long wavelengths. However, the present-day structure is a result of a long evolution of mantle convection, which to a large extent remains poorly resolved. Significant uncertainty still remains on mantle rheology (e.g., *Forte* [2007]), character and properties of mantle heterogeneities (e.g., *Karato and Karki* [2001]; *Simmons et al.* [2009]), and mantle composition (e.g., *Price* [2007]).

In this thesis, we develop a set of geodynamic models since the Late Cretaceous, which link forward and reverse numerical models of mantle convection with plate motions, seismic tomography, stratigraphy, and various other geological and geophysical constraints. We call these models Dynamic Earth Models (DEM),

formulated to better understand and constrain mantle evolution over the last 100 million years, its impact on vertical motion of continents, regional and global sea level, as well as tectonic evolution of the study regions. DEMs contribute to a better understanding of mantle viscosity and structure, both globally and regionally, while addressing significant challenges in the development of a new generation of dynamic models.

In Chapter 2 we present forward models of the New Zealand–Antarctica (NZ-ANT) conjugate margins since the initiation of spreading at the Antarctica-Pacific ridge at 80 Ma. The NZ-ANT models are motivated by observations of ~1km of positive residual bathymetry at the ANT margin, correlated with the location of a large intermediate-wavelength geoid low, low-velocity seismic anomalies within the mid mantle, a high-velocity lower mantle seismic anomaly, and a large (0.5-0.9 km) excess tectonic subsidence of the Campbell plateau (NZ) after it rifted away from ANT [*Sutherland et al.*, 2009]. We demonstrate that evolving mid mantle upwellings, centered above the Ross sea region, and located above a cold downwelling associated with ancient Gondwana subduction, explain the anomalous observations. The upwelling creates a long-lived dynamic topographic high and results in a present-day positive residual bathymetry anomaly, while controlling the excess subsidence of the Campbell plateau when the plateau moved away from the anomaly between 70 and 40 Ma. Incorporation of both time-dependent and instantaneous observations into NZ-ANT forward models enables us to infer fairly high values of relative and absolute mantle viscosities.

In Chapter 3 we use instantaneous dynamic models to explore the global geoid and explain the origin of high-amplitude intermediate-wavelength geoid minima within the global belt of geoid lows. It has been long noted that the global circum-Pacific belt of geoid lows is correlated with the position of Mesozoic subduction [*Chase and Sprowl*, 1983; *Richards and Engebretson*, 1992]. Motivated by our Ross Sea study (Chapter 2), we also explore high-amplitude geoid minima located in the Indian Ocean, northeast Pacific and west Atlantic. We find evidence for the existence of low-density mantle upwellings at upper-to-mid mantle depths globally above the region of subducted Mesozoic slabs. We propose that these upwellings are the primary cause of high-amplitude geoid minima, located within the long-wavelength geoid trough associated with the Mesozoic slab graveyards. We suggest that they constitute a previously unrecognized mode of mantle upwellings that is causally related to the activity of ancient subduction zones. In addition, the geoid has been used extensively to constrain geodynamic models (e.g., *Hager* [1984]; *Steinberger and Calderwood* [2006]), and in particular values of mantle viscosities. The instantaneous dynamic models suggest that the average viscosity ratio between upper and lower mantle has a value of 1:80 to 1:100.

In Chapter 4 we present reverse geodynamic models for North America (NAM) since the Late Cretaceous, constrained by seismic tomography, paleoshorelines, borehole tectonic subsidence and sediment isopachs. We find the NAM vertical motions and relative sea level are controlled by subduction of the Farallon slab. The Farallon slab developed as flat-to-shallow lying subduction over the Late Cretaceous, controlling dynamic subsidence and widespread flooding of the western NAM. As the Farallon

slab sank into the lower mantle during the Cenozoic, NAM moved westward in the plate frame of reference, resulting in the dynamic uplift of western NAM and dynamic subsidence of eastern NAM. We also use the NAM models to infer a relative average mantle viscosity ratio between average upper and lower mantle of 1:15, much smaller than that inferred for the Ross Sea, and to reconstruct Late Cretaceous geometry of the Farallon slab.

In Chapter 5 we explore in more detail Cenozoic dynamics and vertical movement of eastern NAM using dynamic models and hypsometric analysis. We find that the remnants of the Farallon slab, imaged by seismic tomography at mid mantle depths under eastern NAM, cause a long-wavelength dynamic tomography low. Over the Cenozoic, the eastern U.S. experiences overall dynamic subsidence with amplitudes of up to several hundred meters. The dynamic subsidence occurs during the period of overall sea-level fall, resulting in absence of land subsidence. We demonstrate that eastern NAM is likely not stable, explaining discrepancies between low-amplitude sea-level estimates of a long-term sea-level maximum of 70 m from the New Jersey coastal plain [*Miller et al.*, 2005] compared to other, significantly higher, sea-level estimates (e.g., *Kominz* [1984]).

In Chapter 6 we present results of global hybrid models, which combine reverse and forward modeling to better understand sea level and vertical motion of continents globally from Late Cretaceous to present, while systematically incorporating plate motions. The main factors of long-term sea-level change include fluctuations of ocean basins volume due to change in oceanic lithosphere production,

sedimentation and emplacement of oceanic plateaus, dynamic topography, and geoid. The global hybrid models account for these factors self-consistently. We infer the relative importance of dynamic topography versus other factors in controlling regional sea level and relative large-scale vertical motions. We also calculate a global sea-level curve, and infer the relative contribution of different factors of sea-level change since the Late Cretaceous.

Our DEMs are an important step forward toward integrating models of mantle convection with plate motions, seismic tomography and various geologic and geophysical observations. These models demonstrate that mantle dynamics represents an important process controlling vertical motion of continents, regional and global sea level, while addressing a number of regional and global tectonic issues. However, DEMs are relatively poorly resolved due to the limited data sets imposed as constraints, simplified subduction zones and parameterization of the mantle viscosity, and limited resolution of seismic tomography, all of which should be improved in future generations of DEMs. The most important improvement would be incorporation of a much more extensive global stratigraphic data sets, including borehole, paleoshoreline and isopach data, that should enable one to constrain the history of vertical motion of continents and mantle viscosity structure on finer scale, thus more adequately addressing issues related to sea-level change on geologic time scales.

References

Burgess, P. M., M. Gurnis, and L. Moresi (1997), Formation of sequences in the cratonic interior of North America by interaction between mantle, eustatic, and stratigraphic processes, *Geological Society of America Bulletin*, *109*(12), 1515–1535.

Chase, C. G., and D. R. Sprowl (1983), The modern geoid and ancient plate boundaries, *Earth and Planetary Science Letters*, *62*(3), 314–320.

Chase, C. G. (1985), The geological significance of the geoid, *Annual Review of Earth and Planetary Sciences*, *13*, 97–117.

DiCaprio, L., M. Gurnis, and R. D. Muller (2009), Long-wavelength tilting of the Australian continent since the Late Cretaceous, *Earth and Planetary Science Letters*, *278*(3-4), 175–185.

Forte, A. M. (2007), Constraints on seismic models from other disciplines: Implications for mantle dynamics and composition, in *Treatise of Geophysics*, edited by B. Romanowicz and A. M. Dziewonski, 805–854.

Grand, S. P. (2002), Mantle shear-wave tomography and the fate of subducted slabs, *Philosophical Transactions of the Royal Society of London Series A-Mathematical Physical and Engineering Sciences*, *360*(1800), 2475–2491.

Gurnis, M. (1993), Phanerozoic marine inundation of continents driven by dynamic topography above subducting slabs *Nature*, *364*(6438), 589–593.

Gurnis, M., R. Müller, and L. Moresi (1998), Cretaceous vertical motion of Australia and the Australian-Antarctic discordance, *Science*, *279*(5356), 1499–1504.

Hager, B. H. (1984), Subducted slabs and the geoid- Constraints on mantle rheology and flow, *Journal of Geophysical Research*, *89*(B7), 6003–6015.

Hays, J. D., and W. C. Pitman (1973), Lithospheric plate motions, sea-level changes and climatic and ecological consequences, *Nature*, *246*(5427), 18–22.

Karato, S., and B. B. Karki (2001), Origin of lateral variation of seismic wave velocities and density in the deep mantle, *Journal of Geophysical Research, 106*(B10), 21771–21783.

Kominz, M. A. (1984), Oceanic ridge volumes and sea level change- An error analysis, in *Interregional Unconformities and Hydrocarbon Accumulation*, edited by J. Schlee, American Association of Petroleum Geology Memoir,109–127.

Li, C., R. D. van der Hilst, E. R. Engdahl, and S. Burdick (2008), A new global model for P wave speed variations in Earth's mantle, *Geochemistry Geophysics Geosystems*, *9*, Q05018.

Lithgow- Bertelloni, C., and M. Gurnis (1997), Cenozoic subsidence and uplift of continents from time-varying dynamic topography, *Geology*, *25*(8), 735–738.

Miller, K. G., M. A. Kominz, J. V. Browning, J. D. Wright, G. S. Mountain, M. E. Katz, P. J. Sugarman, B. S. Cramer, N. Christie-Blick, and S. F. Pekar (2005), The Phanerozoic record of global sea-level change, *Science*, *310*(5752), 1293–1298.

Mitrovica, J. X., C. Beaumont, and G. T. Jarvis (1989), Tilting of continental interiors by the dynamical effects of subduction, *Tectonics*, *8*(5), 1079–1094.

Mitrovica, J. X., R. N. Pysklywec, C. Beaumont, and A. Rutty (1996), The Devonian to Permian sedimentation of the Russian platform: An example of subduction-

controlled long-wavelength tilting of continents, *Journal of Geodynamics*, *22*(1–2), 79–96.

Price, D. G., Editor (2007), Mineral Physics, *Treatise on Geophysics, 2,* Elsevier, 656 pp.

Ren, Y., E. Stutzman, R. D. van der Hilst, and J. Besse (2007), Understanding seismic heterogeneities in the lower mantle beneath the Americas from seismic tomography and plate tectonic history, *Journal of Geophysical Research*, *112*, B01302, doi:10.1029/2005JB004154.

Richards, M., and D. Engebretson (1992), Large-scale mantle convection and the history of subduction, *Nature*, *355*, 437–440.

Ritsema, J., H. J. van Heijst, and J. H. Woodhouse (2004), Global transition zone tomography, *Journal of Geophysical Research*, *109*, B02302, doi: 10.1029/2003jb002610.

Schubert, G., D. L. Turcotte, and P. Olson (2001), *Mantle convection in the Earth and planets*, Cambridge University Press, Cambridge, 940 pp.

Simmons, N. A., A. M. Forte, and S. P. Grand (2009), Joint seismic, geodynamic and mineral physical constraints on three-dimensional mantle heterogeneity: Implications for the relative importance of thermal versus compositional heterogeneity, *Geophysical Journal International*, *177*(3), 1284–1304.

Steinberger, B., and A. R. Calderwood (2006), Models of large-scale viscous flow in the Earth's mantle with constraints from mineral physics and surface observations, *Geophysical Journal International*, *167*(3), 1461–1481.

Sutherland, R., S. Spasojevic, and M. Gurnis (2009), Mantle upwelling after Gondwana subduction death may explain anomalous topography of West Antarctica and subsidence history of eastern New Zealand, *Geology*, *38*(2), 155–158.

Chapter 2

Inferring mantle properties with an evolving dynamic model of the Antarctica-New Zealand region from the Late Cretaceous[1]

2.1. Abstract

We show that time-dependent models of mantle upwellings above a cold downwelling in the New Zealand-Antarctica region since 80 Ma can explain anomalous geophysical observations: ~1.0 km of positive residual bathymetry at the Antarctica margin, a large Ross Sea geoid low, 0.5-0.9 km of excess tectonic subsidence of the Campbell plateau since 80 Ma, and several seismic wave speed anomalies. Model results indicate that the largest mantle upwelling, centered in the Ross Sea, has an average temperature anomaly of 200°C and density anomaly of 0.6%, and it rose from mid mantle depths at 80 Ma to a present depth of 400-1000 km.

Anomalous Campbell plateau subsidence requires a smaller hot anomaly evolving

[1] Published by Sonja Spasojevic, Michael Gurnis and Rupert Sutherland (2010) in *Journal of Geophysical Research, 115,* B05402, doi:10.1029/2009JB006612.

within the upper mantle under the region of the reconstructed Late Cretaceous Campbell plateau. The excess subsidence of the plateau results from northward drift of New Zealand away from the dynamic topography high created by the smaller hot anomaly. To fit present-day geoid and residual topography observations, we require a large lower:upper mantle viscosity ratio of 100:1. We suggest that the distribution of temperature and viscosity is related to long-lived Gondwana subduction that accumulated high-density high-viscosity lower mantle below a chemically-altered upper mantle with anomalously low density and/or high temperature. Time-dependent observations enable constraints on absolute viscosities of 10^{23} Pa s and 10^{21} Pa s for the lower and upper mantle, respectively.

2.2. Introduction

Conjugate passive continental margins of Antarctica (ANT) and New Zealand (NZ) lie at the edges of Marie Byrd Land and the Campbell plateau. The ANT margin and adjacent ocean crust has approximately 1 km of positive residual bathymetry, relative to both the NZ margin and a reference age-depth model for the Pacific Ocean [*Sutherland et al.*, 2009]. This ANT bathymetric anomaly is spatially correlated with a geoid minimum in the Ross Sea [*Förste et al.*, 2008]. Seismic tomography reveals low velocities within and beneath the lithosphere, low velocities in the transition zone and uppermost lower mantle, and high velocities in the lowermost mantle (e.g*., Grand* [2002]; *Gu et al.* [2001]; *Masters et al.* [2000];

Ritsema and van Heijst [2000]). Campbell plateau (NZ) boreholes record excess tectonic subsidence of 500-900 m, with a maximum in tectonic subsidence rate at 70-40 Ma, coincident with rapid northward drift of NZ away from ANT [*Cook et al.*, 1999; *Sutherland et al.*, 2009]. Mantle upwelling beneath the ANT margin has been suggested on the basis of these anomalous observations [*Sieminski et al.*, 2003; *Sutherland et al.*, 2009], and is consistent with previous suggestions based upon the distribution and chemistry of igneous rocks [*Storey et al.*, 1999; *Weaver et al.*, 1994].

In a previous paper [*Sutherland et al.*, 2009], we presented observations of anomalous topography and subsidence, showed that a simplified geodynamic model of mantle upwelling could be constructed to fit all observations, and we proposed a hypothesis that such an upwelling may have followed the Cretaceous termination of long-lived subduction (>200 Myr) at the Gondwana margin. In this paper, we document and analyze a range of geodynamic models for the evolving mantle flow, and hence we are able to draw conclusions about mantle properties. Our models incorporate mantle upwellings and a downwelling that are geometrically simplified, and are required to evolve to features equivalent to the three anomalous velocity structures imaged in global seismic-tomographic inversions, and we must fit observations of geoid, topography, and subsidence history from 80 Ma to the present.

First, we utilize global time-dependent geodynamic models to constrain the magnitude of buoyancy anomalies and their initial Late Cretaceous geometry and depth. Second, we fit time-dependent (tectonic subsidence) and present-day (geoid,

seismic tomography, and residual bathymetry) observations jointly, to constrain both the relative and absolute values of mantle viscosities in the ANT-NZ region. Geoid observations provide a strong constraint on the radial viscosity gradient in the mantle, and we show that absolute viscosity can also be constrained when seismic tomography is combined with constraints on present-day and evolving dynamic topography. Third, we investigate the association of the observed ANT geoid low with mantle upwelling, which makes this region of particular geodynamic interest, because upwellings are more usually associated with geoid highs [*Richards et al.*, 1988].

2.3. Tectonic history

The ANT-NZ region today has conjugate passive margins that are separated by seafloor spreading at the Pacific-Antarctic Rise [*Cande et al.*, 1995; *Molnar et al.*, 1975], but it was previously a region characterized by a long-lived subduction zone that was active over much of the Late Paleozoic and Mesozoic [*Adams et al.*, 2007; *Mortimer et al.*, 1999; *Veevers*, 2000]. Mesozoic activity along the eastern Gondwana subduction zone (Fig. 2.1) occurred from offshore eastern Australia, New Caledonia, and the Lord Howe Rise [*Adams et al.*, 2007; *Mortimer et al.*, 1998; *Paris*, 1981; *Veevers et al.*, 1994], through New Zealand and the Chatham Rise [*Bradshaw*, 1989; *Davy et al.*, 2008; *Kimbrough et al.*, 1994; *Mortimer et al.*, 1999], to Marie Byrd Land in Antarctica [*Bradshaw et al.*, 1997; *Mukasa and Dalziel*, 2000; *Weaver et al.*, 1994].

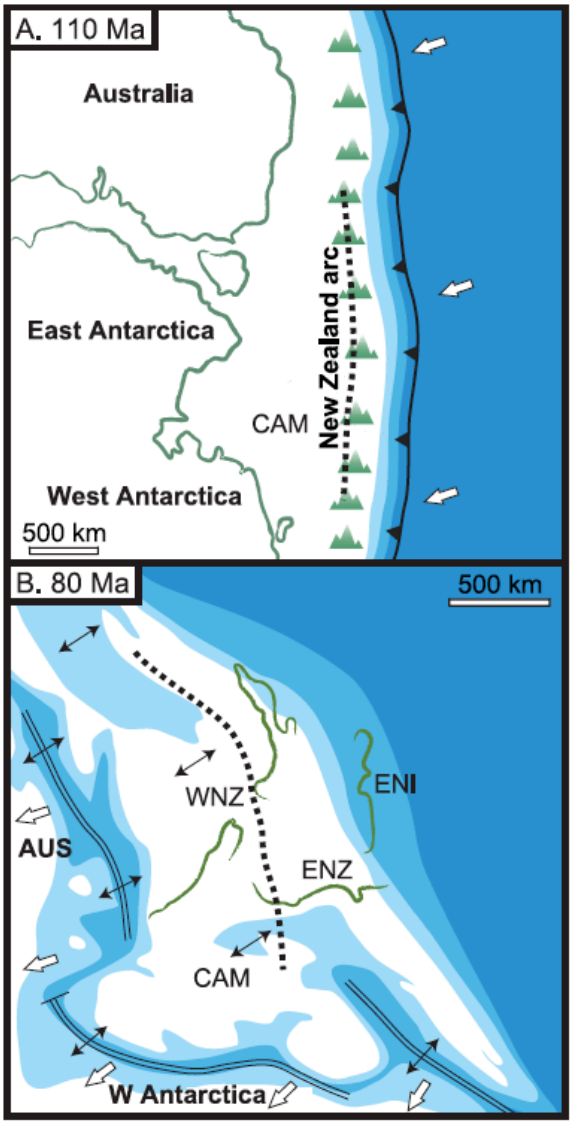

Figure 2.1. Cartoons showing the configuration of Australia, Antarctica, New Zealand, and the Campbell Plateau (CAM) at a time when Gondwana had an active subduction zone and arc (A), and when incipient development of the Tasman Sea and South Pacific oceans during widespread rifting led to final Gondwana breakup (B). The modern coastline of fragments of western New Zealand (WNZ), eastern South Island (ENZ), and eastern North Island (ENI) are shown, with Cenozoic relative motions reconstructed [*Sutherland,* 1995; *King,* 2000]. The position of the reconstructed Gondwana arc in the New Zealand region is shown dotted [*Sutherland*, 1999a, 1999b]. Shades show land (white), shelf (light shade, <400 m), slope (medium shade, 400-3000 m), and abyssal (dark shade, >3000 m) paleodepths. Open arrows show plate motion directions relative to New Zealand, and double-ended arrows show extension directions during rifting.

Subduction continued during the Cenozoic in the Thurston Island and Antarctic Peninsula regions [*Cunningham et al.*, 2002; *Dalziel and Elliot*, 1982; *Larter et al.*, 2002; *Storey and Nell*, 1988], and the subduction zone is still active today in western South America [*Allmendinger et al.*, 1997; *Herve et al.*, 2007].

The termination of subduction was earliest in the New Zealand sector, where the youngest subduction-related igneous rocks formed at c. 115-105 Ma [*Kimbrough et al.*, 1994; *Mortimer et al.*, 1999; *Muir et al.*, 1995; *Muir et al.*, 1998; *Waight et al.*, 1998], and this time corresponds to the end of local convergent deformation [*Mazengarb and Harris*, 1994] and the onset of widespread rifting and intraplate (anorogenic, A-type) magmatism [*Laird and Bradshaw*, 2004; *Weaver et al.*, 1994]. Subduction termination was slightly later at c. 105-95 Ma in Marie Byrd Land [*Bradshaw et al.*, 1997; *Mukasa and Dalziel*, 2000; *Storey et al.*, 1999], and was not until Cenozoic time (<65 Ma) in the Thurston Island and Antarctic Peninsula regions [*Cunningham et al.*, 2002; *Larter et al.*, 2002; *McCarron and Larter*, 1998; *Storey and Nell*, 1988].

Gondwana breakup and voluminous magmatism, which is interpreted to have been plume-related [*Pankhurst et al.*, 2000; *Storey*, 1995], commenced during the Jurassic at c. 180 Ma as South America, Africa, and the Weddell Sea region of Antarctica started to separate and form the South Atlantic and Southern Ocean [*Ferris et al.*, 2000; *Pankhurst et al.*, 2000; *Storey*, 1995]. By c. 120 Ma (Early Cretaceous; Aptian), Gondwana was fragmented everywhere but the New Zealand sector, and the fragments were starting to disperse as seafloor spreading ridges were established

[*Lawver et al.*, 1987; *Marks and Tikku*, 2001; *Müller et al.*, 2000; *Nürnberg and Müller*, 1991]. The final stage of Gondwana breakup (Fig. 2.1) created the Marie Byrd Land and Campbell plateau passive margins at c. 83-79 Ma as New Zealand, Australia, and Antarctica separated to form the Tasman Sea and South Pacific sector of the Southern Ocean [*Cande et al.*, 1995; *Gaina et al.*, 1998; *Molnar et al.*, 1975; *Stock and Molnar*, 1987; *Sutherland*, 1999a; *Weissel et al.*, 1977].

2.4. Observational constraints

Global [*Grand*, 2002; *Gu et al.*, 2001; *Masters et al.*, 2000; *Ritsema and van Heijst*, 2000] and regional [*Ritzwoller et al.*, 2001; *Sieminski et al.*, 2003] seismic tomographic inversions appear to resolve three anomalous structures in the NZ-ANT region (Fig. 2.2): A broad lithospheric and sublithospheric low-velocity anomaly; a low-velocity anomaly spanning the transition zone and upper part of the lower mantle; and a high-velocity anomaly in the lowermost mantle. The lithospheric and sublithospheric mantle of West Antarctica (including the Ross Sea and Marie Byrd Land) is characterized by a broad anomaly of low seismic velocities at <400 km depth (Fig. 2.2). The intermediate-depth low-velocity anomaly spans the transition zone and upper part of the lower mantle between c. 400-1100 km depths (Fig. 2.2). Finally, a region of high S-wave velocities above the core-mantle boundary (CMB) has a depth extent of approximately 2000-2900 km (Fig. 2.2), and is attributed to high-density material that accumulated during Paleozoic and Mesozoic

Gondwana subduction.

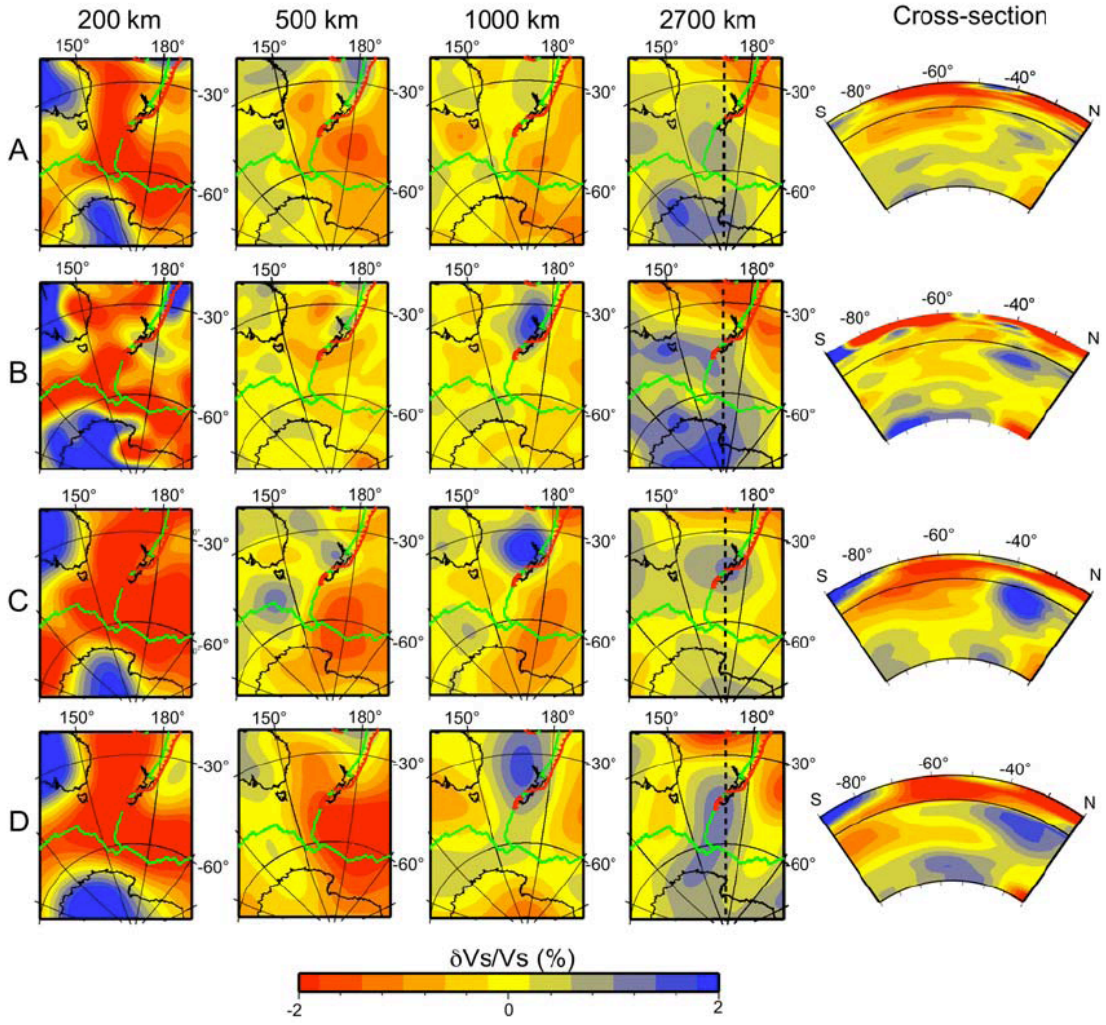

Figure 2.2. Shear-wave seismic tomography maps in the Antarctica–New Zealand region at 200, 500, 1000, and 2700 km depths and N-S cross-section along 170°E. (A) *Ritsema and van Heijst* [2000]. (B) *Grand* [2002]. (C) *Masters et al.* [2000]. (D) *Gu et al.* [2001]. The position of the cross-section is shown on depth slices at 2700 km. The lateral resolution of models varies between 275 km [*Grand*, 2002] and ~1000 km [*Ritsema and van Heijst*, 2000].

The details of three anomalous structures differ between tomographic models (Fig. 2.2). The shallowest low-velocity anomaly appears to be connected to a much larger shallow low-seismic-velocity anomaly that is spatially correlated with the location

of Late Cretaceous and Cenozoic seafloor spreading and continental extension for all of the tomographic inversions (Fig. 2.2). Only one model (Fig. 2.2B; Grand, 2002) has a localized circular low-velocity lithospheric-sublithospheric anomaly in the Ross Sea region.

The intermediate-depth low-velocity anomaly seems to be spatially more localized than the shallow anomaly and all of the inversions resolve it to the east from the Macquarie Ridge (Fig. 2.2), the plate boundary between the Pacific and Australian plates extending south of South Island, New Zealand. At 1000 km depth, based on models by *Masters et al.* [2000] (Fig. 2.2A) and *Ritsema and van Heijst* [2000] (Fig. 2.2C), this anomaly appears to span between ANT and NZ across the Antarctic-Pacific ridge, while the model by *Gu et al.* [2001] defines two separate anomalies (Fig. 2.2D). A low-velocity anomaly in this depth range has previously been interpreted as a mantle upwelling based on regional tomographic inversions [*Sieminski et al.*, 2003]. In addition, in the Ross Sea region the mantle transition zone is inferred from SS and PP precursors to be >20 km thinner than the global average at long wavelengths [*Flanagan and Shearer*, 1998; *Houser et al.*, 2008]. Such a thinning is consistent with a vertically coherent warm (>150°C; seismically low velocity) anomaly that spans 410-660 km depths [*Bina and Helffrich*, 1994; *Houser et al.*, 2008]; this suggests that a part of an intermediate-depth low-velocity anomaly could be associated with mantle upwelling.

Details of the high-velocity anomaly in the lower mantle differ significantly between models (Fig. 2.2), with all models defining it in the region of interest between the

Ross Sea and Marie Byrd Land. Several models (Fig 2.2A, B, D) connect the ANT lower mantle anomaly with high-velocity anomalies located further north and northwest, consistent with the hypothesis that the anomaly corresponds to slabs created during long-lived Mesozoic subduction *[Chase and Sprawl*, 1983*; Gurnis et al*., 1998]. All models have this anomaly restricted to the lower portion of the lower mantle (Fig. 2.2).

One of the largest geoid minimums, with an amplitude of about –60 m over a wavelength of several thousand kilometers [*Förste et al.*, 2008], is centered in the Ross Sea (Fig. 2.3A), roughly coincident with the mid mantle seismic-velocity low (Fig. 2.2) and transition-zone thickness anomaly [*Houser et al.*, 2008]. *Chase and Sprowl* [1983] suggest that the global semi-continuous geoid low, passing from Hudson's Bay through Siberia and India to Antarctica and the Ross Sea (Fig. 2.3A), is correlated with the position of long-lived Mesozoic subduction. On the other hand, the large-scale residual geoid highs, obtained after subtracting the putative effects of subduction, are correlated with locations of present-day hotspots [*Chase*, 1985]. There is a positive correlation between geoid highs and low seismic velocity in the lower mantle at degree 2, and with low seismic velocity in the upper mantle at degree 6 [*Richards et al.*, 1988], suggesting that upwellings of different wavelengths can reproduce geoid highs. For example, the large-scale lower mantle African and Pacific superswells [*Hager et al.*, 1985] and smaller-scale upper mantle Hawaii and Iceland hotspots [*Richards et al.*, 1988] both give rise to geoid highs. The Ross Sea region may be unique because it has a large geoid low located above both ancient subduction and possibly contemporaneous upwelling within the mantle.

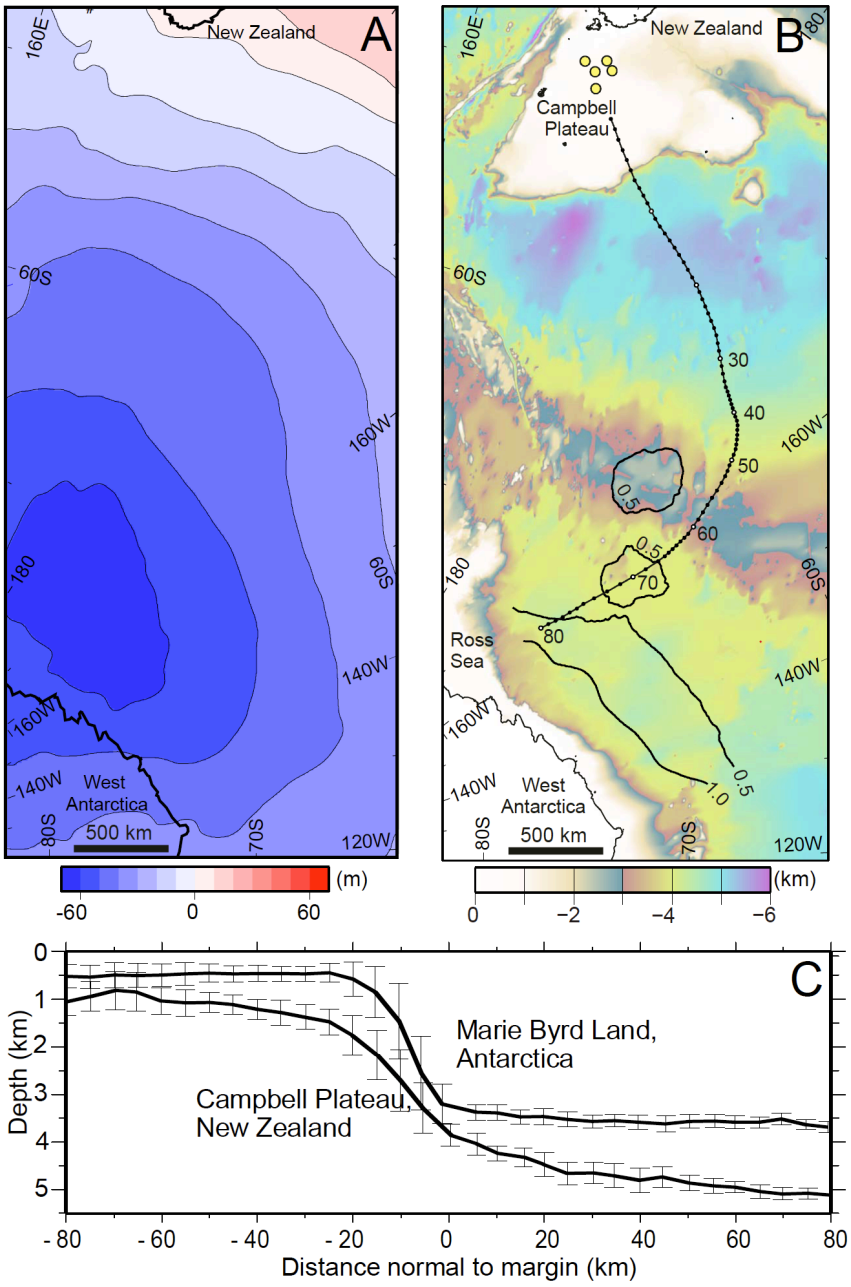

Figure 2.3. Observations used as constraints for our models. (A) Geoid [*Förste et al.*, 2008] with 10 m contour intervals. (B) Residual sea-floor depth [*Sutherland et al.*, 2009], obtained after subtracting age-depth model with GEBCO bathymetry, showed with solid contour lines with 500 m contour intervals. Yellow dots show position of five petroleum wells in Campbell plateau, and dotted line the relocated position of a point on the southern Campbell Plateau with respect to Marie Byrd Land since 80 Ma (1 Ma increments). (C) Bathymetry profiles [*Sutherland et al.*, 2009] perpendicular to Antarctica (145-160°W) and New Zealand margins (166-176°E), as a function of distance from the base of the Cretaceous continental margin, with bars indicating the standard deviation.

Residual bathymetry, obtained by subtracting an age-depth model from observed depths of ocean crust, indicates that a broad region between the ANT margin and the Pacific-Antarctic Rise is 500-1000 m shallower than expected (Fig. 2.3B) [*Sutherland et al.*, 2009]. Bathymetric profiles perpendicular to the passive continental margins indicate that, although the shapes of the conjugate margins are nearly symmetric (Fig. 2.3C), the ANT margin is ~1 km higher than the NZ margin [*Sutherland et al.*, 2009]. In addition, when the effects of sediment loading by up to 4 km of Late Cretaceous and Cenozoic post-rift sediments is accounted for in five petroleum wells of the northern Campbell Plateau [*Cook et al.*, 1999], observed tectonic subsidence is 0.5-0.9 km larger than expected from reasonable rifting models [*Cook et al.*, 1999]. Excess subsidence occurred in the period 70-40 Ma, coincident with the phase of the rapid northward drift of New Zealand away from Antarctica, and significantly after the end of sedimentary basin formation [*Sutherland et al.*, 2009].

2.5. Methods

We use CitcomS version 3.0, a finite-element code for solving thermal convection within the mantle [*Tan et al.*, 2006; *Zhong et al.*, 2000] to develop global three-dimensional spherical models with assimilated plate motions. The plate velocities and plate polygons are defined at 1 Myr intervals [*Gurnis et al.*, 2009], and the velocity field is linearly interpolated for intervening times. We solve the equations

of conservation of mass (1), momentum (2), and energy (3) for an incompressible, Newtonian fluid, while making the Boussinesq approximation:

$$\nabla \cdot \vec{u} = 0 \tag{1}$$

$$\nabla P + \nabla \cdot \left(\eta \nabla \vec{u}\right) = \rho_m \alpha T \vec{g} \tag{2}$$

$$\frac{\delta T}{\partial t} + \vec{u} \cdot \nabla T = \kappa \nabla^2 T + H \tag{3}$$

where $\vec{u}$ is velocity, P dynamic pressure, η dynamic viscosity, ρ_m ambient mantle density, α thermal expansion coefficient, $\vec{g}$ gravitational acceleration, T temperature, κ thermal diffusivity, and H internal heat production. Internal heating is negligible on the <100 Myr time-scales studied here. Values of model parameters held constant are given in Table 2.1.

Table 2.1. Model parameters held constant in our runs.

Parameter	Symbol	Value
Ambient mantle density	ρ_m	3340 kg/m^3
Water density	ρ_w	1000 kg/m^3
Reference viscosity	η_o	1x10^{21} Pa s
Thermal diffusivity	κ	10^{-6} m^2/s
Coefficient of thermal expansion	α	3x10^{-5} 1/K
Gravitational acceleration	g	9.81 m/s^2
Earth's radius	R	6371 km

Dynamic topography h on the top surface is defined from:

$$\sigma_{r,r} = (\rho_m - \rho_w) g h \tag{4}$$

where $\sigma_{r,r}$ is total normal stress in the radial direction, ρ_m-ρ_w is the density contrast across top surface between water and mantle.

Effective viscosities are temperature-dependent according to:

$$\eta = \eta_0 \exp[\frac{E^*}{T + T_o} - \frac{E^*}{0.5 + T_o}] \quad (5)$$

where η is effective viscosity, η_0 is reference viscosity (Table 2.1), E^* is activation energy divided by the product of the gas constant R (8.314 $J K^{-1} mol^{-1}$) and temperature scaling T_S (3000 K) , T is non-dimensional temperature, and T_0 is a temperature offset. We used values of E^*=1 in the upper and E^*=5 in the lower mantle, and T_0 =0.5 for both upper and lower mantle, and these values correspond to relatively weak temperature dependence of viscosity.

Except for initial discrete anomalies, the mantle is isothermal, with a non-dimensional background temperature, T_m=0.5. Top and surface boundary have mantle background temperature, and we do not impose thermal boundary layers. Because the study area is dominated by divergent plate boundaries during its evolution, and has no active mantle plumes originating from the core-mantle boundary, such approximation is appropriate. We introduce upwelling anomalies $0.5<T_U\leq1$, and downwelling anomalies $0\leq T_D<0.5$, as oblate triaxial ellipsoids, with two long diameters (a and b) parallel to Earth surface and the shortest diameter (c) being vertical. Non-dimensional maximum upwelling (downwelling) temperature is defined as $T_U = T_m+\Delta T_a$ ($T_D = T_m-\Delta T_a$), where ΔT_a is maximum non-dimensional temperature of the anomaly. Temperatures in the ellipsoid follow Gaussian in all directions.

The variables we attempt to constrain are: (1) Geometry of buoyancy anomalies defined by ellipsoid diameters a, b and c, their depth (d_u and d_d) and initial geographic position at 80 Ma; (2) Temperature anomalies ΔT_a; and (3) Radial mantle viscosities, where we define a three-layer structure that includes lithosphere, upper mantle, and lower mantle, with the lithosphere viscosity having a constant value of 10^{23} Pa s. The top boundary layer is defined as a distinct high viscosity rheological unit. For each model we define background viscosities for lower and upper mantle, which is modified by a temperature dependency in regions with thermal anomalies. All viscosity ratios reported are those between the background upper and lower mantle.

2.6. Model results

2.6.1. Size and position of buoyancy anomalies

We first attempted to reproduce all observations in a time-dependent model with a single upwelling positioned immediately above a downwelling. The downwelling is designed to correlate with the high-seismic-velocity anomaly deep in the lower mantle (Fig. 2.2). Although the high-velocity region may be the result of slab accumulation, we simplify the downwelling by introducing a single body with c=800 km. The upwelling anomaly, located immediately above the downwelling at 80 Ma, with its lower edge 100 km from the upper edge of the downwelling, is designed to reproduce general features of the seismically low-velocity region at the end of

calculation (0 Ma). The short diameter of the upwelling is varied between 500 and 800 km. The values of diameters *a* and *b* and ΔT_a are assumed to be the same for both the upwelling and downwelling. We start all models at 80 Ma, roughly coincident with proposed initiation of ANT-Pacific spreading [*Stock and Molnar*, 1987; *Sutherland*, 1999a].

The observed geoid and bathymetry anomaly constrains the size and position of the anomalies. If the initial size of the anomalies is too small or large, the predicted geophysical anomalies are spatially smaller or larger than observed. The long-wavelength extent and trend of the geoid and dynamic topography (Fig. 2.3) are best reproduced with anomalous bodies that have longest diameter *a* approximately 4000 km, initially centered at 170°E and 75°S at 80 Ma. Since the observed anomalies are slightly elongated in the east-west direction (Fig. 2.3), parallel to the Antarctica margin, we choose *b*=3000 km. We tested a number of models with larger and smaller values of *a* and *b,* but they fail to reproduce the observed wavelengths.

2.6.2. Magnitude of buoyancy anomalies

From the conservation of momentum and energy, dynamic topography in uniform viscosity and layered viscosity domain can be described as:

$$h(t) = C_1(t)\Delta T \tag{6}$$

$$h(t) = C_2(t)\frac{\eta_{UM}}{\eta_{LM}}\Delta T \quad (7)$$

where h is dynamic topography, ΔT is temperature anomaly, C_1 and C_2 are numerical functions obtained from the solution of flow and are dependent on the viscosity and temperature structure, and η_{LM} and η_{UM} are viscosities of lower and upper mantle, respectively [*Gurnis et al.*, 2000]. The non-dimensional temperature anomaly is defined with respect to a temperature of 3000°C.

Assuming the observed bathymetric anomaly (Fig. 2.3B-C) can be attributed to dynamic topography, we use it to constrain the amplitude of the temperature anomaly. When we systematically vary the initial temperatures (Fig. 2.4), while holding the initial depths (d_u=1300 km and d_d=2000 km) and viscosity ratio (η_{LM} :η_{UM} = 100:1) constant, small values of ΔT_a=0.05 predict dynamic topography on order of only 100 m (Fig. 2.4A), significantly less than the observed 500-1000 m. For large values of ΔT_a (0.2 and 0.3), the predicted maximum dynamic topography is on the order of 5 km, much larger than observed (Fig. 2.4D-E). Observed present-day dynamic topography is reproduced with non-dimensional temperatures of 0.1-0.15 (Fig. 2.4B-C), with a best prediction of the geoid for ΔT_a=0.15 (Fig. 2.4C), and estimated error of 0.05.

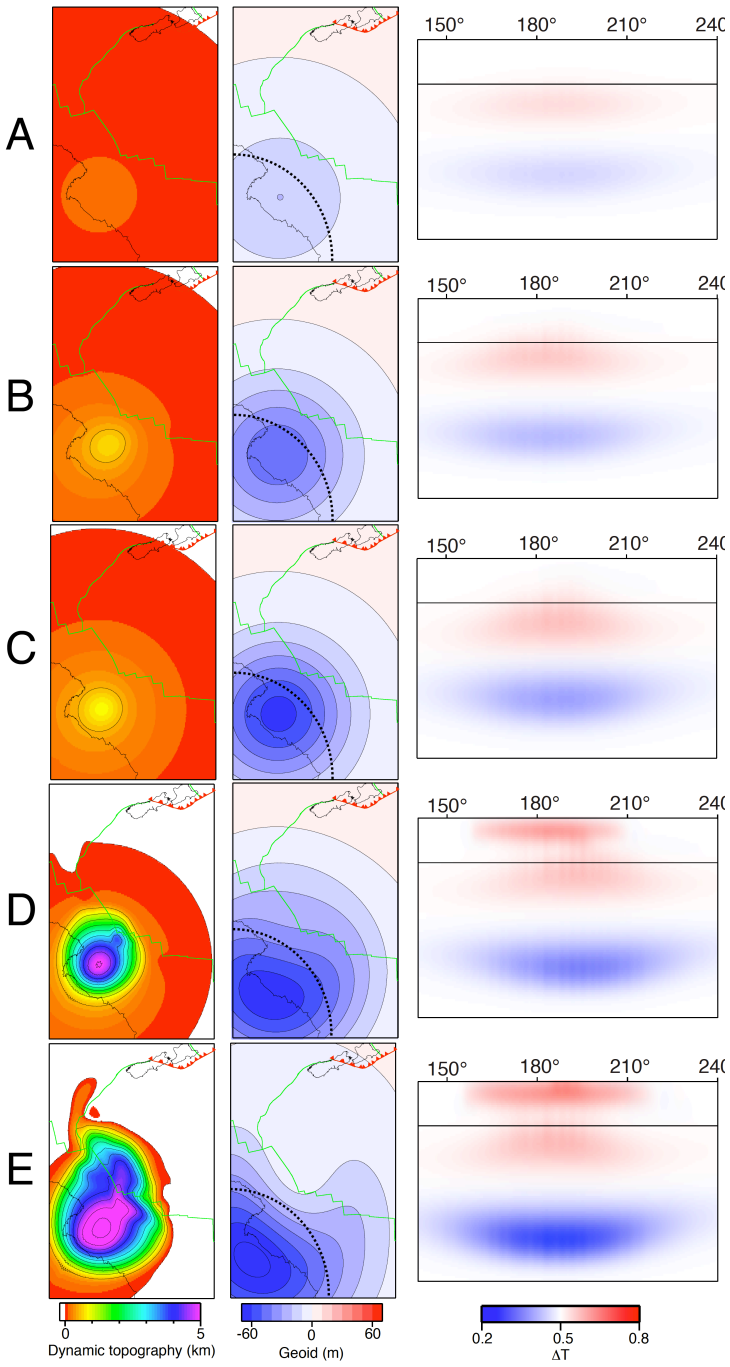

Figure 2.4. Constraining temperature anomaly based on predictions of dynamic topography (500 m contour interval), geoid (10 m countour interval), and upwelling geometry at 0 Ma for ΔT_a of 0.05 (A), 0.10 (B), 0.15 (C), 0.20 (D), and 0.30 (E). Green lines indicate position of mid-ocean ridges, red lines with triangles subduction zones, and dotted black lines indicate location of cross-sections. Cross-sections show whole mantle depth range, with position of 660 km discontinuity shown with horizontal black line.

For large non-dimensional temperatures of $\Delta T_a \geq 0.2$, the upwelling rises quickly, underplates the lithosphere, and overpredicts dynamic topography (Fig. 2.4D-E). Models with $\Delta T_a \geq 0.2$ reproduce both regions of sublithospheric and transition zone-upper mantle high temperatures (Fig. 2.4D-E), equivalent to the two low-seismic velocity regions evident in tomography. However, we find that dynamic topography is significantly overpredicted for all models with $\Delta T_a \geq 0.2$ and all models in which the main mantle upwelling underplates the lithosphere. Only when the main large upwelling ends up within the transition zone–upper lower mantle depth range (Fig 2.4B-C, ΔT_a=0.1-0.15), can we successfully match residual bathymetry (Fig. 2.3B), regardless of the initial depth or mantle viscosities.

There is a trade-off between the magnitude of the temperature anomaly and the mantle viscosities (Eq. 7). We iteratively varied ΔT_a and mantle viscosities, and found that ΔT_a in the range of 0.1-0.15 always best predicted dynamic topography. For all subsequent results, we fixed ΔT_a to 0.15, while noting a slight trade-off with other parameters if a slightly lower temperature is chosen.

2.6.3. Mantle viscosity structure and initial upwelling depths

Once we fix the geometry and amplitude of the temperature anomalies, which define the buoyancy forces, a trade-off remains between the initial anomaly depth and mantle viscosity. We systematically varied the ratio of $\eta_{LM} : \eta_{UM}$ and the initial depth of anomalies at 80 Ma (Fig. 2.5), with the model setup described in Section 2.6.1 and

ΔT_a=0.15. In addition to comparing predicted and observed geoid, present-day dynamic topography and Campbell plateau subsidence history, we also compare the predicted final geometry of the high-temperature anomaly with that of the observed mid mantle low-velocity anomaly (central depth approximately 700 km), to further constrain plausible initial depths for the anomaly and the mantle viscosity structure. All models with $\eta_{LM}:\eta_{UM}$≤60 significantly overpredict dynamic topography (Fig. 2.5A), reproduce either positive or small negative geoid anomalies (Fig. 2.5B), and result in shallow centroid depths of the upwelling anomaly at 0 Ma (Fig. 2.5D). The upwelling rises relatively quickly with lower viscosities, underplating the lithosphere and overpredicting dynamic topography, similar to models with ΔT_a≥0.2. Dynamic topography is also overpredicted when the initial depths d_u are shallower than 1300 km (Fig. 2.5A), while the geoid is underpredicted or has the wrong sign when d_u is deeper than 1300 km (Fig. 2.5B). Final centroid depths are less than 500 km for all models with initial d_u of 800 km and 1200 km.

Present-day observations of dynamic topography and geoid and appropriate mid-mantle centroid anomaly depths are simultaneously reproduced with a single model in which d_u is 1300 km and the viscosity ratio $\eta_{LM}:\eta_{UM}$ is 100. However, the fit to subsidence is only reproduced when $\eta_{LM}:\eta_{UM}$≤40 (Fig. 2.5C). We found that no model with a single upwelling and downwelling could reproduce all observations, even when the parameter range was expanded beyond that shown in Fig. 2.5. This indicates that our assumed initial geometry of the buoyancy anomalies must be

unrealistic, and that a more complex parameterization of initial conditions may be needed to match all observations.

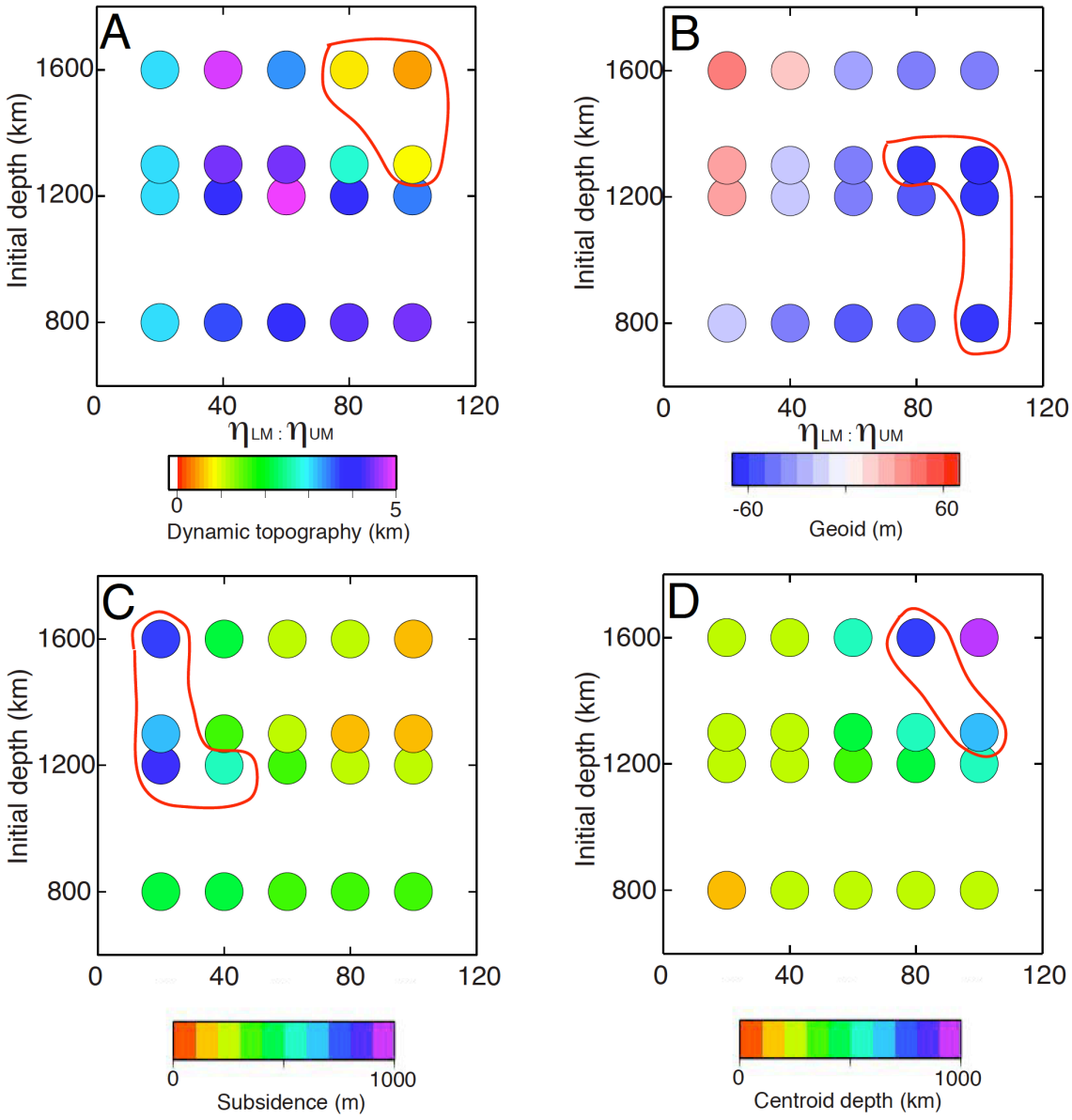

Figure 2.5. Constraining relative mantle viscosity ratio η_{LM}: η_{UM} and initial depth of upwelling anomaly utilizing dynamic topography (A), geoid (B), subsidence (C), and centroid depth of main upwelling anomaly at 0 Ma (D) as constraints. Red outlines indicate set of models satisfying individual constraints. Relative ratios are given with respect to background viscosity of 10^{21} Pa s.

2.6.4. More realistic initial conditions with a second upwelling

In order to match the history of Campbell plateau subsidence and observations of the modern topography, geoid, and tomography, we introduce an additional shallower low-density anomaly in the upper mantle below the reconstructed position of the Campbell plateau at 80 Ma (Fig. 2.6). The location is slightly closer to the surface trace of subduction and would be consistent with an additional shallow upwelling above a south-dipping slab that was subducted at the northern margin of the NZ continent [*Davy et al.*, 2008].

The best-fitting model has an additional hot anomaly with a=b=1500, c=500km, depth 500 km and ΔT_a =0.08, and its center is located at 160ºW and 68°S at 80 Ma, approximately 1200 km NE from the center of the main anomaly. The predicted Campbell plateau dynamic topography for this model at 80 Ma is about 750 m (Fig. 2.6A), with the maximum located on the NW part of the Campbell plateau. As ANT-NZ seafloor spreading progressed, the Campbell plateau (NZ) drifted northward with respect to ANT and the lower mantle (Fig. 2.6A), and moved across the region of high dynamic topography. By 40 Ma, the Campbell plateau had moved completely away from the dynamic topography high. As the larger and deeper upwelling arose from the lower mantle, it produced increased dynamic topography in the Ross Sea, reaching about 1000 m presently (Fig. 2.6A). The smaller and shallower upwelling was split as the spreading ridge passed over the anomaly during the Cenozoic (Fig. 2.6A), producing secondary dynamic topography highs with maximum amplitudes of about 600 m on either side of the Pacific-Antarctic ridge. The model ridge

topography (Fig. 2.6A) matches observed bathymetry along the spreading ridge (Fig. 2.3B). Dynamic topography associated with the shallow anomaly is dominant for most of the model history (Fig. 2.6D), with the effect of the deep-seated anomaly significantly increasing after 20 Ma, and reaching up to 1000 m at the present (Fig. 2.6D). The main upwelling in the model reached the upper mantle at about 20 Ma (Fig 6B), and is now located at 400-1000 km depth, where it matches the low-seismic-velocity anomaly at the transition zone and top of the lower mantle (Fig. 2.2). The smaller upwelling spread out beneath the oceanic lithosphere (Fig. 2.6B), where it matches the sublithospheric region of extremely slow seismic velocities (Fig. 2.2).

The present-day geoid anomaly predicted by this model is -62.5 m (Fig. 2.6F), which is close to the known amplitude (Fig. 2.6E). Considering the simplified geometry and parameterization of our model, the predictions match the general wavelength and location of geoid and topography anomalies well. The amplitude and sign of the geoid are primarily controlled by both the depth of the deep-seated upwelling anomaly at 0 Ma and the relatively large ratio of upper to lower mantle viscosities.

When we track dynamic topography of the Campbell plateau (Fig. 2.6A) from 80 to 0 Ma, we calculate that total excess subsidence of the Campbell plateau is 750 m, which mostly results from the northward drift of the Campbell plateau away from the upwelling. For comparison, when we attempt to match the observed tectonic subsidence of the Campbell plateau with a stretching model alone (no dynamic topography), the subsidence is under predicted by 500-900 m (Fig. 2.7A, grey line).

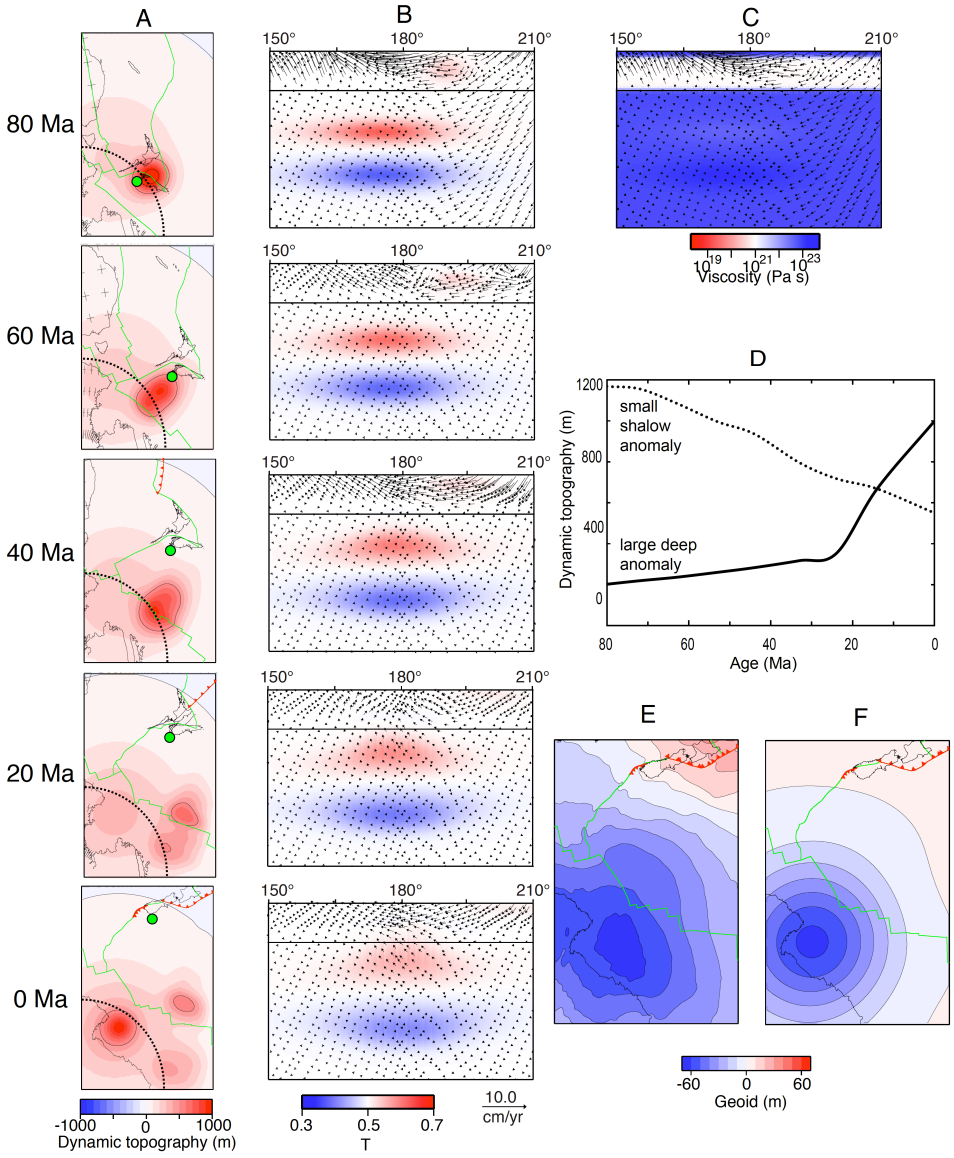

Figure 2.6. Modeling results for a model with two hot anomalies evolving above a cold anomaly (η_{LM}: η_{UM}=100:1, with respect to viscosity of 10^{21} Pa s). (A) Dynamic topography predictions (500 m contour interval). (B) Cross-sections of temperature field at 70°S with velocity vectors overlain. (C) Cross-section of viscosity field at 70°S and 80 Ma with velocity vectors overlain. (D) Evolution of the maximum amplitude of dynamic tomography over the smaller shallow upwelling (dotted line) and the main large upwelling (solid line). (E) Geoid observation [*Förste et al.*, 2008]. (F) Geoid model predictions. Green lines indicate position of mid-ocean ridges, red lines with triangles subduction zones [*Gurnis et al.,* 2009], and dotted black lines indicate location of cross-sections. Cross-sections show whole mantle depth range, with position of 660 km discontinuity shown with horizontal black line (B) or discontinuity in viscosity field (C). The reconstructed location of Campbell plateau is shown with green dot (A).

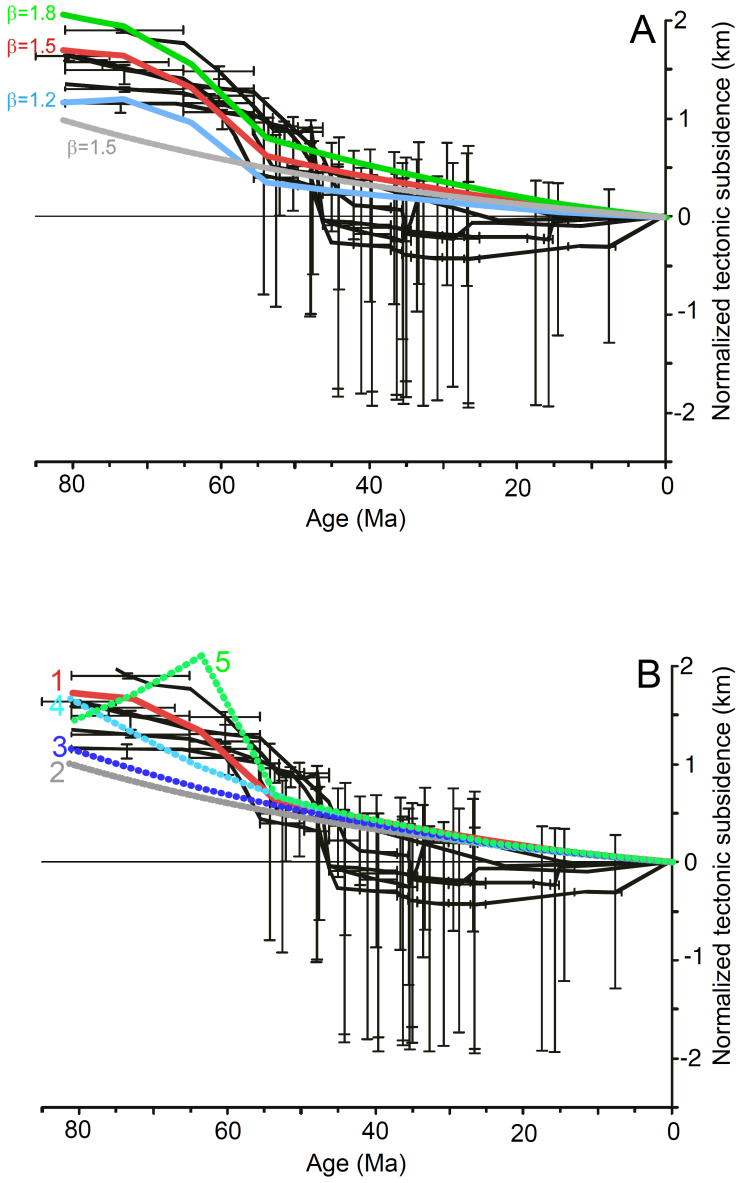

Figure 2.7. Tectonic subsidence of the Campbell plateau. (A) Tectonic subsidence for five wells (black lines) compared with thermal subsidence only (grey line) and thermal+dynamic subsidence for β=1.2 (blue line), β=1.5 (red line) and β=1.8 (green line). (B) Comparison between tectonic subsidence prediction between (1) the best model described in Section 2.4.4; (2) thermal subsidence model with β=1.5; (3) model with a single hot anomaly rising from initial depth 1300 km in a mantle with η_{LM}: η_{UM}=100:1; (4) model with a single hot anomaly rising from depth of 1600 km in a mantle with η_{LM}: η_{UM}=20:1; and (5) model with additional shallower anomaly with rising from central depth of 500 km and ΔT_a=0.11. Error bars indicate uncertainty in determining paleo water depths.

When the predicted dynamic topography is added to a model of thermal subsidence (Fig. 2.7A), the total observed tectonic subsidence is well matched by assuming a stretching factor β=1.5, which is a typical value estimated from crustal thickness or fault heaves from near to the wells that were considered [*Cook et al.*, 1999]. The maximum predicted subsidence rate occurs around 60 Ma, coincident with an observed transition from shallow to deep-water environments in the wells (Fig. 2.7A), and it resulted from the drift of the Campbell plateau away from the upwelling (Fig. 2.6A).

Models with a single large mantle upwelling centered at the ANT margin always under-predict Campbell plateau tectonic subsidence (Fig. 2.7B, blue and cyan curves), and never reproduce the observed inflexion in subsidence rate. Models in which a smaller secondary upwelling anomaly is located slightly deeper at 80 Ma and with a higher-amplitude temperature anomaly, could reproduce the total amplitude of tectonic subsidence, but the shape of the predicted subsidence curve fits the observations slightly worse (Fig. 2.7B, green curve). The exact shape and amplitude of the Campbell plateau subsidence curves is strongly controlled by the movement of the plateau with respect to the dynamic topography high (Fig. 2.6D), so several models with different initial geometries and ΔT_a of the smaller hot anomaly could reproduce observations equally well, because observations have poor spatial coverage.

2.6.5. Absolute values of mantle viscosities

Instantaneous mantle convection models with seismic tomography, geoid, and/or dynamic topography as constraints (e.g., *Hager* [1984]; *King and Masters* [1992]; *Steinberger and Calderwood* [2006]) can be used to derive a radial relative viscosity profile, while postglacial rebound observations are used to derive absolute viscosities (e.g., *Milne et al.* [2004]; *Mitrovica and Forte* [2004]). We show above that observations of geoid and dynamic topography in the ANT-NZ region require a high η_{LM} :η_{UM} ratio of about 100:1 (Fig. 2.5). However, since we have observations of tectonic subsidence as a function of time and seismic tomographic models constrain the present depths of buoyancy anomalies, we can also constrain absolute viscosities within the mantle. For our best-fitting model (section 2.6.4), which includes two hot anomalies at different depths, we systematically vary the absolute value of lower mantle viscosity for models with d_u (depth to larger hot anomaly) of 800 km, 1300 km, and 1600 km (Fig. 2.8).

For models with $\eta_{LM} \leq 10^{22}$ Pa s, the hot anomaly rises too quickly, underplates the lithosphere by 0 Ma (Fig. 2.8D), over predicts dynamic topography (Fig. 2.8A) and subsidence (Fig. 2.8C), while yielding positive geoids (Fig. 2.8B). If the lower mantle viscosity is higher, with η_{LM} of 10^{24} Pa s, the upwelling anomaly rises more slowly, generally resulting in large centroid depths of mid mantle anomaly at 0 Ma (Fig. 2.8D), while under predicting dynamic topography (Fig. 2.8A), the geoid (Fig. 2.8B) and dynamic subsidence (Fig. 2.8C). For a narrow range of lower mantle viscosities η_{LM}=2x10^{22} to 1x10^{23} Pa s, dynamic topography is close to the observed 0.5-1.0 km

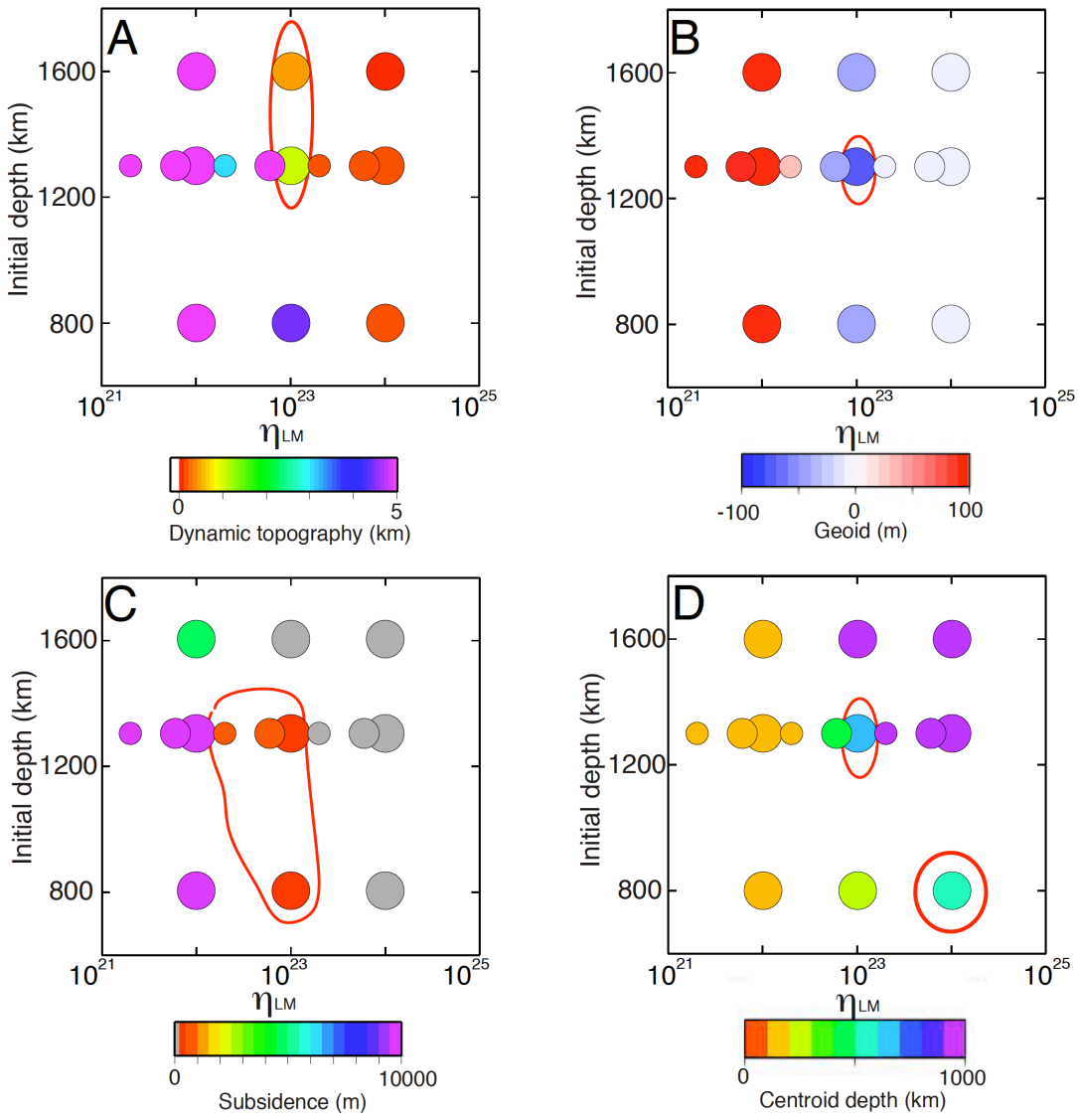

Figure 2.8. Constraining absolute mantle viscosity and initial depth of upwelling anomaly utilizing dynamic topography (A), geoid (B), subsidence (C), and centroid depth of upwelling anomaly at 0 Ma (D) as constraints. The largest circles indicate models with η_{LM}: η_{UM}=100:1, intermediate circles models with η_{LM}: η_{UM}=60:1, and the smallest circles with η_{LM}: η_{UM}=20:1. Red outlines indicate set of models satisfying individual constraints.

for depths d_u<1600 km (Fig. 2.8C). Observations of dynamic topography and geoid (Fig. 2.8A-B) require lower mantle viscosity η_{LM}=10^{23} Pa s, and only depths close to

d_u = 1300 km yield acceptable predictions for all observations. Although a model with the shallow upwelling (800 km) and stiff lower mantle (η_{LM}=10^{24} Pa s) produces reasonable mid mantle centroid upwelling depths compared to seismic tomography (Fig. 2.8D), the model underestimates all other parameters (Fig. 2.8A-C).

2.7. Discussion

2.7.1. Mantle dynamics and viscosity structure

We can fit both the present-day (geoid, dynamic tomography, and seismic structure) and time-dependent (tectonic subsidence of Campbell plateau) observations in a single dynamic model with a relatively simple initial geometry and viscosity structure. We define thermal anomalies as triaxial ellipsoids that are designed to reproduce the large-scale characteristics of mantle flow and evolution, rather than to match the exact shape and extent imaged in seismic tomography. In reality, these anomalies certainly have a more complex geometry, but since tomography models differ significantly in their detail of mid mantle and lower mantle seismic-velocity structure [*Grand*, 2002; *Gu et al.*, 2001; *Masters et al.*, 2000; *Ritsema and van Heijst*, 2000], we choose to use simplified forward models designed to match the general geometrical characteristics and depth ranges of the largest anomalies. When the resolution and coverage of tomography models in the Antarctica-New Zealand region are improved, it will be possible to better separate and define the position

and shape of the velocity anomalies of interest (in particular the mid mantle velocity low and lower mantle velocity high), and seismic properties could then be used as input to inverse models that have a more complex parameterization (e.g*. Liu et al.* [2008]). We also simplify the definition of the boundary layers in a way that is appropriate for the tectonic setting. The top boundary layer is treated as a layer with a high viscosity, with the temperature being equal to the background mantle temperature. This formulation is appropriate since the study region is dominated by divergent boundaries during the whole model history, and the buoyancy anomalies were dominated by advection below the lithosphere when the model results were compared with the observations. A bottom thermal boundary layer is also neglected because the region since the Late Cretaceous was dominated by a large downwelling associated with subducted Gondwana slabs without any active plumes rising from the core-mantle boundary.

Based on the spatial scale of the Ross Sea geoid and topography anomaly, we define the largest (one hot and one cold) buoyancy anomalies to have lateral and vertical dimensions of 4000 km and 600-800 km, respectively. Based upon our fit to the observed present-day dynamic topography and geoid, we determine a maximum temperature anomaly of approximately 450°C, giving an average temperature anomaly within the rising upwelling of about 200°C. Based on direct conversion of seismic velocities to thermal anomalies, maximum temperature anomalies have previously been estimated to be +600°C at 1400 km depth beneath the Ross Sea, and -400°C at 2800 km depth [*Deschamps and Trampert*, 2003]. The global average of temperature variability is estimated to be approximately 190°C at 1400 km depth

[*Deschamps and Trampert*, 2003], while temperature anomalies close to the CMB could reach as much as 900°C [*Deschamps and Trampert*, 2003; *Forte and Mitrovica*, 2001]. Accounting for both a thermal and compositional origin for tomographic anomalies, temperature variation is estimated to be between 200°C [*Karato and Karki*, 2001] and 300°C [*Deschamps and Trampert*, 2003] for upper parts of the lower mantle; and 300-400°C for mid mantle [*Deschamps and Trampert*, 2003]; and 500°C [*Deschamps and Trampert*, 2003] to more than 1000°C [*Karato and Karki*, 2001] for the lowermost mantle. Although the temperature anomaly we infer is in the range of values suggested by these studies, it should be noted that we assume that the entire upwelling/downwelling anomaly is thermal. It is possible that a part of the buoyancy we infer is compositional, which could result in lower estimates of temperature anomalies beneath the ANT margin. If the anomalies were entirely thermal in origin, the corresponding average density difference between the anomaly and the ambient mantle would be about 0.6%. In addition, we use a constant coefficient of thermal expansion (Table 2.1). If a depth-dependent coefficient was used, we would have obtained different estimates of thermal anomaly, but the estimated value of density anomaly would remain unchanged.

By simultaneously introducing instantaneous and time-dependent observations, we are able to infer both relative and absolute mantle viscosities for the assumed initial geometry. Seismic tomography provides information on the present-day distribution of mantle heterogeneity, and is the result of the history of mantle flow. The lower-to-upper mantle viscosity ratio that we find is best able to fit all observations is about 100:1, with present-day dynamic topography and geoid giving

the strongest constraints. Time-dependent observations impose important constraints on the absolute value of the viscosities, with a lower mantle viscosity of 10^{23} Pa s and an upper mantle viscosity of 10^{21} Pa s giving the most acceptable fits. A stiffer mantle, having lower mantle viscosity higher than 10^{23} Pa s, results in underestimated dynamic topography, geoid, and tectonic subsidence, with an overestimated final depth of buoyant anomalies. A less viscous mantle, with lower mantle viscosity being smaller than 10^{23} Pa s, results in a relatively rapid rise of anomalies, over predicting tectonic subsidence and dynamic topography, while having final depth of hot anomaly too shallow. The best initial depth of the large upwelling anomaly in our models is around 1300 km. When individual observational constraints are imposed separately, we find a trade-off between initial depth and viscosity, where deep anomaly/less viscous mantle can give an equally well-constrained prediction as shallow anomaly/more viscous mantle. However, when the observations are used jointly, a narrower range of possible mantle viscosities and anomaly depths are found.

Absolute viscosities can be independently obtained by inversion of postglacial rebound rates [*Milne et al.*, 2004] or joint inversion of convection and glacial isostatic adjustment [*Mitrovica and Forte*, 2004]. Our preferred absolute lower mantle viscosity (10^{23} Pa s) is higher than values obtained by inversion of Fennoscandian GPS data [*Milne et al.*, 2004], while it fits well within the range of the values inferred by [*Mitrovica and Forte*, 2004]. Instantaneous flow models (e.g., *Hager* [1984]; *King and Master* [1992]; *Steinberger and Calderwood*, [2006]) constrained by the geoid are consistent with a jump of viscosities across the 660 km

discontinuity higher than 30, and possibly as high as 100. Therefore, our estimate of a jump at the base of the transition zone by a factor of 100 corresponds to the higher-end estimate obtained from instantaneous models. Our preferred value of relative viscosity ratio is significantly higher than η_{LM}: η_{UM}=15:1 obtained in an adjoint mantle convection model of North America, constrained by seismic tomography, stratigraphy and plate motion [*Liu et al.*, 2008; *Spasojevic et al.*, 2009]. In addition, our estimated lower mantle viscosity is an order of magnitude larger than the $\sim 10^{22}$ Pa s obtained by analytical calculations based on sinking velocities of a subducted fossil slab in the Tasman sea [*Schellart et al.,* 2009]. Differences in the ratio of mantle viscosities inferred by different geodynamic studies could partly be explained by global lateral variations in viscosity. The high viscosity ratio of 100 determined in this study could be related to the long history of subduction that accumulated cold material in the lower mantle, resulting in larger thermally-controlled viscosity contrasts between the upper and lower mantle, and the subduction history may also have regionally altered mantle chemistry. In addition, it should be noted it is possible that these upwelling anomalies are created in a more continuous process, in which upwellings are continuously fed by a process (e.g., slab dehydration), such that there is a constant influx of lower density material. We do not have ability to model such a process and we devised a simplified model in which upwelling with a shape defined at 80 Ma evolves to the present. If we had the ability to model a more continuous process, it is possible that estimated values of mantle viscosities would be different.

The correct sign and amplitude of the geoid could be reproduced only when the large-scale main upwelling is now positioned in the transition zone and top of the lower mantle. Since other mantle upwellings, such as the African superswell and the Iceland and Hawaii plume, are associated with large geoid highs [*Richards et al.*, 1988], the Ross Sea region appears to be rather unique. Geoid dynamic response functions [*Hager*, 1984; *Richards and Hager*, 1984] for a range of wavelengths suggest that both buoyant upwellings in the transition zone and dense slabs in the lower mantle could produce geoid lows, if the viscosity of the upper mantle is significantly less than that of the lower mantle. Alternatively, response functions for a long-wavelength upwelling located in the lower mantle (e.g., African superswell), or a shorter-wavelength anomaly located in the upper mantle (e.g., Hawaii or Iceland), predict a positive geoid response, assuming an appropriate viscosity contrast [*Richards and Hager*, 1984]. Our models demonstrate that the Ross Sea geoid low can be attributed to sharper mantle viscosity gradients and/or the intermediate wavelength of the upwelling at mid mantle depths.

2.7.2. Regional geologic and tectonic implications

Our models were constructed only to fit observations of modern topography, geoid, and seismic-wavespeed anomalies, and the 80-0 Ma subsidence history of the Campbell Plateau. However, the models have indirect implications for other geologic observables, such as the composition of the mantle and derived melts through time.

In addition, the very basic conclusion that such a class of model with upwellings and a downwelling is required by the regional geology and geophysics is worthy of discussion.

The tectonic subsidence histories that we predict are derived from tracking a point on the surface of the Pacific plate as it moved northward across the upper boundary of evolving mantle flow. The shallower and smaller of the discrete upwellings that we infer was initially located beneath the reconstructed Campbell plateau at 80 Ma, where it created a long-lived dynamic topography high that we infer to be partially responsible for anomalously shallow depths to the Pacific-Antarctic rise and adjacent seafloor to Marie Byrd Land. As the Campbell plateau moved northward, it experienced subsidence as it moved off the dynamically supported high. In contrast, the Australian and North American continents are shown to have experienced tectonic subsidence as they moved across mantle downwellings associated with relict slabs [*Gurnis et al.*, 1998; *Spasojevic et al.*, 2009]. Our study further demonstrates that understanding the evolution of mantle flow beneath sedimentary basins is fundamental to predicting their subsidence histories.

We have not attempted to model all the known subsidence histories from around New Zealand, which are complicated by development of the Cenozoic Australia-Pacific plate boundary. However, we suggest it is significant that paleoenvironments inferred for most sedimentary basins around New Zealand were non-marine at c. 85 Ma [*Cook et al.*, 1999; *King et al.*, 1999; *Laird and Bradshaw*, 2004]. It is significant because rifting was already complete and crustal thickness was typically in the

range 20-30 km, so global experience and comparison with the modern setting suggest that it should have been at or below sea level in the absence of dynamic topography associated with mantle flow. The widespread erosion surface that resulted from having an elevation above sea level was called the "Waipounamu Erosion Surface" by *LeMasurier and Landis* [1996] and was inferred by them to have been caused by dynamic topography.

The conclusion that Late Cretaceous dynamic topography existed in southern NZ is implicit in the observed rapid subsidence of the Campbell Plateau during the interval 70-40 Ma, as it moved off the elevated region. This is the reason why we had to introduce an additional shallow mantle upwelling at 80 Ma below NZ (further north of the main deeper upwelling). We are not able to determine the precise pattern of mantle upwelling in the Late Cretaceous beneath southern NZ, due to the sparse observations, but we can constrain the source to have been relatively shallow (transition zone or upper mantle).

Three general classes of upwellings and hence hotspots have previously been identified [*Courtillot et al.*, 2003]: (1) upwellings that originate from the CMB region, (2) upwellings originating from the bottom of the transition zone, and (3) upper mantle plumes; but the upwellings we propose do not correspond to any of the previously identified types. While specific phase transitions may lead to a layered viscosity and density structure and hence to certain modes of plume behavior, we suggest that the role of subduction in the genesis of instabilities that lead to upwelling may have been overlooked [*Sutherland et al.*, 2009]. Slabs that pass

through the transition zone may sequester H_2O in superhydrous B [*Ohtani et al.*, 2003] or D phases [*Hirschmann*, 2006]. *Ohtani et al.* [2004] suggest that decomposition of superhydrous phases could occur at depths as large as 1250 km, resulting in hydration and/or melting of the mantle. Therefore, it is possible that the seismic-low-velocity region imaged in the mid mantle below the Antarctic-New Zealand region has been created by chemical and/or hydration reaction of mantle with subducting slabs below 660 km depth. If such a process is continuously active during subduction, it is possible that buoyancy anomalies have been created continuously, extending from mid mantle depths to the surface. Buoyant material may be released to become upwellings when changes in subduction rate or the termination of subduction occurs and the competing downward force is reduced [*Sutherland et al.*, 2009]. The predicted correlation between reduction in subduction rate and subsequent mantle upwelling could be tested by analysis of the geologic record from ancient subduction systems for which it is possible to compute the past subduction rate.

Tests of the plume generation hypothesis presented above may rest with the details of the geochemistry of mantle-derived rocks. It is outside of our present scope to explore this subject in detail, but we do present a few relevant observations from the NZ-ANT region. Cretaceous igneous rocks from New Zealand have high U/Pb mantle (HIMU) isotopic signatures, interpreted to be plume-related, but Antarctic rocks do not [*Mukasa and Dalziel*, 2000; *Weaver et al.*, 1994]. In contrast, Late Cenozoic mafic igneous rocks are widespread in the Ross Sea and Marie Byrd Land and do have geochemistry that falls on a HIMU trend [*Behrendt et al.*, 1991; *Finn et*

al., 2005; *Rocchi et al.*, 2002]. Superficially, this seems in excellent agreement with the general characteristics of our models. However, to test the plume generation model that we propose requires a specific geochemical prediction from the model, and an understanding of the inherited geochemistry of the mantle, and of the lithospheric processes and chemical history near the sample site. A HIMU descriptor may not be optimal or appropriate. We conclude that initial interpretations support our models, but we leave the development of this discussion to more detailed future study.

2.8. Conclusions

Anomalous geophysical observations at NZ-ANT margin can be reproduced with a dynamic model in which two hot anomalies evolved above a cold downwelling related to Gondwana subduction. The main larger hot mantle anomaly, centered above the Ross Sea region, originates from a mid mantle depth range of 1000-1600 km at 80 Ma, and has an average temperature approximately 200°C higher than the background mantle. If the anomalies were thermal in origin, the corresponding average density variation between the anomaly and background mantle would be about 0.6%. This buoyant anomaly reached the upper mantle at approximately 20 Ma, and it evolved to a present-day depth range of 400-1000 km, resulting in up to 1 km of dynamic topography that is now observed along the ANT margin.

Campbell plateau subsidence and present-day residual bathymetry of the Antarctica-Pacific ridge is related to evolution of an additional hot anomaly, located at 80 Ma in the upper mantle, and which has now underplated the lithosphere to form a shallow seismic-low-velocity anomaly. The mantle upwelling creates a long-lived dynamic topography high, and the anomalous Campbell plateau subsidence was a result of northward drift away from this dynamic topography high.

By using present-day (geoid, dynamic topography, and seismic tomography) and time-dependent (tectonic subsidence) observations, we are able to infer both relative and absolute mantle viscosities. The relative viscosity ratio is rather high, with η_{LM}:η_{UM}=100:1, and the steep gradient of the viscosities could be created by long-lived Gondwanaland subduction that resulted in an extensive pile-up of denser and more viscous material in the lower mantle that is overlain by a region of hydration. The absolute viscosities of the upper and lower mantle in the NZ-ANT region are 10^{21} and 10^{23}, respectively.

The Ross Sea geoid low can be reproduced only when the large-scale main upwelling anomaly is positioned across the transition zone and top of the lower mantle. This globally significant geoid low is reproduced in our model through a combination of the intermediate wavelength of upwelling and the high gradient of mantle viscosity.

References

Adams, C. J., H. J. Campbell, and W. L. Griffin (2007), Provenance comparisons of Permian to Jurassic tectonostratigraphic terranes in New Zealand: Perspectives from detrital zircon age patterns, *Geological Magazine*, *144*(4), 701–729.

Allmendinger, R. W., T. E. Jordan, S. M. Kay, and B. L. Isacks (1997), The evolution of the Altiplano-Puna plateau of the Central Andes, *Annual Review of Earth and Planetary Sciences*, *25*, 139–174.

Behrendt, J. C., W. E. LeMasurier, A. K. Cooper, F. Tessensohn, A. Trefu, and D. Damaske (1991), Geophysical studies of the west Antarctic rift arm, *Tectonics*, *10*, 1257–1273.

Bina, C. R., and G. Helffrich (1994), Phase-transition Clapeyron slopes and transition zone seismic discontinuity topography, *Journal of Geophysical Research, 99*(B8), 15853–15860.

Bradshaw, J. D. (1989), Cretaceous geotectonic patterns in the New Zealand region, *Tectonics*, *8*(4), 803–820.

Bradshaw, J. D., R. J. Pankhurst, S. D. Weaver, B. C. Storey, R. J. Muir, and T. R. Ireland (1997), New Zealand superterranes recognized in Marie Byrd Land and Thurston Island, *International Symposium on Antarctic Earth Sciences*, *7*, 429–436.

Cande, S. C., C. A. Raymond, J. Stock, and W. F. Haxby (1995), Geophysics of the Pitman Fracture Zone, *Science*, *270*, 947–953.

Chase, C. G., and D. R. Sprowl (1983), The modern geoid and ancient plate boundaries, *Earth and Planetary Science Letters*, *62*(3), 314–320.

Chase, C. G. (1985), The geological significance of the geoid, *Annual Review of Earth and Planetary Sciences*, *13*, 97–117.

Cook, R. A., R. Sutherland, and H. Zhu (1999), *Cretaceous-Cenozoic geology and petroleum systems of the Great South Basin, New Zealand*, 188 pp., Institute of Geological and Nuclear Sciences Limited, Lower Hutt, New Zealand.

Courtillot, V., A. Davaille, J. Besse, and J. Stock (2003), Three distinct types of hotspots in the Earth's mantle, *Earth and Planetary Science Letters*, *205*(3-4), 295–308.

Crough, S. T. (1983), The correction for sediment loading of the seafloor, *Journal of Geophysical Research*, *88*(B8), 6449–6454.

Cunningham, A. P., R. D. Larter, P. F. Barker, K. Gohl, and F. O. Nitsche (2002), Tectonic evolution of the Pacific margin of Antarctica 2. Structure of Late Cretaceous-early Tertiary plate boundaries in the Bellingshausen Sea from seismic reflection and gravity data, *Journal Of Geophysical Research*, *107*(B12), 2346, doi:10.1029/2002JB001897.

Dalziel, I. W. D., and D. H. Elliot (1982), West Antarctica: Problem child of Gondwanaland, *Tectonics*, *1*, 3–19.

Davy, B. W., K. Hoernle, and R. Werner (2008), Hikurangi Plateau: crustal structure, rifted formation, and Gondwana subduction history, *Geochemistry Geophysics Geosystems*, *9(7)*, Q07004, doi:07010.01029/02007GC001855.

Deschamps, F., and J. Trampert (2003), Mantle tomography and its relation to temperature and composition, *Physics of the Earth and Planetary Interiors*, *140*(4), 277–291.

Ferris, J. K., A. P. M. Vaughan, and B. C. Storey (2000), Relics of a complex triple junction in the Weddell Sea embayment, Antarctica, *Earth and Planetary Science Letters*, *178*(3–4), 215–230.

Finn, C. A., R. D. Mueller, and K. S. Panter (2005), A Cenozoic diffuse alkaline magmatic province (DAMP) in the southwest Pacific without rift or plume origin, *Geochemistry, Geophysics, and Geosystems*, *6*, Q02005, doi: 02010.01029/ 02004GC000723.

Flanagan, M. P., and P. M. Shearer (1998), Global mapping of topography on transition zone velocity discontinuities by stacking SS precursors, *Journal of Geophysical Research*, *103*(B2), 2673–2692.

Förste, C., R. Schmidt, R. Stubenvoll, F. Flechtner, U. Meyer, R. Konig, H. Neumayer, R. Biancale, J. M. Lemoine, S. Bruinsma, S. Loyer, F. Barthelmes, and S. Esselborn (2008), The GeoForschungsZentrum Potsdam/Groupe de Recherche de Geodesie Spatiale satellite-only and combined gravity field models: EIGEN-GL04S1 and EIGEN-GL04C, *Journal of Geodesy*, *82*(6), 331–346.

Forte, A. M., and J. X. Mitrovica (2001), Deep-mantle high-viscosity flow and thermochemical structure inferred from seismic and geodynamic data, *Nature*, *410*(6832), 1049–1056.

Gaina, C., D. R. Mueller, J.-Y. Royer, J. Stock, J. L. Hardebeck, and P. Symonds (1998), The tectonic history of the Tasman Sea: A puzzle with 13 pieces, *Journal of Geophysical Research*, *103*(6), 12,413–12,433.

Grand, S. P. (2002), Mantle shear-wave tomography and the fate of subducted slabs, *Philosophical Transactions of the Royal Society of London Series A-Mathematical Physical and Engineering Sciences*, *360*(1800), 2475–2491.

Gu, Y. J., A. M. Dziewonski, W. J. Su, and G. Ekstrom (2001), Models of the mantle shear velocity and discontinuities in the pattern of lateral heterogeneities, *Journal of Geophysical Research*, *106*(B6), 11169–11199.

Gurnis, M., R. Müller, and L. Moresi (1998), Cretaceous Vertical Motion of Australia and the AustralianAntarctic Discordance, *Science*, *279*(5356), 1499–1504.

Gurnis, M., J. Mitrovica, J. Ritsema, and H. van Heijst (2000), Constraining mantle density structure using geological evidence of surface uplift rates: The case of the African superplume, *Geochemistry, Geophysics. Geosystems*, *1*(7), 1020.

Gurnis, M., M. Turner, L. DiCaprio, S. Spasojevic, R. D. Müller, J. Boyden, M. Seton, V. C. Manea, and V. Bower (2009), Global Plate Reconstructions with Continuously Closing Plates, *Geochemistry, Geophysics, Geosystems*, in review.

Hager, B. H. (1984), Subducted slabs and the geoid - Constraints on mantle rheology and flow, *Journal of Geophysical Research*, *89*(B7), 6003–6015.

Hager, B. H., R. W. Clayton, M. A. Richards, R. P. Comer, and A. M. Dziewonski (1985), Lower mantle heterogeneity, dynamic topography and the geoid, *Nature*, *313*(6003), 541–546.

Herve, F., R. J. Pankhurst, C. M. Fanning, M. Calderon, and G. M. Yaxley (2007), The South Patagonian batholith: 150 my of granite magmatism on a plate margin, *Lithos*, *97*(3-4), 373–394.

Hirschmann, M. M. (2006), Water, melting, and the deep Earth H2O cycle, *Annual Review of Earth and Planetary Sciences*, *34*, 629–653.

Houser, C., G. Masters, M. Flanagan, and P. Shearer (2008), Determination and analysis of long-wavelength transition zone structure using SS precursors, *Geophysical Journal International*, *174*(1), 178–194.

Karato, S., and B. B. Karki (2001), Origin of lateral variation of seismic wave velocities and density in the deep mantle, *Journal of Geophysical Research 106*(B10), 21771–21783.

Kimbrough, D. L., A. J. Tulloch, D. S. Coombs, C. A. Landis, M. R. Johnston, and J. M. Mattinson (1994), Uranium-lead zircon ages from the Median Tectonic Zone, South Island, New Zealand, *New Zealand Journal of Geology and Geophysics*, *37*(4), 393–419.

King, P.R. (2000), Tectonic reconstructions of New Zealand 40 Ma to the present. *New Zealand Journal of Geology and Geophysics, 43*(4), 611–638.

King, P. R., T. R. Naish, G. H. Browne, B. D. Field, and S. W. Edbrooke (1999), Cretaceous to Recent sedimentary patterns in New Zealand, *Institute of Geological and Nuclear Sciences folio series*, *1*.

King, S. D., and G. Masters (1992), An inversion for radial viscosity structure using seismic tomography, *Geophysical Research Letters*, *19*(15), 1551–1554.

Laird, M. G., and J. D. Bradshaw (2004), The break-up of a long-term relationship: the Cretaceous separation of New Zealand from Gondwana, *Gondwana Research*, *7*(1), 273–286.

Larter, R. D., A. P. Cunningham, and P. F. Barker (2002), Tectonic evolution of the Pacific margin of Antarctica 1. Late Cretaceous reconstructions, *Journal of Geophysical Research*, *107*(B12), 2345, doi:10.1029/2000JB000052.

Lawver, L. A., J.-Y. Royer, D. T. Sandwell, and C. R. Scotese (1987), Evolution of the Antarctic continental margins, in *Geological evolution of Antarctica*, edited by M. R. A. Thomson, et al., 533–539, Cambridge University Press, Cambridge, UK.

LeMasurier, W. E., and C. A. Landis (1996), Mantle-plume activity recorded by low-relief erosion surfaces in West Antarctica and New Zealand, *Geological Society of America Bulletin*, *108*(11), 1450–1466.

Liu, L., S. Spasojević and M. Gurnis (2008), Reconstructing Farallon plate subduction beneath North America back to the Late Cretaceous, *Science, 322,* 934–938, doi:10.1126/science.1162921, 2008.

Marks, K. M., and A. A. Tikku (2001), Cretaceous reconstructions of East Antarctica, Africa and Madagascar, *Earth and Planetary Science Letters*, *186*(3-4), 479–495.

Masters, G., G. Laske, H. Bolton, and A. Dziewonski (2000), The relative behavior of shear velocity, bulk sound speed, and compressional velocity in the mantle: Implications for chemical and thermal structure, in *Geophysical Monograph Series*, edited by S. Karato, et al., 63–88, American Geophysical Union, Washington DC.

Mazengarb, C., and D. H. M. Harris (1994), Cretaceous stratigraphic and structural relationships of Raukumara Peninsula, New Zealand: Stratigraphic patterns associated with the migration of a thrust system, *Annales Tectonicae*, *8*(2), 100–118.

McCarron, J. J., and R. D. Larter (1998), Late Cretaceous to early Tertiary subduction history of the Antarctic Peninsula, *Journal of the Geological Society of London*, *155*, 255–268.

Milne, G. A., J. X. Mitrovica, H. G. Scherneck, J. L. Davis, J. M. Johansson, H. Koivula, and M. Vermeer (2004), Continuous GPS measurements of postglacial adjustment in Fennoscandia: 2. Modeling results, *Journal of Geophysical Research*, *109*(B2), B02412, doi:10.1029/2003JB002619.

Mitrovica, J. X., and A. M. Forte (2004), A new inference of mantle viscosity based upon joint inversion of convection and glacial isostatic adjustment data, *Earth and Planetary Science Letters*, *225*(1–2), 177–189.

Molnar, P., T. Atwater, J. Mammerickx, and S. M. Smith (1975), Magnetic anomalies, bathymetry and the tectonic evolution of the South Pacific since the late Cretaceous, *Geophysical Journal of the Royal Astronomical Society*, *40*, 383–420.

Mortimer, N., R. H. Herzer, P. B. Gans, D. L. Parkinson, and D. Seward (1998), Basement geology from Three Kings Ridge to West Norfolk Ridge, Southwest Pacific Ocean: Evidence from petrology, geochemistry and isotopic dating of dredge samples, *Marine Geology*, *148*(3–4), 135–162.

Mortimer, N., A. J. Tulloch, R. N. Spark, N. W. Walker, E. Ladley, A. Allibone, and D. L. Kimbrough (1999), Overview of the Median Batholith, New Zealand: A new interpretation of the geology of the Median Tectonic Zone and adjacent rocks, *Journal of African Earth Sciences*, *29*(1), 257–268.

Muir, R. J., S. D. Weaver, J. D. Bradshaw, G. N. Eby, and J. A. Evans (1995), The Cretaceous Separation Point Batholith, New Zealand: Granitoid magmas formed by

melting of mafic lithosphere, *Journal of the Geological Society of London*, *152, Part 4*, 689–701.

Muir, R. J., T. R. Ireland, S. D. Weaver, J. D. Bradshaw, J. A. Evans, G. N. Eby, and D. Shelley (1998), Geochronology and geochemistry of a Mesozoic magmatic arc system, Fiordland, New Zealand, *Journal of the Geological Society*, *155*, 1037–1052.

Mukasa, S. B., and I. W. D. Dalziel (2000), Marie Byrd Land, West Antarctica: Evolution of Gondwana's Pacific margin constrained by zircon U-Pb geochronology and feldspar common-Pb isotopic compositions, *Geological Society of America Bulletin*, *112*(4), 611–627.

Müller, R. D., C. Gaina, A. Tikku, D. Mihut, S. C. Cande, and J. M. Stock (2000), Mesozoic/Cenozoic tectonic events around Australia, *Geophysical Monograph*, *121*, 161–188.

Nürnberg, D., and R. D. Müller (1991), The tectonic evolution of the South-Atlantic from Late Jurassic to present, *Tectonophysics*, *191*(1-2), 27–53.

Ohtani, E., M. Toma, T. Kubo, T. Kondo, and T. Kikegawa (2003), In situ X-ray observation of decomposition of superhydrous phase B at high pressure and temperature, *Geophysical Research Letters*, *30*(2), 1029, doi: 10.1029/2002GL015549.

Ohtani, E., K. Litasov, T. Hosoya, T. Kubo, and T. Kondo (2004), Water transport into the deep mantle and formation of a hydrous transition zone, *Earth Planetary Science Letters*, *143–144*, 255–269.

Pankhurst, R. J., T. R. Riley, C. M. Fanning, and S. P. Kelley (2000), Episodic silicic volcanism in Patagonia and the Antarctic Peninsula: Chronology of magmatism associated with the break-up of Gondwana, *Journal of Petrology*, *41*(5), 605–625.

Paris, J.-P. (1981), Geologie de la Nouvelle-Caledonie: Un essai de synthese. Geology of New-Caledonia; a synthetic text, *Memoires du B.R.G.M.*, *113*, 1–278.

Richards, M. A., and B. H. Hager (1984), Geoid anomalies in a dynamic Earth, *Journal of Geophysical Research*, *89*(B7), 5987–6002.

Richards, M. A., B. H. Hager, and N. H. Sleep (1988), Dynamically supported geoid highs over hotspots - Observation and theory, *Journal of Geophysical Research*, *93*(B7), 7690–7708.

Ritsema, J., and H. J. van Heijst (2000), Seismic imaging of structural heterogeneity in Earth's mantle: Evidence for large-scale mantle flow, *Science Progress*, *83*, 243–259.

Ritzwoller, M. H., N. M. Shapiro, A. L. Levshin, and G. M. Leahy (2001), Crustal and upper mantle structure beneath Antarctica and surrounding oceans, *Journal of Geophysical Research*, *106*(B12), 30645–30670.

Rocchi, S., P. Armienti, M. D'Orazio, S. Tonarini, J. R. Wijbrans, and G. D. Vincenzo (2002), Cenozoic magmatism in the western Ross Embayment: Role of mantle plume versus plate dynamics in the development of the West Antarctic Rift System, *Journal of Geophysical Research*, *107*, 2195, doi: 2110.1029/ 2001JB000515.

Schellart, W. P., B.L.N. Kennett, W. Spakman, and M. Amaru (2009), Plate reconstructions and tomography reveal a fossil lower mantle slab below the Tasman Sea, *Earth Planetary Science Letters*, *278*(3–4), 143–151.

Sieminski, A., E. Debayle, and J. J. Leveque (2003), Seismic evidence for deep low-velocity anomalies in the transition zone beneath West Antarctica, *Earth and Planetary Science Letters*, *216*(4), 645–661.

Spasojevic, S., L. Liu, and M. Gurnis (2009), Adjoint models of mantle convection with seismic, plate motion and stratigraphic constraints: North America since the Late Cretaceous, *Geochemistry, Geophysics, Geosystems, 10,* Q05W02, doi: 10.1029/2008GC002345.

Steinberger, B., and A. R. Calderwood (2006), Models of large-scale viscous flow in the Earth's mantle with constraints from mineral physics and surface observations, *Geophysical Journal International*, *167*(3), 1461–1481.

Stock, J. M., and P. Molnar (1987), Revised history of early Tertiary plate motion in the South-west Pacific, *Nature*, *325*(6104), 495–499.

Storey, B. C., and P. A. R. Nell (1988), Role of strike-slip faulting in the tectonic evolution of the Antarctic Peninsula, *Journal of the Geological Society of London*, *145*(2), 333–337.

Storey, B. C. (1995), The role of mantle plumes in continental breakup - Case histories from Gondwanaland, *Nature*, *377*(6547), 301–308.

Storey, B. C., P. T. Leat, S. D. Weaver, R. J. Pankhurst, J. D. Bradshaw, and S. Kelley (1999), Mantle plumes and Antarctica-New Zealand rifting: evidence from mid-Cretaceous mafic dykes, *Journal of the Geological Society*, *156*, 659–671.

Sutherland, R. (1995), The Australia-Pacific boundary and Cenozoic plate motions in the SW Pacific: Some constraints from Geosat data, *Tectonics, 14(4)*, 819–831.

Sutherland, R. (1999a), Basement geology and tectonic development of the greater New Zealand region: An interpretation from regional magnetic data, *Tectonophysics*, *308*(3), 341–362.

Sutherland, R. (1999b), Cenozoic bending of New Zealand basement terranes and Alpine Fault displacement: A brief review, *New Zealand Journal of Geology and Geophysics, 42(2)*, 295–300.

Sutherland, R., S. Spasojevic, and M. Gurnis (2009), Mantle upwelling after Gondwana subduction death may explain anomalous topography of West Antarctica and subsidence history of eastern New Zealand, *Geology*, *38*(2), 155–158.

Tan, E., E. Choi, P. Thoutireddy, M. Gurnis, and M. Aivazis (2006), GeoFramework: Coupling multiple models of mantle convection within a computational framework, *Geochemistry Geophysics Geosystems, 7, Q06001,* doi: 10.1029/ 2005GC001155.

Veevers, J. J., P. J. Conaghan, and C. M. Powell (1994), Eastern Australia, *Geological Society of America Memoir*, *184*, 11–171.

Veevers, J. J. (2000), Synopsis of momentous events in Australi's billion year history, in *Billion-year earth history of Australia and neighbours in Gondwanaland: North Ryde, N.S.W.*, edited by J. J. Veevers, 344–348, Gemoc Press.

Waight, T. E., S. D. Weaver, and R. J. Muir (1998), Mid-Cretaceous granitic magmatism during the transition from subduction to extension in southern New Zealand; a chemical and tectonic synthesis, *Lithos*, *45*(1-4), 469–482.

Weaver, S. D., B. Storey, R. J. Pankhurst, S. B. Mukasa, V. J. Divenere, and J. D. Bradshaw (1994), Antarctica-New Zealand rifting and Marie Byrd Land lithospheric magmatism linked to ridge subduction and mantle plume activity, *Geology*, *22*(9), 811–814.

Weissel, J. K., D. E. Hayes, and E. M. Herron (1977), Plate tectonic synthesis: the displacements between Australia, New Zealand, and Antarctica since the late Cretaceous, *Marine Geology*, *25*, 231–277.

Zhong, S. J., M. T. Zuber, L. Moresi, and M. Gurnis (2000), Role of temperature-dependent viscosity and surface plates in spherical shell models of mantle convection, *Journal of Geophysical Research*, *105*(B5), 11063–11082.

Chapter 3

Mantle upwellings above slab graveyards linked to the global geoid lows[1]

The global belt of geoid lows forms a semi-continuous belt surrounding the Pacific, with isolated minima in the Indian Ocean, Ross Sea, northeast Pacific and west Atlantic (Fig. 3.1A). It has previously been suggested that the geoid lows are causally related to Mesozoic subduction [*Chase and Sprowl*, 1983; *Richards and Engebretson*, 1992], and geodynamic models with lower mantle slab graveyards inferred from seismic tomography or plate reconstructions are able to predict the general trend of geoid lows [*Hager and Richards*, 1989; *Steinberger*, 2000]. However, these models fail to accurately reproduce localized geoid minima in the Indian Ocean, Ross Sea, and northeast Pacific.

Here we show that geoid lows are correlated with high velocity anomalies near the base of the mantle and low velocity anomalies in the mid to upper mantle. Our mantle flow models demonstrate that mid to upper mantle upwellings have to be

[1] Published by Sonja Spasojevic, Michael Gurnis and Rupert Sutherland (2010) in *Nature Geoscience, 3,* 435 - 438, doi:10.1038/ngeo855.

positioned above the inferred positions of ancient subducted slabs to reproduce the geoid minima. We find that the high-density lower mantle slab graveyards reproduce the long-wavelength geoid trough, while upwellings shallower than 1000 km depth cause discrete lows within the larger trough. We suggest that this previously unrecognized mode of upwelling is caused by buoyant hydrated mantle that was created by processes around and above subducted slabs.

The shape of the global geoid is characterized by a semi-continuous 10-30 m amplitude negative anomaly surrounding the Pacific, with high-amplitude (–40 to –90 m) localized minima in the Indian Ocean, Ross Sea, northeast Pacific, and W. Atlantic within this trough (Fig. 3.1A). The more continuous eastern hemisphere low extends from Siberia through India into the Ross Sea. The more segmented western hemisphere low includes a north-south trending anomaly in the northeast Pacific and a zone that includes Hudson Bay and the western Atlantic. Localized geoid lows persist after isostatic corrections for the lithosphere have been applied [*Kaban et al.*, 2004]. Analysis of the gravity field as a simultaneous function of position and spectral content [*Simons and Hager*, 1997] shows that about half of the Hudson Bay anomaly could be explained by incomplete postglacial rebound, but such a mechanism cannot explain any significant component of the other geoid lows, because they are not correlated with positions of past ice sheets. The primary explanation for the shape of the geoid is related to heterogeneity and dynamics within the mantle [*Chase and Sprowl*, 1983; *Richards and Engebretson*, 1992].

It has been previously noted that geoid lows are globally correlated with locations of

Mesozoic subduction [*Chase and Sprowl*, 1983; *Richards and Engebretson*, 1992], while geoid highs are correlated with present-day subduction zones and hotspots [*Richards et al.*, 1988]. Active subduction zones are characterized by geoid highs due to a dominating positive mass anomaly of cold, upper mantle slabs compared to a low from dynamic topography [*Billen et al.*, 2003; *Richards and Hager*, 1984]. As slabs sink into the higher-viscosity lower mantle, the dynamic response functions switch sign [*Richards and Hager*, 1984], resulting in an association of lower mantle slabs with negative geoid anomalies. We analyzed global tomographic images of seismic velocity to explore the hypothesis that geoid lows are spatially correlated with slab graveyards and high seismic velocities [*Chase and Sprowl*, 1983; *Richards and Engebretson*, 1992]. It is clear that geoid lows are indeed underlain by volumes with high seismic velocities near the base of the mantle (Fig. 3.1B, Fig. A1.1A), but we also find that there are anomalously low seismic velocities in the upper part of the mantle in the same regions (Fig. 3.1C, Fig. A1.1B). These low-seismic-velocity anomalies are found at depths up to 1000 km and have absolute amplitudes that are at least as large as the deeper high-velocity anomalies (Fig. 3.1D).

A global analysis of the correlation between different tomography models and the geoid (Fig. A1.1) reveals that slow seismic velocities in the upper half of the mantle and fast seismic velocities in the lower half of the mantle are both correlated with geoid lows, while geoid highs have a similar strength of correlation with fast seismic velocities in the upper c. 800 km of mantle (actively-subducting slabs) and slow seismic velocities in the lower mantle (inferred to be superplumes and hotspots). The relatively high values of correlation between velocity anomalies and geoid lows,

combined with our tectonic interpretations of cross-sections through the tomographic models (Fig. 3.1E, Fig. A1.1C-D), lead us to suggest that buoyant upwellings above slab graveyards play a significant role in producing the global pattern of geoid lows. Similar suggestions have been made previously to explain regional features of tomography models and the geoid. It was suggested that increased water content in the upper mantle beneath the US East Coast [*van der Lee et al.*, 2008] was supplied by the subducted Farallon slab and caused an extensive zone of low seismic velocities in the upper mantle. The geoid low between Antarctica and New Zealand is best explained by middle and upper mantle upwelling that followed the cessation of subduction beneath Gondwanaland [*Sutherland et al.*, 2009].

To further investigate this hypothesis, we developed instantaneous models of global mantle flow based on density structures scaled from seismic tomography. Previous global geodynamic studies have used the geoid and gravity as constraints on seismic velocity-density scaling, and on mantle viscosity as a function of radius [*Forte and Mitrovica*, 2001; *Steinberger*, 2000; *Steinberger and Calderwood*, 2006], or more complex functions with radial and lateral parameterizations based on tectonic regionalizations [*Cadek and Fleitout*, 2003; *Yoshida and Nakakuki*, 2009]. Regional models of the Tonga-Kermadec and Aleutian subduction zones [*Billen and Gurnis*, 2001; *Billen et al.*, 2003] show that significant lateral viscosity variations are required between upper mantle slabs and adjacent mantle wedges to match the geoid, while some global studies indicate that weak plate margins in lithosphere are needed to match positive geoid anomalies over subduction zones [*Yoshida and*

Nakakuki, 2009].

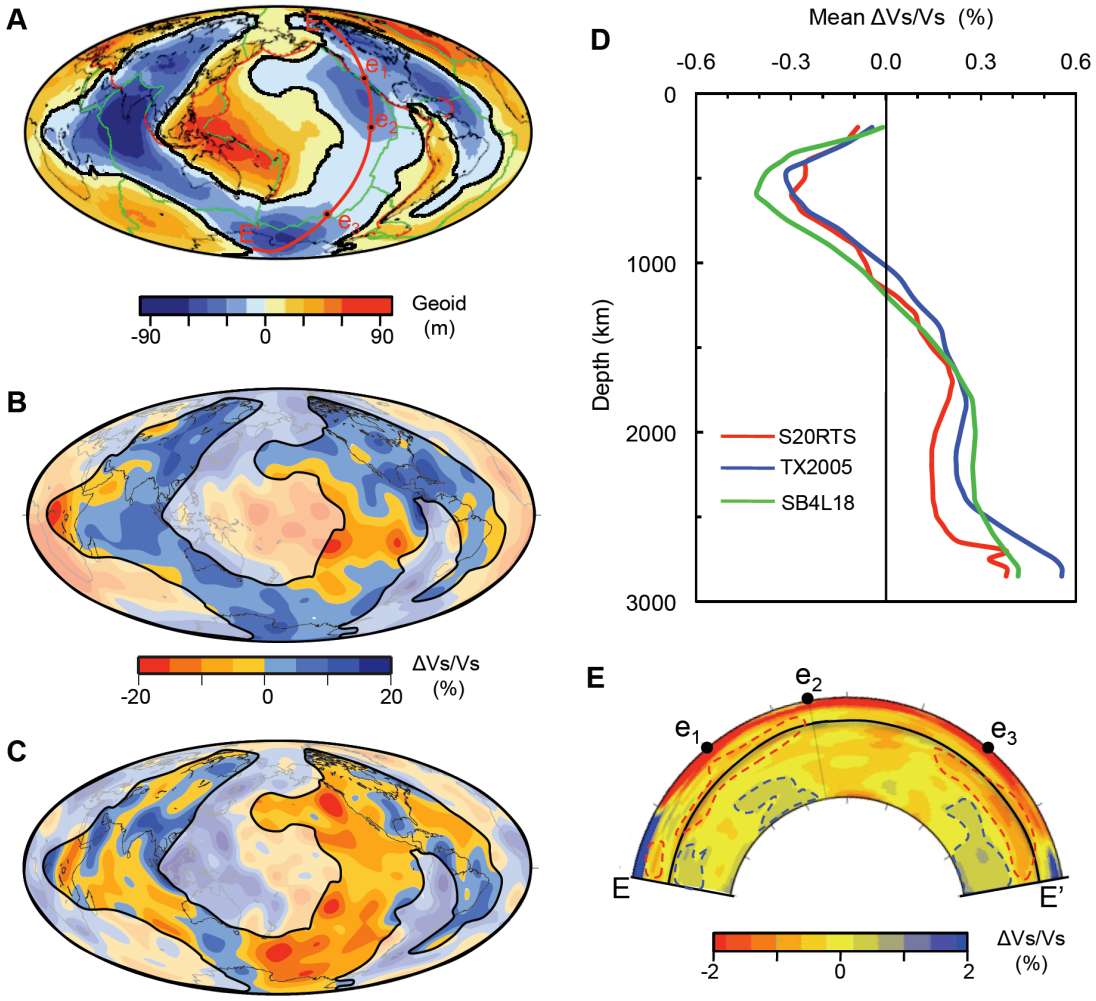

Figure 3.1. Relationship between geoid (A) and seismic tomography (B-E). (B-C) Integrated S20RTS [*Ritsema et al.*, 2004] tomographic images for depth ranges 2000-2890 km (B) and 300-1000 km (C). (D) Difference of mean value of wavespeed anomaly [*Masters et al.*, 2000; *Ritsema et al.*, 2004; *Simmons et al.*, 2006] between localized geoid lows (<-30 m) and global tomography for different tomographic models. (E) Cross-section through S20RTS [*Ritsema et al.*, 2004] model. Tomography (B-C) is integrated at every 50 km; semi-transparent overlay covers area of positive geoid anomaly, and the cross-section position is shown on (A) by a red line; dashed blue and red lines (D) represent high-velocity lower mantle and low-velocity mid to upper mantle anomalies, respectively.

Viscosity variation is defined differently for two sets of models: (1) viscosity variation as a function of radius and temperature; and (2) lateral viscosity variation in the upper mantle based on tectonic regionalization in addition to radial and temperature viscosity variation (Fig. A1.2). Acceptable geoid predictions are made by both classes of models (Fig. A1.3), and all of the best-fitting models have a viscosity increase across the 660 km discontinuity by a factor of 80 to 100. Different seismic-tomographic inputs result in geoid predictions of varying success in different parts of the world (Fig. A1.4). Model S20RTS [*Ritsema et al.*, 2004] as input yields better predictions in the Pacific and circum-Pacific, SB4L18 [*Masters et al.*, 2000] fits the region extending from the North Atlantic to south of Africa, and TX2005 [*Simmons et al.*, 2006] best predicts the Indian Ocean geoid low (Fig. A1.4). The choices of different tomographic models as input, and alternate models of lateral and vertical viscosity variation, have relatively greater impacts on geoid predictions than the choice of seismic-velocity-to-density scaling relationship (Fig. A1.5).

The best-fitting model (Fig. 3.2A) was found by a systematic parameter search (Fig. A1.1-A1.5). The eastern hemisphere geoid low is predicted as a relatively continuous structure with distinct Ross Sea minima. Two separate geoid lows emerge in the western hemisphere in the northeast Pacific and western Atlantic. The amplitudes of the Ross Sea and northeast Pacific geoid minima are predicted well, while the Indian Ocean low is systematically under predicted, which could be attributed to poor regional sampling by seismic body waves. To investigate the importance of mantle upwellings, we removed the low-density anomalies in the

upper to mid mantle depth range (Fig. 3.2B-C). With positive buoyancy variations shallower than 1000 km depth removed, predictions of localized geoid minima in the northeast Pacific and Ross Sea regions disappear (Fig. 3.2C). The largest negative geoid anomaly in the Indian Ocean remains, but the amplitude is reduced. We could not find a model with reasonable seismic velocity-density scaling (Fig. A1.5) that reproduces the observed amplitudes of geoid minima with only lower mantle slabs. Therefore, we conclude that buoyant upwellings above c. 1000 km depth cause localized high-amplitude geoid minima, and the longer-wavelength geoid trough of amplitude -10 to -30 m that surrounds the Pacific is related to accumulations of high-density Mesozoic slabs near the base of the mantle.

The negative geoid anomaly in the northeast Pacific appears to be due to upwelling located in the upper to mid mantle (Fig. 3.2; Table A1.1), and we suggest a possible causal relationship between this upwelling and lowermost mantle high-velocity material (Fig. 3.1E, Fig. A1.1C). If this high-velocity material is related to ancient subduction, it is substantially west of the Farallon slab [*Grand*, 2002], and the exact timing and origin of its subduction zone source is unknown. For the Ross Sea geoid low, about 40% of the predicted low disappears as upwellings are striped out of the upper mantle (Fig. 3.2B; Table A1.1), and only 40% of the geoid low remains once the upwellings are removed in the upper 1000 km (Fig. 3.2C, Table A1.1). We have previously proposed that anomalously high topography of Ross Sea–Marie Byrd land, excess Campbell plateau subsidence, and the geoid low in the Ross Sea are causally related to low-density material above the Gondwana slab graveyard in this region [*Sutherland et al.*, 2009]; [*Spasojevic et al.*, 2010].

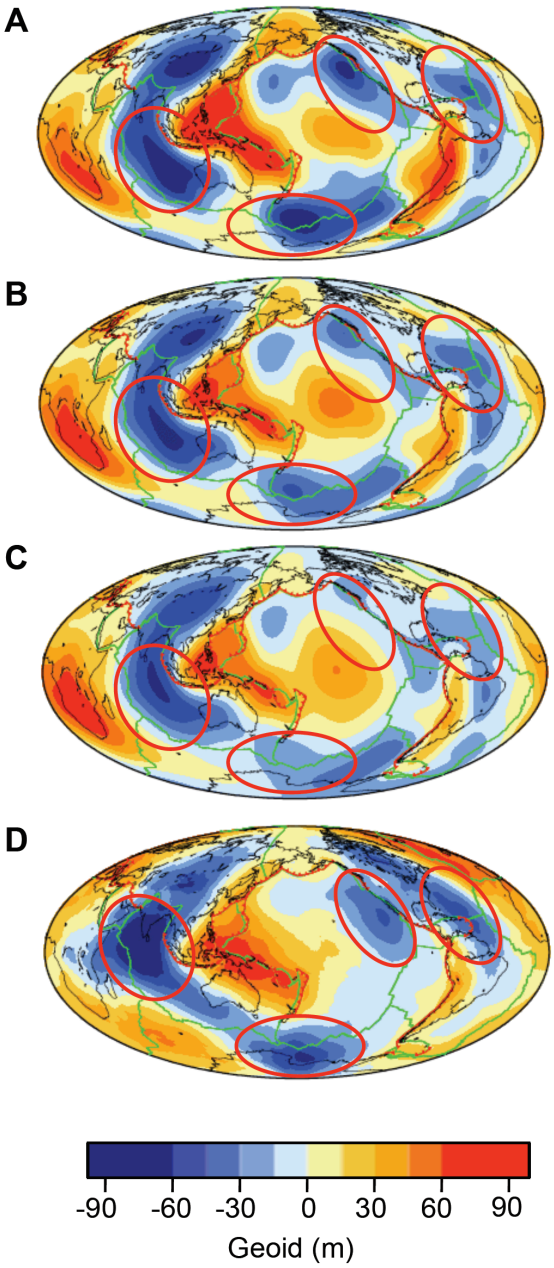

Figure 3.2. Predicted and observed geoid. (A) Geoid prediction for best-fitting model (C_1=0.61; C_2=0.79). (B-C) Geoid prediction for the best model with upwellings removed in depths 0-660 km (B; C_1=0.60; C_2=0.74) and 0-1000 km (C; C_1=0.59; C_2=0.71). (D) Observed geoid. See FigA1.3b,g for radial viscosity structure and seismic velocity-density scaling (viscosity ratio at 660 km is 1:100). All buoyancy anomalies are scaled from S20RTS tomography [*Ritsema et al.*, 2004]. Correlation coefficients C_1 and C_2 between predicted and observed geoid are calculated for the whole Earth's surface (C_1) and the region of geoid low (C_2). Red ellipses indicate four zones of localized geoid minima.

The Indian Ocean geoid low is not fit well by models that reproduce other geoid anomalies, but models do show that about 20% of the predicted anomaly is related to mantle structure shallower than 1000 km (Table A1.1). The position of the Indian Ocean geoid low corresponds to the reconstructed position of Tethyan subduction [*Aitchison et al.*, 2007]. It is possible that an upwelling was created by interaction of this slab with the upper to mid mantle, as implied by the TX2005 [*Simmons et al.*, 2006] model (Fig. A1.1). Such an upwelling may not be well imaged by tomographic models, but could explain the relatively small Cenozoic subsidence of India [*Fleitout and Singh*, 1988], as compared to that expected from movement over a mantle downwelling, such as the observed subsidence of Australia [*Gurnis et al.*, 1998] and North America [*Spasojevic et al.*, 2009]. If the upwelling was located above the subducting slab when India drifted northward, the dynamic effects of these two opposing anomalies could cancel and India would not experience significant subsidence or uplift, consistent with the record of limited marine flooding on the Indian continent [*Fleitout and Singh*, 1988].

The western Atlantic geoid signal is complicated by incomplete postglacial rebound in North America, with our geodynamic models predicting a geoid low to be more spatially constrained than the observed geoid low (Fig. 3.2). However, tomography inversions reveal an extensive zone of low seismic velocities in the upper mantle along the US East Coast [*van der Lee et al.*, 2008] located above the subducted Farallon slab. The upwelling in the western Atlantic along the US east coast has been previously attributed to increased water content in the upper mantle, probably supplied by subduction of the Farallon slab [*van der Lee et al.*, 2008]. Our models

indicated that about 40% of the geoid low in the western Atlantic results from upper to mid mantle low-density upwellings (Fig. 3.2; Table A1.1).

Since the low-density material that we identify is often above ancient subducted slabs, we suggest that it is causally related. We propose that the low density of the mantle in these regions could be a result of phase separation (e.g., melting), hydration reactions, or some other form of chemical alteration by ancient subducted slabs. This hypothesis is supported by mineral physics studies that have investigated phase relationships in the olivine-water system [*Ohtani et al.*, 2004] and the mantle [*Hirschmann*, 2006] water storage capacity. Experimental studies of water on kinetics of the olivine–wadsleyite system [*Ohtani et al.*, 2004] indicate that, in addition to the mantle wedge in subduction zones and mantle transition zone, two dehydration sites exist in the lower mantle: the top of the lower mantle where hydrous ringwoodite and superhydrous phase B decomposes, and a 1200-1500 km depth where phase D(G) decomposes. However, there are currently no mineral physics studies we are aware of that link the amount of water in the upper reaches of the lower mantle to perturbations in seismic velocities.

Our models confirm that deep slab graveyards are responsible for the long-wavelength geoid trough. We also find evidence for low-density mantle upwellings at upper to mid mantle depths above this region of subducted Mesozoic slabs, and confirm them to be a primary cause of high-amplitude intermediate-wavelength geoid minima within the global belt of geoid lows. We could not construct a model with reasonable velocity-to-density scaling and viscosity structure that reproduced

localized geoid minima without these low-density upwellings in the upper 1000 km of the mantle. Although recognized in regional studies of the US east coast [*van der Lee et al.*, 2008] and the Antarctica-New Zealand conjugate margins [*Spasojevic et al.*, 2009; *Sutherland et al.*, 2010], such upwellings have not previously been investigated globally and we propose that they constitute a previously unrecognized mode of mantle upwellings [*Courtillot et al.*, 2003] that is causally related to the activity of ancient subduction zones.

References

Aitchison, J. C., J. R. Ali, and A. M. Davis (2007), When and where did India and Asia collide?, *Journal of Geophysical Research, 112*(B5), B05423, doi: 10.1029/2006JB004706.

Billen, M. I., and M. Gurnis (2001), A low viscosity wedge in subduction zones, *Earth and Planetary Science Letters*, *193*(1–2), 227–236.

Billen, M. I., M. Gurnis, and M. Simons (2003), Multiscale dynamics of the Tonga-Kermadec subduction zone, *Geophysical Journal International*, *153*(2), 359–388.

Cadek, O., and L. Fleitout (2003), Effect of lateral viscosity variations in the top 300 km on the geoid and dynamic topography, *Geophysical Journal International*, *152*(3), 566–580.

Chase, C. G., and D. R. Sprowl (1983), The modern geoid and ancient plate boundaries, *Earth and Planetary Science Letters*, *62*(3), 314–320.

Courtillot, V., A. Davaille, J. Besse, and J. Stock (2003), Three distinct types of hotspots in the Earth's mantle, *Earth and Planetary Science Letters*, *205*(3–4), 295–308.

Fleitout, L., and R. H. Singh (1988), Surface topography associated with mantle heterogeneities and geoid: Observational constraints over India (abstract), *17th Mathematical Gephysical Congress*, 143.

Forte, A. M., and J. X. Mitrovica (2001), Deep-mantle high-viscosity flow and thermochemical structure inferred from seismic and geodynamic data, *Nature*, *410*(6832), 1049–1056.

Grand, S. P. (2002), Mantle shear-wave tomography and the fate of subducted slabs, *Philosophical Transactions of the Royal Society of London Series A-Mathematical Physical and Engineering Sciences*, *360*(1800), 2475–2491.

Gurnis, M., R. Müller, and L. Moresi (1998), Cretaceous Vertical Motion of Australia and the Australian-Antarctic Discordance, *Science*, *279*(5356), 1499.

Hager, B. H., and M. A. Richards (1989), Long-wavelength variations in Earth's geoid- Physical models and dynamic implications, *Philosophical Transactions of the Royal Society of London Series A-Mathematical Physical and Engineering Sciences*, *328*(1599), 309–327.

Hirschmann, M. M. (2006), Water, melting, and the deep Earth H_2O cycle, *Annual Review of Earth and Planetary Sciences*, *34*, 629–653.

Kaban, M. K., P. Schwintzer, and C. Reigber (2004), A new isostatic model of the lithosphere and gravity field, *Journal of Geodesy*, *78*(6), 368–385.

Masters, G., G. Laske, H. Bolton, and A. Dziewonski (2000), The relative behavior of shear velocity, bulk sound speed, and compressional velocity in the mantle: Implications for chemical and thermal structure, in *Geophysical Monograph Series*, edited by S. Karato, et al., 63–88, American Geophysical Union, Washington DC.

Ohtani, E., K. Litasov, T. Hosoya, T. Kubo, and T. Kondo (2004), Water transport into the deep mantle and formation of a hydrous transition zone, *Earth and Planetary Science Letters*, *143–144*, 255–269.

Richards, M., and D. Engebretson (1992), Large-scale mantle convection and the history of subduction, *Nature*, *355*, 437–440.

Richards, M. A., and B. H. Hager (1984), Geoid anomalies in a dynamic Earth, *Journal of Geophysical Research*, *89*(B7), 5987–6002.

Richards, M. A., B. H. Hager, and N. H. Sleep (1988), Dynamically supported geoid highs over hotspots - Observation and theory, *Journal of Geophysical Research 93*(B7), 7690–7708.

Ritsema, J., H. J. van Heijst, and J. H. Woodhouse (2004), Global transition zone tomography, *Journal of Geophysical Research*, *109*, B02302, doi: 10.1029/2003JB002610.

Simmons, N. A., A. M. Forte, and S. P. Grand (2006), Constraining mantle flow with seismic and geodynamic data: A joint approach, *Earth and Planetary Science Letters*, *246*(1–2), 109–124.

Simons, M., and B. Hager (1997), Localization of the gravity field and the signature of glacial rebound, *Nature*, *390*(6659), 500–504.

Spasojevic, S., M. Gurnis, and R. Sutherland (2010), Inferring mantle properties with an evolving dynamic model of the Antarctica-New Zealand region from the Late Cretaceous, *Journal of Geophysical Research*, *115*, B05402, doi: 10.1029/2009JB006612.

Spasojevic, S., L. J. Liu, and M. Gurnis (2009), Adjoint models of mantle convection with seismic, plate motion, and stratigraphic constraints: North America since the Late Cretaceous, *Geochemistry Geophysics Geosystems*, *10*(5), Q05W02, doi: 10.1029/2008gc002345.

Steinberger, B. (2000), Slabs in the lower mantle - Results of dynamic modelling compared with tomographic images and the geoid, *Physics of Earth and Planetary Interiors*, *118*(3–4), 241–257.

Steinberger, B., and A. R. Calderwood (2006), Models of large-scale viscous flow in the Earth's mantle with constraints from mineral physics and surface observations, *Geophysical Journal International*, *167*(3), 1461–1481.

Sutherland, R., S. Spasojevic, and M. Gurnis (2009), Mantle upwelling after Gondwana subduction death may explain anomalous topography of West Antarctica and subsidence history of eastern New Zealand, *Geology*, *38*(2), 155–158.

van der Lee, S., K. Regenauer-Lieb, and D. A. Yuen (2008), The role of water in connecting past and future episodes of subduction, *Earth and Planetary Science Letters*, *273*(1–2), 15–27.

Yoshida, M., and T. Nakakuki (2009), Effects on the long-wavelength geoid anomaly of lateral viscosity variations caused by stiff subducting slabs, weak plate margins and lower mantle rheology, *Physics of Earth and Planetary Interiors*, *172*(3–4), 278–288.

Chapter 4

Adjoint models of mantle convection with seismic, plate motion and stratigraphic constraints: North America since the Late Cretaceous[1]

4.1. Abstract

We apply adjoint models of mantle convection to North America since the Late Cretaceous. The present-day mantle structure is constrained by seismic tomography, and the time-dependent evolution by plate motions and stratigraphic data (paleoshorelines, borehole tectonic subsidence and sediment isopachs). We infer values of average upper and lower mantle viscosities, provide a synthesis of North American vertical motions (relative sea level) from the Late Cretaceous to the present, and reconstruct the geometry of the Farallon slab back to the Late Cretaceous. In order to fit Late Cretaceous marine inundation and borehole subsidence, the adjoint model requires a viscosity ratio across 660 km discontinuity of 15:1 (reference viscosity of 10^{21} Pa s), which is consistent with values previously

[1] Published by Sonja Spasojevic, Lijun Liu, and Michael Gurnis (2009) in *Geochemistry, Geophysics, Geosystems, 10*(5), Q05W02, doi: 10.1029/2008GC002345. Reproduced by permission of American Geophysical Union.

inferred by postglacial rebound studies.

The dynamic topography associated with subduction of the Farallon slab is localized in western North America over the Late Cretaceous, representing the primary factor controlling the widespread flooding. The east coast of the United States is not stable, rather it has been experiencing continuous dynamic subsidence over the Cenozoic, coincident with an overall eustatic fall, explaining a discrepancy between sea level derived from the New Jersey coastal plain and global curves. The east coast subsidence further constrains the mantle viscosity structure and require an uppermost mantle viscosity of 10^{20} Pa s. Imposed constraints require that the Farallon slab was flat lying during Late Cretaceous, with an extensive zone of shallow-dipping Farallon subduction extending beyond the flat-lying slab further east and north by up to 1,000km than previously suggested.

4.2. Introduction

The Cretaceous marine inundation of western North America (NAM) has been a stratigraphic enigma because of the combination of large thicknesses of sediments deposited over a large horizontal length scale (nearly 10^3 km) [*Bond,* 1976; *Cross and Pilger,* 1978; *Liu and Nummedal,* 2004; *Liu et al.,* 2005]. Using hypsometric analysis and assuming isostasy, *Bond* [1976] suggests that the observed flooding of NAM (45% by area), would have required a 310 m sea-level rise, resulting in the accumulation of approximately 700 meters of sediments. Since nearly half of the

area of NAM Cretaceous marine sediments is significantly thicker than 700 m, *Bond* [1976] argued that eustasy could not have been the only process that had operated. *Cross and Pilger* [1978] attributed the excessive sediment thickness and subsidence to subcrustal loading induced by a shallow-dipping slab. *Liu et al.* [2005] determine that regional subsidence of the Western Interior consists of a short-wavelength flexural loading component that changed on a time scale of a few million years, and a long-wavelength dynamic component that changed over a time scale of tens of million years. *Liu and Nummedal* [2004] determine that the wavelength of the dynamic subsidence component is on the order of 1,500 km.

Cretaceous marine sediments at present lie at an elevation of approximately 1 km, but since putative long-term global sea levels vary from 70 meters [*Miller et al.,* 2005] to 250 meters [*Haq and Al-Qahtani,* 2005], NAM must have subsided and then uplifted over a large length scale [*Bond,* 1976]. Several numerical models have attempted to explain these inferred vertical motions in terms of the dynamic topography induced by negatively buoyant subducted slabs [*Mitrovica et al.,* 1989; *Burgess et al.,* 1997; *Lithgow-Bertelloni and Gurnis,* 1997]. *Mitrovica et al.* [1989] attributed the Western Interior Seaway (WIS) to shallow subduction of the Farallon plate that could create a ~1,400 km wide region of dynamic subsidence. Specifically, using 2D isoviscous forward models, subsidence and subsequent uplift was attributed to changes in the dip angle of the Farallon plate. *Burgess et al.* [1997] expanded on this concept with three-dimensional, variable-viscosity models that attempted to match stratigraphic sequence boundaries. These models shared the common attributes of fixing the dynamics to the frame of reference of the over-

riding (NAM) plate, and fits to the stratigraphic constraints were obtained by changing the subduction depth and dip to obtain the best fits to either continental tilt [*Mitrovica et al.,* 1989] or sediment thickness and sequence boundaries [*Burgess et al.,* 1997]. *Lithgow-Bertelloni and Gurnis* [1997] used a parameterized global mantle flow model with the slabs falling vertically at a constant rate, in which NAM subsided and then uplifted as it moved to the west over the Farallon slab. However, the subsidence and uplift were phase shifted by about 20 Myr in the models toward the present compared to the inferred timings [*Lithgow-Bertelloni and Gurnis*, 1997]. *Le Stunff and Ricard* [1997] proposed that partial advection of mantle equidensity surfaces by vertical motion induced by driving loads enables better prediction of the amplitude and phase of flooding.

The Farallon slab may have also influenced the stratigraphic record further to the east and later in time. By deconvolving the influence of paleobathymetry from sediment accumulation within five wells from the New Jersey coastal plain, *Miller et al.* [2005] estimated a maximum long-term sea level change of 70 m between the Late Cretaceous and the present, an amplitude that is significantly smaller than other published global estimates [e.g., *Kominz,* 1984; *Haq et al.,* 1987; *Müller et al.,* 2008b]. With higher-resolution seismic tomography [*Grand et al.,* 1997; *Van der Hilst et al.,* 1997; *Ren et al.,* 2007], the Farallon slab is resolved in the present day at mid mantle depths as a high seismic-velocity anomaly beneath eastern NAM. In this paper, we investigate if both extensive Cretaceous flooding of the interior of NAM and the discrepancy between the *Miller et al.* [2005] sea-level estimates and other putatively eustatic estimates can be explained by a single geodynamic model that

includes the dynamic effect of Farallon slab subduction. This paper is a detailed investigation of this problem; preliminary results for the inversion of the flat slab phase of Farallon subduction [*Liu et al.,* 2008] and the subsidence of the US east coast [*Spasojević et al.,* 2008] have recently appeared.

We combine advances in mantle convection modeling with stratigraphy, plate motion, and seismic tomography to better understand the relation of Farallon plate subduction and vertical motions and long-term sea level change. We use the concept of separate frames of reference for the mantle and plate to better link vertical motions to the stratigraphic record, as demonstrated for the evolution of Australia [*Gurnis et al.,* 1998]. Secondly, in order to use the seismic constraints directly we implement adjoint (inverse) models of convection [*Bunge et al.,* 2003; *Ismail-Zadeh et al.,* 2004; *Liu and Gurnis,* 2008]. Thirdly, we use a new generation of plate reconstructions in which plate margins continuously change with plate motion [*Gurnis et al.,* 2009]. The dynamic models are constrained by observations of paleo shorelines [*Smith et al.,* 1994; *Bond,* 1978], borehole tectonic subsidence [*Pang and Nummedal,* 1995; *Liu and Nummedal,* 2004; *Liu et al.,* 2005], and isopach thickness [*Cook and Bally,* 1975] in the WIS. In addition, we test the models through the Cenozoic vertical motions of the eastern United States using paleoshoreline analyses [*Spasojević et al.,* 2008] and borehole-inferred, regional sea-level variations [*Van Sickel et al.,* 2004; *Miller et al.,* 2005].

Our new results include empirical analysis of correlation between stratigraphy and seismic tomography, inferred values of effective temperatures of the Farallon slab, a

preferred viscosity profile using stratigraphic constraints, and a post-Late Cretaceous differentiation between (dynamic) relative sea-level and eustatic factors for NAM. In addition, we compare our model predictions against inferred sediment thicknesses for the western Canadian shield from the thermochronology of basement samples [*Flowers*, 2009].

4.3. Observational constraints

4.3.1. Tomography

Seismic tomography constrains present-day mantle convection, including the Farallon slab. Global seismic tomography inversions reveal linear positive seismic anomalies beneath the Americas with shear (S) [*Grand et al.,* 1997] and compressional (P) waves [*Van der Hilst et al.,* 1997]. Although more blurred, global models with spherical harmonic basis functions also detect this structure [*Mégnin and Romanowicz,* 2000; *Ritsema et al.,* 2004]. Recent regional models that invert both S- and P- wave travel times [*Ren et al.,* 2007] or use multiple-frequency P-wave tomography [*Sigloch et al.,* 2008] reveal the Farallon remnants with similar geometries. Given uncertainties in the detailed structure of the slab and differences between S and P sensitivity, all these models, especially ones with block basis functions, agree on the spatial distribution, wavelength, and magnitude of the anomaly. The present-day Farallon remnant largely strikes north-south along the North American east coast from Central America to the Arctic. In a map view, it has a width of 500-1,000 km while extending from 800 to 2,000 km depth with typical S-

wave anomaly of about 1%. In this study, we use an updated version of a shear wave model [*Grand*, 2002].

To convert tomography into density, we first remove the signal above 250 km that correlates with the craton, assuming it is neutrally buoyant [*Jordan,* 1975; *Goes and van der Lee,* 2002]. Because we consider differential dynamic topography, removal of this layer will not affect our results. If this structure were attached to the moving plate and neither local convective instability nor thickening/thinning of the layer were significant, it would not change topography. We also remove seismic structures below 2,400 km depth, where there is a clear gap in the seismic image. From 2,400 km up to 800 km, we adopt a constant density-to-velocity perturbation ratio (Sec 4.4.1 and Eq. 5), constrained by vertical motions.

4.3.2. Continental stratigraphy and sea level

The WIS has relatively well-preserved Cretaceous sediments, mapped in outcrops and boreholes. As constraints to dynamic models, we use paleo shorelines [*Smith et al.,* 1994; and *Bond*, 1978], borehole tectonic subsidence curves [*Pang and Nummedal,* 1995; *Liu et al.,* 2004], and a Late Cretaceous isopach [*Cook and Bally,* 1975]. The WIS started developing in early Cretaceous by southward transgression from the Arctic and northward transgression from the Gulf of Mexico [*Sloss*, 1988]. By Late Cretaceous the WIS (Fig. 4.1) developed into a large epicontinental sea stretching from the Gulf of Mexico to the Arctic, and having a width of thousands of

kilometers east-west [*Smith et al.,* 1994]. Using the boundary between preserved marine and non-marine sediments, *Smith et al.* [1994] defined eight paleo shorelines from Late Cretaceous to present (at 95, 85, 70, 60, 45, 30, 20, 12 Ma). During the Late Cretaceous, the western edge of the seaway was located close to the Sevier belt [*Sloss*, 1998; *Liu at al.,* 2005], while the eastern shoreline migrated slightly eastward from 95 Ma (Fig. 4.1) to 70 Ma [*Smith et al.,* 1994]. The retreat of the seaway commenced at the end of the Late Cretaceous, and the inland sea withdrew completely by the early Cenozoic [*Smith et al.,* 1994]. We use digitized maps of *Smith et al.* [1994] for Late Cretaceous to qualitatively constrain the position of the dynamic topography low associated with subduction, as illustrated by the 95 Ma shoreline reconstruction (Fig. 4.1). We also use reconstructed Miocene and Eocene shorelines elevations [*Bond,* 1978; *Spasojević et al.,* 2008] to infer dynamic subsidence of the US east coast [*Spasojević et al.,* 2008]. The total and tectonic subsidence in boreholes have been inferred from 1D subsidence analysis after accounting for decompaction, changes in water depth, eustasy, and Airy isostatic backstripping [*Liu et al.,* 2005; *Liu and Nummedal,* 2004; *Pang and Nummedal,* 1995]. We selected a total of 12 tectonic subsidence curves, six on an east-west profile (Fig. 4.1, locations EW1-EW6) in Wyoming [*Liu et al.,* 2005], and six representative locations from *Pang and Nummedal* [1995] (Fig. 4.1; locations NS1 to NS6).

Cook and Bally [1975] used outcrops and boreholes between mid Cenomanian and the top of the Maeastrichtian to define three separate isopach maps (mid Cenomanian to top Turonian; Coniacian-Santonian; Campanian-Maestrichtian).

Since the spatial extent of these isopachs is similar, we use a total Late Cretaceous isopach [*Cook and Bally,* 1975] from mid Cenomanian to Maestrichtian. The area of late Cretaceous sedimentation is approximately 1,300 km wide east-west, and 3,000 km north-south (Fig. 4.1). The maximum thickness of the total Late Cretaceous sediments is around 3 km, with the thickest sediments (Fig. 4.1) located close to the Sevier belt [*Sloss,* 1988; *Cross and Pilger,* 1978]. The oldest isopach (Upper Albian to Santonian strata) is thickest along a north-south trending depositional trough parallel to the Sevier belt [*Cross and Pilger,* 1978]. The remaining Upper Albian to Santonian strata occurs more broadly with thicknesses diminishing to the east [*Cross and Pilger,* 1987]. The younger isopach (Santonian to Maestrichtian) was deposited throughout most of the WIS, with its center in a broad region of southern Wyoming, northwestern and north central Colorado, and eastern Utah [*Cross and Pilger,* 1978]. There was no prominent linear depositional trough parallel to the Sevier belt in the Santonian to Maestrichtian [*Cross and Pilger,* 1978].

There is significant disagreement on the amplitude of eustasy since the Late Cretaceous with maximum long-term estimates varying between 70 m [Miller et al., 2005] to more than 250 m [*Haq et al.,* 1987]. *Miller et al.* [2005] made sea-level estimates based on the backstripping of sedimentary sections at five boreholes on the New Jersey coastal plain [*Van Sickel et al.,* 2004] with the maximum long-term sea level around 70 m. High estimates of sea level with a maximum on order of 250-300 m are based on global correlations of stratigraphic sequences [*Haq et al.,* 1987; *Haq and Al-Qahtani,* 2005]. Low estimates of 120 m are based on backstripping of wells on the eastern NAM continental margin [*Watts and Steckler,* 1979]. *Kominz*

[1984] estimates global sea level from changing mid ocean ridge volume, which matches sea level required to flood continental interiors, especially since the Eocene [*Bond,* 1979; *Harrison,* 1990]. The maximum amplitude of sea-level change according to *Kominz* [1984] is 220 m, slightly higher than 213 m from an updated estimate [*Müller et al.,* 2008b].

4.3.3. Plate motions

We use GPlates reconstructions of global plate motions at one million year intervals, in which the plate margins continuously evolve with self-consistent velocities between plates and plate margins [*Gurnis et al.,* 2009]. The rotation poles of *Müller et al.* [2008a] are used, implemented in a moving hotspot reference frame. There has been significant discussion of the influence of absolute reference frames on convection models [e.g., *Quéré and Forte*, 2006]. The hotspot reference frame [*Morgan*, 1971] is originally based on the hypothesis that hotspots originate from plumes that are fixed relative to the mantle with no relative motion between them. The moving hotspot reference frame corrects for known relative motion between different groups of hotspots [*O'Neill et al.,* 2005], which results in significantly different plate motions compared to the fixed reference frames prior to 80 Ma. The no-net-rotation reference frame [*Solomon and Sleep,* 1974] assumes uniform coupling between lithosphere and asthenosphere. *Conrad and Husson* [2009]

propose that the sea-level estimates from dynamic models can be influenced by the implementation of different absolute reference frames.

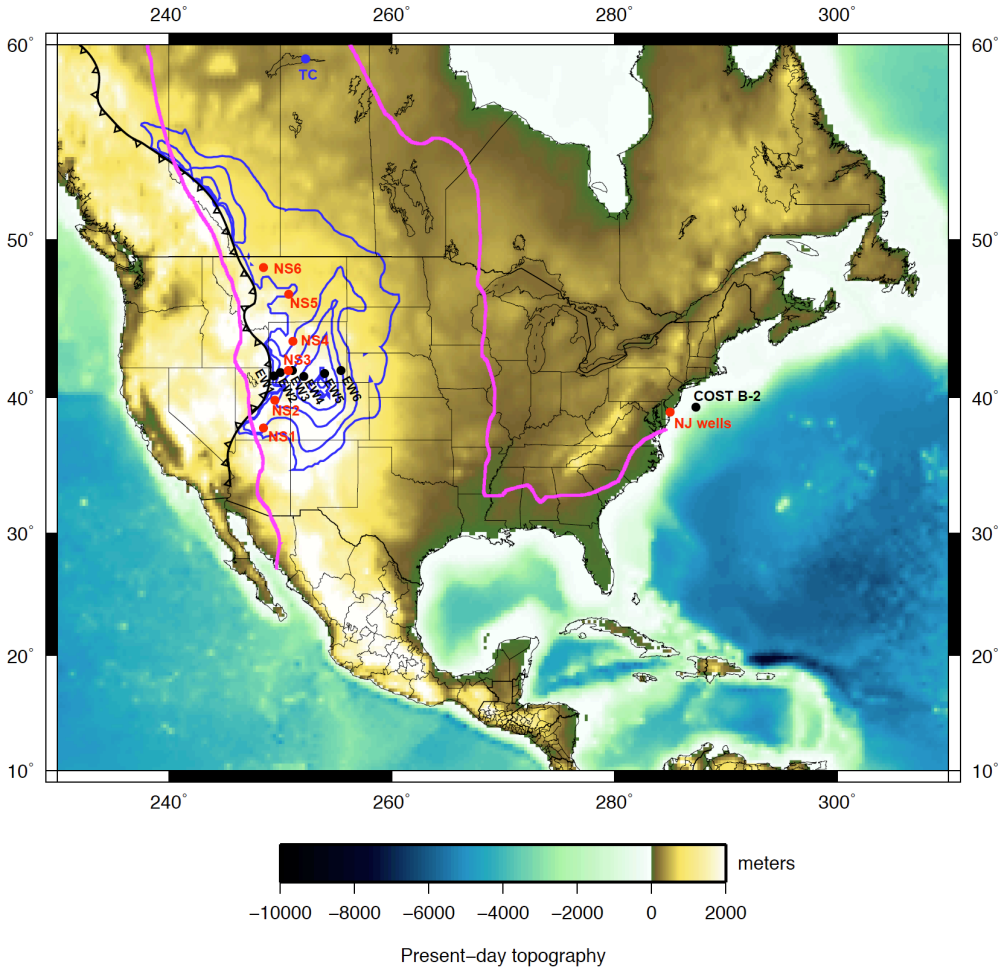

Figure 4.1. Position of data constraints used in the study. Pink line shows reconstructed 95 Ma paleo shoreline *[Smith et al.,* 1995], blue contours total Late Cretaceous isopach [*Cook and Bally,* 1975] with 2,000 ft contour interval, and black line position of the Sevier thrust belt [*Cook and Bally,* 1975]. Black and red dots, marked as EW1-6 and NS1-NS6, indicate location of boreholes of tectonic subsidence curves [*Liu et al.,* 2005; *Pang and Nummedal,* 1995]. Red dot marked NJ wells shows position of wells located on the New Jersey coastal plain [*Miller et al.,* 2005], and black dot marked COST-B2 indicates position of the offshore well used by *Watts and Steckler* [1978] for sea-level curve derivation. Blue dot marked TC indicates location of East Lake Athabasca thermochrology study of *Flowers* [2009].

However, since we are examining dynamic effects of Farallon slab subduction on NAM regional vertical motion, we ensure that the reference frame we utilize is

appropriate by requiring that temporal and spatial evolution of subsidence and uplift is well correlated by NAM observations, as we will describe below.

The reconstructions are global, but some of the details within the NAM region are as follows. At 100 Ma, the western margin of NAM is continuously converging from north to south. This persists to 31 Ma, when the Farallon-Pacific ridge intersects the Farallon-NAM trench [*Atwater and Stock,* 1998], and the San Andreas Fault forms by a small jump to the east in California. The transform segment enlarges at the expense of the convergent margin [*Atwater and Stock,* 1998] and the Juan de Fuca to the north and the Cocos plates to the south continuously shrink (Fig. 4.2). In the south of our region, the Caribbean reconstruction closely follows that of *Pindell et al.* [2006]. From 100 to 80 Ma, North and South America are separated by a spreading center, while the Caribbean region grows by the eastward motion of the Farallon plate between North and South America. At 60 Ma, a new trench and island arc initiates to subsequently become the western margin of southern Mexico and Central America [*Pindell et al.,* 2006].

4.4. Simple sedimentary-tomography correlations

If the anomalous Late Cretaceous vertical motions were indeed related to dynamic topography associated with Farallon subduction, then correlations between the stratigraphic record and Farallon slab imaged by seismic tomography might be revealing. The Farallon slab is well defined at mid mantle depths (800, 1,225, and

1,675 km) as a positive S-wave velocity anomaly, while the position of the slab is less evident at a depth of 1,975 km (Fig. 4.2). Paleo shorelines and sediment isopachs rotated to mantle frame of reference are poorly correlated with the position of the slab at 800 km and 1,975 km (Fig. 4.2). The isopach at 100 Ma correlates well with the positive seismic anomaly at 1,675 km, while the 70 Ma isopach and shoreline are moderately well correlated with the positive seismic anomaly at 1,225 km. Assuming that the positive seismic anomaly corresponds to the subducted Farallon slab, we can infer that the originally shallow-dipping slab causing flooding in the WIS has been subducted to depths of approximately 1,200-1,700 km.

We define the correlation, *C(d,t)*, between total Late Cretaceous isopach and seismic tomography at age *t* as:

$$C(d,\tau) = \frac{1}{N}\sum_{n=1}^{N}(S(n,\tau)\cdot\frac{\delta V_S}{V_S}(n,d)) \qquad (1)$$

where *S(n,t)* is isopach thickness and $\delta V_S/V_S$ is seismic velocity anomaly at depth *d*, where the summation is taken over *N* grid points. We systematically determine *C(d,t)* for seismic tomography at depths *d*=700-2,800 km and *t*=110-0 Ma. The value of isopach thickness *S* is always positive, while values of seismic anomaly $\delta V_S/V_S$ vary between -1 and 1, with large positive values being attributed to the Farallon slab. Therefore, it is expected that maxima in *C(d,t)* are obtained when the rotated seismic isopach has the highest level of correlation with the positive seismic anomaly associated with the Farallon slab.

Isopach thickness and seismic velocity anomaly, normalized by the maximum value of *C,* are strongly correlated during the Late Cretaceous for depths 1,000-1,800 km (Fig. 4.3). There is strong anti-correlation between sediment isopach and seismic tomography for the Late Cretaceous for depths shallower than approximately 1,000 km. The correlation increases with depth and reaches a maximum at around 1,500 km in the period 95-80 Ma. Maximum correlation at 100 Ma occurs at somewhat greater depths of 1,675 km. The correlation decreases for depths greater than 1,700 km, and a strong drop in the correlation at about 2,200 km depth reflects the lowest extent of the Farallon remnants in tomography. The correlation is significantly reduced for the period before 100 Ma and after 55 Ma (Fig. 4.3).

The tomography-isopach correlation is spatially and temporally well defined, with a maximum correlaton at depths from 1,500-1,600 km, implying that this portion of the Farallon slab was probably subducting beneath the WIS during the Late Cretaceous. In addition, there is a general trend of increasing depth correlating with increased age, with the 80 Ma isopach having maximum correlation at 1,525 km, and the 100 Ma isopach at 1,675 km. The increase of level of correlation close to the core-mantle boundary is due to a large area of positive seismic anomaly in this region.

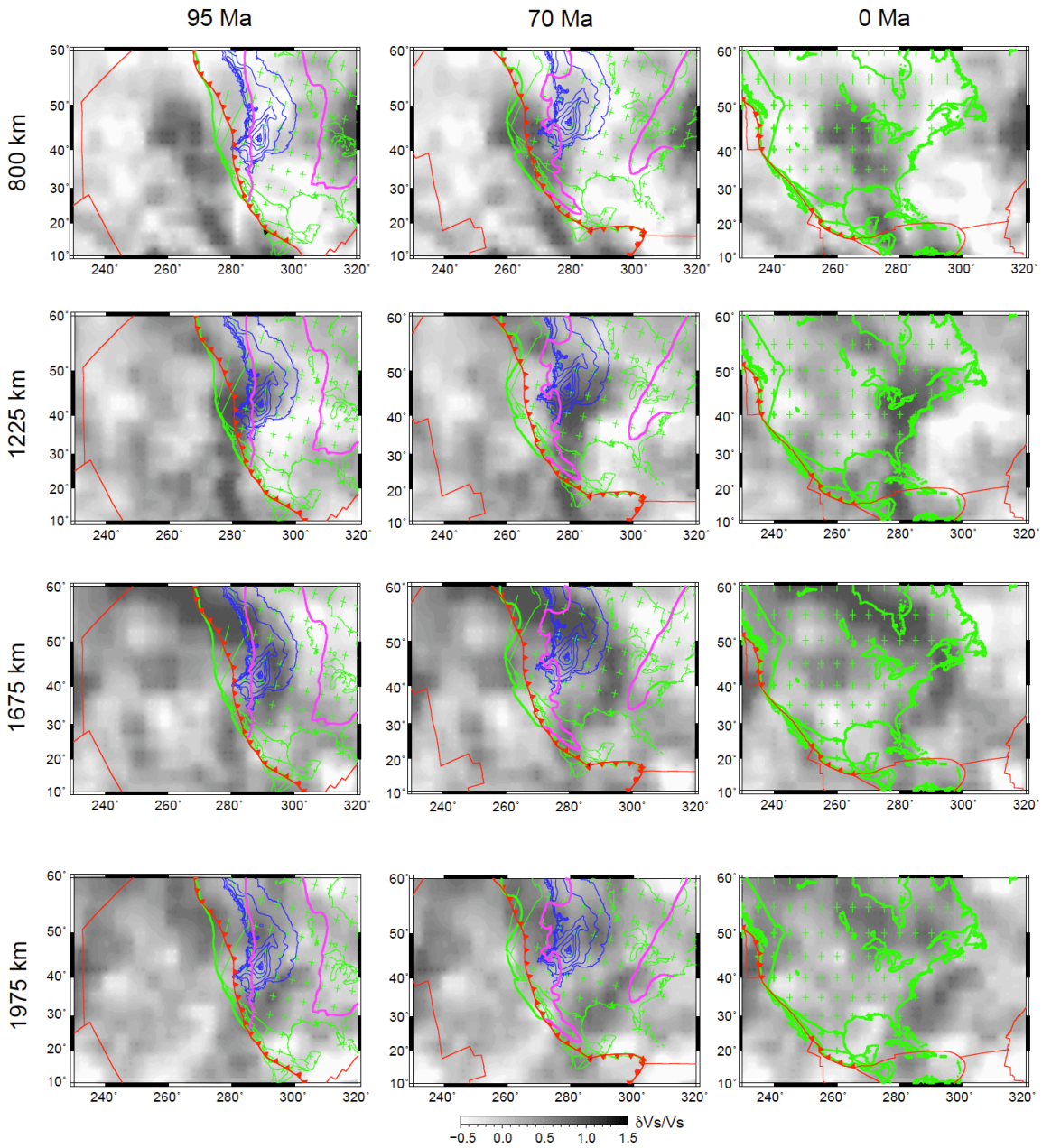

Figure 4.2. Map-view of correlation between present-day seismic tomography [Grand, 2002] and total Late Cretaceous isopach [*Cook and Bally,* 1975] rotated back 95 and 70 Ma to mantle frame of reference. Positive seismic anomaly associated with the Farallon slab is shown with dark grey shading, blue lines show total Late Cretaceous isopach contours [*Cook and Bally,* 1975] with 2,000 ft contour interval, and pink line indicates position of 95Ma shoreline [*Smith et al.,* 1995]. Red lines show position of reconstructed plate boundaries from GPlates [*Gurnis et al.,* 2008].

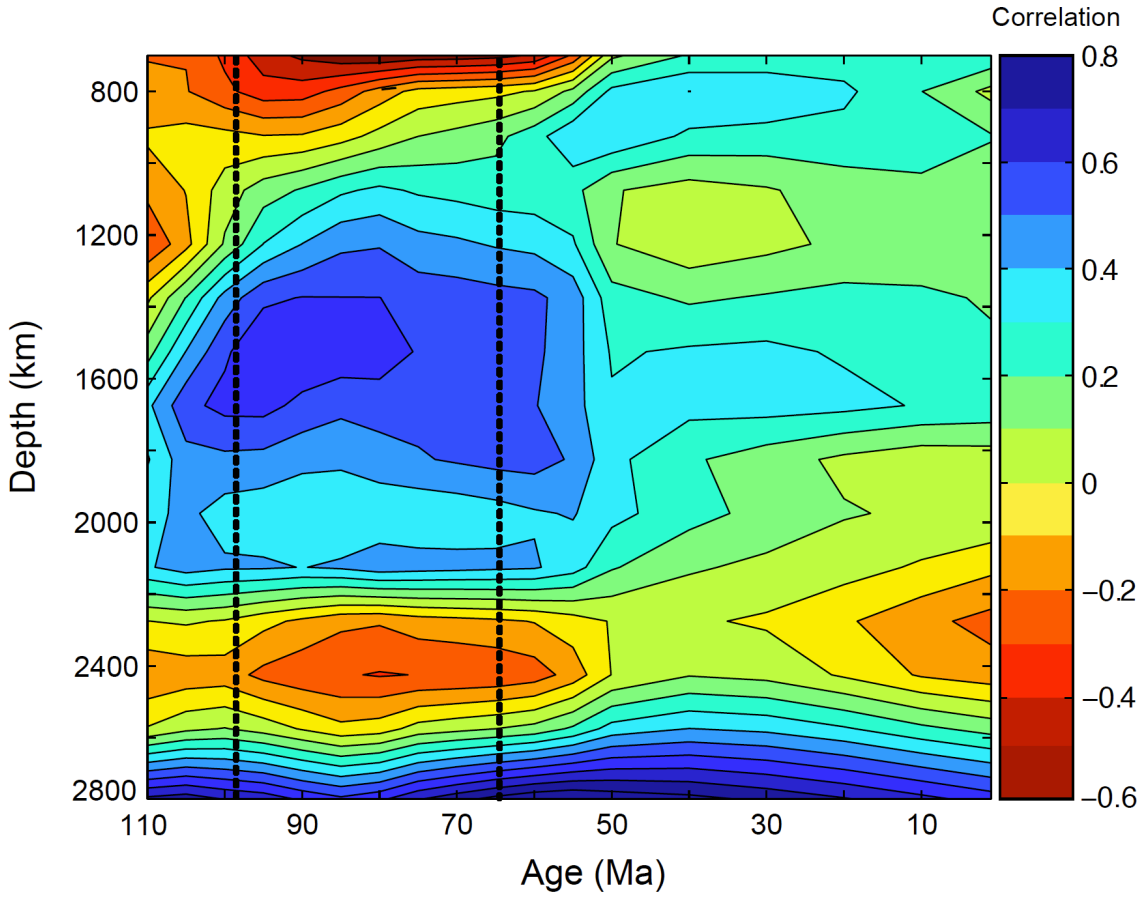

Figure 4.3. Correlation between seismic tomography [*Grand,* 2002] and total Late Cretaceous isopach rotated to mantle reference frame [*Cook and Bally,* 1975] for depth interval 700-2,800 km and time interval 110-0 Ma. Correlation is normalized by maximum value of $C(d,\tau)$.

4.5. Methodology

4.5.1. Adjoint models of mantle convection

We invert for mantle convection backward in time with a method that uses a series of forward and adjoint calculations. The forward model solves for thermal convection within an incompressible fluid with equations for conservation of mass, momentum, and energy

$$\nabla \cdot \vec{u} = 0 \tag{2}$$

$$\nabla P + \nabla \cdot (\eta \nabla \vec{u}) = \rho_m \alpha T_e \vec{g} \tag{3}$$

$$\frac{\partial T_e}{\partial t} + \vec{u} \cdot \nabla T_e = \kappa \nabla^2 T_e + H \tag{4}$$

where $\vec{u}$ is velocity, P dynamic pressure, η dynamic viscosity, ρ_m ambient mantle density, α thermal expansion coefficient, $\vec{g}$ gravitational acceleration, *Te* effective temperature, κ thermal diffusivity, and *H* internal heat production (negligible over 100 Myr). Values of relevant parameters are given in Table 4.1.

Te is scaled from shear velocity anomaly through a transfer function Γ by

$$T_e = \Gamma(\delta V_S / V_S) \tag{5}$$

We refer to *Te* as effective temperature because we are unable to uniquely invert for temperature due to limited resolution of tomography and compositional controls on the shear velocity. Trade-off between seismic anomaly and grid spacing exists below the tomographic resolution, resulting in non-unique absolute seismic velocity

anomalies as well as underestimates of effective temperature (assuming thermal seismic anomalies). However, since dynamic topography is most sensitive to net buoyancy, the seismic ambiguity does not adversely influence our inversion. In addition to thermal effects, there is substantial chemical heterogeneity in the mantle [*Ni et al.,* 2002; *Ishii and Tromp,* 2004; *Trampert et al.,* 2004] and the mapping between seismic anomaly and temperature and density is likely to be both depth and geography dependent. In the adjoint models, the dynamic topography and its rate of change are sensitive to density anomalies [*Liu and Gurnis,* 2008] which could have both thermal and compositional contributions. However, since the inferred quantity is diffusive, we refer to it as 'effective temperature' as opposed to 'effective density'. We have assumed the scaling in Eq. 5 is depth independent.

Table 4.1. Relevant parameters used in this study.

Parameter	Symbol	Value
Ambient mantle density	ρ_m	3340 kg/m^3
Reference viscosity	η_o	1×10^{21} Pa s
Thermal expansion coefficient	α	3×10^{-5} 1/K
Gravitational acceleration	g	9.81 m/s^2
Thermal diffusivity	κ	10^{-6} m^2/s
Earth's radius	R	6371 km
Sedimentation rate	SR	50 m/Myr

The mismatch between predicted temperature at the present, T_p , and the seismically inferred temperature, T_d, is

$$J = \int_V (T_p - T_d)^2 dv \tag{6}$$

or the cost function. By solving a constrained minimization problem with its Lagrangian function constructed by appending Eq. (4) to Eq. (6) (cf. *Bunge et al.* [2003], *Ismail-Zadeh et al.* [2004], *Liu and Gurnis* [2008], and many other papers in atmospheric sciences such as *Talagrand and Courtier* [1987], *Sun et al.* [1991], *Sirkes and Tziperman* [1997]), we get the adjoint equation

$$\frac{\partial \lambda}{\partial t} + \vec{u} \cdot \nabla \lambda + \kappa \nabla^2 \lambda = (T_d - T_p)\delta(t - t_1) \tag{7}$$

where λ, the Lagrangian multiplier, is the adjoint temperature and t_1 is the present time. As the conjugate operator of the forward energy equation, the adjoint model back-propagates the residual field T_d-T_p to the initial time, t_0, where the corresponding velocities $\vec{u}$ are stored from the previous forward iteration [*Bunge et al.,* 2003; *Liu and Gurnis,* 2008].

Starting with the temperature field scaled from present-day tomography, we generate a first guess to the initial condition with a simple backward integration (SBI) of the forward model with gravity and plate motions reversed. This initial condition is subsequently updated according to a conjugate gradient algorithm

$$T_0^{i+1} = T_0^i - \gamma(i) \cdot \lambda_0^i \tag{8}$$

where i is the iteration number and γ a damping factor. The iteration process terminates upon convergence of the cost function.

We solve equations 2-4 and 7 with CitcomS, a finite-element code for solving

thermal convection [*Zhong et al.,* 2000]. Plate motions calculated at 1 Myr intervals and linearly interpolated for intervening times are used as boundary conditions. Other boundary conditions include an isothermal surface and an isothermal, free-slip core-mantle boundary. *Liu and Gurnis* [2008] developed an adjoint version by modifications of CitcomS Version 2.0, obtained from the Computational Infrastructure for Geodynamics (http://geodynamics.org).

We use global flow models to avoid artifacts associated with imposed vertical boundaries. Our global model uses 12 caps with 129×129 nodes in each cap (approximately 40 km resolution in map view) and 65 grid points in radial direction. We also designed a regional model that covers a domain twice as wide (east-west) as the NAM plate, allowing the plate to move since 100 Ma with all observations remaining >1,000 km from the vertical boundaries. The reflecting side boundaries caused a lower mantle return flow restricting the horizontal motion and resulting in Farallon slab positioned further to the west in the Late Cretaceous compared to the global model, implying that only global models are suitable for this and similar studies.

4.5.2. Sedimentation model

The models are tested by comparing dynamic topography (predicted stratigraphy) against observations. The model dynamic topography is rotated into the plate frame of reference [*Gurnis et al.,* 1998]. During the initial step (100 Ma), we assume an

initial topography to which we add computed dynamic topography, defining the initial shape of basins and topographic highs. We impose eustasy based on published curves initially $SL(t_0)$, assuming marine deposition with constant rate (SR) in areas topographically lower than the water surface. The maximum sediment thickness Δz_S deposited during a time step, Δt, is

$$\Delta z_S = SR \cdot \Delta t \tag{9}$$

SR, 50 m/Myr (Table 4.1), is determined from the total long-wavelength thickness of Late Cretaceous isopach, [*Cook and Bally,* 1975]. Since the ratio between geoid and dynamic topography is small, we assume a flat water surface [*Gurnis,* 1991]. We assume uniform thickness of sediments across the basin. If the accommodation is less than allowed isostatically, we only fill to the maximum allowed value. We correct for Airy isostasy at the end of each time step:

$$\delta = \Delta z_S \cdot \frac{\rho_S - \rho_W}{\rho_M - \rho_W} \tag{10}$$

where δ is basin depth correction, ρ_S, ρ_W and ρ_M are density of sediments (2,300 kg/m^3), water (1,000 kg/m^3), and mantle (3,300 kg/m^3), respectively. Isostatically adjusted topography becomes the input into each subsequent time step. For steps 1 to n we add the differential dynamic topography between steps n and $n-1$, account for eustatic sea-level change $SL(t_n)$, deposit sediments, and apply the isostatic adjustment, until we reach the final time step at 0 Ma.

At each time step, we predict shoreline position as the 0 m contour and track dynamic topography at the position of each borehole. Cumulative Late Cretaceous

isopach thickness is calculated as accumulated sediment thickness 100 to 65 Ma, with sediment compaction being neglected. Following the inference of mantle properties, we will determine the influence which initial NAM topography and eustatic sea level have on the stratigraphic predictions.

4.5.3. Constraining mantle properties

The effective temperature scaling and mantle viscosities are treated as free variables that we attempt to constrain with dynamic topography and its rate of change, with relations following from the conservation of momentum and energy (Eq. 3-4):

$$h = C_1 T_e \tag{11}$$

$$\dot{h} = \frac{C_2}{\eta_{um}} h_1^{\,2} \tag{12}$$

where h is dynamic topography and $\dot{h}$ it's rate of change; C_1 and C_2 are numerical constants obtained from the solution of flow and are dependent on the viscosity and temperature structure [*Gurnis et al.,* 2000]. Derivation and recovery of mantle properties with synthetic data can be found in *Liu and Gurnis* [2008].

We use two steps to constrain mantle properties. First the scaling between the magnitude of seismic anomalies and effective temperature is inferred, followed by the estimation of mantle viscosities. For a given thermal anomaly (density) in the

upper mantle, Eq. 11 implies that the magnitude of surface dynamic topography is linearly related to the amplitude of thermal anomalies. This relation is not always valid since dynamic topography depends on the ratio of upper/lower mantle viscosity, but it is a good approximation for active subduction (*cf. Richard and Hager* [1984]). For Farallon subduction, the modeled dynamic topography is associated with Cretaceous flooding over a lateral scale >1,000 km, which, as we will show, requires the slab to be shallow and flat-lying, and thus enabling a constraint on the amplitude of T_e (Eq. 11).

The upper mantle viscosity is inversely proportional to the rate of change of dynamic topography [*Liu and Gurnis,* 2008, Eq. 10], which is constrained from stratigraphic data. Temporal evolution of flooding (shown by paleo shorelines) including its sudden appearance in the Late Albian and gradual demise in the Late Cretaceous provide constraints on mantle viscosity. Tectonic subsidence rate extracted from the boreholes is equivalent to the rate of change of dynamic topography in the NAM frame of reference.

4.5.4. Subduction parameterization

We started with simple models that include a three layer viscosity profile: a lithosphere with a viscosity of 5×10^{22} Pa s above 100 km depth, and an upper and lower mantle separated at 660 km with viscosities to be constrained. We also use a temperature-dependent viscosity, where a temperature decrease of 200 °C results

in an increase of viscosity by one order of magnitude. In the SBI, the cold Farallon anomaly rises instead of sinks. By 70 Ma, within the upper mantle, the cold material diverges and partly deflects toward the east due to the reversely imposed plate motions (Fig. 4.4A), resulting in geophysically unreasonable subduction inconsistent with the temporal sequence of subsidence and uplift of the WIS.

In order to direct the Farallon slab toward the oceanic plate on the surface we implement a stress guide, a simple approach that couples the oceanic plate with the Farallon slab using the viscosity field. The implementation uses a high-viscosity layer (HVL) overlain by a low-viscosity channel (LVC) beneath the NAM plate [*Manea and Gurnis,* 2007; *Humphreys and Coblentz,* 2007] with one end of the HVL attached to the oceanic plate at the trench (Fig. 4.4B). The stress guide has a total thickness of 150 km. The recovery of the slab is almost identical in cases we explored as long as the stress guide is longer than 3,000 km (Fig. 4.4C-E), while the HVL with a viscosity larger than 5×10^{22} Pa s always produces nearly the same slab geometry (Fig. 4.4F-I). Imposed plate motion and the stress guide neither increases nor decreases the vertical velocities in models with plate motions (Fig. 4.4A) or with both plate motions and the stress guide (Fig. 4.4J), compared to those without imposed plate motions (Fig. 4.4K). With such a stress guide, the adjoint method recovers the Farallon subduction while maintaining reasonable subduction geometry over time while reproducing the general characteristics of dynamic topography (Fig. 4.4J) (as described below).

4.6. Results

4.6.1. Effective temperature anomaly

Comparing model results with stratigraphy we attempt to bound three variables: upper mantle viscosity η_{UM}, lower mantle viscosity η_{LM}, and the scaling Γ between seismic shear-velocity anomaly and effective temperature T_e. Using a range of Γ (1×10^3, 2×10^3, 3×10^3 °C/km/s) which give different effective temperature anomalies, we find that the recovered slabs will have nearly identical geometries if the lower mantle viscosity is compensated so that the effective Rayleigh number remains invariant. In these cases, the convective velocities were nearly the same, except for small differences in the lateral variations in viscosity associated with temperature. Although the dynamic topography has the same spatial pattern, their magnitudes differ (Fig. 4.5A-C). Predicted flooding varies depending on dynamic subsidence: With an effective temperature anomaly of 80°C, the flooding occurs widely over the west at 95 Ma, but disappears soon after (Fig. 4.5E); with a larger anomaly (240 °C), the flooding is well correlated with WIS, but persists after the Cretaceous (Fig. 4.5G); the flooding is well predicted with an anomaly of 160°C in both time and space (Fig. 4.5F). The effective temperature scaling is about Γ=2×10^3°C/km/s, giving an effective temperature anomaly of 160°C. This value will be used in subsequent models.

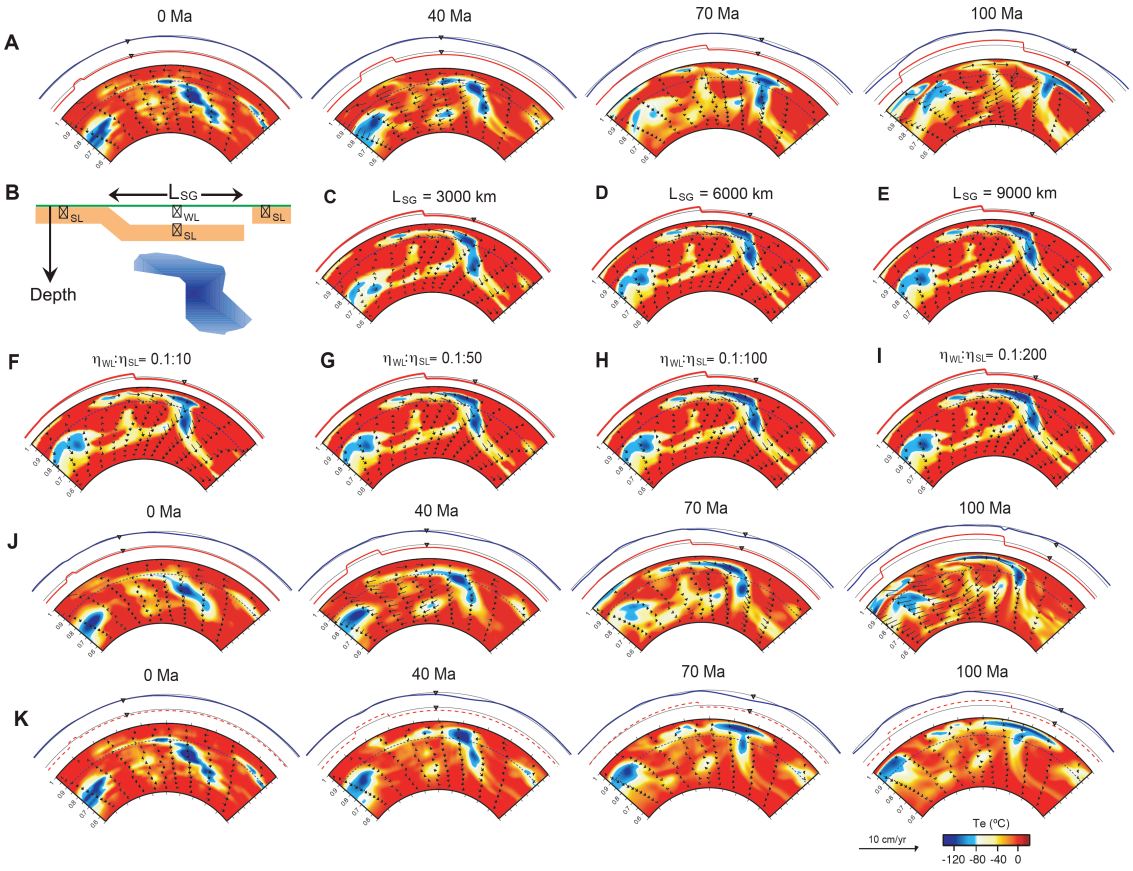

Figure 4.4. Subduction modeling with inverse method. All cross-sections are at 41 °N, with the velocity vectors (black arrows) plotted over the temperature field (in color). Dynamic topography (blue) and plate motions (red) along the profile are shown above the cross-section. The black triangle denotes a borehole site (41.6 °N, 254 °E) that moves with the continent. All runs have a lower mantle viscosity η_{LM}=15, η_{UM}=1 and an effective temperature anomaly T_e=160 °C. (A) An SBI run with a standard model from present-day mantle structure leads to unrealistic subduction geometry back in time, indicating the requirement of a stress guide. (B) A sketch of the parameterized stress guide showing an imposed small viscosity (η_{WL}) layer overlying a large viscosity (η_{SL}) layer underneath the continent, where L_{SG} indicates the length of the guide. (C-E) show the recovered slab at 70 Ma with the different values of L_{SG}, and (F-I) with various viscosity ratios (relative to 10^{21} Pa s) within the two layers, showing the solutions converge as long as L_{SG}>3,000 km and η_{WL}: η_{WL}<0.1:50. (J) The evolution of the slab after five forward-adjoint iterations including a stress guide with L_{SG}=6,000 km and η_{WL}: η_{WL}=0.1:100, where reasonable subduction geometry develops. (K) A free convection test showing that, without the imposed plate motions and stress guide, the slab has almost the same vertical velocities as can be seen from the depth the structure at different times.

4.6.2. Mantle viscosities

Once the effective temperature is constrained, upper and lower mantle viscosities can be retrieved from dynamic topography and its rate of change by comparing the fit to borehole tectonic subsidence and subsidence rate. We selected models with lower mantle viscosities η_{LM} between 1×10^{22} Pa s and 3×10^{22} Pa s and upper mantle viscosities η_{UM} between 0.1×10^{21} Pa s and 2×10^{21} Pa s, which are within the range of post-glacial rebound-inferred values [*Milne et al.,* 2004; *Mitrovica and Forte,* 2004]. We tested models with lower mantle viscosities as high as 6×10^{22} Pa s, but these models yielded little or no flooding in the WIS.

We calculated the RMS misfit (Fig. 4.6) between tectonic subsidence and dynamic topography for each WIS borehole (Fig. 4.1). While holding η_{LM} =1.5×10^{22} Pa s fixed, the largest misfit for borehole subsidence is found for the smallest upper mantle viscosity, η_{UM} =0.1×10^{21} Pa s (Fig. 4.6A-B) because the model subsidence is too large at the beginning of the Late Cretaceous and too small from 70-60 Ma. A larger upper mantle viscosity provides a better fit: Along the E-W line (Fig. 4.6A), a model with η_{UM} =2×10^{21} Pa s provides the best prediction, while for the N-S line (Fig. 4.6B) η_{UM} =1×10^{21} Pa s is the preferred value. Alternatively, by fixing η_{UM} =10^{21} Pa s, the largest misfits occur for the smallest lower mantle viscosity (η_{LM} =1×10^{22} Pa s) (Fig. 4.6C-D). Models with lower mantle viscosities between 1.5-3.0$\times10^{22}$ Pa s give borehole subsidence prediction with lower RMS misfits (Fig. 4.6C-D). There is a general trend of the westernmost boreholes (Fig. 4.6A,B) having under predicted subsidences, which could be related to proximity to the Sevier belt (Fig. 4.1) and

super-crustal loading, which we do not account for.

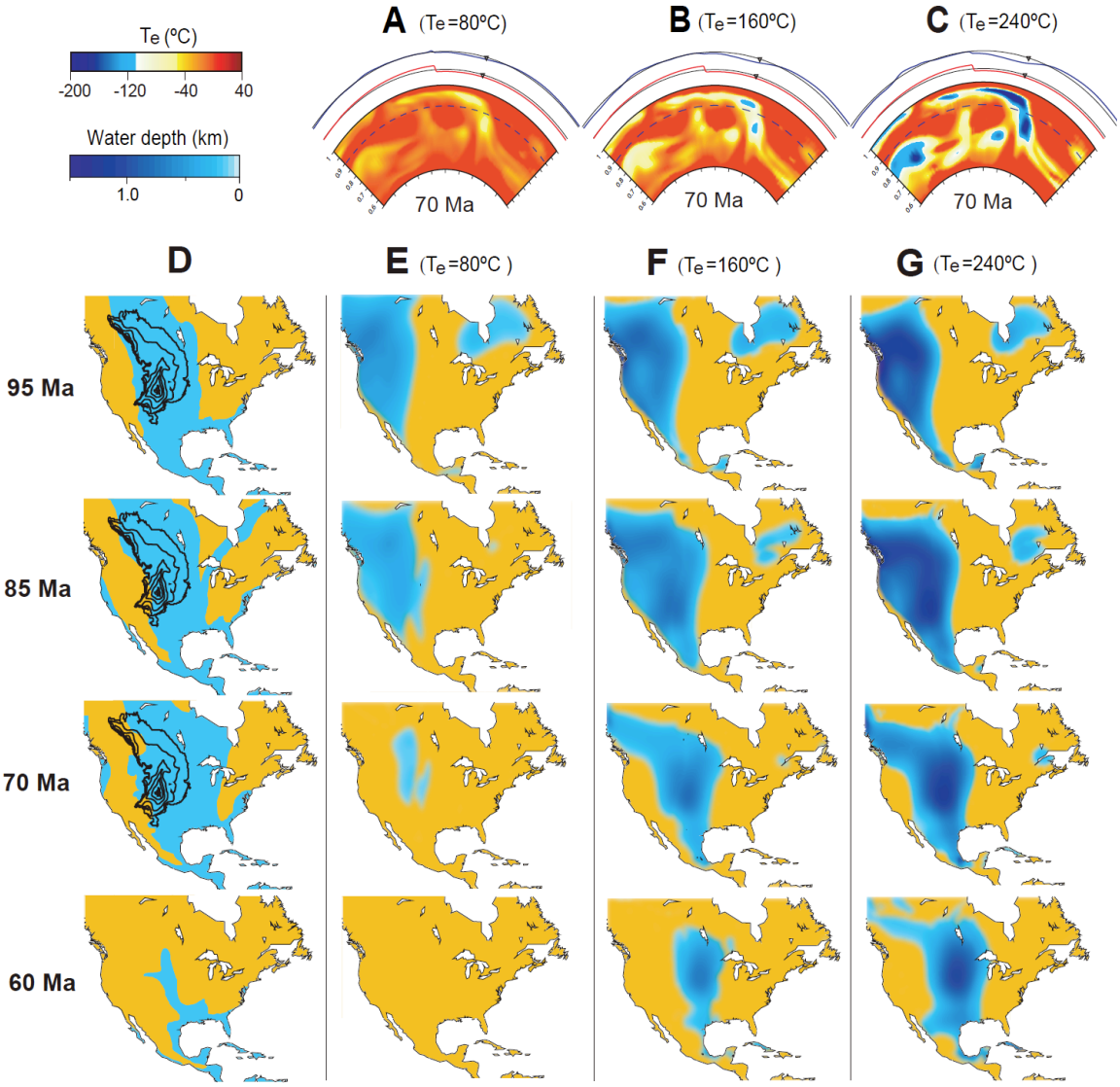

Figure 4.5. Selection of the effective temperature through flooding predictions. (A-C) Recovered Farallon slab at 70 Ma with three different magnitudes of temperature anomaly (80, 160, 240 °C, respectively) and lower mantle viscosities largely traded off with temperature (7×, 15×, 30×10^{21} Pa s, respectively; all cases have an upper mantle viscosity 10^{21} Pa s), where all three models see the same slab geometries. (D) Reconstructed WIS flooding (blue; *Smith et al.* [1994]) and sediment isopachs (black contours with 2,000 ft contour interval; *Cook and Bally* [1975]). The predicted Late Cretaceous flooding (E-G) with different T_e, with the 160 °C temperature anomaly (F) matching observations (D) to the best extent.

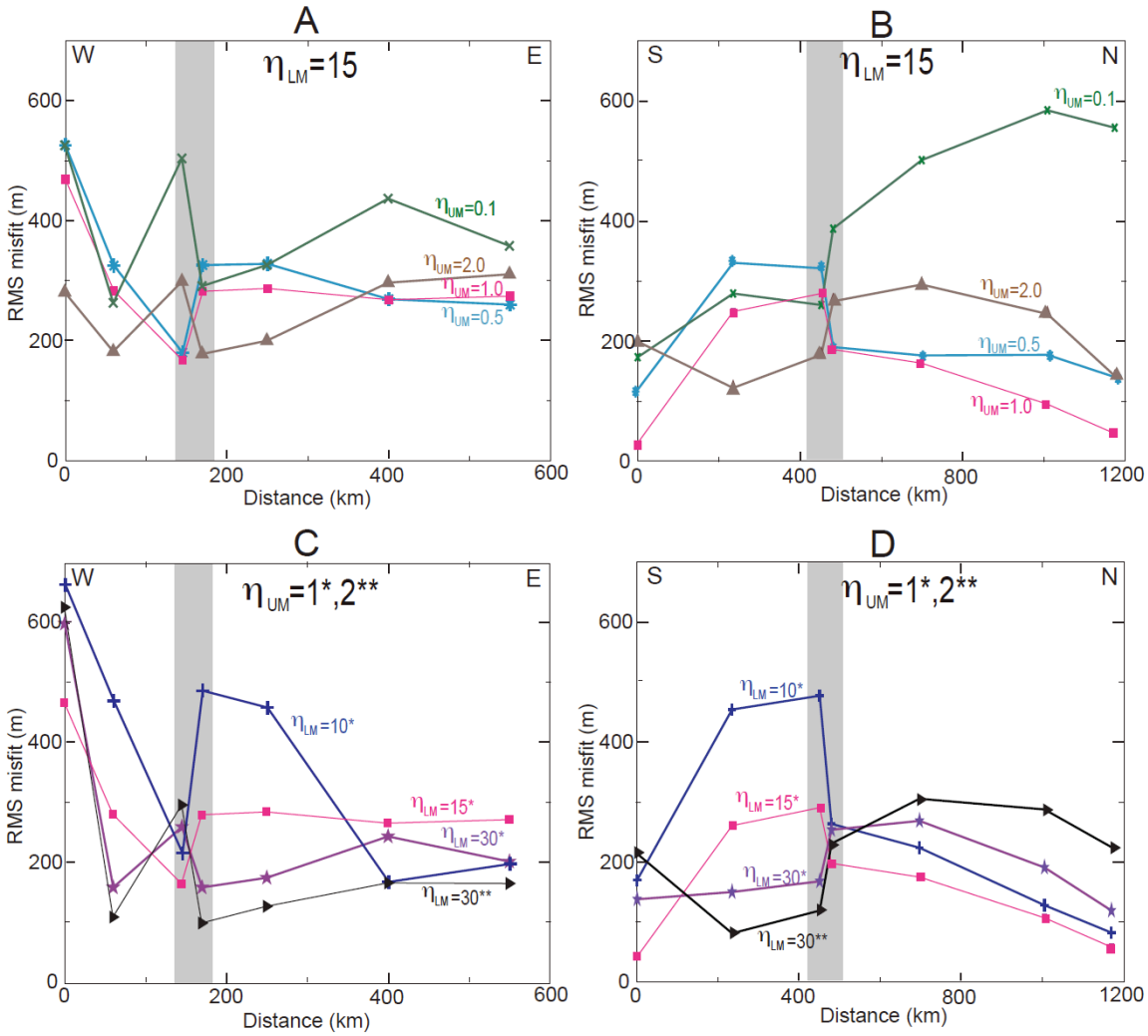

Figure 4.6. RMS amplitude misfit between observed and model borehole tectonic subsidence. (A-B) Misfit for models with constant lower mantle viscosity η_{LM}=1.5x10^{22} Pa s. (C-D) Misfit for models with upper mantle viscosity η_{LM}=1-2x10^{21} Pa s. Grey vertical bar indicates intersection of N-S and E-W profiles. All viscosity values are shown with respect to reference viscosity of 10^{21} Pa s.

Since change of dynamic topography constrains upper mantle viscosity, η_{UM} (Eq. 12), we compare the slope of tectonic subsidence curves (subsidence rate) against model results (Fig. 4.7) by fitting a linear trend to the modeled and observed subsidence. The agreement between model predictions and observation vary significantly from location to location at greater than the 95% confidence level, indicating that this may not be the most robust parameter for the selection of

mantle viscosities. However, we can confidently eliminate certain models, and models with ratios of lower/upper mantle viscosity that are either too high or too low. Specifically, the model with η_{LM}/η_{UM} =30:1 (η_{LM} =1.5×10^{22} Pa s and η_{UM} =0.5×10^{21} Pa s) (Fig. 4.7A-B) and η_{LM}/η_{UM} =10:1 (η_{LM} =1.0×10^{22} Pa s and η_{UM} =1.0×10^{21} Pa s) (Fig. 4.7C-D) can both be eliminated based on subsidence rate.

Based on the RMS misfit of tectonic subsidence (Fig. 4.6) and subsidence rate (Fig. 4.7) alone, there is no clear "best model" that yields the most robust fit. We therefore summarize the boreholes fits individually (Table 4.2) to define models with overall consistency with data. A successful model (+ on Table 4.2) selection is based on two criteria: the smallest RMS misfit and the smallest discrepancy between observed, and model subsidence rate. Once summarized in this fashion, two models emerge (Table 4.2): (1) a model with η_{LM} =3×10^{22} Pa s and η_{UM} =2×10^{21} Pa s, and (2) a model with η_{LM} =1.5×10^{22} Pa s and η_{UM} =1×10^{21} Pa. In addition, models with upper mantle viscosity smaller than 0.5×10^{21} Pa s never fit borehole subsidence satisfactorily (Table 4.2). Both models that yield good predictions of the borehole subsidence have lower/upper mantle viscosity ratios of η_{LM}:η_{UM}=15:1, suggesting that differential dynamic subsidence (with respect to 97 Ma) constrains the ratio of upper/lower mantle viscosity. This trade-off in absolute viscosities occurs within a limited range related to data uncertainties, i.e., the case with η_{LM} = 6×10^{22} Pa s and η_{UM} = 4×10^{21} Pa s is safely ruled out because the borehole subsidence rates are all under-predicted.

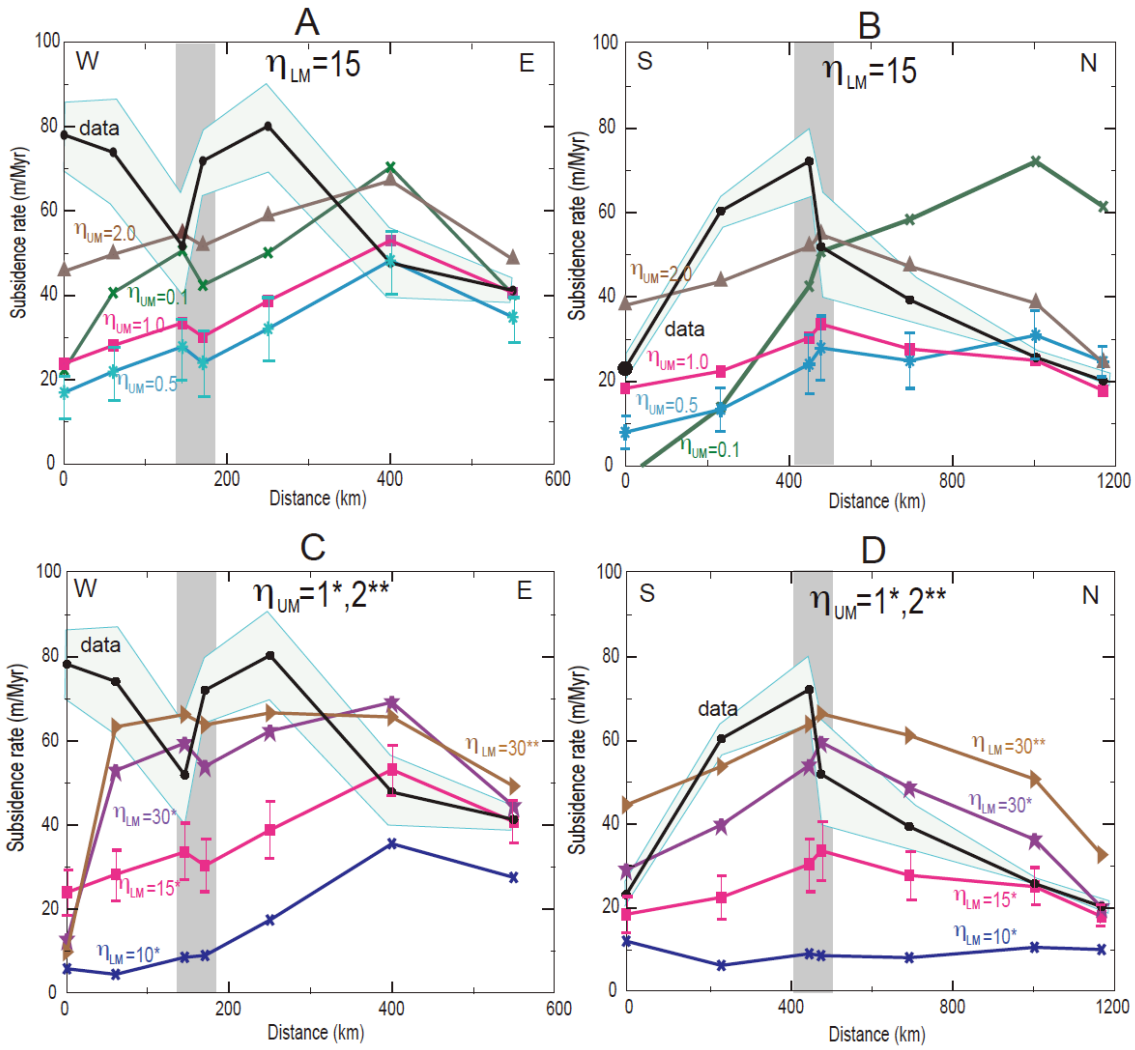

Figure 4.7. Comparison between observed and model subsidence rate. (A-B) Comparison for models with constant lower mantle viscosity η_{LM}=1.5x10^{22} Pa s. (C-D) Comparison for models with upper mantle viscosity η_{LM}=1-2x10^{21} Pa s. Observation (data) curve is shows with black line, and models are shown with colored lines. Light blue colored outline indicates 95% confidence interval for the observation, and colored bars indicates 95% confidence interval for a representative model, with all other models having similar confidence intervals. Grey vertical bar indicates area of intersection of N-S and E-W profiles. All viscosity values are shown with respect to reference viscosity of 10^{21} Pa s.

Table 4.2. Summary of misfits between observed and model tectonic subsidence based on RMS amplitude and subsidence rate criteria. For each well, we evaluated the model with the smallest misfits based on two criteria and marked it with symbol "+". Values of upper mantle viscosity η_{UM} and lower mantle viscosity η_{LM} is given with respect to reference value of 10^{21} Pa s.

η_{LM}	η_{UM}	Criteria	EW line						NS line						Total
			1	2	3	4	5	6	1	2	3	4	5	6	
10	1	Slope									+				2
		RMS					+								
15	0.1	Slope													0
		RMS													
15	0.3	Slope													0
		RMS													
15	0.5	Slope					+								1
		RMS													
15	1	Slope						+	+				+		8
		RMS							+		+	+	+	+	
15	1.5	Slope										+			1
		RMS													
15	2	Slope	+												2
		RMS	+												
20	0.3	Slope													0
		RMS													
30	1	Slope												+	1
		RMS													
30	2	Slope		+	+	+				+					9
		RMS		+	+	+		+		+					

The final selection of the preferred upper and lower mantle viscosities is based on the pattern of Cretaceous flooding. One of the best-fitting models from borehole subsidence analysis (η_{UM}=10^{21} Pa s and η_{LM}=1.5×10^{22} Pa s) predicts the flooding well (Fig. 4.8B) in terms of the position of WIS between 85 and 60 Ma (Fig. 4.8A-B), with individual borehole tectonic subsidence also being well predicted (Fig. 4.8G-I). Decreasing η_{UM} to 3×10^{20} Pa s (Fig. 4.8C) and further to 10^{20} Pa s (Fig. 4.8D) results in eastward and northward migration of flooding from 95 to 70 Ma, which is

different from observations, where the flooding remains in the same location through the Late Cretaceous (Fig. 4.8A). Smaller η_{UM} values lead to insufficient flooding at 95 Ma and excess flooding at 60 Ma (Fig. 4.8C, D). Out of two models with the best predictions of the borehole subsidence, the model with η_{UM}=10^{21} Pa s and η_{LM}=1.5×10^{22} Pa s gives the best predictions of the Cretaceous flooding and subsequent withdrawal of the interior seaway (Fig. 4.8B). The model with η_{UM}=2x10^{21} Pa s and η_{LM}=3.0×10^{22} Pa s predicts flooding at 95 Ma and 85 Ma too far to the west (Fig. 4.8E), and predicts a withdrawal of the interior seaway around 70 Ma, too early compared to the paleogeographic reconstructions. The preferred model with η_{UM}=10^{21} Pa s and η_{LM}=1.5×10^{22} Pa s (Fig. 4.8B) predicts flooding that is too far to the west only at 95 Ma, while the spatial localization of the flooding corresponds to paleogeographic reconstructions at all subsequent times.

When the descent of the Farallon anomaly is reversed from its present-day depth to the surface, the structure traverses a much longer path through the lower mantle compared to the upper mantle. Thus, the lower mantle viscosity largely controls the timing and position of flat-slab formation during Farallon subduction, and the position and timing of Late Cretaceous flooding. When the lower mantle viscosity is 3×10^{22} Pa s (Fig. 4.8E), the slab remains in the lower mantle for a longer duration leading to a smaller magnitude of dynamic topography at 70 Ma with little flooding (Fig. 4.8E).

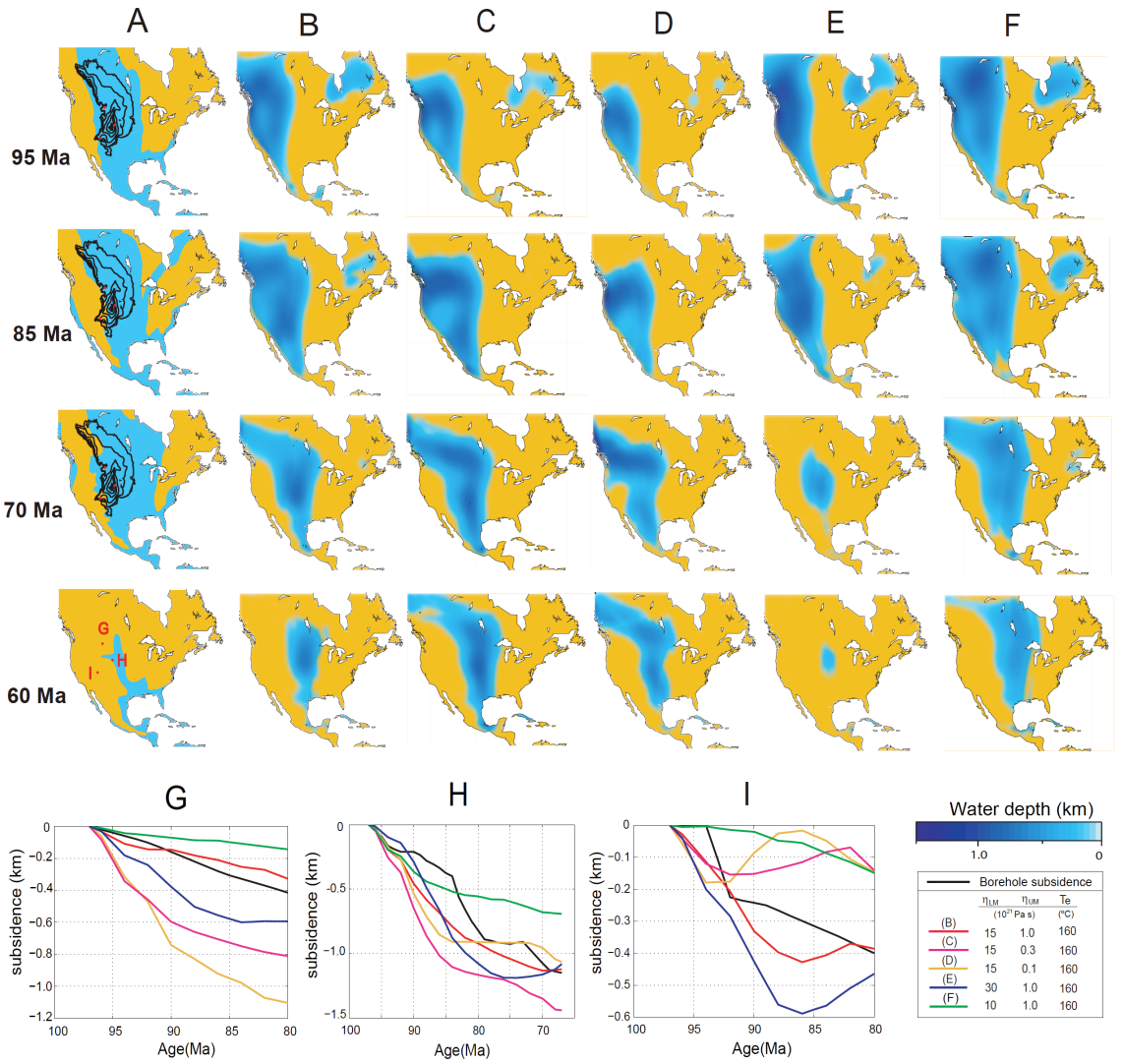

Figure 4.8. Effects of mantle viscosities on flooding predictions and borehole subsidence. (A) Observed flooding [*Smith et al.,* 1994]. (B-F) Predicted flooding with different models (parameters are given in the lower right corner; viscosities relative to10^{21} Pa s). (G-I) Borehole subsidence predictions (colored lines) compared to observations (black line).

A smaller lower mantle viscosity (10^{22} Pa s) allows the slab to stay in the upper mantle longer, and this leads to sustained flooding over an unreasonably large area throughout the Late Cretaceous (Fig. 4.8F). Another aspect is the extent of the flat-slab underneath the continent (Fig. 4.4J): The slab stays for a longer (shorter)

period in a higher (lower) viscosity lower mantle, so the flat subduction has a smaller (larger) spatial extent as the overriding plate moves toward the west at a given velocity. This is reflected in the position of flooding, where a lower mantle with a higher viscosity (Fig. 4.8E) shows a westward shift of flooding, and that with a lower viscosity (Fig. 4.8F) shows an eastward shift, compared to intermediate value of lower mantle viscosity (Fig. 4.8B).

4.6.3. Influence of eustasy and initial topography on model predictions

Since the assumed eustatic curve may influence our results, we explored the sensitivity of this assumption using our preferred mantle viscosity model (η_{UM}=1x10^{21} Pas, η_{LM}=1.5x10^{22} Pas) (Fig. 4.9). When we impose no eustatic change (Fig. 4.9B) or the *Miller et al.* [2005] sea-level curve (Fig. 4.9C), we predict less widespread flooding, comparing to one using the *Haq et al.* [1987] or *Müller et al.* [2008b] curves (Fig. 4.9 D-E). Initially (at 90 Ma), by imposing small sea levels, we produce a narrower epicontinental sea and more constrained flooding north-south (Fig. 4.9B,C), compared with predictions using significantly higher (Fig. 4.9D-E) Late Cretaceous sea levels.

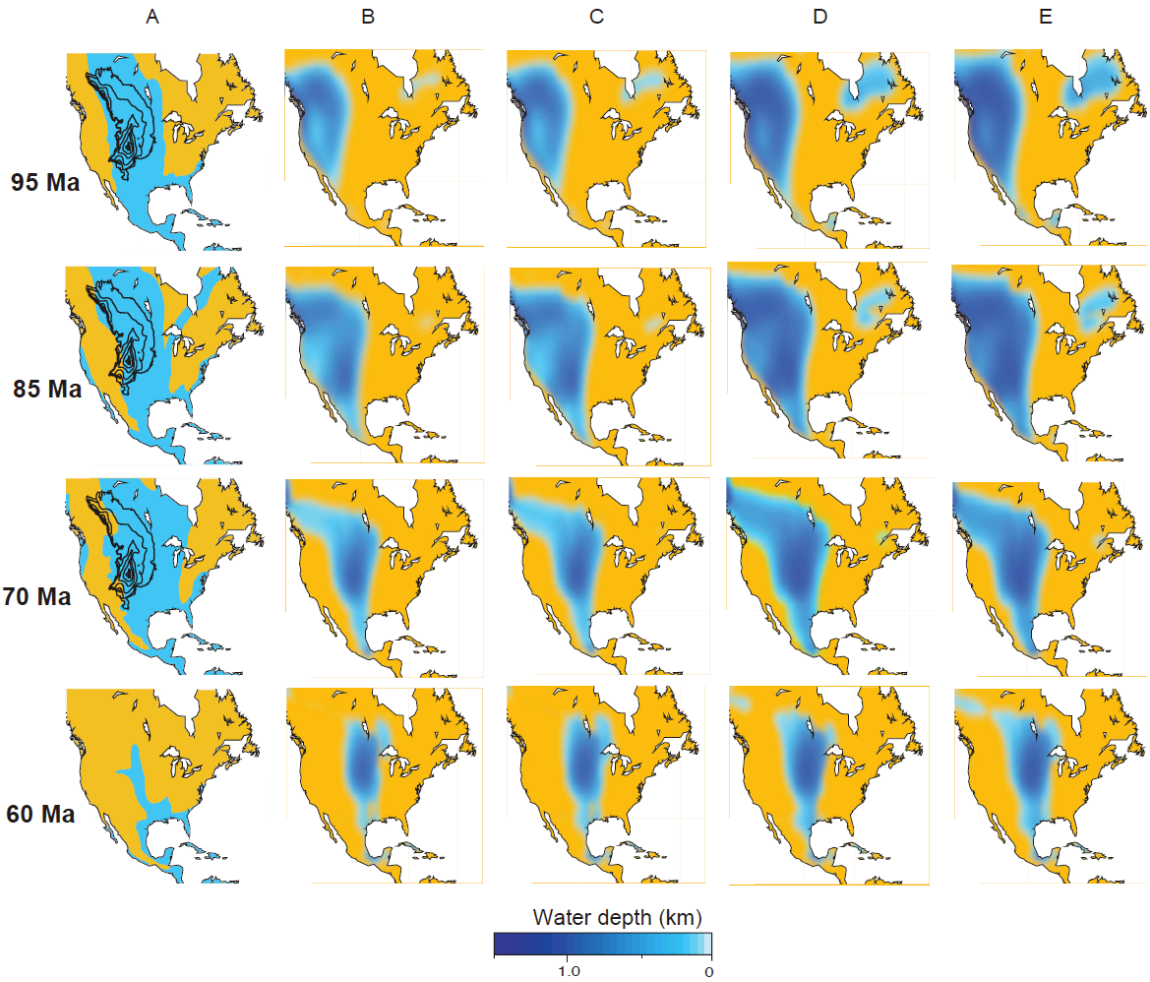

Figure 4.9. Effect of eustasy on predicted flooding. (A) Reconstructed flooding [blue; *Smith et al.,* 1994]. (B) Prediction with no change in sea level. (C) Prediction using *Miller et al.* [2005] sea level. (D) Prediction using *Müller et al.* [2008b] sea level. (F) Prediction using *Haq and Al-Qahtani* [2005] sea level. Black contours show Late Cretaceous isopach [*Cook and Bally,* 1975] with 2000 ft contour interval. All predictions are using initially flat Earth topography.

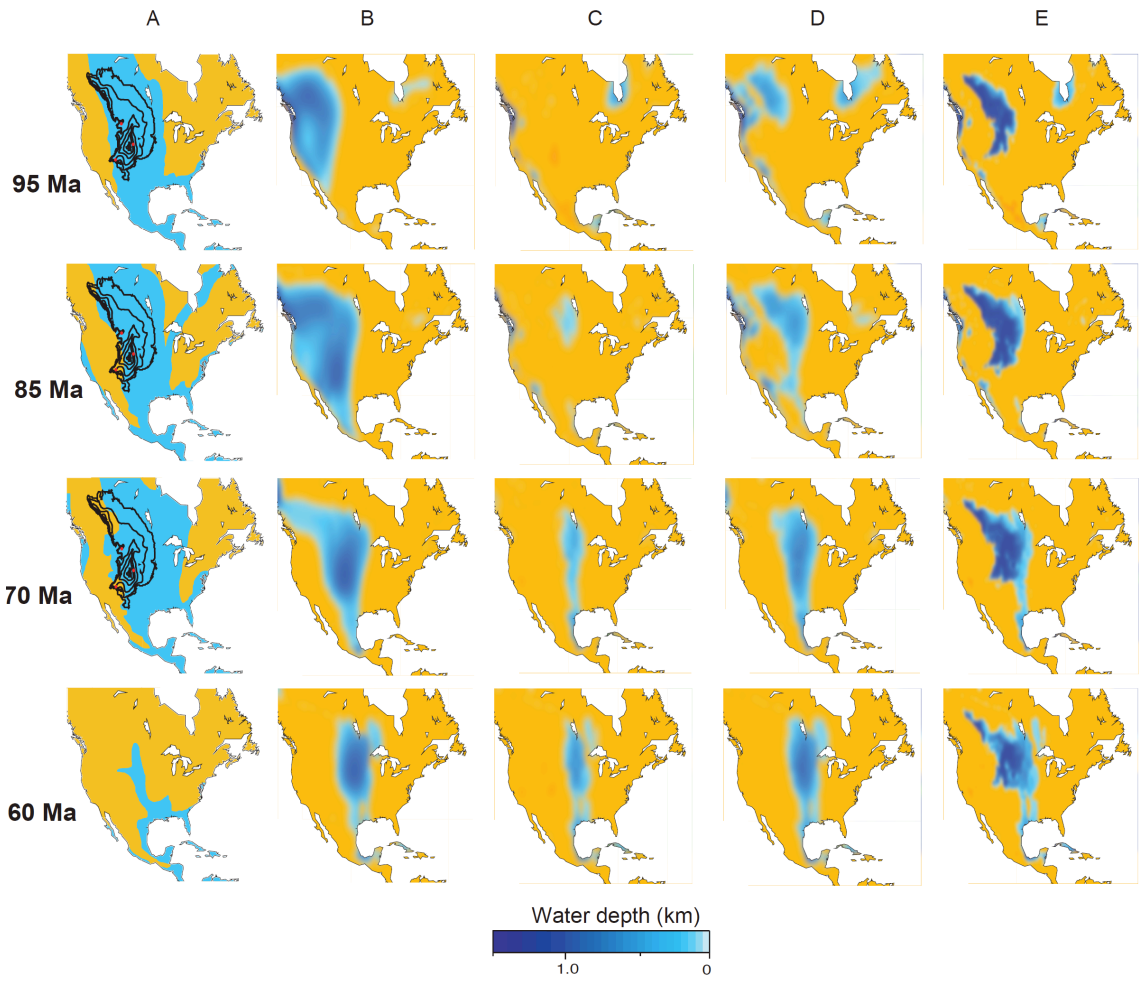

Figure 4.10. Effect of initial topography on predicted flooding. (A) Reconstructed flooding [blue; *Smith et al.,* 1994]. (B) Prediction using initially flat Earth topography. (C) Prediction using present-day North America topography. (D) Prediction using present-day North America topography multiplied by 0.5. (F) Prediction using present-day topography with Cretaceous sediments isostatically removed. Black contours show Late Cretaceous isopach [*Cook and Bally,* 1975] with 2,000 ft contour interval. All predictions are using *Haq and Al-Qahtani* [2005] sea level.

At 85 and 70 Ma, we predict wider flooding east-west when we *impose Haq and Al-Qahtani* [2005] or *Müller et al.* [2008b] sea levels. All cases predict reduced extents of flooding at 60 Ma compared to 95, 80 and 70 Ma, consistent with overall withdrawal of the interior seaway at the end of Cretaceous. However, in all cases

(Fig. 4.9B-E) we still predict widespread flooding during Cretaceous and subsequent early Cenozoic withdrawal. Different sea levels give minor differences in flooding patterns, implying that dynamic topography represents a primary control of long-wavelength Late Cretaceous marine inundation within the interior of NAM, and that eustasy is maybe secondary.

Our flooding model starts with a given initial topography and plays a significant role in the overall results. Since little knowledge exists on NAM topography during the Late Cretaceous, we used several alternative initial topographies: A flat Earth (Fig 4.10B), present-day (Fig 4.10C), present-day scaled by 0.5 (Fig. 4.10D), and present-day with Cretaceous sediments isostatically removed (Fig. 4.10E). To maximize flooding estimates, we applied the *Haq and Al-Qahtani* [2005] curve. A model with an initially flat surface (Fig. 4.10B) predicts a pattern and duration closest to the observed (Fig. 4.10B). When initialized with the present-day topography, we obtain little flooding (Fig. 4.10C), even with the high-amplitude eustasy. Similarly, when we use half value of the present-day topography (Fig. 4.10D) or that modified by removal sediments (Fig. 4.10E), we still under predict Cretaceous flooding.

4.6.4. Influence of eustasy and initial topography on model predictions

Presently, the Farallon slab is imaged in the mid mantle under the US east coast (Fig. 4.2), creating a long-wavelength small-amplitude dynamic topography low.

Spasojević et al. [2008] analyzed Eocene and Miocene paleo shorelines, suggesting at least 50 m, and probably as much as 200 m of dynamic subsidence since the Eocene (Fig. 4.11), consistent with the discrepancy between regional and global sea level. Similarly, *Conrad et al.* [2004] predict a modeled dynamic topography low on the east coast from the Farallon slab, while *Moucha et al.* [2008] suggested that the same region is not a stable reference frame due to effect of time-dependent dynamic topography.

All models that we explored predict Tertiary subsidence of the US east coast (Fig. 4.11). Models that yielded the best fits to WIS borehole subsidence (Fig. 4.11, cases 2-3) predict 700-900 m subsidence since the early Eocene, and 250 m since the early Miocene. Models scaling both positive and negative S-wave anomalies (Fig. 3.11, case 1) yield the largest estimate of post Eocene subsidence. These models (Fig. 3.11, cases 1-3) overestimate the amount of subsidence, compared with paleo-shorelines and sea-level discrepancies.

In order to reduce dynamic subsidence since 55 Ma, we introduce an additional viscosity layer in the uppermost mantle that was not required to fit Late Cretaceous flooding and subsidence. This layer extends from the base of the lithosphere to 410 km depth with a viscosity of 10^{20} Pa s, while the transition zone has a viscosity of 10^{21} Pa s. Estimates of dynamic subsidence since the early Eocene for this four-layer mantle are 480-560 m (Fig. 4.11, cases 4-5), consistent with subsidence estimates based on paleo shorelines and sea-level discrepancies. Models with an additional layer in the upper mantle yield the same Late Cretaceous subsidence and flooding as

the three-layer models, given that lower mantle viscosity is the same in both three- and four-layer models, and that upper mantle viscosity in the 3-layer model is the same as transition zone viscosity in the 4-layer model.

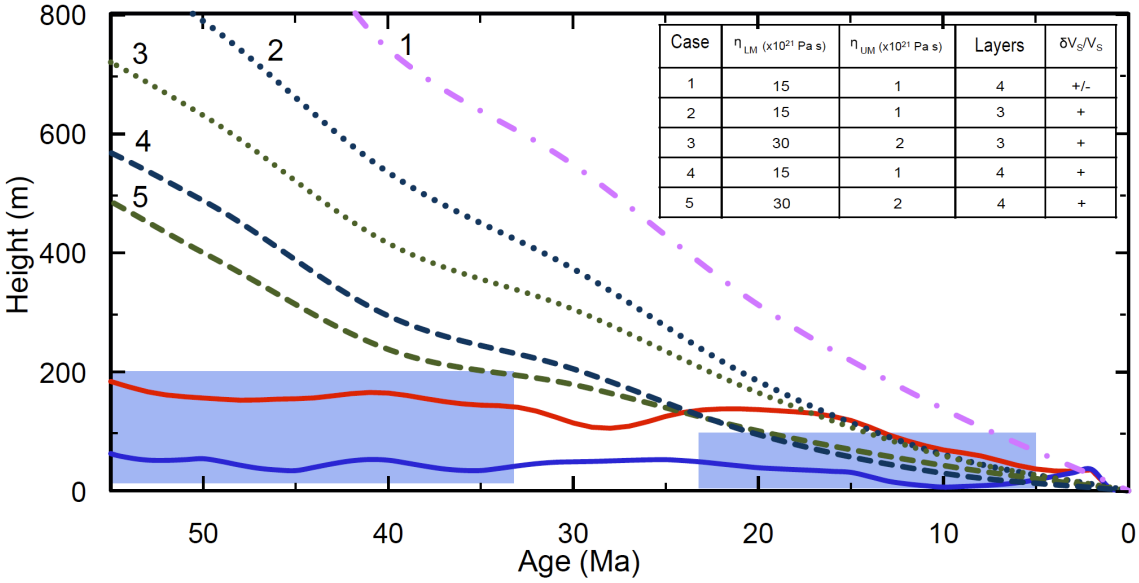

Figure 4.11. Predictions of the US east coast subsidence. Dynamic topography change for a well in New Jersey coastal plain (coordinates 285°30', 39°30'N) for five dynamic models is shown with colored dotted and dashed lines, solid red and blue lines show difference between sea-level models of *Haq and Al-Qahtani* [2005] and *Miller et al.* [2005], and *Kominz* [1984] and *Miller et al.* [2005], respectively. Blue colored boxes show estimated subsidence range from paleo shoreline analysis for Eocene and Miocene. Table insert shows model parameters (η=viscosity, LM=lower mantle, UM=upper mantle viscosity, $\delta V_S/V_S$= seismic anomaly with positive (+) or both positive and negative (+/-) signals included). Dynamic topography was calculated as if were an interface between mantle and water.

4.7. Discussion and Conclusions

The results presented here were obtained using adjoint convection models for the evolution of the Farallon slab since the Late Cretaceous, constrained by seismic tomography and plate motions. The algorithm implements an optimal first guess to

the initial condition, temperature-dependent viscosity, and it is constrained by time- and spatially-dependent stratigraphic data. A simple correlation between NAM Cretaceous stratigraphy and seismic tomography shows that Late Cretaceous total isopach correlates well with present-day remnants of the Farallon slab with maximum correlation at depths 1,500-1,700 km. The maximum correlation between large seismic velocities anomalies, presumed to represent the Farallon remnants, and Late Cretaceous isopach rotated in the mantle frame of reference, occurs at a depth of 1,525 km for a rotation to 80 Ma and 1,675 km to 100 Ma. The average descent velocity of the Farallon slab back to 100 Ma and 80 Ma are 1.6 and 1.8 cm/yr, respectively. The smaller of the two velocities averaged over the longer time period implies that the Farallon slab has a slower vertical speed in its early stage of subduction between 100 and 80 Ma. The rather fast convergence of the Farallon and NAM plates during this time, therefore, suggests that the Farallon plate must have been moving faster laterally than vertically, consistent with flat subduction epoch [e.g., *Saleeby,* 2003].

In order to obtain reasonable subduction geometry, we parameterized a stress guide. By computing a range of cases in which the thickness, length, and strength of the guide were varied, we found that the onset of flat-lying subduction was not strongly affected by stress guide details as long as one was incorporated. The variation in upper and lower mantle viscosity and seismic scaling had a larger influence. How slabs are represented can be improved. First, seismic models showing the connection of the Juan de Fuca slab to the Farallon anomaly are improving (e.g., *Roth et al.* [2008]). This should allow one to use a purely seismic-

based approach to define present structure. Secondly, forward models incorporating realistic rheologies are improving [*Billen,* 2008]), and so higher-resolution methods will eventually be used in inversions as improvements in hardware and software allow.

We attempt to infer upper and lower mantle viscosities iteratively with stratigraphic constraints. The misfit with observed subsidence and its rate of change allow us to narrow the range of viscosities, with the preferred values primarily based on flooding. Our preferred viscosity model has an upper mantle viscosity of $1x10^{21}$ Pa s, and a lower mantle viscosity of $1.5x10^{22}$ Pa s. These represent background viscosities locally modified by the Farallon slab. Consequently, the average profiles inferred from post glacial rebound and the present day geoid are more complex in depth [*Mitrovica and Forte,* 2004] than ours. Thus, the ratio of mantle viscosities across 660 km discontinuity in our preferred model is 15:1, slightly smaller than the factor of 30 or more suggested using the geoid as a constraint on instantaneous flow models [*Hager,* 1984; *King and Masters,* 1992]. However, the values we propose for effective viscosities under NAM are within the range proposed through studies of postglacial isostatic adjustment. *Milne et al.* [2004] define the range of upper mantle viscosities between $5x10^{20}$ Pa s and 10^{21} Pa s, and lower mantle viscosities between $5x10^{21}$ Pa s and $5x10^{22}$ Pa s. Compared to the values proposed by joint inversion of convection and glacial isostatic adjustment data [*Mitrovica and Forte,* 2004], our effective upper mantle viscosity is equivalent to the value proposed for the bottom of the upper mantle and top of the lower mantle, while the proposed lower mantle viscosity has the same value as the one

defined by *Mitrovica and Forte* [2004] for the depth range of roughly 2,200-2,500 km.

Downwelling associated with subduction of the Farallon slab creates a dynamic topography low in the western interior during the Cretaceous (Fig. 4.12B). The dynamic topography low migrates eastward from 100 Ma to the present in the NAM frame of reference. Over the Late Cretaceous, the dynamic topography low has the largest amplitude (up to 1.5 km), and is located in the area of the WIS. This dynamic topography low is inundated by epicontinental seas, resulting in widespread Cretaceous flooding (Fig. 4.12C). Since there is disagreement between different authors on the amplitude of the global sea level since the Late Cretaceous, we model Cretaceous flooding with different sea-level curves [*Miller et al.,* 2005; *Müller et al.,* 2008b, *Haq and Al-Qahtani*, 2005]. We obtain flooding patterns that match long-wavelength features of shorelines that vary in amplitude from 0 to 250 m depending on the assumed eustasy (Fig. 4.9). Based on the analysis of observed sediment thickness and eustatic sea level, *Bond* [1976] also proposed that North America experienced significant continental submergence. The long-wavelength dynamic subsidence on order of 1,500 km was attributed to subduction of the Farallon slab [*Mitrovica et al.,* 1989; *Liu et al.,* 2005; *Liu and Nummedal,* 2004]. However, our results suggest that the first-order flooding patterns of the WIS is controlled primarily by long-wavelength dynamic topography attributed to the subduction of the Farallon slab, with eustasy playing a smaller role. The short-wavelength flexural loading component that changes on the time scale of a few million years has been attributed to the loading of the thrust belt [*Liu and Nummedal,* 2004], not accounted

for in our models. However, this component probably plays an important role for controlling sediment deposition on short length scales over hundreds of km [*Currie,* 2002], and it is not a primary factor affecting long wavelength flooding.

As the Farallon slab continues sinking under the continent during the Cenozoic, NAM moves westward in the mantle reference frame over this downwelling. A dynamic topography low, therefore, moves eastward in the NAM frame of reference. At 40 Ma (Fig. 4.12B) the dynamic topography low is located under the central portions of the continent, while at the present day the dynamic topography low is located under the US east coast (Fig. 4.12B). As the locus of dynamic topography moves eastward from the WIS at the end of Cretaceous, flooding is reduced and the interior seaway eventually vanishes, and no significant flooding is developed in the interior of the NAM during Cenozoic, as suggested by paleogeographic reconstructions [*Smith et al.,* 1994]. A region of high dynamic topography subsequently develops in the western North America during the Cenozoic, contributing to the overall uplift of the region previously located in WIS. The Laramide orogeny started in the Late Cretaceous, 70 to 80 million years ago [*Bird,* 1998], and ended 35 to 55 million years ago, although the exact timing is under discussion [*English and Johnston,* 2004]. The region affected by the orogeny extends from Alaska to northern Mexico, forming the Rocky Mountain fold-and-thrust belt in Canada and the United States, and the Sierra Madre Oriental fold-and-thrust belt in east-central Mexico [*English and Johnston,* 2004]. Dynamic effects of flat slab subduction have been suggested as one of the possible driving mechanisms for Laramide uplift [*English and Johnston,* 2004], along with other mechanisms such as

retroarc thrusting, the effects of Cordillerean collision [*English and Johnston,* 2004], crustal processes (such as horizontal shortening, magmatic injection or lower crust displacement) or partial delamination of the lithosphere [*McQuarrie and Chase,* 2000]. *Mitrovica et al.* [1979] proposed that the interior of NAM rebounds and uplifts after convergence slows down or ceases due to the detachment of the slab or accretion of a terrane. Our model predicts a continuous contribution of high dynamic topography to the overall uplift of the region once occupied by the WIS since the end of Late Cretaceous.

Heller et al. [2003] analyzed widespread conglomeratic units that were deposited in the Mesozoic and Cenozoic over large length scales in NAM, recording regional tilts of the continent, associated with 400-800 m of differential uplift on areas as wide as 800 km and in time periods of 1 to 10 million years. Westward movement of the plate in the mantle frame of reference over a downwelling created by Farallon slab subduction and associated change of dynamic topography (Fig. 4.12B) provides a dynamic model that could potentially explain tilting of sedimentary units, such as gravel deposits overlying the Morrison Formation in the Rocky Mountains [*Heller et al.*, 2003] and the gravel-rich Ogallala Group of the Miocene-Pliocene age in Western Nebraska and southern Wyoming. *Heller et al.* [2003] suggest that rarity of preserved evidence of the widespread units could be attributed to either low preservation potential of the conglomeratic units or relatively unusual episodes of tilting. Our model suggests that the tilting due to development of differential dynamic uplift should be a continuous process. Thus, the absence of more geological evidence of the widespread conglomeratic units [*Heller et al.,* 2003] could be related

to limited preservation potential in an environment that is continuously uplifting and being exposed to erosion.

Presently, the dynamic topography low is located under the east coast, and all models we computed predict overall subsidence during the Cenozoic. The accumulated subsidence on the east coast due to the sinking of the Farallon slab remnant during the Cenozoic is on the order of 500 m, with approximately 250 m of subsidence occurring since the end of Eocene. Analysis of Eocene and Miocene paleo shorelines indicates that these paleo shorelines have present-day elevations 50-200 m lower than respective sea levels in these time intervals, which is consistent with the overall subsidence of the east coast [*Spasojević et al.,* 2008]. The proposed dynamic subsidence can possibly explain the discrepancy between the *Miller et al.* [2005] sea-level curve and other eustatic curves [*Spasojević et al.,* 2008]. Geodynamically, the region of the US east coast is not stable over longer time scales due to the sinking of the Farallon slab and should not be used as a type-locality when determining global sea-level curves, as also suggested by others [*Moucha et al.*, 2008; *Müller et al.*, 2008b]. We fit a wide range of Late Cretaceous stratigraphy in an adjoint with a simple viscosity structure, including fewer layers than sometimes used [e.g., *Mitrovica and Forte,* 2004]. However, to obtain more realistic amplitudes of dynamic subsidence on the US east coast, our model requires an introduction of an additional low-viscosity layer below the lithosphere, with a viscosity of $1x10^{20}$ Pa s. Models with this extra layer of low-0viscosity upper mantle produce the same patterns of Late Cretaceous flooding (Fig. 4.12C) and subsidence as those without (Fig. 4.8B).

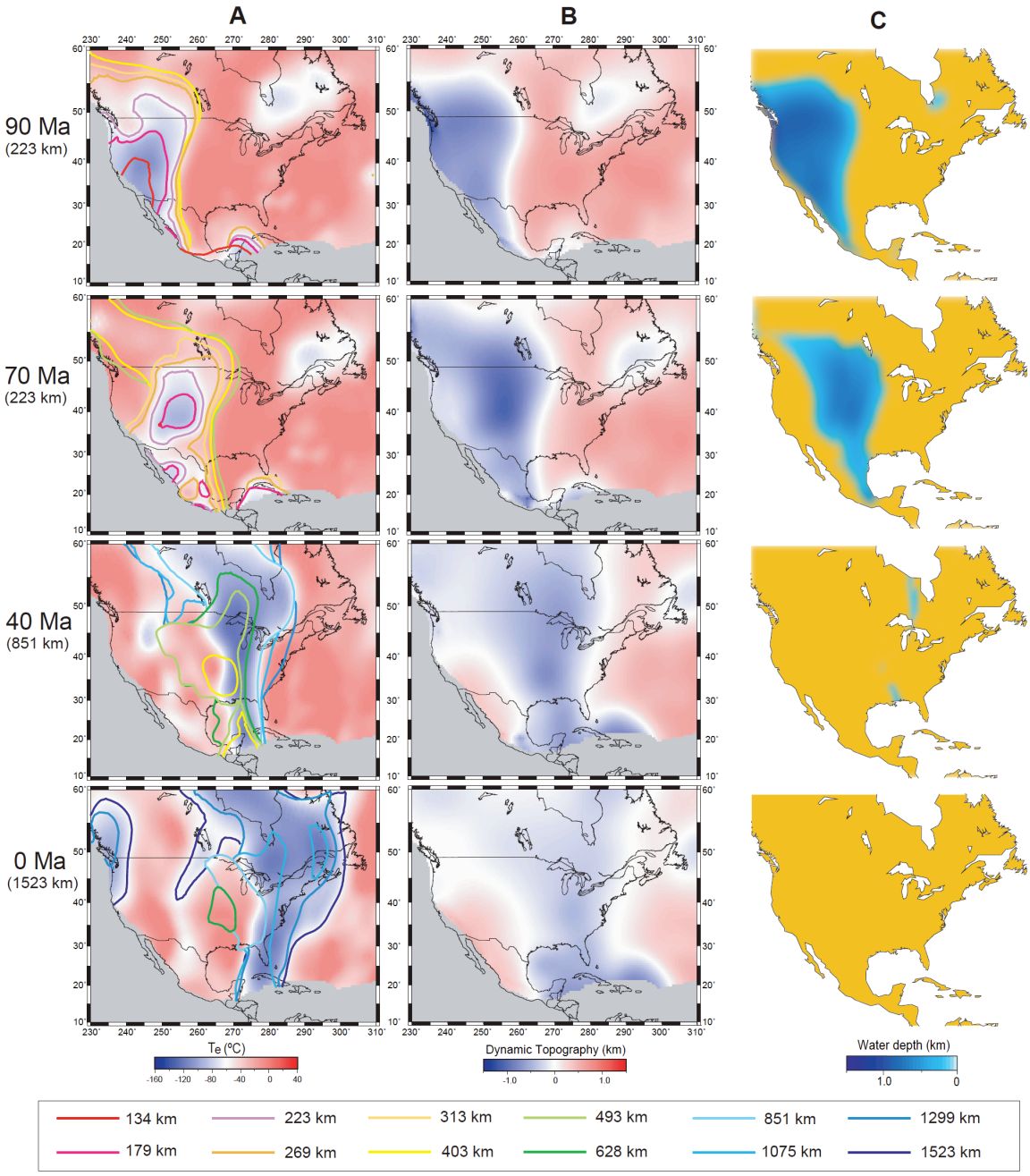

Figure 4.12. Evolution of the Farallon subduction viewed in the NAM reference frame. This model has a viscosity of the upper mantle at 10^{20} Pa s, of the transition zone at 10^{21} Pa s, and of the lower mantle at 1.5×10^{22} Pa s; an effective temperature anomaly of 160 °C. (A) Slab geometries at different depth, where the background color represents the temperature field at depth denoted at the left margin, color contours show boundaries of the slab at different depths. (B) The associated surface dynamic topography. (C) Predicted continental flooding at different geological times using initially flat continent at 100 Ma and *Haq and Al-Qahtani* [2005] sea level.

This indicates that more layers of mantle radial viscosity structure can be inferred when incorporating constraints over a larger time scale. Our scheme for constraining upper and lower mantle viscosities using stratigraphy combines quantitative and qualitative criteria iteratively. In the future, as databases with stratigraphic data are expanded, and as adjoint modeling capabilities and tomography models are improved, it may be possible to develop a fully automated scheme that iteratively updates mantle structure.

Predictions of Cretaceous flooding from model dynamic topography are dependent on the assumption of initial topography of NAM. When we use present-day topography, we cannot predict any significant flooding of the western interior over the Cretaceous, even when we impose the highest proposed eustatic sea levels [*Haq and Al-Qahtani,* 2005] since 100 Ma. The widespread Cretaceous flooding [*Sloss,* 1988; *Smith et al.,* 1994] can be reproduced from dynamic topography only when initial topography was flat or with a gentle relief. This implies that the Late Cretaceous topography was very different from the present-day, where most of the western portions of the continent, especially the region once occupied by the WIS, was probably low lying at 100 Ma. This is consistent with previous inferences since a significant part of the continent has been uplifted since 70-80 Ma [*McMillan et al.*, 2006; *English and Johnston*, 2004; *Mitrovica et al.,* 1989] and this uplift has been especially significant in the western interior. However, the details of paleoelevation of the WIS are controversial. Structural and unroofing history studies of the Laramide mountains suggest that 1.5-3 km of relief was produced during the Paleocene and early Eocene [*DeCelles et al.,* 1991]. This is supported by $\delta^{18}O$ analysis

of apatite [*Fricke,* 2003], which suggests that the Laramide mountain regional paleoelevation in Wyoming in the early Eocene was on the order of 475 m, and that most of the high present-day elevation developed since the early Eocene. *Dettman and Lohmann* [2000], on other hand, use the study of $\delta^{18}O$ of river waters from the Late Cretaceous and Paleogene basins of Alberta, Montana, Wyoming, and Colorado using aragonite mollusk fossils, concluding that the estimated altitude difference of river profiles is similar to the present-day value, suggesting that the WIS had significant paleoelevation [*Dettman and Lohmann,* 2000].

The western Canadian shield (Fig. 4.1) is located at the edge of the region of influence of Farallon subduction (Fig. 4.12). In order to infer burial history, *Flowers* [2009] analyzes the role of radiation damage on apatite (U-Th)/He ages of basement samples on the Canadian shield (near East Lake Athabasca). She proposes that ≥1.0 km of late Paleozoic-Mesozoic strata were deposited in the East Lake Athabasca region, hundreds of kilometers east of the preserved extent of sediments of the same age. These sediments have presumably been subsequently removed during periods of uplift. In addition, based on thermo-chronology, deposition of more than several hundred meters of sediments during the Cretaceous was unlikely [*Flowers,* 2009]. Two models preferred by the analysis of the borehole subsidence in the WIS predict a total of 600 m of subsidence in Late Cretaceous–early Cenozoic in the East Lake Athabasca region, followed by subsequent uplift (Fig. 4.13). The maximum depth of depression created due to dynamic topography is 280 m, assuming a flat initial topography. Accounting for isostasy, the maximum thickness of potentially

deposited sediments is 650 m, if the whole surrounding region was at sea level. This value is similar to one proposed by *Flowers* [2009], indicating that dynamic models can be used in conjunction with thermo-chronology to infer regions that have been inundated in the past, but where the sedimentary record has been subsequently removed.

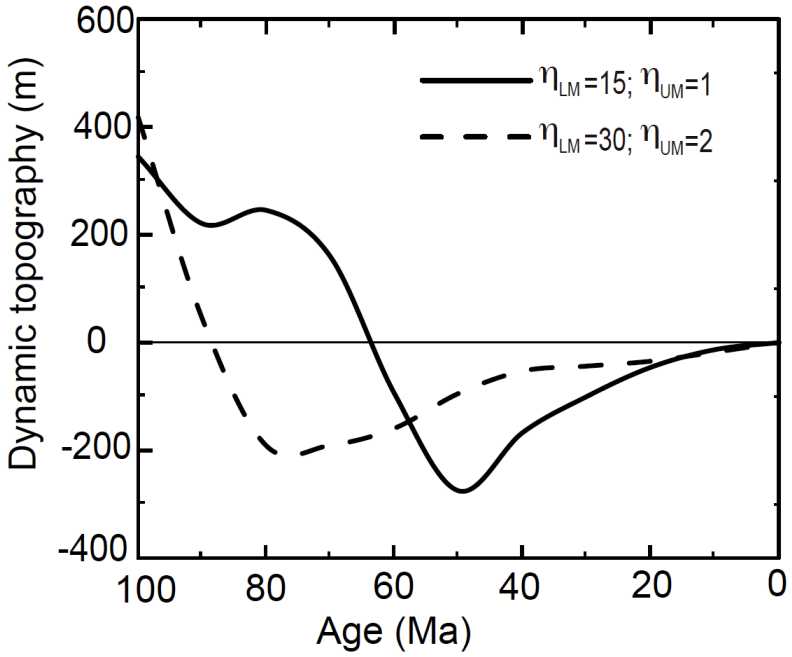

Figure 4.13. Time-dependent predictions of dynamic subsidence for East Lake Athabasca region (coordinates 252, 59°15'N) for two dynamic models. Values of upper mantle viscosity η_{UM} and lower mantle viscosity η_{LM} is given with respect to reference value of 10^{21} Pa s.

Our inverse dynamic models based on seismic tomography, reversed to the Late Cretaceous, show the formation of flat subduction associated with broad surface dynamic subsidence [*Liu et al*, 2008]. The model best fitting Cretaceous stratigraphy displays a flat to shallow-dipping slab extending ~2,000 km inland at around 70 Ma (Fig. 4.4B). Further attempting to fit the models to east coast subsidence requires

weaker upper mantle, but the evolution of the Farallon slab and associated Late Cretaceous dynamics remain similar (Fig. 4.12) as in models with simpler vertical viscosity (Fig. 4.8). Our model reproduces a flat slab that correlates well with the region of basement-cutting Laramide-type faults in the western US from 80 to 65 Ma [*Saleeby,* 2003]. Beyond the flat slab, there is a vast zone of shallow-dipping subduction that extends more than 1,000 km eastward and northward especially from 90 to 70 Ma (Fig. 4.12A). The zone is significantly larger than inferred from a simplified set of forward models that neither incorporated the details of subduction nor attempted to match stratigraphy [*Bunge and Grand,* 2000].

References

Atwater, T., and J. M. Stock (1998), Pacific-North America plate tectonics of the Neogene Southwestern United States - An update, *International Geological Review, 40,* 375-402.

Billen, M. (2008), Modeling the dynamics of subducting slabs, *Annual Review of Earth and Planetary Sciences,* 36, 325–356.

Bird, P. (1998), Kinematic history of the Laramide orogeny in latitudes 35º-49°N, western United States, *Tectonics, 17,* 780-801.

Bond, G. (1976), Evidence for continental subsidence in North America during the Late Cretaceous global submergence, *Geology, 4,* 557-560.

Bond, G. (1978), Speculations on real sea-level changes and vertical motions of continents at selected times in Cretaceous and Tertiary periods, *Geology, 6,* 274-250.

Bond, G. C. (1979), Evidence for some uplifts of large magnitude in continental platforms, *Tectonophysics, 61,* 285-305.

Bunge, H.-P., and S.P. Grand (2000), Mesozoic plate-motion history below the northeast Pacific Ocean from seismic images of the subducted Farallon slab, *Nature, 405,* 337 - 340.

Bunge, H.-P., C. R. Hagelberg, and B. J. Travis (2003), Mantle circulation models with variational data assimilation: inferring past mantle flow and structure from plate motion histories and seismic tomography, *Geophysical Journal International, 152*(2), 280-301.

Burgess, P. M., M. Gurnis, and L. Moresi (1997), Formation of sequences in the cratonic interior of North America by interaction between mantle, eustatic and stratigraphic processes, *Bulletin of the Geological Society of America, 108,* 1515-1535.

Conrad, C.P., C. Lithgow-Bertelloni, and K.E. Louden (2004), Iceland, the Farallon slab, and dynamic topography of the North Atlantic, *Geology, 32,* 177-180; doi: 10.1130/G20137.1

Conrad, C.P., and L. Husson (2009), Influence of dynamic topography on sea level and its rate of change, *Lithosphere, 1*(2), 110-120.

Cook, T. D., and A.W. Bally (1975), Stratigraphic Atlas of North and Central America, *Princeton University Press,* 272 pp.

Cross, T.A., and R.H. Pilger, Jr. (1978), Tectonic controls of late Cretaceous sedimentation, western interior, USA, *Nature, 274,* 653-657, doi: 10.1038/ 274653a0.

Currie, B. (2002), Structural configuration of the early Cretaceous Cordilleran Foreland-Basin system and Sevier Thrust Belt, Utah and Colorado, *Journal of Geology, 110,* 697–718.

DeCelles, P. G., M. B. Gray, K. D. Ridgway, R. B. Cole, P. Srivastava, N. Pequera, and D.A. Pivnik (1991), Kinematic history of a foreland uplift from Paleocene synorogenic conglomerate, Beartooth Range, Wyoming and Montana*, Geological Society of America Bulletin, 103,* 1458–1475.

Dettman, D. L., and K. C. Lohmann (2000), Oxygen isotope evidence for high-altitude snow in the Laramide Rocky Mountains of North America during the Late

Cretaceous and Paleogene, *Geology, 28,* 243-246.

English, J. M, and S. T. Johnston (2004), Laramide orogeny: what were the driving forces?, *International Geology Review, 46,* 833-838.

Flowers, R. M. (2009), Exploiting radiation damage control on apatite (U-Th)/He dates in cratonic regions, *Earth and Planetary Science Letters, 277,* 148-155.

Fricke, H.C. (2003), Investigation of early Eocene water-vapor transport and paleoelevation using oxygen isotope data from geographically widespread mammal remains, *Geological Society of America Bulletin, 115,* 1088-1096.

Grand, S. P., R. D. van der Hilst, and S. Widiyantoro (1997), Global seismic tomography: A snapshot of convection in the Earth, *GSA Today, 7,* 4, 1-7.

Grand, S. P. (2002), Mantle shear-wave tomography and the fate of subducted slabs, *Philosophical Transactions of the Royal Society of London Series A-Mathematical Physical and Engineering Sciences*, *360*(1800), 2475-2491.

Goes, S., and S. van der Lee (2002), Thermal structure of the North American uppermost mantle inferred from seismic tomography, *Journal of Geophysical Research, 107(B3),* 2050, doi:10.1029/2000JB000049.

Gurnis, M. (1991), Continental flooding and mantle-lithosphere dynamics*, in Glacial Isostasy, Sea-Level, and Mantle Rheology (edited by R. Sabadini, K. Lambeck, and E. Boschi),* Kluwer Academic Publishers, Dordrect, 445-492.

Gurnis, M., R. D. Müller, and L. Moresi (1998), Dynamics of Cretaceous vertical motion of Australia and the Australian-Antarctic discordance, *Science, 279*(5356) *, 1499*-1504.

Gurnis, M., J. X. Mitrovica, J. Ritsema, and H.-J. van Heijst (2000), Constraining

mantle density structure using geological evidence of surface uplift rates: The case of the African Superplume, *Geochem. Geophys. Geosyst., 1(7),* 1020, doi:10.1029/1999GC000035..

Gurnis, M., M.Turner, L. DiCaprio, S. Spasojevic, R. D. Müller, J. Boyden, M. Seton, V. C. Manea, and D. J. Bower (2009), Global plate reconstructions with continuously closing plate, *Geochm., Geophys., Geosys, in review.*

Hager, B.H. (1984), Subducted slabs and the geoid: Constraints on mantle rheology and flow*, Journal of Geophysical Research 89, B7,* 6003-6015.

Harrison, C.G.A., 1990, Long-term eustasy and epeirogeny in continents, *Revelle, R., ed., Sea-level change,* Washington, D.C., National Academy Press, 141-160.

Haq, B.U., J.Hardenbol, and P.R. Vail (1987), Chronology of fluctuating sea levels since the Triassic, *Science, 235,* 1156-1167.

Haq, B.U., and A. Motaleb Al-Qahtani (2005), Phanerozoic cycles of sea-level change on the Arabian Platform, *GeoArabia, 10,* 2, 127-160.

Heller, P.L., K. Dueker, and M.E.McMillan (2003), Post-Paleozoic alluvial gravel transport as evidence of continental tilting in the U.S. Cordillera, *Geological Society of America Bulletin, 115,* 1122–1132.

Humphreys, E. D., and D. D. Coblentz (2007), North American dynamics and western U.S. tectonics, *Reviews of Geophysics, 45,* RG3001, doi:10.1029/2005RG000181.

Ishii, M. and J. Tromp (2004), Constraining large-scale mantle heterogeneity using mantle and inner-core sensitive normal modes, *Physics of Earth and Planetary Interiors, 146,* 113-124.

Ismail-Zadeh, A., G. Schubert, I. Tsepelev, and A. Korotkii (2004), Inverse problem of

thermal convection: numerical approach and application to mantle plume restoration, *Physics of Earth and Planetary Intiors, 145,* 99-114.

Jordan, T. H. (1975), The continental tectosphere, *Reviews of Geophysics, 13*(3)*,* 1-12.

King, S.D. and G. Masters (1992), An inversion for radial viscosity structure using seismic tomography, *Geophysical Research Letters,19,* 15, 1551-1554.

Kominz, M.A. (1984), Oceanic ridge volumes and sea level change: An error analysis, in *Interregional Unconformities and Hydrocarbon Accumulation (Ed. by J. Schlee), AAPG Memoirs, 36,* 109-127.

Le Stunff, Y., and Y. Ricard (1997), Partial advection of equidensity surfaces: A solution for the dynamic topography problem?, *Journal of Geophysical Research, 102, B11,* 24655-24667.

Lithgow-Bertelloni, C., and M. Gurnis (1997), Cenozoic subsidence and uplift of continents from time-varying dynamic topography, *Geology, 25,* 735-738.

Liu, L., and M. Gurnis (2008), Simultaneous inversion of mantle properties and initial conditions using an adjoint of mantle convection, *Journal of Geophysical Research, 113,* B08405, doi:10.1029/2008JB005594.

Liu, L., S. Spasojević and M. Gurnis (2008), Reconstructing Farallon plate subduction beneath North America back to the Late Cretaceous, *Science, 322,* 934-938, DOI:10.1126/science.1162921, 2008.

Liu, S., and D. Nummedal (2004), Late Cretaceous subsidence in Wyoming: Quantifying the dynamic component, *Geology, 32,* 397-400.

Liu, S., D. Nummedal, P-G. Yin, and H-J. Luo (2005), Linkage of Sevier thrusting episodes and Late Cretaceous foreland basin megasequences across southern

Wyoming (USA), *Basin Research, 17,* 487-506.

McMillan, M.E., P.L Heller, and S.L. Wing (2006), History and causes of post-Laramide relief in the Rocky Mountain orogenic plateau, *Geological Society of America Bulletin, 108,* 393–405; doi: 10.1130/B25712.

Mégnin, C. and B. Romanowicz (2000), The shear velocity structure of the mantle from the inversion of body, surface and higher modes waveforms, *Geophysical Journal International, 143,* 709-728.

Manea, V.and M. Gurnis (2007), Subduction zone evolution and low viscosity wedges and channels, *Earth and Planetary Science Letters, 264,* 22-45.

McQuarrie, N., and C.G. Chase (2000), Raising the Colorado Plateau, *Geology, 28,* 91–94.

Miller, K.G., M. A. Kominz, J.V. Browning, J. D. Wright, G.S. Mountain, M.E. Katz, P.J. Sugarman, B.S. Cramer, N. Christie-Blick, and S.F. Pekar (2005), The Phanerozoic record of global sea-level change, *Science, 310,* 1293-1298.

Milne, G. A., J. X. Mitrovica, H.-G. Scherneck, J. L. Davis, J. M. Johansson, H. Koivula, and M. Vermeer (2004), Continuous GPS measurements of postglacial adjustment in Fennoscandia: 2. Modeling results, *Journal of Geophysical Research, 109,* B02412, doi:10.1029/2003JB002619.

Mitrovica, J.X., C. Beaumont, G.T. Jarvis (1989), Tilting of continental interiors by the dynamical effects of subduction, *Tectonics, 8,* 1079-1094.

Mitrovica, J.X., and A.M. Forte (2004), A new inference of mantle viscosity based upon joint inversion of convection and glacial isostatic adjustment data, *Earth and Planetary Science Letters, 225,* 177-189.

Morgan,W.J. (1971), Convection plumes in the lower mantle, *Nature, 230,* 42–43.

Moucha, R., A.M. Forte, J.X. Mitrovica, D.B. Rowley, S. Quéré, N.A. Simmons, and S.P. Grand (2008), Dynamic Topography and Long-Term Sea-Level Variations: There Is No Such Thing as a Stable Continental Platform, *Earth and Planetary Science Letters, 271,* 101-108.

Müller, R.D., M.Sdrolias, C. Gaina and W.R. Roest (2008a), Age, spreading rates and spreading asymmetry of the world's ocean crust, *Geochemistry, Geophysics, Geosystems, 9*, Q04006, doi:10.1029/2007GC001743.

Müller, R.D., M. Sdrolias, C. Gaina, B. Steinberger, and C. Heine (2008b), Long-term sea-level fluctuations driven by ocean basin dynamics, *Science, 319,* 1357-1362.

Ni, S., E. Tan, M. Gurnis, and D. Helmberger (2002), Sharp sides to the African superplume, *Science, 296,* 1850.

O'Neill, C., R.D. Muller, and B. Steinberger, 2005, On the uncertainties in hotspot reconstructions and the significance of moving hot spot reference frames, *Geochemistry, Geophysics, Geosystems,6,* Q04003. doi:10.1029/2004GC000784

Pang, M., and D. Nummedal (1995), Flexural subsidence and basement tectonics Cretaceous Western Interior basin, United States, *Geology, 23,* 2, 173-176.

Pindell, J., L. Kennan, K. P. Stanek, W. V. Maresch, and G. Draper (2006), Foundations of Gulf of Mexico and Caribbean volution: Eight controversies resolved, *Geological Acta, 41,* 303-341.

Quéré, S., and A.M. Forte, 2006. Influence of past and present-day plate motions on spherical models of mantle convection: Implications for mantle plumes and hotspots, *Geophysical Journal International, 165* (3), 1041-1057.

Ren, Y., E. Stutzmann, R.D. Van der Hilst, and J. Besse (2007), Understanding seismic heterogeneities in the lower mantle beneath the Americas from seismic tomography and plate tectonic history, *Journal of Geophysical Research, 112,* B01302.

Richard, M., and B. Hager (1984), Geoid anomalies in a dynamic earth, *Journal of Geophysical Research, 89,* 5987–6002.

Ritsema, J., H. J. van Heijst, and J. H. Woodhouse (2004), Global transition zone tomography*, Journal of Geophysical Research, 109,* B02302, 10.1029/2003JB002610.

Roth, J.B., M.J. Fouch, D.E. James, and R.W. Carlson (2008), Three-dimensional seismic velocity structure of the northwestern United States, *Geophysical Research Letters, 35,* L15304, doi:10.1029/2008GL034669.

Saleeby, J., 2003, Segmentation of the Laramide slab-evidence from the southern Sierra Nevada region, *Geological Society of America Bulletin, 115,* 655-668.

Sigloch, K., N. McQuarrie, and G. Nolet (2008), Two-stage subduction history under North America inferred from multiple-frequency tomography*, Nature Geoscience, 1,* 458 – 462, doi:10.1038/ngeo231.

Sirkes, Z. and E. Tziperman (1997), Finite difference of adjoint or adjoint of finite difference?, *American Meteorogical Society, 125,* 3373-3378.

Sloss, L. L. (1988), Tectonic evolution of the craton in Phanerozoic time, *In L.L. Sloss (Editor), Sedimentary Cover-North America Craton, Vol. D-2,* The Geology of North America, Geol. Soc. Am., 25-51.

Smith, A. G, D.G. Smith, and B.M. Funnel (1994), Atlas of Mesozoic and Cenozoic

coastlines, Cambridge University Press, 99 pp.

Solomon, S.C., and N.H. Sleep (1974), Some simple physical models for absolute plate motions, *Journal of Geophysical Research, 79,* 2557–2567.

Spasojević, S., L. Liu, M. Gurnis, and R. D. Müller (2008), The case for dynamic subsidence of the United States east coast since the Eocene, *Geophysical Research Letters, 35,* L08305, doi:10.1029/2008GL033511.

Sun, J., D. W. Flicker, D. K. Lilly (1991), Recovery of 3D wind and temperature fields from simulate single-Doppler radar data, *Journal of Atmospheric Science, 48,* 876-890.

Talagrand, O., and P. Courtier (1987), Variational assimilation of meteorological observation with the adjoint vorticity equation, *Quarterly Journal of Royal Meteorological Society, 113,* 1211-1328.

Trampert, J., F. Deschamps, J. Resovsky, and D. Yuen, (2004), Probabilistic tomography maps chemical heterogeneities throughout the lower mantle, *Science, 306,* 853-856.

Van der Hilst, R.D, S. Widiyantoro, and E.R. Engdahl (1997), Evidence of deep mantle circulation from global tomography, *Nature, 386,* 578-584.

Van Sickel, W.A., M. Kominz, K.G. Miller, and J.V. Browning (2004), Late Cretaceous and Cenozoic sea-level estimates: Backstripping analysis of borehole data, onshore New Jersey*, Basin Research, 16,* 451-465.

Watts, A.B., and M.S. Steckler, 1979, Subsidence and eustasy at the continental margin of eastern North America, *Maurice Ewing Series No. 3,* 218-234.

Zhong, S., M. T. Zuber, L. Moresi, M. Gurnis (2000), Role of temperature-dependent

viscosity and surface plates in spherical shell models of mantle convection, *Journal of Geophysical Research, 105*, 11063-11082.

Chapter 5

The case for dynamic subsidence of the United States east coast over the Cenozoic[1]

5.1. Abstract

The dynamic subsidence of the United States east coast is addressed using the discrepancy between regional and global estimates of sea level, elevation of paleoshorelines, and adjoint models of mantle convection that assimilate plate motions and seismic tomography. The positions of Eocene and Miocene paleoshorelines are lower than predicted by global sea levels, suggesting at least 50 m, and possibly as much as 200 m of subsidence since the end of the Eocene. Dynamic models predict subsidence of the east coast since the end of the Eocene, although the exact magnitude is uncertain. This subsidence has been occurring during an overall global sea-level fall, with the eustatic change being larger than the dynamic subsidence; this results in a regional sea-level fall in the absence of land subsidence. Dynamic subsidence is consistent with the difference between eustasy and regional sea level at the New Jersey coastal plain.

---

[1] Published by Sonja Spasojevic, Lijun Liu, Michael Gurnis and R. Dietmar Müller (2008) in *Geophysical Research Letters, 35,* L08305, doi:10.1029/2008GL033511.

5.2. Introduction

The mantle density structure drives a large-scale pattern of surface dynamic topography that may play an important role in controlling the geoid [*Richards and Hager,* 1984; *Hager et al.,* 1985]. North America has been suggested as a dynamic topography low using density structures either inferred from seismic tomography [*Hager et al.* 1985; *Steinberger,* 2007] or the history of subduction [*Lithgow-Bertelloni and Richards,* 1998]. Both global [*Grand,* 2002; *Ritsema and van Heijst,* 2000] and regional [*Ren et al.,* 2007] seismic tomography models show a linear high seismic velocity anomaly beneath eastern North America at mid mantle depths, interpreted as the remnants of Farallon plate subduction [*Bunge and Grand,* 2000; *Ren et al.,* 2007].

Independent of these geophysical concepts, *Miller et al.* [2005] made new sea-level estimates that putatively reflect eustasy, based on the backstripping of sedimentary sections at five boreholes located on the New Jersey coastal plain [*Van Sickel et al*., 2004]. The maximum long-term sea level is around 70 m [*Miller et al*., 2005], which is lower than most other published global sea-level estimates (Fig. 5.1A). The high-end estimates of sea level with a maximum on order of 250-300 m (Fig. 5.1A) are based on correlations of stratigraphic sequences in wells, outcrops, and seismic data [*Haq et al*., 1987; *Haq and Al-Qahtani,* 2005], with the long-term trend linked to the estimates from changing mid-ocean ridge volume [e.g., *Kominz,* 1984]. Low-end estimates with maximum of 120 m are based on backstripping of wells on the

continental margin of eastern North America [*Watts and Steckler,* 1979]. *Müller et al.* [2008] assimilated marine geophysical data into reconstruction of ancient ocean basins, modeling a Late Cretaceous maximum of 170 m (Fig. 5.1A). *Kominz* [1984] estimated global sea-level variations due to changing mid ocean ridge volume (Fig. 5.1A and 5.1B), which closely matched the component of sea level required to flood continental interiors (Fig. 5.1B), especially since the Eocene, as determined through hypsometric analysis [*Harrison,* 1990; *Bond,* 1979]. In addition, by compensating for regional variations in flooding with respect to average trends, *Bond* [1979] determined long-wavelength vertical epeirogenic motions that are consistent with geodynamic models [e.g., *Lithgow-Bertelloni and Gurnis,* 1997].

Although all global sea-level estimates are subject to considerable uncertainty [*Miller et al.,* 2005], the flooding of continental interiors seems most reasonable to us. First, the method averages over large length scales within relatively stable continental interiors, hence avoiding the need to subtract the much larger change due to thermal subsidence of rifted margins. Second, geodynamic models suggest that most locations are subject to long-term vertical motions [e.g., *Gurnis,* 1992; *Lithgow-Bertelloni and Gurnis,* 1997] and hence methods that depend on a few boreholes in close proximity could be subject to regional effects, as we will describe below. Finally, it has been argued that methods that depend on global correlation of stratigraphic sequences only extract higher frequency sea-level change and long-term sea-level fluctuations must be obtained by calibration with flooding of continental interiors.

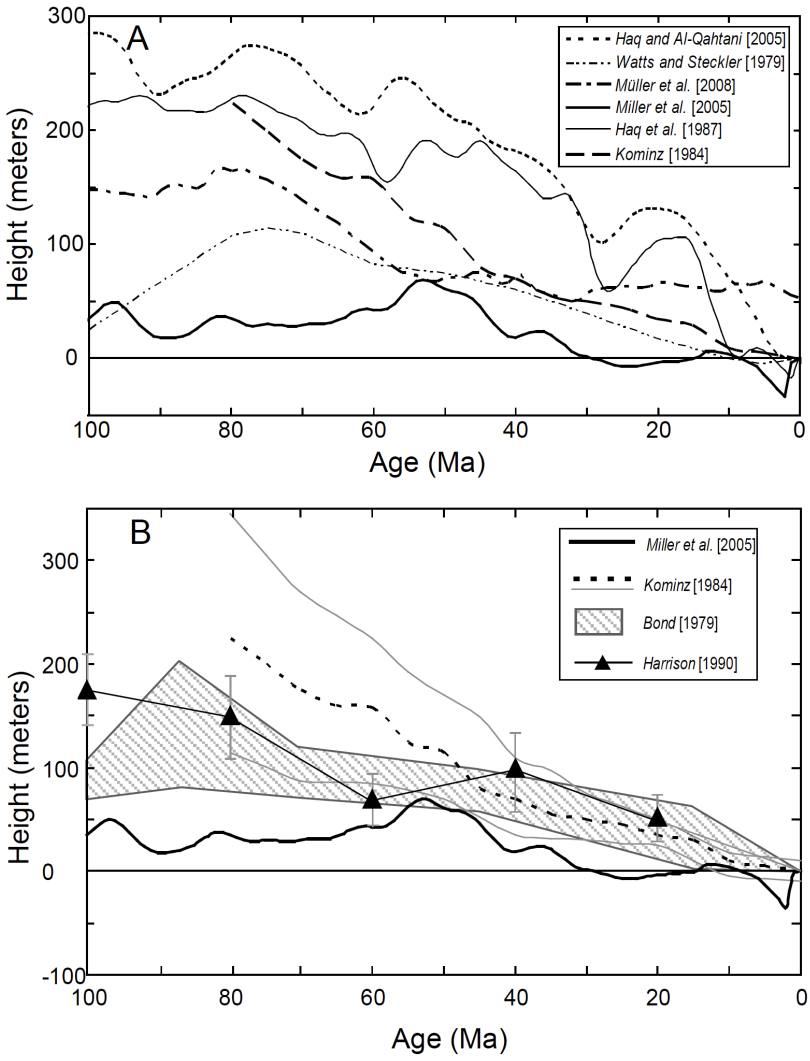

Figure 5.1. Comparison between sea-level curves. (A) Comparison between *Haq et al.* [1987], *Haq and Al-Qahtani* [2005], *Müller et al.* [2008], *Kominz* [1984], and *Watts and Steckler* [1979] curves with sea-level curve derived for New Jersey coastal plain [*Miller et al.,* 2005] for last 100 million years, smoothed by a 10 m.y. cosine arch filter to isolate long-term sea-level change. (B) Comparison between sea-level estimates based on the analysis of continental flooding [*Harrison,* 1990; *Bond,* 1979] and *Miller et al.* [2005] and *Kominz* [1984] sea-level curves. Thin continuous lines indicate maximum and minimum estimates from *Kominz* [1984], hatched area shows range of estimates from *Bond* [1979], and black line with triangles indicate average estimates of *Harrison* [1990] with associated error bars.

If we compare the *Miller et al*. [2005] long-term sea-level estimate with other estimates, especially those consistent with the flooding of continental interiors, there appears to be a significant discrepancy between maximum Late Cretaceous

sea levels on the order of 50-200 meters (Fig. 5.1). Consequently, we hypothesize that the estimate of *Miller et al*. [2005] reflects regional, rather than global, sea-level variations on the 10^7 year scale considered here. Further, we suggest that the discrepancy is driven by a dynamic subsidence of the eastern areas of the United States but the magnitude of the subsidence has been somewhat smaller than the fall in global sea level over the same period. We approach this hypothesis from two directions, one empirical and the other involving mantle flow models. First, we reconstruct paleoshorelines in the eastern United States and use them to estimate subsidence that is independent of the New Jersey boreholes. Second, we use adjoint models of mantle convection from *Liu et al.* [2008] that assimilate plate motions and seismic tomography to determine if reasonable dynamic models can predict the requisite dynamic subsidence. These complementary approaches suggest that the Atlantic coastal region of the USA has been experiencing dynamic subsidence since at least the Eocene.

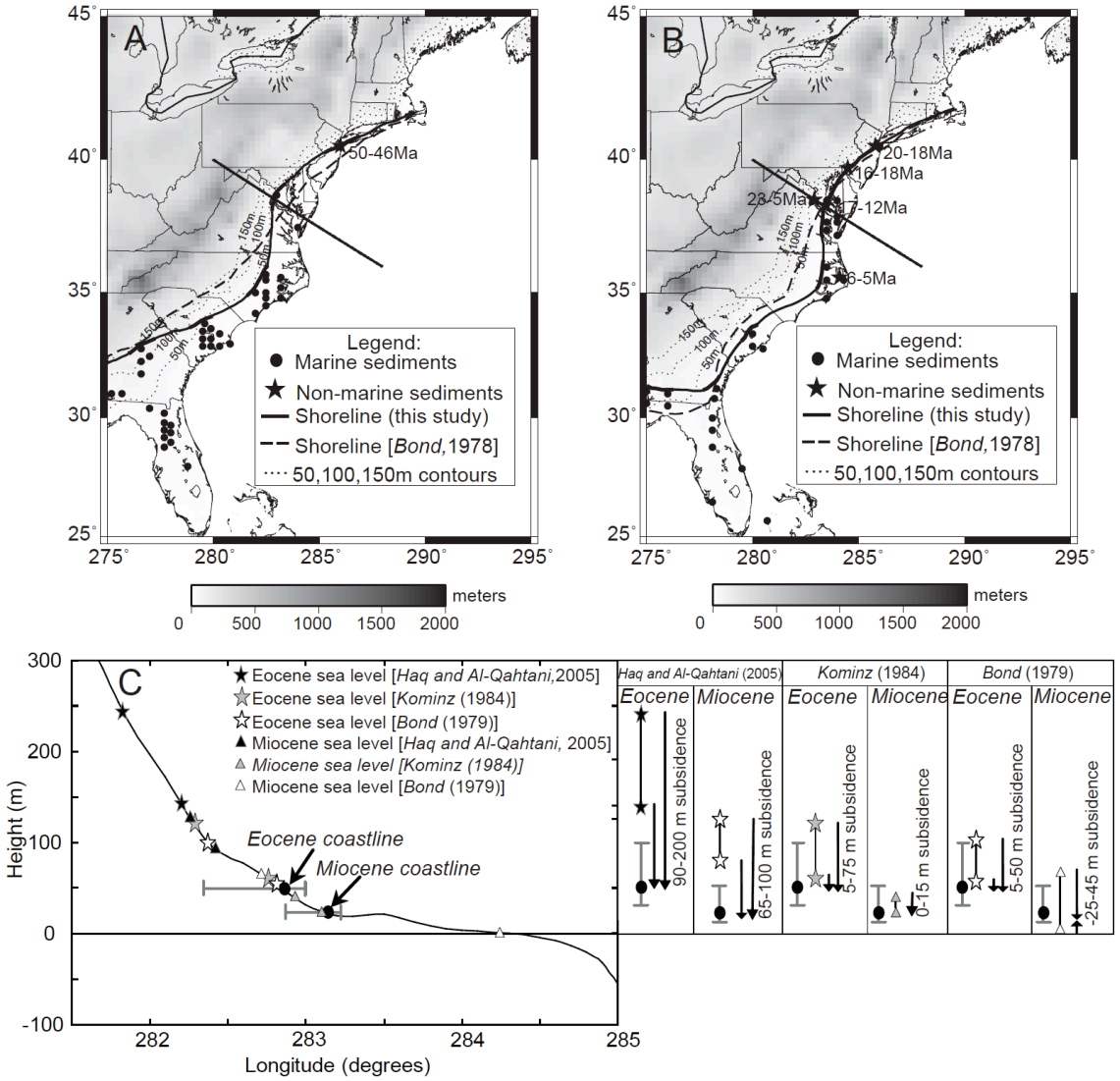

Figure 5.2. Paleoshoreline and hypsometric analysis of the U.S. east coast. (A) Eocene paleoshoreline reconstructions. (B) Miocene paleoshoreline reconstructions. (C) topographic profile through Chesapeake Bay (shown with a straight line on Figures 5.2A and 5.2B). Dots and stars on Figures 5.2A and 5.2B indicate locations of marine (*Paleobiology database,* 2007) and non-marine [*Tedford and Hunter,* 1984; *Wright and Eshelman,* 1987; *Gazin*, 1953] sediments, respectively, with ages of the non-marine sediments indicated. Continuous thick lines show position of reconstructed paleoshorelines, and dashed lines indicate paleoshorelines from *Bond* [1979]. Dotted lines correspond to 50 m, 100 m, and 150 m topographic contours. Stars and triangles on Figure 5.2C indicate maximum and minimum sea levels for Eocene and Miocene (18 – 12 Ma), respectively. Dots on the profile show positions of reconstructed shorelines in this study. Figure 5.2C (right) shows summary of the analysis results, with grey bars indicating qualitatively estimated uncertainty in shoreline reconstruction.

5.3. Paleoshoreline analysis

We analyze elevation of the paleoshoreline with respect to predictions from global sea level to infer vertical motions. If a reconstructed paleoshoreline is topographically lower (higher) that global sea level at the same time, then we can infer relative subsidence (uplift) of the region since that time. We reconstruct Miocene and Eocene shorelines using abundant marine [*Paleobiology database,* 2007] and less preserved non-marine sediments [*Tedford and Hunter,* 1984*; Wright and Eshelman,* 1987; *Gazin*, 1953] along the US Atlantic coast (Fig. 5.2 A, B). Paleoshorelines for the Eocene (Fig. 5.2A) and Miocene (Fig. 5.2B) are defined as the furthermost inland location of the marine sediments, positioned just oceanward from the non-marine location, with the exception of the youngest non-marine sediments in North Carolina (Fig. 5.2B), which we did not take into account since it captures the lowest Miocene sea level.

Considering significant disagreement regarding inferred global sea levels described earlier, we will perform our analysis with sea levels defined by *Bond* [1979], *Kominz* [1984], and *Haq and Al-Qahtani* [2005] in order to define a range of possible vertical motions. The singular Eocene and Miocene levels reconstructed based on the flooding of the continents [*Bond*, 1979] are most probably eustatic, as discussed earlier. They are generally consistent with the predicted sea level of *Kominz* [1984], which will also be used in the analysis since it is continuously defined for the Cenozoic. We also perform analysis using the *Haq and Al-Qahtani* [2005] sea level to define upper bounds on the subsidence values utilizing paleoshorelines.

The elevation of the reconstructed Eocene shoreline along a northwest-southeast topographic profile through the Chesapeake Bay region is approximately 50 m, which is lower than Eocene sea levels (Fig. 5.2C). The estimated subsidence varies between 5-50 m (compared with *Bond* [1979]), 5-75 m (*Kominz* [1984]) and 90-200 m (*Haq and Al-Qahtani* [2005]). However, the Eocene shoreline defined by *Bond* [1979] is 20-30 m topographically lower along the profile (Fig. 5.2A) than the one we reconstructed, suggesting a higher amount of subsidence. The elevation of the Miocene paleoshoreline, with an age constrained to 18-12 Ma along the profile, is about 20 m (Fig. 5.2C), suggesting up to 100 meters of subsidence since the mid Miocene (compared to *Haq and Al-Qahtani,* 2005). The paleoshoreline analysis is limited by the accuracy in estimating the position of paleoshorelines. In an attempt to account for limited sediment preservation, resulting in oceanward biases in estimates of paleoshoreline locations, we also include a qualitative estimate of the elevation errors (Fig. 5.2C). Our subsidence estimate since 12 Ma based on a comparison with *Kominz* [1984] and *Bond* [1979] sea levels is small, only several tens of meters, and within their error estimates. However, the estimated subsidences for the Eocene are outside of the error estimates.

In summary, although the paleoshorelines analysis is characterized by relatively large uncertainty, the trends from the paleoshorelines indicate at least 50 m, and possibly as much as 200 m of subsidence since the Eocene. The subsidence since the late Miocene is probably relatively small, and it is hard to constrain using the paleoshoreline analysis alone.

5.4. Mantle convection model: The changing Cenozoic dynamic topography in the eastern US

As mantle buoyancy forces rearrange, dynamic topography changes; as plates move with respect to these changes, sea level undergoes global fluctuations while continental interiors experience epeirogenic motions [*Gurnis*, 1992]. Using a global flow model, *Lithgow-Bertelloni and Gurnis* [1997] showed that as North America moved westward since the Cretaceous, the western interior subsided and then uplifted. Ever since the model of *Mitrovica et al*. [1989] predicting Cretaceous subsidence and Tertiary uplift, it has been generally thought that the Western Interior Seaway subsidence was driven by dynamic topography (e.g., *Liu and Nummedal* [2004]). However, up to this point no detailed estimates of dynamic motions have been made for the eastern region of the continent. As North America moved to the west, is it possible that the Cretaceous subsidence and subsequent uplift of the western interior and the putative subsidence of the eastern US can both be predicted with a single geodynamic model?

This question is addressed with three-dimensional regional spherical finite-element models for North America with temperature- and pressure-dependant viscosity, and imposed plate kinematics using the software package *CitcomS* [*Tan et al*., 2006]. When comparing predicted and inferred paleoshorelines and dynamic topography with borehole tectonic subsidence curves, it is essential that the topography on a mesh fixed to the plate be continuously tracked over the changing mantle [*Gurnis et al*., 1998]. An inverse methodology is used to solve mantle convection [*Liu and*

Gurnis, 2008], where past mantle structure is recovered through backward integration of the convection equations using the scaled seismic tomography of *Grand* [2002]. The regional North American model was developed for the period from 100 Ma to present, and is constrained by observations of flooding, sediment thickness and tectonic subsidence, mainly in the Cretaceous interior seaway (see *Liu et al.* [2008] for a complete discussion).

Dynamic models predict a broad present-day dynamic topography low over the eastern portion of the US (Fig. 5.3A). Since the early Eocene, total subsidence due to the change of dynamic topography is on order of 500 m (Fig. 5.3B), but it varies from 350 m to 700 m, depending on the rheological parameters and the seismic wave speed to temperature scaling (Fig. 5.3C). The predicted uplift in the interior of the USA is on order of 500 m (Fig. 5.3B) to 1 km, depending on model parameters. Although a suite of models were run [*Liu et al.,* 2008], as illustrated by four models in Fig. 5.3C, a model that predicts that the US east coast is either stable or uplifting was never found. Dynamic predictions of subsidence (Fig. 5.3C) since the late Miocene are around 50 m, which is consistent with an intermediate estimate from the paleoshoreline analysis using the *Haq and Al-Qahtani* [2005] sea level, and with a high-end estimate using the *Bond* [1979] sea level. On other hand, the range of estimated dynamic subsidence since the end of the Eocene is 120-225 m (Fig. 5.3C), which is higher than estimates from paleoshoreline analysis using the *Bond* [1979] and *Kominz* [1984] sea levels, and consistent with estimates based on the *Haq and*

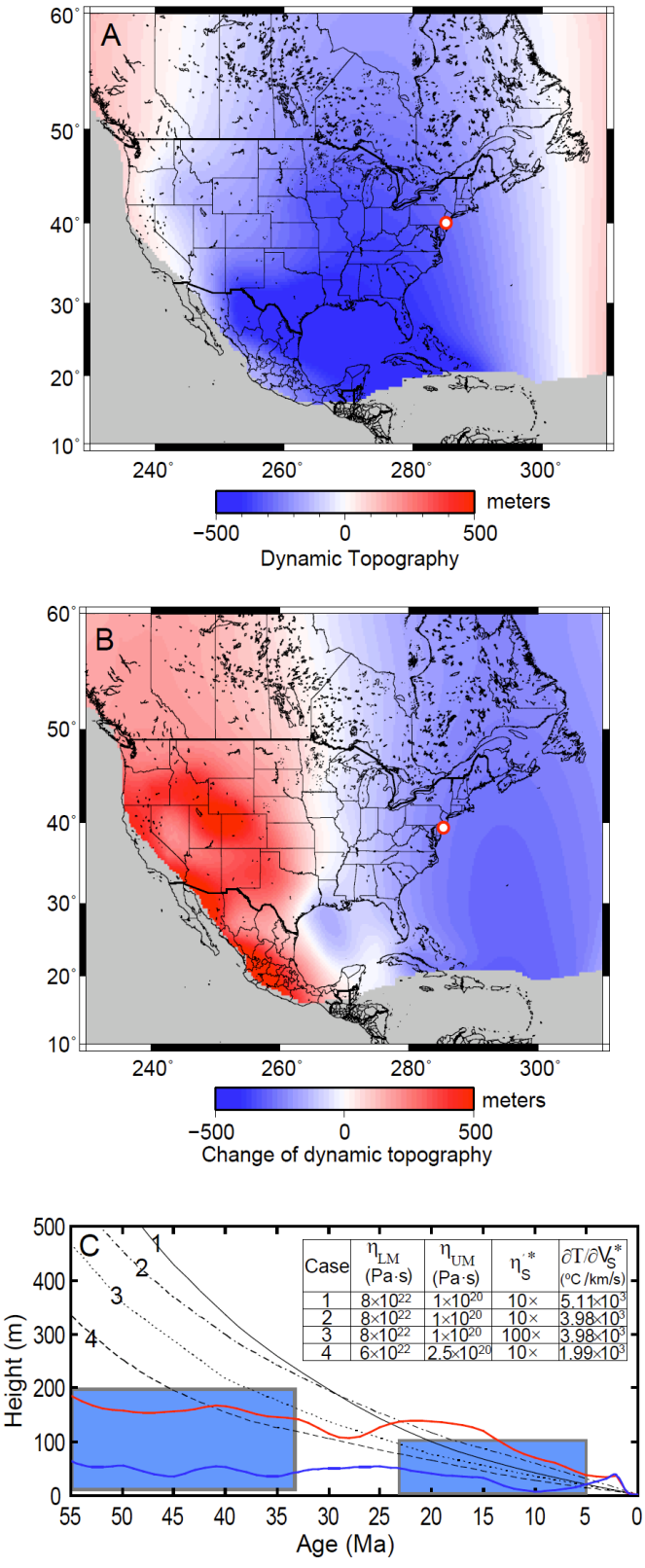

Figure 5.3. Dynamic topography predictions from the North American mantle convection models. (A) Predicted present-day dynamic topography. (B) difference between predicted dynamic topography for early Eocene (50 Ma) and present-day (0 Ma). (C) dynamic topography subsidence for a well in New Jersey coastal plain (location is shown with a white circle on Figures 5.3A and 5.3B). The model shown in Figures 5.3A and 5.3B is Case 4, with the parameters given in Figure 5.3C. Dynamic topography change for a well in New Jersey coastal plain (coordinates 285°30', 39°30'N) for four dynamic models is shown with black lines, solid red and blue lines show difference between sea-level models of *Haq and Al-Qahtani* [2005] and *Miller et al.* [2005], and *Kominz* [1984] and *Miller et al.* [2005], respectively. Blue colored boxes show estimated subsidence range from paleoshoreline analysis for Eocene and Miocene. Table insert shows model parameters (η= viscosity, *LM* = lower mantle, *UM* = upper mantle viscosity, η_S' = non-dimensional variation in viscosity across the slab compared to ambient values at the same depth, T = temperature, V_s = shear-wave velocity, * = values are evaluated at 2000 km depth). Dynamic topography was calculated as if it were an interface between mantle and water.

Al-Qahtani [2005] sea-level curve. If the subsidence occurred in the earlier parts of the Eocene, dynamic models [*Liu et al.,* 2008] overpredict the magnitude of subsidence (Fig 5.3C). Discrepancies between the *Miller et al.* [2005] and other analyzed curves (Fig. 5.3C) are also consistent with the proposed subsidence. Although all analyzed data are consistent with an overall subsidence since the Eocene (Fig. 5.3C), its magnitude and timing are not well constrained due to the uncertainties in all of the applied methodologies.

5.5. Conclusions

Analysis of paleoshorelines and dynamic models is mutually consistent and provides evidence for dynamic subsidence of the Atlantic coast of the US over the Cenozoic. The paleoshorelines analysis is characterized by relatively large uncertainty related to errors in defining the paleoshoreline position and different global sea-level curves that can be used. However, the trends from the paleoshorelines indicate at least 50 m, and possibly as much as 200 m, of subsidence since the Eocene, if the sea level defined by *Haq and Al-Qahtani* [2005] is used in the analysis. The subsidence since the late Miocene is probably relatively small, and it is hard to constrain using the paleoshoreline analysis alone. Adjoint mantle convection models constrained by globally consistent plate motions, present-day tomographic structure and stratigraphic observations [*Liu et al.*, 2008] never predict stability or uplift on the east coast of the US since the Eocene. Dynamic models, rather, predict a broad dynamic topography depression that produces dynamic topography

subsidence of 350-700 m over the Cenozoic, and 125-225 m since the end of Eocene. Although the exact amplitude and timing of the Cenozoic subsidence is difficult to constrain, dynamic models and paleoshoreline analysis seem to be consistent with subsidence of at least 50 m, and possibly as large as 200 m, since the Eocene.

The dynamic subsidence in the US east coast is explained in an integrated mantle convection model, which also predicts Cretaceous subsidence and subsequent uplift in the western interior [*Liu et al*., 2008]. The widespread flooding of the North American interior is caused by coincident maximum global sea level in the Cretaceous and motion of the interior of the continent over a broad dynamic topography low. Since the Eocene, the dynamic subsidence of the US east coast occurred simultaneously with a lowering of the global sea level, with the eustatic fall being larger than dynamic subsidence. This results in a dynamic subsidence that cannot be as easily recognized in the stratigraphic record, compared to the western interior flooding during the Cretaceous. The discrepancy between the sea-level fall for the last 100 Ma derived for New Jersey coastal plain wells [Miller *et al*., 2005] and global sea-level curves [*Bond*, 1979; *Kominz*, 1984; *Haq and Al-Qahtani*, 2005] is consistent with the proposed dynamic subsidence. We propose that this discrepancy can be eliminated if vertical movements of the North American continent due to dynamic topography are taken into account.

References

Bond, G. (1979), Evidence for some uplifts of large magnitude in continental platforms, *Tectonophysics, 61,* 285–305.

Bunge, H.-P., and S.P. Grand (2000), Mesozoic plate-motion history below the northeast Pacific ocean from seismic images of the subducted Farallon slab, *Nature, 405*, 337–340.

Gazin, C. L. (1953), The Tillodontia: An early Tertiary order of mammals, *Smithsonian Misc. Collection, 121*, 10, 1–110.

Grand, S. P. (2002), Mantle shear-wave tomography and the fate of subducted slabs, *Philosophical Transactions of the Royal Society of London Series A-Mathematical Physical and Engineering Sciences*, *360*(1800), 2475–2491.

Gurnis, M. (1992), Long-term controls on eustatic and epeirogenic motions by mantle convection, *GSA Today, 2*, 141–157.

Gurnis, M., R.D. Müller, and L. Moresi (1998), Cretaceous Vertical Motion of Australia and the Australian-Antarctic Discordance, *Science, 279*(5356), 1499–1504.

Hager, B.H., C.W. Clayton, M.A. Richards, R.P. Comer, and A.D. Dziewonski (1985), Lower mantle heterogeneity, dynamic topography and the geoid, *Nature, 313*, 6003, 541–545.

Harrison, C.G.A. (1990), Long-term eustasy and epeirogeny in continents, *Revelle, R., ed., Sea-level change, Washington, D.C., National Academy Press,* 141–160.

Haq, B.U., J. Hardenbol, and P.R. Vail (1987), Chronology of fluctuating sea levels since the Triassic, *Science, 235,* 1156–1167.

Haq, B.U., and A. Motaleb Al-Qahtani (2005), Phanerozoic cycles of sea-level change on the Arabian Platform, *GeoArabia, 10,* 2, 127–160.

Kominz, M.A. (1984), Oceanic ridge volumes and sea level change: An error analysis, *in Interregional Unconformities and Hydrocarbon Accumulation (Ed. by J. Schlee),* AAPG Memoir, 36, 109–127.

Lithgow-Bertelloni, C., and M. Gurnis (1997), Cenozoic subsidence and uplift of continents from time-varying dynamic topography, *Geology, 25*, 735–738

Lithgow-Bertelloni, C., and M.A. Richards (1998), The dynamics of Cenozoic and Mesozoic plate motions, *Reviews of Geophysics, 36*, 27–78.

Liu, L., and M. Gurnis (2008), Simultaneous inversion of mantle viscosity and initial conditions from an adjoint of mantle convection, *Journal of Geophysical Research, 113,* B08405, doi:10.1029/2008JB005594.

Liu, L., S. Spasojevic and M. Gurnis (2008), Reconstructing Farallon plate subduction beneath North America back to the Late Cretaceous, *Science, 322*, 934–938, DOI:10.1126/science.1162921, 2008.

Liu, S., and D. Nummedal (2004), Late Cretaceous subsidence in Wyoming: Quantifying the dynamic component, *Geology*, 32, 397–400.

Miller, K.G., M. A. Kominz, J.V. Browning, J. D. Wright, G.S. Mountain, M.E. Katz, P.J. Sugarman, B.S. Cramer, N. Christie-Blick, and S.F. Pekar (2005), The Phanerozoic Record of Global Sea-Level Change, *Science, 310,* 1293–1298.

Mitrovica, J.X., C. Beaumont, and G.T. Jarvis (1989), Tilting of continental interiors by the dynamical effects of subduction. *Tectonics, 8*, 1079–1094.

Müller, R.D., M. Sdrolias, C. Gaina, B. Steinberger, and C. Heine (2008), Long-term sea-level fluctuations driven by ocean basin dynamics, *Science, 319,* 1357–1362.

Paleobiology database (www.paleodb.org) (2007), The data were downloaded from the Paleobiology Database in November 2007, using the following parameters: time intervals = Miocene and Eocene, region = United States, paleoenvironment = marine.

Ren, Y., E. Stutzmann, R. van der Hilst, and J. Besse (2007), Understanding seismic heterogeneities in the lower mantle beneath the Americas from seismic tomography and plate tectonic history*, Journal of Geophysical Research, B01302*, doi:10.1029/2005JB004154.

Richards, M.A., and B.H. Hager (1984), Geoid anomalies in a dynamic Earth*, Journal of Geophysical Research, 89,* B7, 5987-6002.

Ritsema, J., and H.J. van Heijst (2000), Seismic imaging of structural heterogeneity in Earth's mantle: Evidence for large-scale mantle flow, *Scientific Progress 83*, 243–259.

Steinberger, B. (2007), Effects of latent heat release at phase boundaries on flow in the Earth's mantle, phase boundary topography and dynamic topography at the Earth's surface, *Physics of Earth and Planetary Interiors*, *164*, 2–20, doi:10.1016/j.pepi.2007.04.021.

Tan, E., E. Choi, P. Thoutireddy, M. Gurnis, and M. Aivazis (2006), GeoFramework: Coupling multiple models of mantle convection within a computational framework, *Geochemistry, Geophysics, Geosystems, 7*, Q06001, doi: 10.1029/ 2005GC001155, 14 pp.

Tedford, R.H. and M. E. Hunter (1984), Miocene marine-nonmarine correlations, Atlantic and Gulf Coastal Plains, North America, *Palaeography, Palaeoclimatology, Palaeoecology, 47*, 129–151.

Van Sickel, W.A., M. Kominz, K.G. Miller, and J.V. Browning (2004), Late Cretaceous and Cenozoic sea-level estimates: backstripping analysis of borehole data, onshore New Jersey, *Basin Research, 16,* 451–465.

Watts, A.B., and M.S. Steckler (1979), Subsidence and eustasy at the continental margin of eastern North America, *Maurice Ewing Series No. 3,* 218–234.

Wright, D.B., and R. E. Eshelma (1987), Miocene Tayassuidae (Mammalia) from the Chesapeake Group of the Mid-Atlantic coast and their bearing on marine-nonmarine correlation, *Journal of Paleontology, 61*, 3, 604–618.

Chapter 6

Sea level and vertical motion of continents from dynamic earth models since the Late Cretaceous

6.1. Abstract

We develop hybrid dynamic earth models combining inverse and forward models of mantle convection, with the goal to better understand the impact of mantle dynamics on vertical motion of continents, and regional and global sea-level change since the Late Cretaceous. These models account for the principle contributors to long-term sea-level change: evolving ocean floor age, dynamic topography in oceanic and continental regions, and geoid. We infer relative importance of dynamic versus other factors of sea-level change, determine time-dependent patterns of dynamic subsidence and uplift of continents, and derive a sea-level curve.

We find that both dynamic factors and the evolving age of sea floor are important in controlling sea level. The dominant factor controlling global sea level is changing oceanic lithosphere production, inferred from the evolving ocean floor age, resulting in a large amplitude sea-level fall since the Late Cretaceous, with dynamic topography offsetting this fall. We find the maximum amplitude of sea level of 286 m to be reached at 80 Ma.

We track movement of continents over large-scale dynamic topography by consistently mapping between mantle and plate frames of reference, and we find that this movement results in dynamic subsidence and uplift of continents. Regional sea level is largely controlled by mantle dynamics in North and South America in the last 90 million years, Australia during the Cenozoic, North Africa and Arabia in the last 40 million years, and southeast Asia in the Oligocene-Miocene period. Dynamic uplift affects East and South Africa over the last 20-30 million years. We also find evidence for Cenozoic tilting of Siberia experiences (down to east) and Australia (down to NNE).

6.2. Introduction

Continental interiors experienced extensive marine inundation and sedimentation during the Cretaceous. This inundation is associated with a global sea level high, often called a eustatic, high [*Hallam*, 1992]. The marine inundation of North America is a clear example of the extensive flooding, where approximately 40% of the continental interior flooded, resulting in more than 1 km of sediments deposited over a horizontal scale of a thousand kilometers [*Bond*, 1976; *Liu and Nummedal*, 2004]. The eustatic change on time-scales of millions of years may be controlled by changes in ocean basin volume due to variations in oceanic spreading rates or ridge lengths [*Hays and Pitman*, 1973; *Kominz*, 1984]. However, analysis of North American Cretaceous stratigraphic sequences [*Sloss*, 1963] suggests that observed

continental-scale transgressional and regressional cycles cannot be explained by eustasy alone [*Bond*, 1976; *Sleep*, 1976], and that large-scale tectonic or dynamic mechanisms are also required. Analysis of the Cretaceous sediments of North America suggests that the observed flooding would require a sea-level rise of 310 m, resulting in accumulation of 700 m of sediments [*Bond*, 1976]. Since observed isopachs [*Cook and Bally*, 1975] are significantly thicker, eustasy could not have been the only process causing the marine transgression in North America during the Cretaceous .

Continental flooding can be controlled by dynamic topography, a vertical deflection of the surface due to mantle flow (e.g., *Richards and Hager* [1984]). Although dynamic topography results in large-amplitude geoid anomalies, because these anomalies are small compared to topography [*Hager*, 1984], thus sea-level variations should be mainly controlled by changes in dynamic topography [*Gurnis*, 1990]. Early geodynamic studies explored the basic process of dynamic controls of sea level, including simple 2D isoviscous models of convection that showed that slabs create broad topographic depressions that can be filled with sediments [*Mitrovica and Jarvis*, 1985], and that continental flooding is influenced by movement of continents over large-scale patterns of dynamic topography [*Gurnis*, 1990]. Early regional studies linked mantle dynamics and vertical motions with observations. Models of North America showed that general features of Phanerozoic strata can be explained by dynamic topography created by subduction and supercontinent aggregation and dispersal [*Burgess et al.*, 1997]. The extensive Cretaceous flooding and subsequent uplift of the Western Interior Seaway have

been interpreted first with simple 2D models of Farallon slab subduction [*Mitrovica et al.*, 1989] and more recently with 3D variable viscosity inverse models assimilating seismic tomography and plate motions [*Liu et al.*, 2008; *Spasojevic et al.*, 2009]. Three-dimensional models have also been applied to Australia showed that anomalous Cretaceous vertical motions can be related to movement of the continent over a slab associated with long-lived Gondwanaland-Pacific subduction while also explaining the equally anomalous geochemistry and geophysics of the present-day seafloor south of Australia [*Gurnis et al.*, 1998; *Gurnis et al.*, 2000b]. Two episodes of long-wavelength tilting of the Russian platform during the Devonian to Permian period have been attributed to separate episodes of subduction [*Mitrovica et al.*, 1996], while the excess subsidence of the Campbell plateau between 70-40 Ma have been related to the drift of New Zealand away from a dynamic topography high associated with a Ross Sea mantle upwelling [*Spasojevic et al.*, 2010a; *Sutherland et al.*, 2009]. Several global models of mantle flow predicting time-varying dynamic topography have been developed as well. Global models of mantle flow driven by paleogeographically-constrained subduction match patterns of flooding in the Middle Ordovician, Late Permian and Early Cretaceous (i.e., periods of flooding during eustatic highs) [*Gurnis*, 1993] as well as the Cenozoic uplift and subsidence of North America, Australia, and Indonesia [*Lithgow- Bertelloni and Gurnis*, 1997]. In addition dynamic topography should also modify the shape (depth) of the oceans' basins globally, which will affect the time-dependent trends of sea-level change [*Conrad and Husson*, 2009; *Gurnis*, 1993].

These studies demonstrate the importance of mantle dynamics in modulating global and regional sea level, and in some cases they have linked the models to stratigraphic constraints, but they have significant limitations. Most dynamic topography models were in a mantle frame, with the exception of regional models of Australia [*DiCaprio et al.*, 2009b; *Gurnis et al.*, 1998; *Gurnis et al.*, 2000b] and North America [*Liu et al.*, 2008; *Spasojevic et al.*, 2009], while geologic observations are made in the plate frame of reference. Previous global models of sea-level change did not account for dynamic topography, changing age of ocean floor, and the geoid self-consistently. Here we present spherical Dynamic Earth Models (DEMs) since the Late Cretaceous that overcome these limitations by assimilating plate tectonic reconstructions into models of mantle convection with vertically and laterally variable viscosity. We combine inverse and forward methods for solving for mantle convection, allowing estimates of initial conditions with improved formulations for density, viscosity, and convergent plate margins. We also use globally distributed stratigraphic data to constrain the mantle's control on uplift and subsidence, but on regional and global sea-level change. Global DEMs are computed in the mantle frame, but the integrated plate reconstruction-mantle convection system enables a linkage between geologic observations in plate frames of reference. We first compute the shape of the ocean and eustasy that accounts for changing ocean floor age [*Müller et al.*, 1997; *Müller et al.*, 2008b], time-dependent dynamic topography, and the geoid. Second, we compute marine inundation and paleoshorelines within continental interiors and compare them with geologic observations. Such DEMs account for the most important factors controlling long-term sea-level change self-

consistently, and from them we infer the relative importance of different factors for the control of vertical motions of continents and sea-level change since Late Cretaceous.

6.3. Method

DEMs link plate reconstructions and seismic images with forward and inverse mantle convection models, in which the resulting predictions are compared with stratigraphic observations. DEMs are developed for the periods spanning from the Late Cretaceous to the present, with a goal of improving our understanding of the history of vertical motion of earth's surface and global and regional sea level.

6.3.1. Plate reconstructions

We use plate reconstructions in which plate geometry is represented as continuously evolving closed plate polygons using the GPlates package [*Boyden et al.*, 2010] (Fig. 6.1). Each plate is defined as a rigid plate with its own Euler pole, and a set of evolving margins, each having a different Euler pole [*Gurnis et al.*, 2010] defined in a moving hotspot reference frame [*Müller et al.*, 2008a]. We dynamically close plates by continuously finding the intersection of all margins with no gaps or overlaps between adjacent plates [*Gurnis et al.*, 2010]. The continuously closed plate polygons are self-consistent with paleoage grids that give the age of oceanic

lithosphere [*Müller et al.*, 2008a]. The time interval between reconstructions can be as small as needed, but we use one million year (Myr) here.

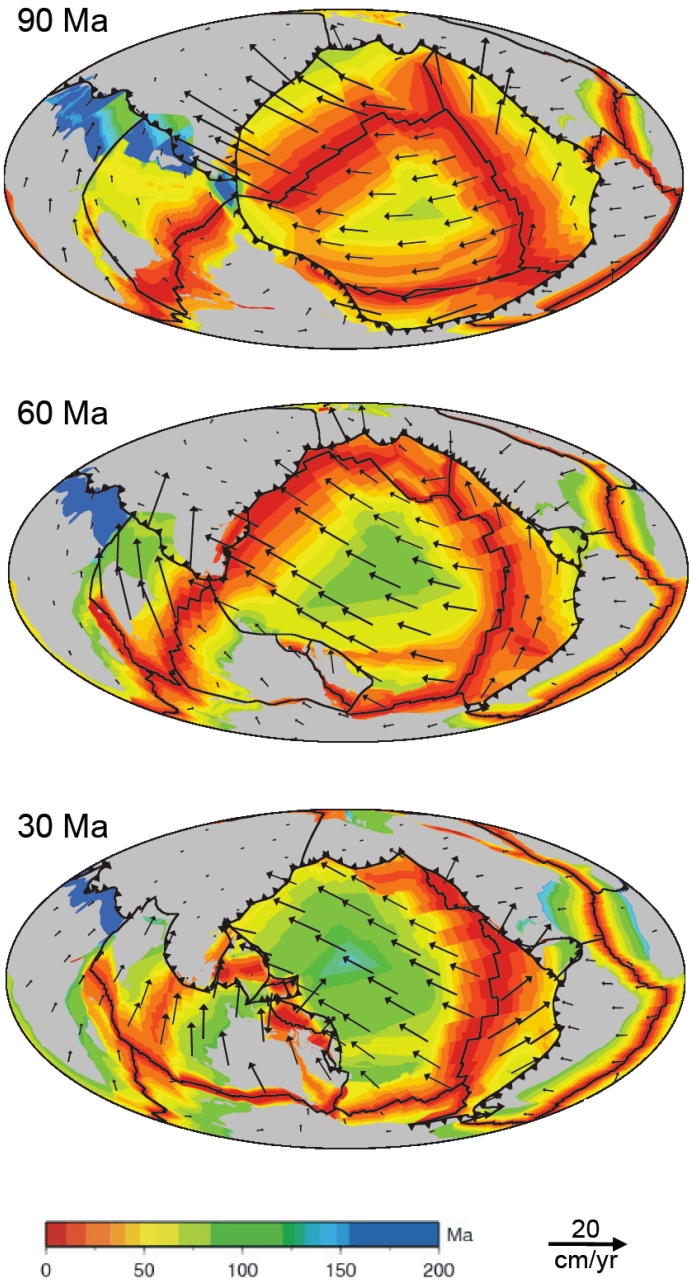

Figure 6.1. GPlates reconstructions at 90 Ma, 60 Ma, and 30 Ma. Colors represent reconstructed age of the sea floor [*Müller et al.,* 2008a], arrows show plate velocities in the moving hotspot frame of reference. Black lines with filled black triangles indicate position of subduction zones, while plain black line indicate ridges and transform plate boundaries.

Different aspects of the plate reconstructions are assimilated into the DEMs. First, plate velocities, defined at 1 Myr steps and linearly interpolated at intermediate times, are used as surface kinematic boundary condition on the convection models. Second, the position and character of plate boundaries are used to define buoyancy associated with subduction in hybrid models. Third, the paleoage grids are used with the hybrid models as well as for global time-dependent sea-level calculations. Finally, the plate reconstructions are used for mapping outputs from the mantle to plate frames of reference using closed plate polygons and rotation poles, enabling comparison of model predictions with the stratigraphic constraints.

6.3.2. Mantle convection models

Models of mantle convection are formulated with the finite-element code CitcomS version 3.2 [*Tan et al.*, 2006; *Zhong et al.*, 2000], which solves the equations of mass, momentum, and energy conservation for an incompressible, Newtonian fluid, while making the Boussinesq approximation. Previous mantle convection models investigating dynamic effects on sea level are defined either as forward or inverse models. The main limitation of forward models, run from the geologic past to the present, is the unknown past structure of the mantle. Inverse models on other hand are run from the present to the past, with the present-day mantle structure constrained by scaled seismic tomography. However, inverse models are limited by: (1) not being able to reverse thermal diffusion to predict past structures, which is reasonable for the mantle interior, away from boundary layers, on time scales

studied here [*Conrad and Gurnis*, 2003; *Liu and Gurnis*, 2008]; (2) long-wavelength and low-resolution mantle structure, and (3) inability to realistically treat subduction zones in viscous models [*Liu et al.*, 2008].

We formulate hybrid geodynamic models that combine inverse [*Conrad and Gurnis*, 2003; *Liu and Gurnis*, 2008] with forward models, to overcome their individual limitations. First, we simply integrate backwards (e.g., SBI of *Liu and Gurnis* [2008]) from the present to the Late Cretaceous, with kinematic surface velocity by reversing the direction of plate motions (Fig. 6.1). The initial global SBI temperature field at 0 Ma is defined from seismic tomographic inversions of surface and body waves using models SB4L18 [*Masters et al.*, 2000] or S20RTS [*Ritsema et al.*, 2004], with tomography-to-density scaling constrained by fitting the observed geoid [*Spasojevic et al.*, 2010b]. Second, we create a hybrid buoyancy field in the past by merging the SBI with synthetic subducted slabs. Namely, for each time step in the past, we define lower mantle buoyancy from the SBI, while in the upper mantle we merge high-resolution synthetic slabs with positive buoyant anomalies from the SBI. Geometry and thermal structure of subducted slabs in the upper mantle are defined from the reconstructed subduction zones from GPlates (Fig. 6.1), age of the subducted lithosphere [*Müller et al.*, 2008a], and relations among subduction zone parameters [*Tape et al.*, 2010]. SBI buoyancy is stripped from the upper 250 km of mantle, as it likely neutrally buoyant [*Goes and van der Lee*, 2002; *Jordan*, 1988].

Finally, the Stokes equation is solved in a forward model with this hybrid buoyancy, imposing a no slip boundary condition at the top surface, so as to obtain the

dynamic topography ,and geoid at each instant of time. Dynamic topography on the top surface is determined from the total normal stress in the radial direction while accounting for self-gravitation [*Zhong et al.*, 2008]. Fig. 6.2 shows the predicted dynamic topography, geoid and buoyancy for a hybrid model. A four-layer mantle viscosity structure, consisting of high-viscosity lithosphere, upper mantle, transition zone, and lower mantle is modified by a temperature-dependent viscosity, which introduces lateral viscosity variations, shown to be an important influence on dynamic topography and geoid in subduction zones [*Billen and Gurnis*, 2001; *Billen et al.*, 2003] and for present-day plate motions [*Stadler et al.*, 2010]. Details of the viscosity, resolution, and other model parameters are given in Appendix 2.

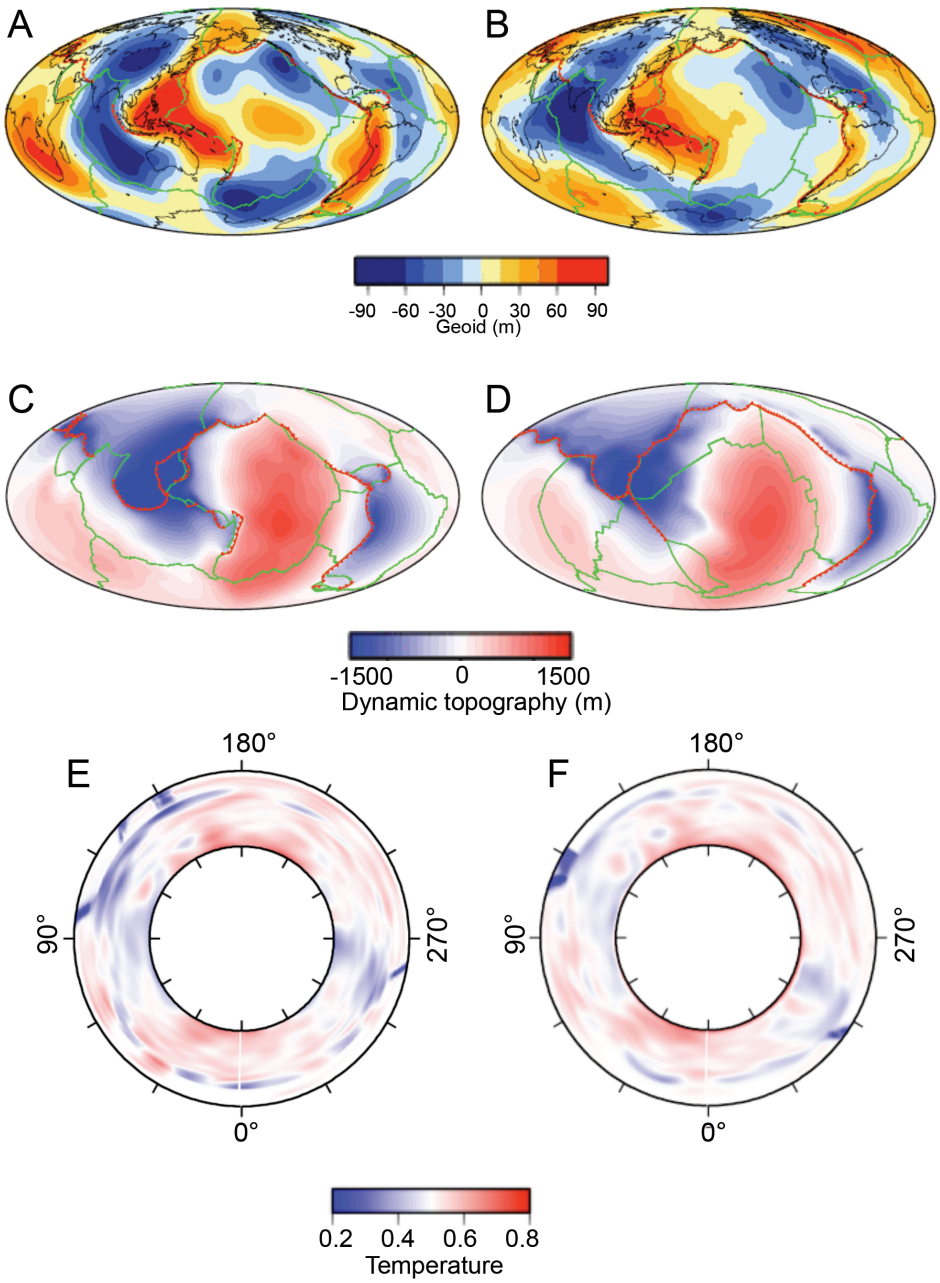

Figure 6.2. Dynamic topography and geoid prediction for model M3. (A) Predicted geoid at 0 Ma. (B) Observed geoid. (C-D) Predicted dynamic topography at 0 Ma (C) and 80 Ma (D). (E-F) Global Equatorial spherical cross-section through temperature field at 0 Ma (E) and 80 Ma (F).

6.3.3. Paleogeographic constraints and relative sea-level change

The primary geologic constraints are a set of published global and regional inferred paleo shorelines from the Late Cretaceous to the present. We use two sets of global Cretaceous and Cenozoic shorelines, one from [*Smith et al.*, 1994] determined at every 10 million years intervals from 90 to 10 Ma, and a second from [*Blakey*, 2008] defined for the Late Cretaceous (90 Ma), Cretaceous-Tertiary boundary (65 Ma), Eocene (50 Ma), Oligocene (35 Ma), and Miocene (20 Ma). We also use a regional set of reconstructions for: 1) North and Central Africa and Arabia [*Guiraud et al.*, 2005] in Latest Albian–Early Senonian (98.9–85 Ma), Late Santonian–Maastrichtian (84-65 Ma), Paleocene (65-54.8 Ma), Early–Middle Eocene (54.8-37 Ma), Oligocene (33.7-23.8 Ma), and Miocene (23.8-5.3 Ma); (2) Southeast Asia [*Hall and Morley*, 2004] in Late Oligocene (28.4- 23 Ma), Early Miocene (23- 16 Ma), and Middle Miocene (16-11.6 Ma); and (3) Australia at 77 Ma, 68 Ma, 60 Ma, 44 Ma, 33 Ma, 20 Ma, 8, and 4 Ma [*Langford et al.*, 1995], with numerical ages indicating the middle of the respective reconstruction periods. Paleshoreline maps are simplified by division into marine and subaerial units. We infer relative sea-level change by differencing these maps between a more recent (t_1) from an earlier age (t_2; $t_2 > t_1$). Marine regression occurs when a submerged area at t_2 is exposed above the sea level at t_1, implying a eustatic fall, a sedimentation rate that outpaces accommodation space creation regionally, or a relative uplift regionally [*Hallam*, 1992]. Marine transgression occurs when subaerially exposed area at t_2 is flooded at subsequent time period t_1, which can be the result of a eustatic rise, a sea-level rise outpacing

sedimentation regionally, or regional subsidence. When an area of interest is subaerially exposed (or flooded) at both times, it is possible that it is also experiencing vertical motions and sedimentation, but with amplitudes and wavelengths insufficient to result in changes of flooding.

We compare maps of relative sea-level change to maps of differential dynamic topography, created by subtracting dynamic topography at time interval t_1 from dynamic topography at t_2 ($t_1 < t_2$). We hypothesize that good agreement between maps of relative sea-level change and maps of differential dynamic topography might imply that dynamic topography is one of the factors contributing to the observed regional shoreline migration. If such agreement does not exist, then shoreline migration is likely controlled by factors other than mantle convection-induced subsidence and uplift. This reasoning will be limited if the hybrid model fails to predict the correct trends in dynamic topography due to incorrect estimates of the mantle buoyancy field. We attempt to overcome this limitation by finding alternative dynamic models that provide a better agreement between differential dynamic topography and inferred relative sea-level change.

6.3.4. Global sea-level calculations

In order to calculate global sea level, we first determine global topography at each time step (Fig. 6.3A-B), which is subsequently inundated for paleo-shoreline predictions (Fig. 6.3C). The ocean-continent function is defined from oceanic age

grids [*Müller et al.*, 2008a], such that areas with ocean-floor ages are defined as oceanic, with the remaining assumed continental. For oceanic regions, bathymetry is nominally determined from age-depth relationships (Fig. 6.3A) using a half-space, thermal cooling model [*Parsons and Sclater*, 1977] without flattening:

$$d = 2500m + 350m\sqrt{t} \tag{1}$$

where d is ocean floor depth in meters and t is sea-floor age in million of years. We assume a half-space without flattening because age-depth relationships that include flattening [*Parsons and Sclater*, 1977; *Stein and Stein*, 1992] likely have a component of dynamic topography. Air-loaded topography of ocean-floor is:

$$d_{al} = \frac{\rho_m - \rho_w}{\rho_m - \rho_a} = 0.689 \cdot d \tag{2}$$

where d_{al} is air-loaded depth of ocean floor, and ρ_m, ρ_w and ρ_a are densities of mantle, water and air, respectively (Appendix 2).

For continental regions, we first define air-loaded isostatic topography (Fig. 6.3A). At present, the topography is assumed to be the sum of an isostatic and a dynamic component. We determine the isostatic component at t by subtracting predicted dynamic topography at 0 Ma from the observed topography (Fig. 6.3A), and merging the rotated field for each plate from 0 Ma to t. This assumes isostatic topography remains unchanged from 0 Ma to t, a significant limitation in places since it ignores orogenesis and complicates global sea-level predictions. The final air-loaded topography at time step t is obtained by summing air-loaded dynamic topography (Fig. 6.3B) and isostatic topography.

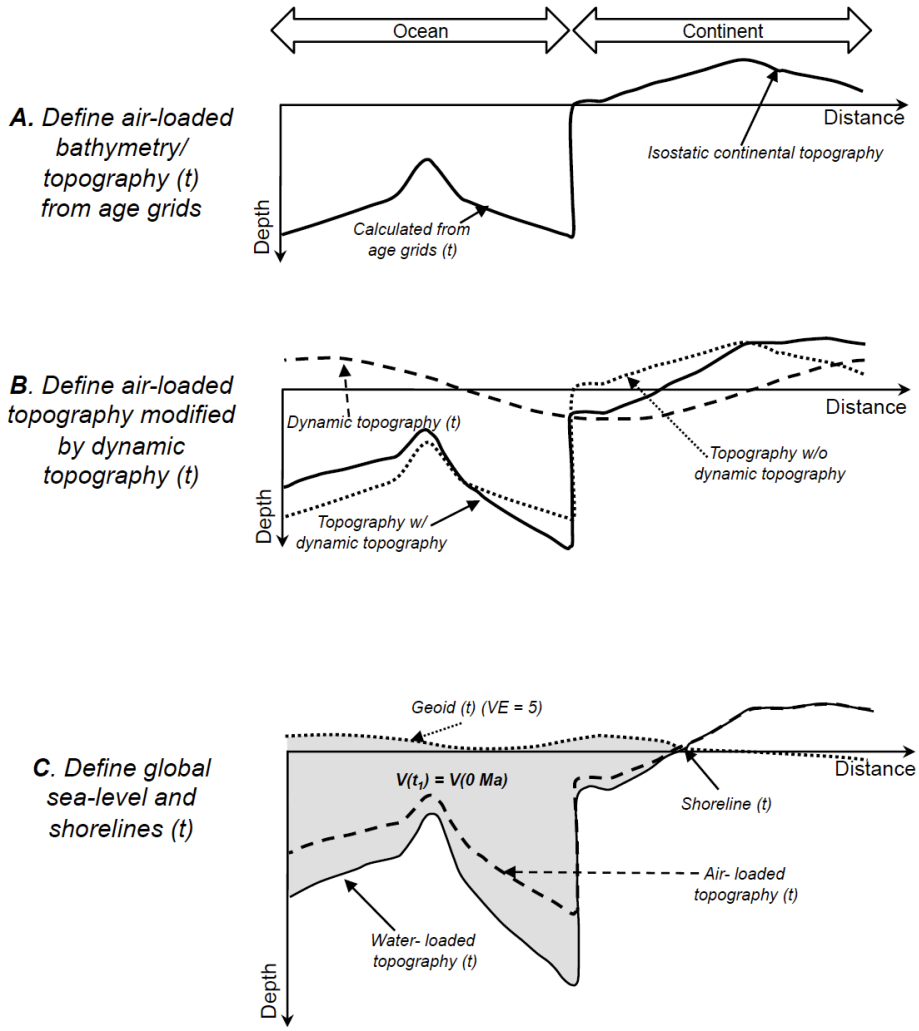

Figure 6.3. Two-dimensional schematic of the algorithm used for global sea-level calculations in DEMs.

The air-loaded global topography is inundated (Fig. 6.3C): Starting with the lowest parts of the air-loaded topography, we fill depressed areas with the present-day volume of ocean water so that the water surface conforms to the evolving geoid, well predicted at present (Fig. 6.2) [*Spasojevic et al.*, 2010b]. In areas covered with water, isostatic adjustment for water loading is applied, and the final topography is a combination of water-loaded areas and air-loaded continents (Fig. 6.3C).

Paleoshorelines are the intersection of the final topography with the ocean surface (Fig. 6.3C) at each time step.

We compare shoreline predictions that only account for the changing ocean floor age (OFA) with those that account for dynamic topography, geoid, and ocean floor age (DYN-OFA). We infer the relative importance of dynamic factors versus ocean floor age on sea-level change based on comparison of these two predictions at 80 Ma (Late Cretaceous), 60 Ma (early Cenozoic), and 30 Ma (mid Cenozoic). Results for India are excluded since they are biased by the time-invariant isostatic assumption (because of the Himalayan orogen).

We quantify global sea-level change: (1) due to variations in ocean age using half-space model without flattening (Eq. 1; OFA-HS), half-space model with flattening (Appendix 2; OFA-HSF), and GDH-1 model (Appendix 2; OFA-GDH) by calculating mean ocean bathymetry using relationships (2)-(5) in Appendix 2; and (2) by calculating variations in sea level for DYN-OFA with the half-space cooling model, while tracking contributions due to dynamic topography in oceanic regions (e.g., regions with defined ocean-floor ages in age grids), dynamic topography in flooded continental regions (e.g., regions that are predicted to be inundated, but have no values of ocean-floor ages in age grids), and geoid. DYN-OFA sea-level estimates are corrected for sedimentation and ocean plateau emplacement using previously published time-dependent estimates [*Müller et al.*, 2008a].

6.4. Results

6.4.1. Global dynamic topography

For each tomography model, we compute hybrid models (Table 6.1) for three different radial viscosity profiles (where the ratios of transition zone to lower mantle viscosity are 1:20, 1:60, and 1:100). In each case, the reference viscosity is 10^{21} Pa s (Appendix 2), with an upper mantle average background viscosity of 10^{20} Pa s. Dynamic topography decreases with increasing lower mantle viscosity (Fig. A2.1). The largest dynamic topography lows are located in the regions of subduction, so that at 0 Ma large dynamic topography lows develop in the western Pacific, Southeast Asia, South America, and the Mediterranean. During the Late Cretaceous dynamic topography lows are in western North America, associated with subduction of the Farallon slab, and the region of Alpine Tethys subduction. Dynamic topography highs are associated with oceanic regions (Pacific Ocean, Northern Atlantic and Indian Ocean) and Africa between the Late Cretaceous and the present (Fig. A2.1).

Table 6.1. Hybrid model summary

Model name	M1	M2	M3	M4	M5	M6
Tomography model in SBI	S20RTS	S20RTS	S20RTS	SB4L18	SB4L18	SB4L18
Average transition zone to lower mantle viscosity ratio	1:20	1:60	1:100	1:20	1:60	1:100

6.4.2. Regional sea level and vertical motions

6.4.2.1. North America

North America experienced widespread marine inundation during the Late Cretaceous, resulting in development of the western interior seaway (WIS) [*Sloss*, 1988], a large epicontinental sea a thousand kilometers across, followed by extensive uplift in the Cenozoic during the Laramide orogeny [*English and Johnston*, 2004]. Maps of Late Cretaceous relative sea-level change (Fig. 6.4A) show the western interior seaway (WIS) being continuously flooded, its eastern edge experiencing marine transgression, and the rest of North America remaining subareal and presumably high [*Blakey*, 2008; *Smith et al.*, 1994]. DEMs predict an increasing dynamic topography low in the WIS (Fig. 6.4A), with the western edge being approximately aligned with the position of the Sevier belt during the Late Cretaceous. Models based on SB4L18 tomography (M4) predict well the eastern edge of the WIS, while models based on S20RTS tomography (M1) predict a wider differential dynamic topography low covering both the WIS and eastern North America (Fig. 6.4A). Model M1 predicts up to 200 m of Late Cretaceous dynamic uplift of westernmost North America (Fig. 6.4A).

Cenozoic relative sea-level maps indicate that North America either experienced uplift or remained high (Fig. 6.5A) in the last 60 million years. The global hybrid models show accumulated dynamic uplift of western North America (Fig. 6.5A) over the Cenozoic, and dynamic subsidence of the eastern part of the continent, with the east coast subsiding between 100 m to 400 m, depending on model parameters.

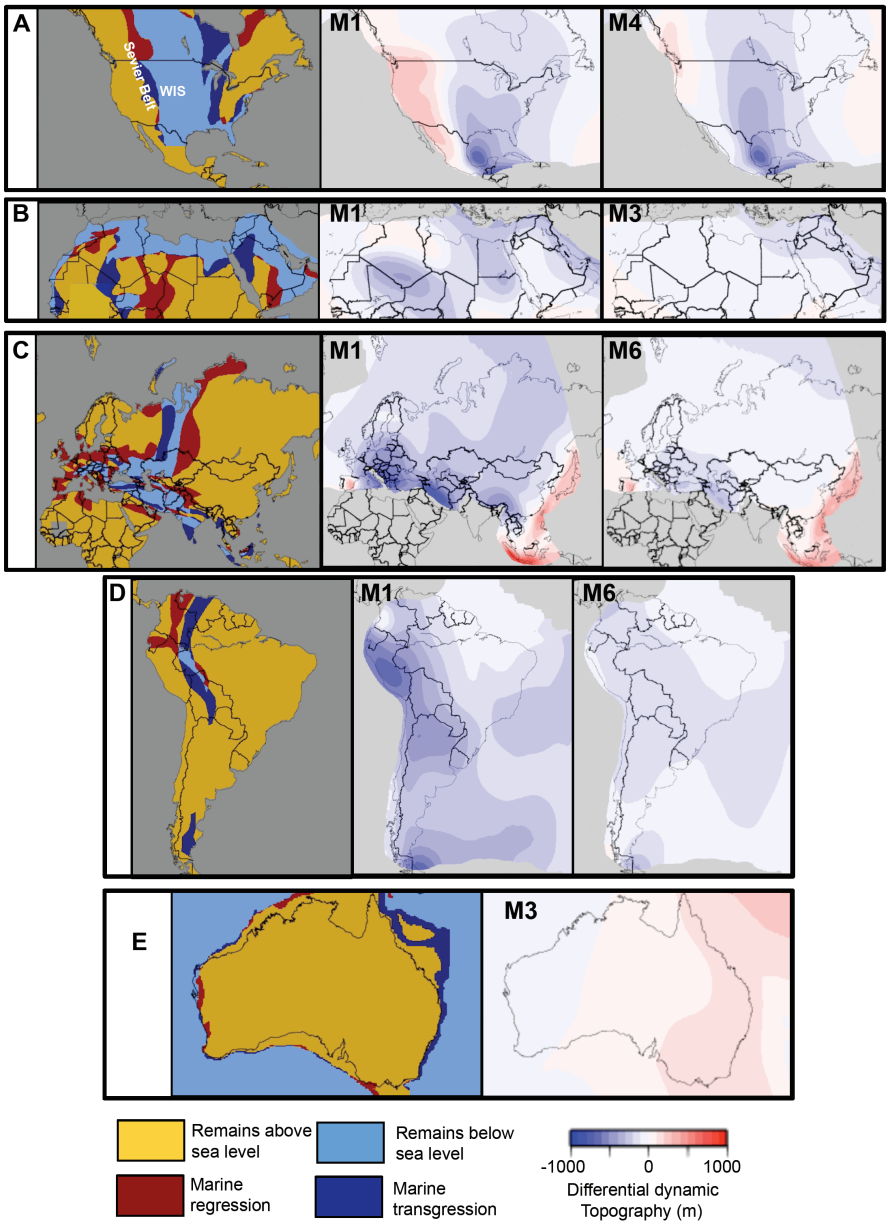

Figure 6.4. Inferred relative sea-level change in the Late Cretaceous for (A) North America, (B) North Africa and Arabia, (C) Eurasia, (D) South America, and (E) Australia. First image in (A-E) represents relative sea-level inferred from paleogeography using reconstructions at: (A) 70 and 90 Ma [*Smith et al.*, 1994]; (B) Late Santonian–Maastrichtian and Latest Albian- Early Senonian times [*Guiraud et al.*, 2005]; (C-D) 65 and 90 Ma [*Blakey*, 2010]; (E) 60 and 77 Ma [*Langford et al.*, 1995]. Relative vertical motions inferred from dynamic models are shown with symbol M corresponding to specific hybrid model (Table 6.1).

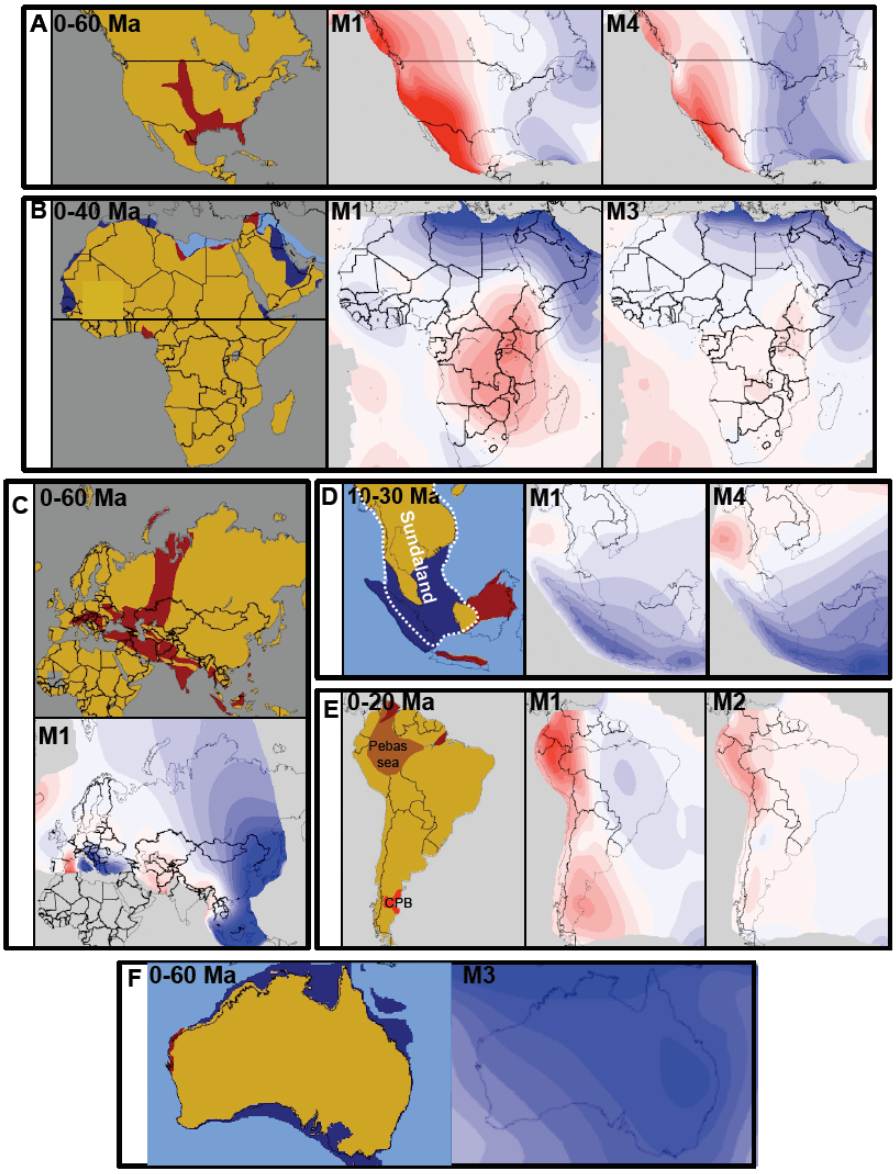

Figure 6.5. Inferred relative sea-level change in the Cenozoic. (A) 0-60 Ma in North America. (B) 0-40 Ma in North Africa and Arabia. (C) 0-60 Ma in Eurasia. (D) 10-30 Ma in southeast Asia. (E) 0-20 Ma in South America. (F) 0-60 Ma in Australia. First image in (A-E) represents relative sea-level inferred from paleogeography using reconstructions at: (A) 60 Ma [*Smith et al.*, 1994]; (B) Miocene and Early–Middle Oligocene in north Africa [*Guiraud et al.*, 2005] and 35 Ma in south and central Africa [*Blakey*, 2010]; (C) 65 Ma [*Blakey,* 2010]; (D) Middle Miocene and Late Oligocene [*Hall and Morley*, 2004]; (E) 20 Ma [*Blakey*, 2010], and (F) 60 Ma [*Langford et al.*, 1995]. Relative vertical motions inferred from dynamic models are shown with symbol M corresponding to specific hybrid model (Table 6.1). CPB on (E) indicates Central Patagonian Basin. The legend is the same as for Fig 6.4.

Table 6.2. Inferred dynamic subsidence (—) and uplift (+) from DEMs

Continent	Late Cretaceous	Paleocene-Eocene	Oligocene- Miocene
North America (WIS)	—	+	+
North America (East)		—	—
North Africa	—	—	—
South and East Africa			+
Southeast Asia	+	—	—
Eurasia (North-Central)		Siberian tilt	Siberian tilt
Alpine Tethys	—	—	—
South America (western interior)	—		+
South America (Amazon)	—	—	—
South America (Patagonia)			+
Australia	+ (?)	—	—

This pattern of vertical motions (Table 6.2) is related to subduction of the Farallon slab, as shown previously [*Liu et al.*, 2008; *Mitrovica et al.*, 1989; *Spasojevic et al.*, 2009]. Remnants of the Farallon slab are presently imaged as a north-south trending high-seismic-velocity anomaly under the east coast of North America at depths of 800- 2000 km [*Grand*, 2002; *Masters et al.*, 2000; *Ritsema et al.*, 2004]. As the mantle flow and plate motions are reversed in the SBI from the present to the Late Cretaceous, the Farallon slab rises upward and North America moves eastward in the mantle frame of reference, so that it is located in the upper mantle under the WIS during the Late Cretaceous. High-density Farallon slab creates a dynamic topography low with amplitude of about 1 km (Fig. A2.1), with 500 m of Late Cretaceous dynamic subsidence (Fig. 6.4A). DEMs confirm previous results of a shallow to flat-lying Farallon slab during the Late Cretaceous [*Liu et al.*, 2008; *Mitrovica et al.*, 1989; *Spasojevic et al.*, 2009], potentially due to subduction of the

conjugate of Shatsky oceanic plateau [*Liu et al.*, 2010]. We could not match observations of differential vertical motions and flooding without the introduction of a shallow-dipping slab, with a dip of about 10°. As North America moves westward in the mantle reference frame from the Late Cretaceous to the present, and the Farallon slab sinks into the lower mantle, the dynamic topography low migrates eastward in the plate frame, resulting in overall Cenozoic subsidence of eastern North America, and dynamic uplift in the west (Fig. 6.5A). The Cenozoic subsidence does not create land subsidence, as it is contemporaneous with an overall sea-level fall. The proposed dynamic subsidence may help explain discrepancies between most global sea-level curves and those derived exclusively on the New Jersey coastal margin [*Spasojevic et al.*, 2008]. The timing of the Laramide orogeny is currently debated but it was probably initiated in the Late Cretaceous. Timing of termination of Laramide orogeny is also debated, with the proposed end varying 35 to 50 Ma [*Bird*, 1998] to recent times [*Bird*, 1998; *Liu et al.*, 2010]. We find that there is a continuous dynamic contribution to western US uplift since the end of the Late Cretaceous (Fig. 6.5A), resulting from movement of Farallon slab away from this region, similar to findings of adjoint geodynamic models [*Spasojevic et al.*, 2009].

Late Cretaceous flooding predictions in North America are closer to observations in DYN-OFA calculations, compared to estimates made solely accounting for changing age of sea floor (Fig. 6.6, Table 6.3). This further supports previous findings that the dynamic effects of the Farallon subduction are important in controlling widespread

WIS flooding [*Spasojevic et al.*, 2009], and that eustatic sea level alone cannot explain creation of thick sedimentary sequences [*Bond et al.*, 1976]. Our predicted Late Cretaceous flooding is shifted toward the east compared to that inferred (Fig. 6.6), which is related to assumed isostatic topography containing Laramide orogen. Early Cenozoic flooding is slightly better predicted when dynamic effects are taken into account (Fig. 6.7), while the Oligocene-Miocene flooding is equally well predicted in OFA and DYN-OFA models (Fig. 6.8). This suggests that the dynamic effects probably plays secondary role in controlling North American Cenozoic flooding during this time period, probably related to the significant decrease of the dynamic topography as the Farallon slab sinks into the lower mantle.

Table 6.3. Relative importance of factors controlling regional sea level

Continent	Late Cretaceous	Paleocene-Eocene	Oligocene- Miocene
North America	Dynamic + OFA	OFA +Dynamic	OFA (Dynamic secondary)
North Africa, India and South America	*	*	*
Eurasia	OFA**	OFA**	OFA**
Australia	Dynamic	Dynamic	Dynamic

** Interpretation complicated by unknown paleotopography and/or difference in paleogeographic reconstructions*

*** Subduction-related dynamic subsidence might be important in the Alpine Tethys region*

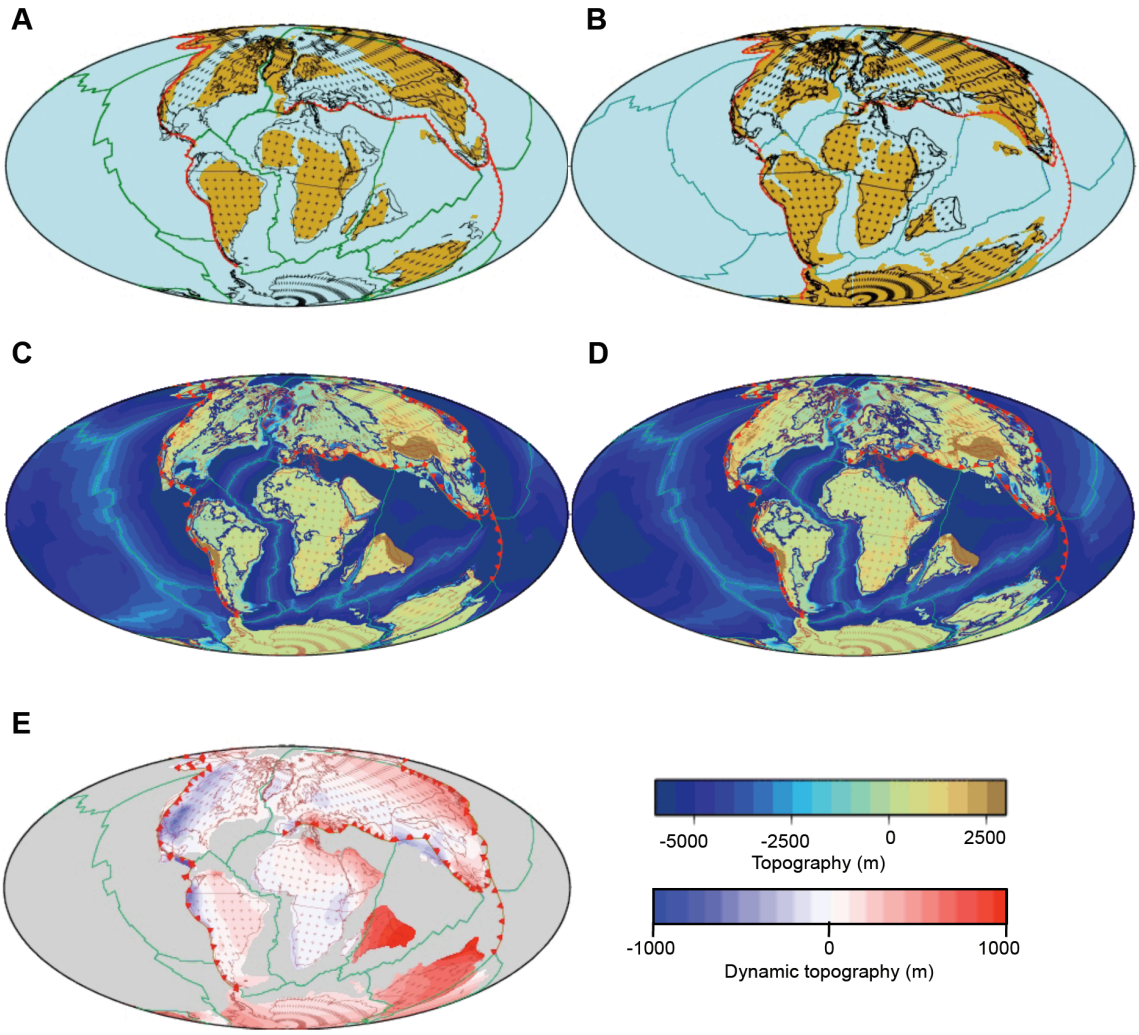

Figure 6.6. Late Cretaceous global sea-level predictions. (A-B) Paleogeographic reconstructions at 80 Ma [*Smith et al.*, 1994] (A) and 90 Ma (B) [*Blakey*, 2010]. (C) 80 Ma DYN-OFA flooding predictions accounting for changing age of the sea-floor, dynamic topography and geoid and using model M3 (Table 2). (D) 80 Ma OFA flooding predictions accounting only for changing age of sea-floor using half-space model without flattening [*Parsons and Sclater*, 1977]. (E) Difference between dynamic topography in past (80 Ma) and present-day predicted dynamic topography for model M3.

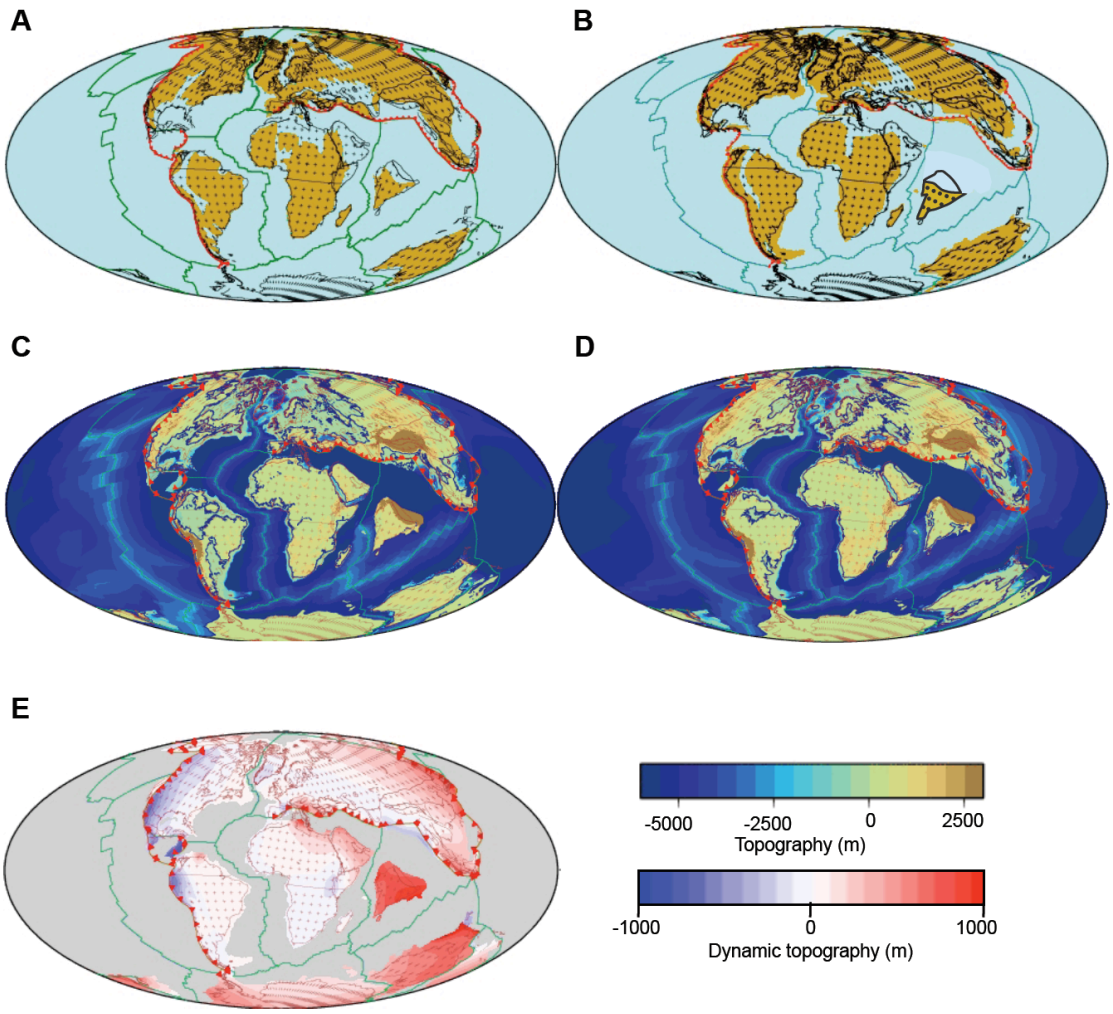

Figure 6.7. Early Cenozoic global sea-level predictions. (A-B) Paleogeographic reconstructions at 60 Ma (A) [*Smith et al.*, 1994] and 65 Ma (B) [*Blakey*, 2010]. (C) 60 Ma DYN-OFA flooding predictions accounting for changing age of the sea-floor, dynamic topography and geoid and using model M3 (Table 2). (D) 60 Ma OFA flooding predictions accounting only for changing age of sea-floor using half-space model without flattening [*Parsons and Sclater*, 1977]. (E) Difference between dynamic topography in past (60 Ma) and present-day predicted dynamic topography for model M3.

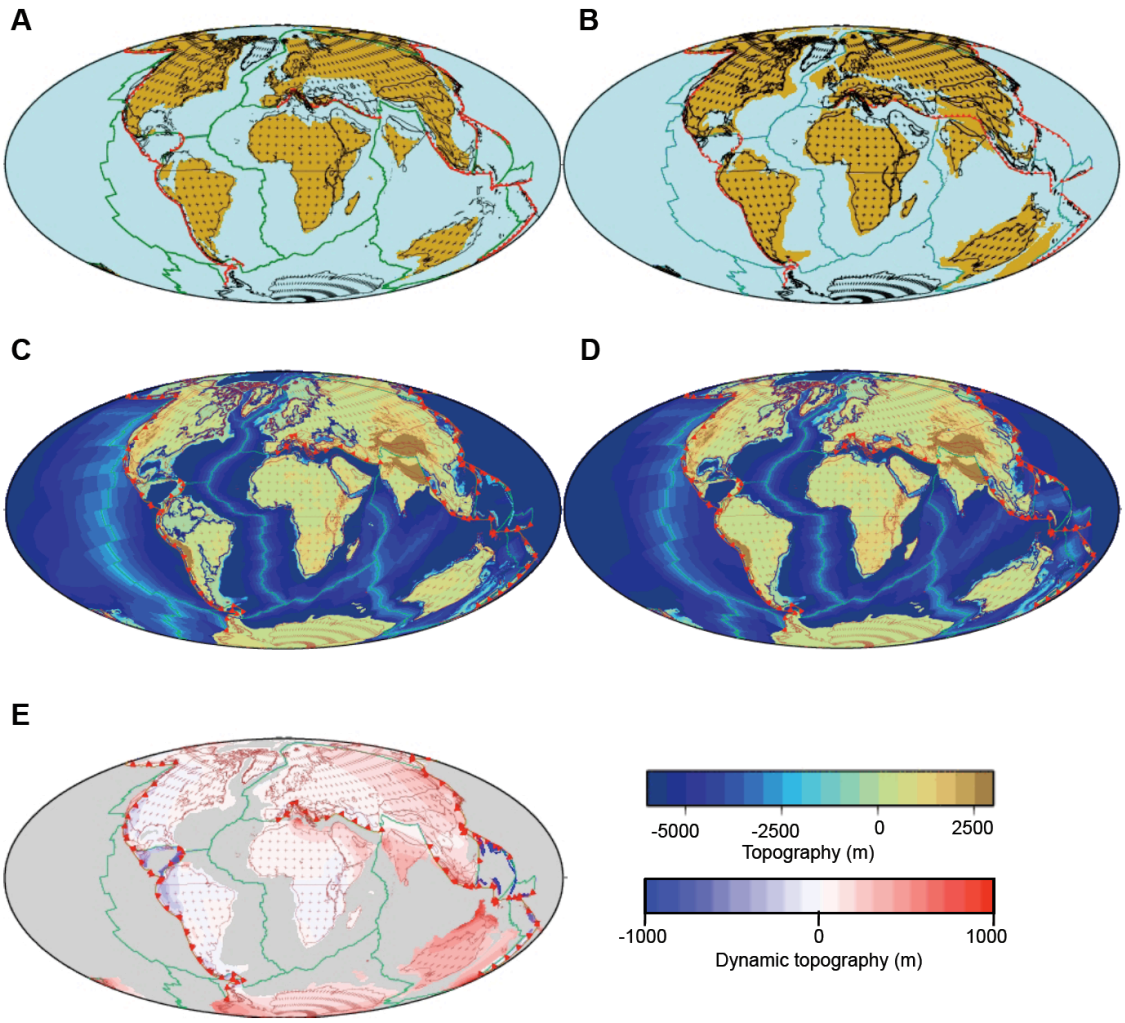

Figure 6.8. 30 Ma global sea-level predictions. (A-B) Paleogeographic reconstructions at 30 Ma (A) [*Smith et al.*, 1994] and 35 Ma (B) [*Blakey*, 2010]. (C) 80 Ma DYN-OFA flooding predictions accounting for changing age of the sea-floor, dynamic topography and geoid and using model M3 (Table 2). (D) 80 Ma OFA flooding predictions accounting only for changing age of sea-floor using half-space model without flattening[*Parsons and Sclater*, 1977]. (E) Difference between dynamic topography in past (30 Ma) and present-day predicted dynamic topography for model M3.

6.4.2.2. Africa and Arabia

Major Late Cretaceous to mid-Eocene transgressions are known from the development of carbonate platforms in northern and central Africa and Arabia [*Guiraud et al.,* 2005]. The relative sea-level change inferred by paleogeography [*Guiraud et al.*, 2005] shows continuous flooding of northernmost Africa and east Arabia, and shifting pattern of marine transgression and regression in the north African interior during the Late Cretaceous (Fig. 6.4B). DEMs predict long-wavelength dynamic subsidence of north and west Africa and Arabia (Fig. 6.4B, Table 6.2), having larger amplitudes for models with the lower average viscosity ratio of 1:20 between the transition zone and lower mantle (Fig. 6.4B; model M1). For model M1, dynamic subsidence is concentrated in three regions: central west Africa, northeast Africa and Arabia, broadly equivalent to inferred marine transgression (Fig. 6.4B). The dynamic subsidence results from the combined effect of overall northward mantle flow of large positively buoyant lower mantle structures and isolated negatively buoyant structures in the uppermost lower mantle below the central part of west Africa. The complex inundation patterns in the interior of north and west Africa are not predicted by the dynamic models. This is expected as African intracontinental seas developed in response to NW-SE to N-S trending intra-continental rifting [*Guiraud et al.*, 2005], ignored in the DEMs. The relation between geologically inferred and predicted vertical motions indicate that dynamic topography is a secondary factor controlling regional sea level here, and that other effects, such as eustatic changes due to changing age of sea floor and/or

rift tectonics [*Guiraud et al.*, 2005], play a more important role.

From the Late Eocene to Late Miocene, there is a pronounced transgression in eastern Arabia, while the eastern parts of north Africa margin remained continuously flooded (Fig. 6.5B) [*Guiraud et al.*, 2005], coincident with an overall fall in global sea level, empirically suggesting sea-level controls beyond eustasy. DEMs show overall dynamic subsidence in the last 40 million years (Fig. 6.4B, Table 6.2) in the regions of eastern north Africa and Arabia. The proposed subsidence and Cenozoic tilt of the Arabian platform toward the northeast develop as a combined effect: (1) increasing negative dynamic topography in the Alpine Tethys region from the increasing age of the reconstructed sea-floor from Late Cretaceous (Fig. 6.1); and (2) northeastward movement of Arabia toward and over a high seismic-velocity anomaly presently located between 300 and 800 km below easternmost Arabia and Persian Gulf, and (3) overall uplift of east Africa and Red Sea due to mantle upwelling associated with the African superplume [*Daradich et al.,* 2003; *Lithgow-Bertelloni and Silver*, 1998].

Since the Eocene, substantial uplift of eastern and southern Africa is predicted with models that have a smaller ratio between the transition zone and lower mantle viscosity (Fig. 6.4B - model M1; Fig. A2.2), related to upwelling of low-density material in the lower mantle below Africa (e.g., *Gurnis et al. [2000a]; Lithgow-Bertelloni and Silver* [1998]). Uplift of eastern Africa occurs continuously from the Late Eocene to present-day (Fig. A2.2), and the uplift in South Africa largely develops in the last 20 Ma. The modeled southward progression of the African uplift

is consistent with geologic studies that suggest that southern Africa experienced Miocene uplift [*Partridge and Maud,* 1987], while uplift and rifting in east Africa initiated earlier, between 20 and 30 Ma [*Burke*, 1996].

The Mesozoic and Cenozoic sedimentary sequences of Africa and Arabia consist of a succession of depositional cycles thought to be controlled by a combination of eustasy and regional tectonics [*Guiraud et al.* 2005]. Flooding for the entire period since Late Cretaceous is underpredicted using both OFA and DYN-OFA calculations (Fig. 6.6-6.8), which we think is at least partially a result of significant change in continental isostatic topography, which is not accounted for by our methodology, as overall uplift of Africa occurs at least since Eocene [*Bond,* 1979; *Gurnis et al.*, 2000a]. The onset of basin inversion and folding, related to the collision of African-Arabian and Eurasian plates initiated in the Late Santonian, affecting both northern African-Arabian plate margin and central African rifts [*Guiraud and Bosworth,* 1997; *Guiraud et al.,* 2005]. A brief compressional phase around the end of Cretaceous and major plate-scale compression in the early Late Eocene [*Guiraud et al.*, 2005] may have both strongly affected development of topography in the region. As the flooding predictions are complicated by unknown isostatic changes, we cannot speculate further on the relative importance of sea-level change factors for north Africa (Table 6.3).

6.4.2.3. Eurasia

In western Siberia and the Alpine Tethys region, there was transgression in the

Cretaceous (Fig. 6.4C) followed by overall regression in the Cenozoic (Fig. 6.5C), equivalent to expected global sea-level trends. Cretaceous differential dynamic topography (Fig. 6.4C) ranges from subsidence on order of 100-200 m (model M1) to neutral values (model M6) over a large portion of Eurasia, suggesting absence or little dynamic control on vertical motions (Table 6.2). Similar to the observed trends, the Alpine Tethys region is predicted to have high-amplitude dynamic subsidence (Fig. 6.4C), related to the increasing age of subducted oceanic lithosphere (Fig. 6.1). The region of southeast and east Asia is predicted to experience overall uplift, related to a decreasing age of the subducted oceanic lithosphere in the east and closing of the easternmost part of Tethys sea by early Cenozoic in the south (Fig. 6.1). For margin in eastern Asia there is the eventual total consumption of the Izanagi plate by 60 Ma (Fig. 6.1) [*Gurnis et al.*, 2010], resulting in progressive subduction of younger seafloor. During the Cenozoic, models predict subsidence in the east and southeast Asia and Alpine Tethys region (Fig. 6.5C), related to increasing age of subducted oceanic lithosphere (Fig. 6.1).

In terms of predicted sea level, OFA models predict well the observed patterns of flooding (Fig. 6.6-6.8, Table 6.3), and the introduction of dynamic effects in DYN-OFA models does not strongly perturb the inundation. This leads us to suggest that mantle dynamics is secondary in controlling platform flooding (Table 6.3), with a possible exception of the Alpine Tethys region.

However, more recent geomorphic indicators might indicate a present-day influence by mantle dynamics in Siberia. Analysis of regional incision and lateral shifts of

rivers in the West Siberian basin indicate that it is currently tilting over a long wavelength *[Allen and Davies,* 2007]. The tilting is generally down to the east, away from the Urals and central Asian mountains, towards the Siberian craton. There are significant drainage shifts in the river systems of the Yenisei, Ob', and Irtysh caused by this long-wavelength tilt of the West Siberian basin and surroundings [*Allen and Davies*, 2007]. Subtle faulting of the basement, located under the thick basin fill of Mesozoic and Lower Cenozoic sediments, has been proposed as a cause of this long-wavelength deformation [*Allen and Davies*, 2007], speculated to potentially be a far-field effect of the India-Eurasia collision [*Allen and Davies*, 2007]. The hybrid models predict overall increasing dynamic subsidence in the general west-to-east direction (Fig. 6.9) for all models, with the total amplitude dependent on the tomography and viscosity. The gradient of differential dynamic topography has the same direction as the inferred direction of tilting from geomorphic analysis [*Allen and Davies*, 2007] (Fig. 6.9C), and we propose that it is related to dynamic effects of mantle convection. Two structures in the lower mantle (Fig. 6.9C) cause the increasing dynamic subsidence and tilting of the Western Siberian basin from west to east. A warm upwelling structure is located on the western edge of the basin, causing it to be dynamically higher than the eastern edge of the basin, which is associated with a large cold mantle downwelling located in the lower mantle.

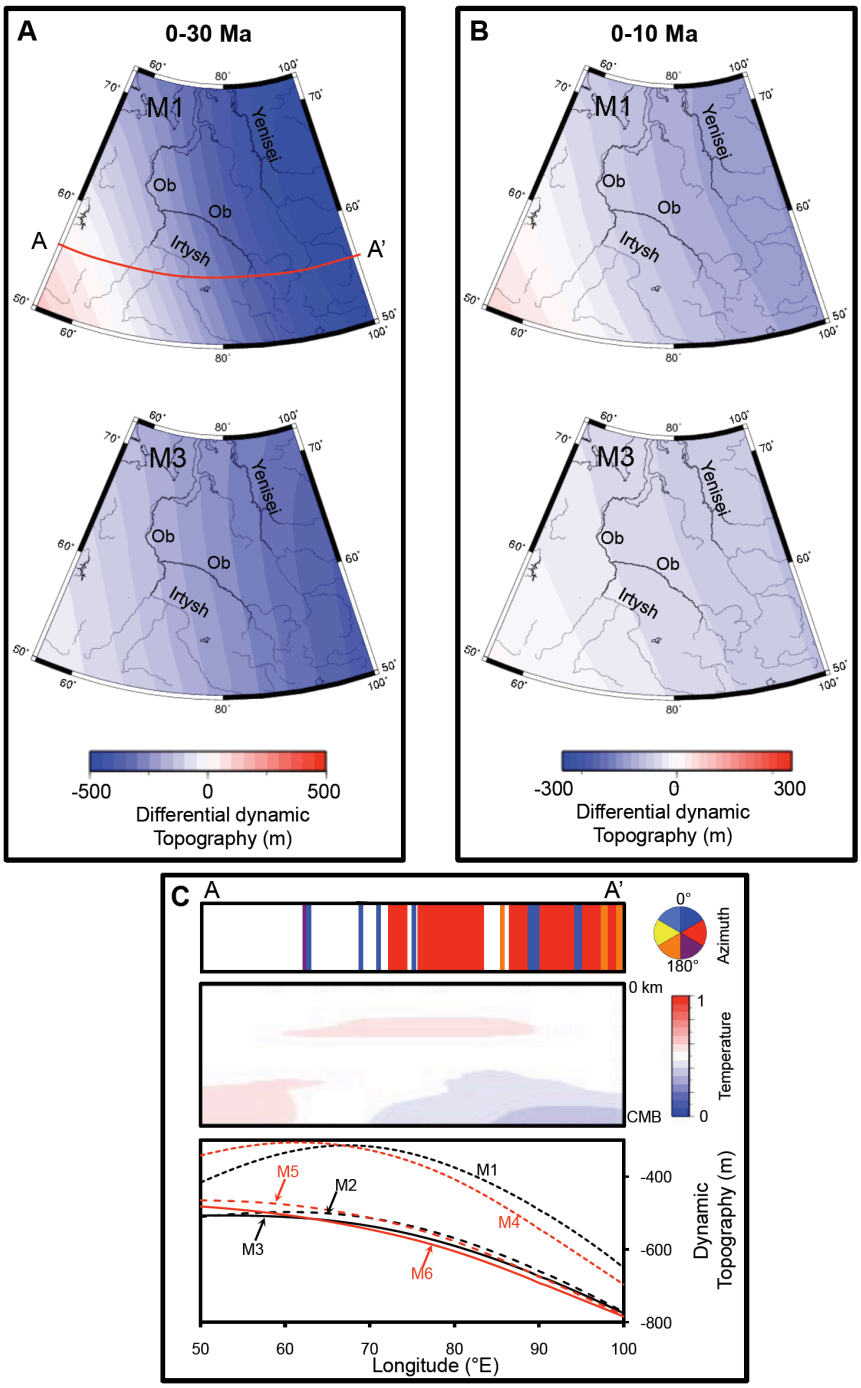

Figure 6.9. Inferred tilting of the Western Siberia basin based on differential dynamic tomography. A-B) Differential dynamic topography for models M1 and M3 in the period 0-30 Ma (A) and 0-10 Ma (B); (C) E-W cross-section (location shown on (A)) showing dynamic topography trends for models M1-M6 (bottom panel), thermal buoyancy field (middle panel) and drainage shift azimuth directions [*Allen and Davies,* 2007] (top panel, azimuth is shown in 60° bins with respect to north).

6.4.2.4. Southeast Asia

The Sundaland core was subaerially exposed during the Late Oligocene but was significantly flooded by the Middle Miocene [*Hall and Morley*, 2004] (Fig. 6.5D), concurrent with overall fall of eustatic sea level, suggesting control beyond eustasy. DEMs predict overall dynamic subsidence within the southern portion of Sundaland and Borneo (Fig. 6.5D, Table 6.2). A large, fast seismic-velocity anomaly exists below southeast Asia between 400 and 1200 km [*Masters et al.,* 2000; *Ritsema et al.,* 2004]. As the mantle flow is reversed in SBI, this anomaly rises upward, with a large portion within the upper mantle in the Eocene, resulting in predicted dynamic subsidence. Integrated forward, DEMs suggest that southeast Asia experienced an event similar to a mantle avalanche, when a significant portion of subducting slabs penetrated into lower mantle, resulting in a significantly increased dynamic topography low, potentially causing observed marine transgression. The predicted amplitudes of subsidence are dependent on tomography and viscosity, and have amplitudes up to 500 m within 1500 km of subduction zones (Fig. 6.5D), while higher subsidence amplitudes are predicted along the subduction zone itself. The wavelength of predicted dynamic subsidence is much larger than that associated with the anomalous Sundaland basins, that have relatively small widths and post-rift sedimentary sequences with thickness up to 12 km of [*Hall and Morley, 2004; Morley and Westaway,* 2006], so that processes beyond simple rifting must be invoked to explain their formation. The amplitude of predicted dynamic subsidence in the Sundaland interior (Fig. 6.5D) has a similar magnitude as dynamic subsidence

estimated based on borehole subsidence in Southeast Asia [*Wheeler and White,* 2002], suggesting that dynamic topography might have an important influence on subsidence and overall flooding during the Neogene. The zone of predicted dynamic subsidence is relatively well correlated with the zone of inferred Sundaland flooding. However, we predict that Borneo and Java subsided, opposite to their inferred trends, which suggests that vertical motions are controlled by more regional tectonics in this region. We propose that dynamic subsidence between 30 Ma and 10 Ma might be contributing to overall platform drowning between Late Oligocene and Middle Miocene.

6.4.2.5. South America

In South America, a north-south trending interior seaway developed between 90 and 50 Ma (Fig. 6.4D) with relative stability of the inundated region in the early Cenozoic [*Blakey,* 2010]. DEMs predict in the Late Cretaceous a region of dynamic subsidence with amplitudes from 100-500 m located in western South America (Fig. 6.4D, Table 6.2), with a wavelength larger than inferred paleogeographically. Although the development of the South America interior seaway has been previously related to flexural loading by the Andes [*Hoorn et al.,* 1995], we postulate that there may a component due to increasing dynamic topography (Fig. 6.6D).

Global paleogeographic reconstructions during the Cenozoic imply relatively isolated regions of vertical motions in the north and northeast (Fig. 6.5E), with most

of South America being stable. However, more regionally focused studies indicate that central Patagonia has been experiencing Neogene uplift [*Guillaume et al.,* 2009], and that the interior Pebas sea developed in the Miocene [*Hoorn et al.,* 1995; *Shepard et al.,* 2010] (Fig. 6.5D). DEMs indicate overall Neogene uplift of Patagonia, concentrated in the Central Patagonian Basin in the last 20 million years (Fig. 6.5D, Table 6.2). From the Cretaceous to Cenozoic, subsidence migrates eastward in the plate frame and is concentrated in the northern part of central South America in the last 20 Ma for models with a lower viscosity ratio between transition zone and lower mantle (Fig. 6.5D; Model M1). Continuous dynamic uplift of the Andes and western South America emerge from the models for the last 20 Ma (Fig. 6.5D, Table 6.2).

The observed pattern of eastward migration of subsidence from the Late Cretaceous to the present is related to the geometry of the subducting Farallon (Nazca slab). Presently, the slab is imaged as a continuous structure in seismic tomography up to mid mantle depths under the whole of South America. As the plate motions and mantle flow are reversed in an SBI from 0 Ma to Late Cretaceous, the high-density material moves upward, and it is located under the western South America in Late Cretaceous, which causes subsidence. The modeled pattern of vertical motions associated with the subducting slab below South America is equivalent to the scenario described for North America.

Late Cretaceous and Paleocene flooding are over predicted, caused by relatively low isostatic topography of South America in the flooded regions (Fig. 6.6-6.7). This

might imply that isostatic topography of South America has changed since Late Cretaceous, and that the continent has experienced overall subsidence. This putative subsidence could be attributed to active subduction, which creates a progressive dynamic topography low in South America (Fig. A2.1). Flooding at 30 Ma is best predicted by OFA models (Fig. 6.8), while inclusion of dynamic effects in DYN-OFA models over predicts flooding. However, if more regional reconstructions (e.g., *Hoorn* [1996]) including those that include the interior Pebas Sea are taken into account, than the DYN-OFA predictions yield a better match to observations. The dynamics of Farallon (more recently Nazca) plate subduction might have controlled the Miocene switch in the direction of the Amazon river at 11 Ma [*Shepard et al.,* 2010]. A similar outcome emerges from our DEMs, but more detailed stratigraphic data and paleogeographic information are needed to clarify the link.

6.4.2.6. Australia

Australia was significantly more subaerial during the Cretaceous than now, remaining high from Late Cretaceous until early Cenozoic, with uplift and subsidence limited to marginal areas (Fig. 6.4E). The models have overall neutral to positive dynamic topography change from 80 to 60 Ma (Fig. 6.4E). Modeled dynamic uplift is consistent with the movement of Australia away from a subducted Gondwanaland slab, as it was previously proposed [*Gurnis et al.,* 2000b; *Gurnis et al.,* 1998]. Australia experienced overall marine transgression over a large portion of the Cenozoic (Fig. 6.5F), suggesting a control beyond eustasy. Dynamic models

predict overall dynamic subsidence over the Cenozoic (Fig. 6.5F, Table 6.2), increasing from S-SW to N-NE, causing an overall tilt of Australia. The Cenozoic tilt has been inferred from detailed study of paleoshorelines [*DiCaprio et al.,* 2009*; Sandiford*, 2007], and was also previously attributed to the dynamic topography and geoid [*Sandiford*, 2007] and dynamic topography low due to developing subduction zones toward north and east [*DiCaprio et al., 2009; DiCaprio et al.,* 2010]. DEMs supports findings of [*DiCaprio et al.*, 2009b; *DiCaprio et al.*, 2010], showing dynamic subsidence due to development of subduction zones in the surrounding regions. In terms of prediction of sea level in Late Cretaceous and early Cenozoic (Fig. 6.6-6.7), DYN-OFA models yield predictions more similar to observations, suggesting that dynamics plays an important role in controlling regional sea level in Australia (Table 6.3).

6.4.3. Global sea-level estimates

With the volume of ocean water assumed constant over millions of years, global sea level results from a change of: ocean bathymetry due to variations in ocean floor age, dynamic topography in oceanic and flooded continental areas, emplacement of oceanic plateaus, and sedimentation. Predicted global sea level shows an overall decrease from the Late Cretaceous to the present, with a maximum at 80 Ma (Fig. 6.10), similar to previous studies (Fig. 6.10C). The predicted sea-level fall from changing ocean-floor age varies significantly between 304 m and 528 m for different cooling models (Fig. 6.10A); a half-space without flattening (OFA-HS) gives the

largest prediction, while with flattening (OFA-GDH) gives the smallest. The sea-level decrease from OFA is caused by deepening of bathymetry from the aging sea floor from Late Cretaceous to present-day (Fig. 6.1), as discussed previously (e.g., *Kominz*, [1984]; *Kominz et al.* [2008]; *Müller et al.* [2008a]). In isolation, changing dynamic topography in oceanic regions causes a sea-level rise since the Late Cretaceous with amplitudes between 100 m and 200 m (Fig. 6.10A), In general, higher sea-level estimates correspond to the models with lower average viscosity ratios, related to higher overall amplitudes of dynamic topography in these models (Fig. A2.1). The contribution of dynamic topography in the flooded continental areas is much smaller than in the oceanic regions, having maximum amplitudes from -10 m to 80 m (Fig. 6.10A) of sea-level rise. The amplitudes of dynamic topography contributions are the largest at 70 Ma, and they significantly decrease during the Cenozoic (Fig. 6.10A). The dynamic topography contribution to global sea level in oceanic regions is largely driven by positive dynamic topography from low-density mantle upwellings. As low-density anomalies rise from the Late Cretaceous to present, the amplitude of dynamic topography increases, resulting in sea-level rise, which offsets overall sea-level fall associated with the increasing age of seafloor (Fig. 6.10A). The contribution of high-density downwelling anomalies in the oceanic regions to overall sea-level change is less significant, as the regions of dynamic topography lows in the oceans are much more spatially limited (Fig. A2.1). The contribution of dynamic topography in the flooded continental regions is largely driven by dynamic topography lows, which have overall increasing mean amplitude (Fig. 6.10A). The contribution of the geoid to global-sea level is much smaller than

that from dynamic topography (Fig. 6.10A), as the ratio between geoid and topography is small (Fig. 6.2).

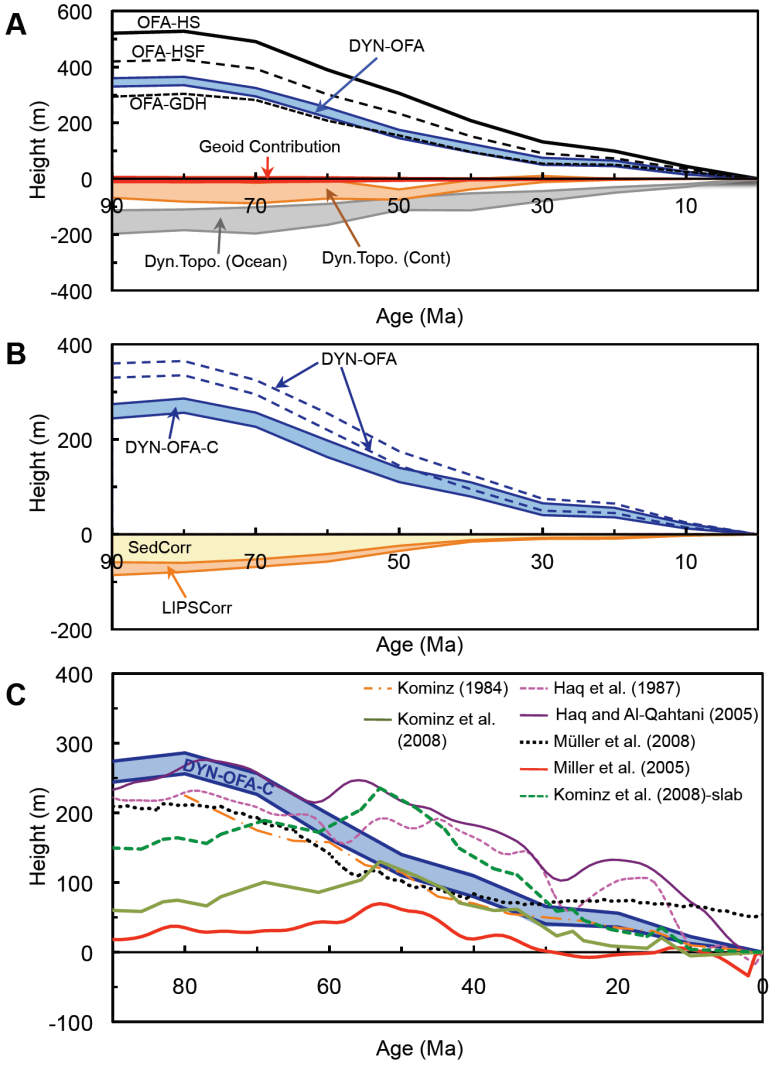

Figure 6.10. Global sea-level predictions. (A) Predictions accounting for changing age of sea floor using half-space (OFA-HS), half-space model with flattening (OFA-HSF), GDH-1 model (OFA-GDH), and DYN-OFA models. Blue area shows range of sea level values estimated from DYN-OFA models; gray, orange and red areas range of dynamic topography in oceanic areas, dynamic topography in flooded continental areas, and geoid contribution to global sea level, respectively. (B) Final predictions of sea level from DYN-OFA models (blue area; DYN-OFA-C accounting for corrections due to sedimentations (yellow area; SedCorr) and emplacement of large igneous provinces (orange area; LIPSCorr). (C) Comparison between final prediction of sea level from DYN-OFA-C models (blue area) and previously published sea-level curves.

Therefore, the sea-level estimates for DYN-OFA models, before accounting for sedimentation and oceanic plateau emplacement, have maximum amplitudes at 80 Ma between 330 m and 365 m (Fig. 6.10A) for the six DEMs. The predicted range of dynamic sea level for DYN-OFA models lies between the predictions for the two cooling models that include flattening (Fig. 6.10A; OFA-HSF, OFA-GDH). This is not unexpected if dynamic topography is the ultimate cause for the flattening of old seafloor, empirically included in the age-to-depth relationships for OFA-HSF and OFA-GDH. Sedimentation and emplacement of large igneous provinces result in overall sea-level rise from Late Cretaceous to present [*Müller et al.,* 2008b]. Maximum amplitudes of sea-level change due to sedimentation and igneous provinces are much smaller at 60 m and 27 m, respectively, so that the combined effect of all of the processes still results in an overall fall with maximum amplitude of up to 286 m since the Late Cretaceous (Fig. 6.10B; DYN-OFA-C). DYN-OFA-C global sea level is within the range of those previously proposed (Fig. 6.10C).

6.5. Discussion

We use DEMs to better understand regional and global sea level from the Late Cretaceous. We find that oceanic regions on average have a positive dynamic topography, which is increasing from the Late Cretaceous to the present due to overall rise of upwelling low-density anomalies, resulting in a sea-level rise with the estimated amplitude varying between 100-200 m in the last 90 Myr (Fig. 6.10). *Conrad and Husson* (2009) use forward convection models to estimate Cenozoic sea-

level change due to seafloor dynamic topography of 90±20 m, which is similar to the estimated amplitudes in DEMs of 90-140 m of sea-level change in last 60 Myr. We also find that dynamic topography in flooded continental areas contributes to sea-level change by introducing up to 80 m of sea-level rise since the Late Cretaceous (Fig. 6.10). *Conrad and Husson* [2009] also find that dynamic topography in continental areas has an effect on sea level, but that its rate of change is more than three times smaller than the one due to oceanic dynamic topography. The sea-level rise due to dynamic topography, along with the rise due emplacement of oceanic plateaus and sedimentation, partially offsets the larger amplitude sea-level fall due to increases in OFA (Fig. 6.10). The overall fall of the sea level due to change in OFA and spreading-ridge crustal production are largely driven by changes in the Pacific ocean, as the largest drop in the global crustal production of approximately 50% occurs between 65 and 60 Ma due to subduction of the Izanagi-Pacific spreading ridge [*Müller et al.*, 2008b](Fig. 6.1), followed by subsequent ridge subduction beneath the Americas [*Müller et al.*, 2008b].

When calculating sea-level amplitudes, we prefer to use the half-space cooling model so as not to double count the effect of sea floor flattening [*Kido and Seno,* 1994], which can arise when dynamic topography is considered from a mantle flow model [*Müller et al.*, 2008b]. However, if we implemented cooling models that include flattening (e.g., OFA-HSF and OFA-GDH1), the final sea level would have the same trend, but with a significantly smaller amplitude (Fig. 6.10A). We predict the total global sea-level fall from the Late Cretaceous, with maximum amplitude of up to 286m reached at 80 Ma. The Late Cretaceous sea levels are on the high end of

previous estimates (Fig. 6.10C) [*Haq et al.*, 1987; *Haq and Al-Qahtani*, 2005; *Kominz*, 1984; *Kominz et al.*, 2008; *Miller et al.*, 2005; *Müller et al.*, 2008b; *Watts and Steckler*, 1979], with the values being similar to the ones inferred by *Haq and Al-Qahtani* (2005). During the Cenozoic, the proposed sea levels are generally lower than ones derived using global correlation of stratigraphic sequences [*Haq and Al-Qahtani*, 2005; *Watts and Steckler*, 1979], but higher than the ones derived based on the backstripping of sedimentary sections at five boreholes located on the New Jersey coastal plain [*Miller et al.,* 2005], and within the range of other studies (Fig. 6.10C). Our study demonstrates the importance of accounting for effects of dynamic topography when calculating global sea level, but the actual amplitudes should be more constrained when more comprehensive stratigraphic and geologic constraints are used in the future.

While positive dynamic topography associated with mantle upwellings represents the main dynamic factor controlling global sea level, the dynamic topography associated with subducting or previously subducted slabs is also an important factor controls the pattern of continental flooding and relative vertical motion. We find that the Farallon slab in North America creates a dynamic topography low that controlling Cretaceous flooding and subsidence in the WIS, similar to previous inverse models [*Liu et al.*, 2008; *Spasojevic et al.,* 2009]. As North America moves westward and the Farallon slab sinks into lower mantle during Cenozoic, the western interior experiences dynamic uplift and eastern North America experiences overall subsidence. The Farallon and Nazca plates continuously subduct in South America, contributing to interior flooding developed from 90 to 50 Ma, and

potentially contributing to a Miocene switch in the direction of drainage from a predominantly northward direction to formation of the eastward-draining Amazon river [*Shepard et al.,* 2010]. Subduction in the Alpine Tethys region causes overall subsidence and flooding of the Mediterranean region, and Cenozoic dynamic subsidence and flooding of north Africa and Arabia. A mantle-avalanche-type event in the southeast Asia between Late Oligocene and Miocene resulted in dynamic subsidence and potential drowning of Sundaland. Development of subduction zones north and east from Australia contributes to overall tilting toward N-NE that potentially explain discrepancies between Australian and global sea level during the Cenozoic, as previously found [*DiCaprio et al.*, 2009a; *DiCaprio et al.,* 2010].

In the post-Mesozoic, we find that mantle upwelling anomalies have had a relatively limited effect on pattern of the large-scale vertical motion of continents and regional sea level for most continents except Africa. The African superplume has caused uplift in eastern and southern Africa since the Eocene, and it contributes to the Cenozoic tilting down to NNE of Arabia. Mid and lower mantle upwelling located to the west of the Siberian basin, and adjacent to the east Siberia lower mantle downwelling, resulting in W-E tilting of Siberia that potentially results in shifting of drainage patterns in this region.

Sea-level predictions are affected by a number of underlying assumptions: (1) time-invariant isostatic topography; (2) the neglect of continental margin extension; and (3) constant ocean volume used in sea-level calculations. First, since paleoelevation represents one of the most difficult variables to reconstruct from the geologic

record [*Garzione et al.,* 2008], and detailed maps of the past global topography have yet to be assembled, we use present-day topography but rotated with plate motions and corrected for dynamic topography. As crustal columns experienced significant changes due to orogeny, such as the Laramide, the Andean, Alpine, and Himalayan orogenies [*English and Johnston*, 2004; *Ghosh et al.*, 2006; *Saleeby*, 2003; *Spencer*, 1974], the quality of sea-level predictions is significantly affected in orogenic regions. Second, because continental margin extension has been estimated to results in about 20 m of sea-level change since the beginning of Pangea breakup [*Kirschner et al.,* 2010], significantly smaller than overall sea-level change (Fig. 6.10), its neglect is reasonable. Third, we assume constant water volume, as we examine sea-level changes at time scales greater than 1 Myr, which is longer than ocean volume fluctuations from glacial cycles occurring on time scales of hundreds of thousand of years or shorter [*Kominz,* 2001].

The main limitations of current method are: use of a single average vertical viscosity structure and seismic velocity-to-density scaling; treatment of subduction zones; use of one paleogeographic reconstruction; and limited assimilation of stratigraphic data. A significant uncertainty remains regarding the viscosity profile of the mantle, with suggestions that significant differences might exist between viscosity structures in different regions (e.g., *Liu et al.* [2008]; *Schellart et al.* [2009]; *Spasojevic et al.* [2010a]), or that the mantle on average might have the same vertical viscosity profile (e.g., *van der Meer et al.* [2010]). A single seismic velocity-to-density scaling, devised from the fit to global geoid [*Spasojevic et al.,* 2010] is used for all models, although it was suggested that 3D velocity-to-density scaling

model, which might differ for upwelling and downwelling anomalies [*Simmons et al.,* 2009; *Forte,* 2007] might be more appropriate. As both viscosity structure and velocity-to-density scaling influence dynamic topography, and in turn sea-level estimates, in the future it would be important to test sensitivity of regional and global sea level to variations of these parameters. Definition of subduction zones in the models can be improved by introducing much higher resolution, variable viscosity slabs, and surrounding mantle wedges, possibly implementing methods at ultra high resolution (1 km where needed) [*Stadler et al.,* 2010], and introducing more realistic treatment of diffusion in an adjoint solution to the equations instead of current SBI [*Liu and Gurnis,* 2008]. The importance of strong viscosity variations has been demonstrated in regional models of the Tonga-Kermadec and Aleutian subduction zones [*Billen et al.*, 2003; *Billen and Gurnis,* 2003], which show that significant lateral viscosity variations are required between upper mantle slabs and adjacent mantles wedges to match the geoid, dynamic topography, and stress patterns in subduction zones; while strong slabs also give rise to a better match to observed, present-day plate motions [*Stadler et al.,* 2010]. It has been shown that use of different reconstructions in the west Pacific substantially affects sea-level estimates since the Cenozoic [*Xu et al.,* 2006], in the future we can test alternative paleogeographic reconstructions and their effect on patterns of vertical motions and relative and global sea level. Inclusion of more stratigraphic data, including more comprehensive borehole data, sediment isopach maps, and detailed regional paleoshoreline reconstructions, might impose better constraints on the history of vertical motion of continents and enable us to infer mantle viscosity structure on a

finer scale.

6.6. Conclusions

We present results of dynamic earth models that combine inverse and forward methods for solving for mantle convection, and assimilate plate tectonic reconstructions into mantle convection models with vertically and laterally variable viscosity. We self-consistently account for changing age of seafloor, dynamic topography, and the geoid, with the goal to better understand vertical motion of continents, and regional and global sea level.

We find that both changing age of ocean floor and dynamic topography represent important factors controlling sea level. Predicted sea level shows an overall fall from the Late Cretaceous to the present, with maximum amplitude of 286 m at 80 Ma. The largest contribution to the sea-level fall comes from the reduced oceanic crust production from Late Cretaceous to present, inferred from ocean age grids. Dynamic topography in oceans and flooded continental regions result in sea-level rise with maximum amplitudes varying between 100-200 m, and -10-80 m, respectively; reducing overall amplitude of sea-level fall inferred from age grids. Movement of continents with respect to large-scale dynamic topography causes dynamic subsidence and uplift of continents, and controls regional sea level for North America and South America from Late Cretaceous to present, Australia during Cenozoic, North Africa and Arabia since the Eocene. East and South Africa uplift

dynamically in the last 20-30 million years, while Siberia and Australia experience Cenozoic tilting.

References

Allen, M. B., and C. E. Davies (2007), Unstable Asia: Active deformation of Siberia revealed by drainage shifts, *Basin Research*, *19*, 379–392.

Billen, M. I., and M. Gurnis (2001), A low viscosity wedge in subduction zones, *Earth and Planetary Science Letters*, *193*(1–2), 227–236.

Billen, M. I., M. Gurnis, and M. Simons (2003), Multiscale dynamics of the Tonga-Kermadec subduction zone, *Geophysical Journal International*, *153*(2), 359–388.

Bird, P. (1998), Kinematic history of the Laramide orogeny in latitudes 35 degrees-49 degrees N, western United States, *Tectonics*, *17*(5), 780–801.

Blakey, R. (2008), Gondwana paleogeography from assembly to breakup—A 500 m.y. odyssey, in *Resolving the Late Paleozoic Ice Age in Time and Space*, edited by C. R. Fielding, et al., 1–28.

Blakey, R. (2010), Global palogeographic maps (http://jan.ucc.nau.edu/~rcb7/globaltext2.html), Last access March 2010.

Bond, G. (1976), Evidence for continental subsidence in North America during Late Cretaceous global submergence, *Geology*, *4*(9), 557–560.

Bond, G. C. (1979), Evidence for some uplifts of large magnitude in continental platforms, *Tectonophysics*, *61*(1-3), 285–305.

Boyden, J. A., R. D. Müller, M. Gurnis, T. H. Torsvik, J. A. Clark, M. Turner, H. Ivey-Law, R. J. Watson, and J. S. Cannon (2010), Next-generation plate-tectonic reconstructions using GPlates, in *Geoinformatics: Cyberinfrastructure for the Solid Earth Sciences*, edited by G. R. Keller and C. Baru, submitted, Cambridge University

Press.

Burgess, P. M., M. Gurnis, and L. Moresi (1997), Formation of sequences in the cratonic interior of North America by interaction between mantle, eustatic, and stratigraphic processes, *Geological Society of America Bulletin*, *109*(12), 1515–1535.

Burke, K. (1996), The African plate, *South African Journal of Geology*, *99*, 341–409.

Conrad, C. P., and M. Gurnis (2003), Seismic tomography, surface uplift, and the breakup of Gondwanaland: Integrating mantle convection backwards in time, *Geochemistry Geophysics Geosystems*, *4*(3), 1031, doi:10.1029/2001GC000299.

Conrad, C. P., and L. Husson (2009), Influence of dynamic topography on sea level and its rate of change, *Lithosphere*, *1*(2), 110–120.

Cook, T. D., and A. W. Bally (1975), *Stratigraphic atlas of North and Central America*, 272 pp., Princeton University Press, Princeton, N.J.

Daradich, A., J. X. Mitrovica, R. N. Pysklywec, S. D. Willett, and A. M. Forte (2003), Mantle flow, dynamic topography, and rift-flank uplift of Arabia, *Geology*, *31*(10), 901–904.

DiCaprio, L., M. Gurnis, and R. D. Muller (2009a), Long-wavelength tilting of the Australian continent since the Late Cretaceous, *Earth and Planetary Science Letters*, *278*(3–4), 175–185.

DiCaprio, L., M. Gurnis, and R. D. Muller (2009b), Long-wavelength tilting of the Australian continent since the late Cretaceous, *Earth and Planetary Science Letters*, 175–185.

DiCaprio, L., M. Gurnis, R. D. Müller, and E. Tan (2010), Mantle dynamics of

continent-wide Cenozoic subsidence and tilting of Australia, *Geophysical Research Letters*, in review.

English, J. M., and S. T. Johnston (2004), The Laramide orogeny: What were the driving forces?, *International Geology Review*, *46*(9), 833–838.

Forte, A. M. (2007), Constraints on seismic models from other disciplines: Implications for mantle dynamics and composition, in *Treatise of Geophysics*, edited by B. Romanowicz and A. M. Dziewonski, 805–854.

Garzione, C. N., G. D. Hoke, J. C. Libarkin, S. Withers, B. MacFadden, J. Eiler, P. Ghosh, and A. Mulch (2008), Rise of the Andes, *Science*, *320*(5881), 1304–1307.

Ghosh, P., C. N. Garzione, and J. M. Eiler (2006), Rapid uplift of the Altiplano revealed through C-13-O-18 bonds in paleosol carbonates, *Science*, *311*(5760), 511–515.

Goes, S., and S. van der Lee (2002), Thermal structure of the North American uppermost mantle inferred from seismic tomography, *Journal of Geophysical Research*, *107*(B3), 2050, doi: 10.1029/2000JB000049

Grand, S. P. (2002), Mantle shear-wave tomography and the fate of subducted slabs, *Philosophical Transactions of the Royal Society of London Series A-Mathematical Physical and Engineering Sciences*, *360*(1800), 2475–2491.

Guillaume, B., J. Martinod, L. Husson, M. Roddaz, and R. Riquelme (2009), Neogene uplift of central eastern Patagonia: Dynamic response to active spreading ridge subduction?, *Tectonics*, *28*, TC2009, doi:10.1029/2008TC002324.

Guiraud, R., and W. Bosworth (1997), Senonian basin inversion and rejuvenation of rifting in Africa and Arabia: synthesis and implications to plate-scale tectonics, *Tectonophysics*, *282*(1–4), 39–82.

Guiraud, R., W. Bosworth, J. Thierry, and A. Delplanque (2005), Phanerozoic geological evolution of Northern and Central Africa: An overview, *Journal of African Earth Sciences*, *43*(1–3), 83–143.

Gurnis, M. (1990), Bounds on global dynamic topography from Phanerozoic flooding of continental platforms, *Nature*, *344*(6268), 754–756.

Gurnis, M. (1993), Phanerozoic marine inundation of continents driven by dynamic topography above subducting slabs, *Nature*, *364*(6438), 589–593.

Gurnis, M., R. Müller, and L. Moresi (1998), Cretaceous Vertical Motion of Australia and the Australian-Antarctic Discordance, *Science*, *279*(5356), 1499–1504.

Gurnis, M., J. Mitrovica, J. Ritsema, and H. van Heijst (2000a), Constraining mantle density structure using geological evidence of surface uplift rates: The case of the African superplume, *Geochemistry, Geophysics, Geosystems*, *1*(7), 1020.

Gurnis, M., L. Moresi, and R. D. Müller (2000b), Models of mantle convection incorporating plate tectonics: The Australian region since the Cretaceous, in *The History and Dynamics of Global Plate Motions*, edited by M. A. Richards, et al., 211–238, American Geophysical Union, Washington, D.C.

Gurnis, M., M. Turner, S. Zahirovic, L. DiCaprio, S. Spasojevic, R. D. Müller, J. Boyden, M. Seton, V. C. Manea, and D. V. Bower (2010), Global Plate Reconstructions with Continuously Closing Plates, *Computers and Geosciences*, in review.

Hager, B. H. (1984), Subducted slabs and the geoid- Constraints on mantle rheology and flow, *Journal of Geophysical Research*, *89*(B7), 6003–6015.

Hall, R., and C. K. Morley (2004), Sundaland basins, in *Continent-Ocean Interactions within East Asian Marginal Seas*, edited by P. E. A. Clift, 55–85, AGU, Washington,

D.C.

Hallam, A. (1992), *Phanerozoic Sea-Level Changes*, 266 pp., Columbia University Press, New York.

Haq, B. U., J. Hardenbol, and P. R. Vail (1987), Chronology of fluctuating sea levels since the Triassic, *Science*, *235*(4793), 1156–1167.

Haq, B. U., and A. M. Al-Qahtani (2005), Phanerozoic cycles of sea-level change on the Arabian Platform, *GeoArabia*, *10*(2), 127–160.

Hays, J. D., and W. C. Pitman (1973), Lithospheric plate motions, sea-level changes and climatic and ecological consequences *Nature*, *246*(5427), 18–22.

Hoorn, C., J. Guerrero, G. A. Sarmiento, and M. A. Lorente (1995), Andean tectonics as a cause for changing drainage patterns in Miocene northern South America *Geology*, *23*(3), 237–240.

Hoorn, C. (1996), Miocene deposits in the Amazonian foreland basin, *Science*, *273*(5271), 122–123.

Jordan, T. H. (1988), Structure and formation of the continental tectonosphere, *Journal of Petrology*, *Special Volume 1*, 11–37.

Kido, M., and T. Seno (1994), Dynamic topography compared with residual depth anomalies in oceans and implications for age-depth curves, *Geophysical Research Letters*, *21*(8), 717–720.

Kirschner, J. P., M. A. Kominz, and K. E. Mwakanyamale (2010), Quantifying extension of passive margins: Implications for sea level change, *Tectonics*, *29*, TC4005.

Kominz, M. A. (1984), Oceanic ridge volumes and sea level change - An error

analysis, in *Interregional Unconformities and Hydrocarbon Accumulation*, edited by J. Schlee, pp. 109–127, American Association of Petroleum Geology Memoir.

Kominz, M. A. (2001), Paleo-oceanography: Variations in Sea Level (MS 255), in *Encyclopedia of Ocean Sciences*, edited by J. Steele, Thorpe, S., Turekian, K., 2605–2613, Academic Press.

Kominz, M. A., J. V. Browning, K. G. Miller, P. J. Sugarman, S. Mizintseva, and C. R. Scotese (2008), Late Cretaceous to Miocene sea-level estimates from the New Jersey and Delaware coastal plain coreholes: An error analysis, *Basin Research*, *20*(2), 211–226.

Langford, R. P., G. E. Wilford, E. M. Truswell, and A. R. Isern (1995), *Palaeogeographic Atlas of Australia – Cainozoic, Cretaceous*, Australian Geological Survey Organisation, Canberra.

Lithgow- Bertelloni, C., and M. Gurnis (1997), Cenozoic subsidence and uplift of continents from time-varying dynamic topography, *Geology*, *25*(8), 735–738.

Lithgow- Bertelloni, C., and P. G. Silver (1998), Dynamic topography, plate driving forces and the African superswell, *Nature*, *395*(6699), 269–272.

Liu, L., S. Spasojević and M. Gurnis (2008), Reconstructing Farallon plate subduction beneath North America back to the Late Cretaceous, *Science, 322,* 934–938, DOI:10.1126/science.1162921, 2008.

Liu, L., M. Gurnis, M. Seton, J. Saleeby, R. D. Müller, and J. M. Jackson (2010), The role of oceanic plateau subduction in the Laramide orogeny, *Nature Geoscience*, *3,* 353–357, doi:10.1038/NGEO829.

Liu, L., and M. Gurnis (2008), Simultaneous inversion of mantle properties and

initial conditions using an adjoint of mantle convection, *Journal of Geophysical Research, 113,* B08405, doi:10.1029/2008JB005594.

Liu, S. F., and D. Nummedal (2004), Late cretaceous subsidence in Wyoming: Quantifying the dynamic component, *Geology*, *32*(5), 397–00.

Masters, G., G. Laske, H. Bolton, and A. Dziewonski (2000), The relative behavior of shear velocity, bulk sound speed, and compressional velocity in the mantle: Implications for chemical and thermal structure, in *Geophysical Monograph Series*, edited by S. Karato, et al., pp. 63–88, American Geophysical Union, Washington DC.

Miller, K. G., M. A. Kominz, J. V. Browning, J. D. Wright, G. S. Mountain, M. E. Katz, P. J. Sugarman, B. S. Cramer, N. Christie-Blick, and S. F. Pekar (2005), The Phanerozoic record of global sea-level change, *Science*, *310*(5752), 1293-1298.

Mitrovica, J. X., and G. T. Jarvis (1985), Surface deflections due to transient subduction in a conventing mantle *Tectonophysics*, *120*(3-4), 211–237.

Mitrovica, J. X., C. Beaumont, and G. T. Jarvis (1989), Tilting of continental interiors by the dynamical effects of subduction, *Tectonics*, *8*(5), 1079–1094.

Mitrovica, J. X., R. N. Pysklywec, C. Beaumont, and A. Rutty (1996), The Devonian to Permian sedimentation of the Russian platform: An example of subduction-controlled long-wavelength tilting of continents, *Journal of Geodynamics*, *22*(1–2), 79–96.

Morley, C. K., and R. Westaway (2006), Subsidence in the super-deep Pattani and Malay basins of Southeast Asia: a coupled model incorporating lower-crustal flow in response to post-rift sediment loading, *Basin Research*, *18*(1), 51–84.

Müller, R. D., W. R. Roest, J. Y. Royer, L. M. Gahagan, and J. G. Sclater (1997), Digital

isochrons of the world's ocean floor, *Journal of Geophysical Research*, *102*(B2), 3211–3214.

Müller, R.D., M. Sdrolias, C. Gaina and W.R. Roest (2008a), Age, spreading rates and spreading asymmetry of the world's ocean crust, *Geochemistry, Geophysics, Geosystems, 9*, Q04006, doi:10.1029/2007GC001743.

Müller, R. D., M. Sdrolias, C. Gaina, B. Steinberger, and C. Heine (2008b), Long-term sea-level fluctuations driven by ocean basin dynamics, *Science*, *319*(5868), 1357–1362.

Parsons, B., and J. G. Sclater (1977), Analysis of variation of ocean-flow bathymetry and heat-flow with age, *Journal of Geophysical Research*, *82*(5), 803–827.

Partridge, T. C., and R. R. Maud (1987), Geomorphic evolution of southern Africa since the Mesozoic, *South African Journal of Geology*, *90*, 179–208.

Richards, M. A., and B. H. Hager (1984), Geoid anomalies in a dynamic Earth, *Journal of Geophysical Research*, *89*(B7), 5987–6002.

Ritsema, J., H. J. van Heijst, and J. H. Woodhouse (2004), Global transition zone tomography*, Journal of Geophysical Research, 109,* B02302, doi: 10.1029/ 2003JB002610.

Saleeby, J. (2003), Segmentation of the Laramide slab - Evidence from the southern Sierra Nevada region, *Geological Society of America Bulletin*, *115*(6), 655–668.

Sandiford, M. (2007), The tilting continent: A new constraint on the dynamic topographic field from Australia, *Earth and Planetary Science Letters, 261*(1–2), 152–163.

Schellart, W. P., B. L. N. Kennett, W. Spakman, and M. Amaru (2009), Plate

reconstructions and tomography reveal a fossil lower mantle slab below the Tasman Sea, *Earth and Planetary Science Letters*, *278*(3–4), 143–151.

Shepard, G. E., R. D. Müller, L. Liu, and M. Gurnis (2010), Miocene Amazon River drainage reversal caused by plate-mantle dynamics, *Nature*, in review.

Simmons, N. A., A. M. Forte, and S. P. Grand (2009), Joint seismic, geodynamic and mineral physical constraints on three-dimensional mantle heterogeneity: Implications for the relative importance of thermal versus compositional heterogeneity, *Geophysical Journal International*, *177*(3), 1284–1304.

Sleep, N. H. (1976), Platform subsidence mechanisms and eustatic sea-level changes *Tectonophysics*, *36*(1–3), 45–56.

Sloss, L. L. (1963), Sequences in the cratonic interior od North America, *Geological Society of America Bulletin*, *74*(2), 93–114.

Sloss, L. L. (1988), Tectonic evolution of the craton in Phanerozoictime, in *Sedimentary Cover—North America Craton*, edited by L. L. Sloss, 22–51, Geological Society of America, Boulder, CO.

Smith, A. G., D. G. Smith, and B. M. Funnel (1994), *Atlas of Mesozoic and Cenozoic coastlines*, Cambridge University Press, New York.

Spasojević, S., L. Liu, M. Gurnis, and R. D. Müller (2008), The case for dynamic subsidence of the United States east coast since the Eocene, *Geophysical Research Letters, 35,* L08305, doi:10.1029/2008GL033511.

Spasojevic, S., L. Liu, and M. Gurnis (2009), Adjoint models of mantle convection with seismic, plate motion and stratigraphic constraints: North America since the

Late Cretaceous, *Geochemistry, Geophysics, Geosystems, 10,* Q05W02, doi:10.1029/2008GC002345.

Spasojevic, S., M. Gurnis, and R. Sutherland (2010a), Inferring mantle properties with an evolving dynamic model of the Antarctica-New Zealand region from the Late Cretaceous, *Journal of Geophysical Research-Solid Earth*, *115*, B05402.

Spasojevic, S., M. Gurnis, and R. Sutherland (2010b), Mantle upwellings above slab graveyards linked to the global geoid lows, *Nature Geoscience*, *3*, 435–438.

Spencer, A. M. (Ed.) (1974), *Mesozoic-Cenozoic orogenic belts*, The Geological Society, London.

Stadler, G., M. Gurnis, C. Burstedde, L. C. Wilcox, L. Alisic, and O. Ghattas (2010), The dynamics of plate tectonics and mantle flow: From local to global scales, *Science*, in press.

Stein, C., and S. Stein (1992), A model for the global variation in oceanic depth and heat flow with lithospheric age, *Nature*, *359*(6391), 123–129.

Sutherland, R., S. Spasojevic, and M. Gurnis (2009), Mantle upwelling after Gondwana subduction death may explain anomalous topography of West Antarctica and subsidence history of eastern New Zealand, *Geology*, *38*(2), 155–158.

Tan, E., E. Choi, P. Thoutireddy, M. Gurnis, and M. Aivazis (2006), GeoFramework: Coupling multiple models of mantle convection within a computational framework, *Geochemistry Geophysics Geosystems, 7, Q06001,* doi:10.1029/2005GC001155.

Tape, C., M. Gurnis, H. Kanamori, and M. Simons (2010), The seismic signature of

nascent to ancient subduction, *manuscript in preparation.*

van der Meer, D. G., W. Spakman, D. J. J. van Hinsbergen, M. L. Amaru, and T. H. Torsvik (2010), Towards absolute plate motions constrained by lower-mantle slab remnants, *Nature Geoscience*, *3*(1), 36–40.

Watts, A. B., and M. S. Steckler (1979), Subsidence and eustasy at the continental margin of eastern North America, in *Deep Drilling Results in the Atlantic Ocean: Continental Margins and Paleoenvironment, Maurice Ewing Ser.*, edited by M. Talwani, Hay, W., Ryan, W.B.F, 218–234, AGU, Washington, D.C. .

Wheeler, P., and N. White (2002), Measuring dynamic topography: An analysis of Southeast Asia, *Tectonics*, *21*(5), 1040, doi:10.1029/2001TC900023

Xu, X. Q., C. Lithgow-Bertelloni, and C. P. Conrad (2006), Global reconstructions of Cenozoic seafloor ages: Implications for bathymetry and sea level, *Earth and Planetary Science Letters*, *243*(3–4), 552–564.

Zhong, S. J., M. T. Zuber, L. Moresi, and M. Gurnis (2000), Role of temperature-dependent viscosity and surface plates in spherical shell models of mantle convection, *Journal of Geophysical Research, 105*(B5), 11063–11082.

Zhong, S. J., A. McNamara, E. Tan, L. Moresi, and M. Gurnis (2008), A benchmark study on mantle convection in a 3-D spherical shell using CitcomS, *Geochemistry Geophysics Geosystems*, *9*(10), Q10017, doi:10.1029/2008GC002048.

Appendix 1

Supplementary material for Chapter 3[1]

A1.1. Methods

We develop instantaneous models of mantle convection using the finite-element code CitcomS version 3.1 [*Tan et al.*, 2006], which solves the equations of mass, momentum, and energy for an incompressible, Newtonian fluid, while making the Boussinesq approximation. We calculate dynamic topography and geoid accounting for the effect of self-gravitation using a no slip surface boundary condition. The background mantle is defined as isothermal with non-dimensional temperature of 0.5, and thermal anomalies are defined with respect to the background mantle by combining seismic tomography in the whole mantle and a synthetic slab model in the upper mantle. Lower mantle thermal anomalies are always defined by appropriate scaling of seismic tomography (Fig. A1.5). Upper mantle cold downwelling anomalies are defined either by appropriate scaling of positive seismic tomography anomalies or from contours of Benioff zone seismicity used in the regionalized upper mantle (RUM) seismic model [*Gudmundsson and Sambridge*,

[1] Published as Supplementary Material in: Sonja Spasojevic, Michael Gurnis and Rupert Sutherland (2010) in *Nature Geoscience, 3,* 435-438, doi:10.1038/ngeo855. Reprinted by permission from Macmillan Publishers Ltd: Nature Geoscience, copyright 2010.

1998], while upper mantle hot upwelling anomalies are scaled negative seismic anomalies. Seismic-to-density scaling follows a similar approach as previous studies [*Forte and Mitrovica*, 2001; *Steinberger*, 2000], we assume that all buoyancy anomalies are thermal in origin and calculate the temperature anomaly using constants defined in Table A1.1, a depth-independent value of coefficient of thermal expansion and a depth-dependent scaling. Mantle background viscosity is defined as four layers, which is modified by tectonic regionalization and temperature dependence (Fig. A1.2). The resolution of models is approximately 50 km, as we use 129x129 nodes per CitcomS cap in map view, and 65 nodes in the vertical direction. Resolution tests are shown on Fig. A1.6. Parameters that remained constant in the model runs are shown in Table A1.2.

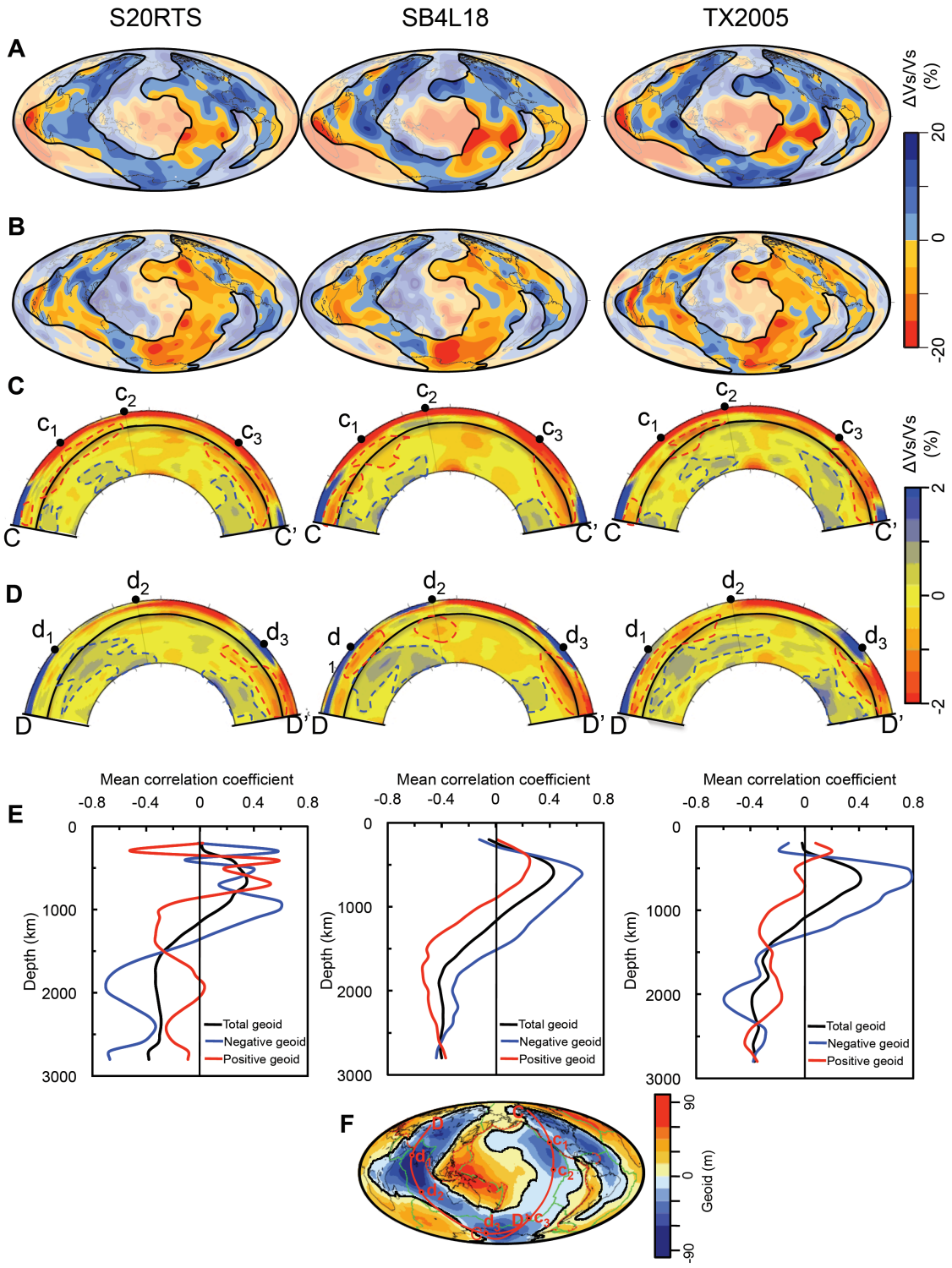

Figure A1.1. Details of velocity structure for models S20RTS [*Ritsema et al.*, 2004] (first column) and SB4L18 [*Masters et al.*, 2000] (second column), and model TX2005 [*Simmons et al.*, 2006] (third column) in the zones of geoid minima. (A) Integrated tomography in depth range 2050-2850 km. (B) Integrated tomography in depth range 300-1000 km. (C) Cross-section from North America to Ross Sea. (D)

Cross-section from central Asia to Ross Sea. (E) Correlation coefficient between observed geoid and tomography calculated at every 100 km depth. (F) Observed geoid. Semi-transparent outlines on (A-B) cover zone of global geoid high; blue and red dashed lines (C-D) indicate lower mantle high velocity and upper-to-mid mantle low velocity anomalies of interest, respectively; black, blue, and red lines on (E) show mean correlation coefficient between whole geoid, areas of negative geoid, and areas of positive geoid, respectively; red lines on (F) indicate position of great circle cross-sections intersecting geoid low. Correlation coefficient between observed geoid and tomography models (E) is calculated as a product of values divided by product of standard deviations at every 100 km depth. The mean value of correlation coefficient is than calculated for whole geoid, areas of geoid lows, and geoid highs.

Integrated tomography plots (A-B) show a correlation between geoid low (F) and both seismically fast regions in lower mantle (A) and slow regions in upper-to-mid mantle (B) for all investigated tomography models. In the region of NE Pacific geoid low, all models define a seismically fast anomaly in the lower 500-1000 km of mantle (C), which is probably related to an ancient subducted slab that has not been recognized previously, except by analysis of SKS-SKKS splitting discrepancies [*Long*, 2009]. A zone of upper-mid mantle seismically slow velocities is located above this fast anomaly (C), model SB4L18 [*Masters et al.*, 2000] defines this structure largely in the lower mantle, while models S20RTS [*Ritsema et al.*, 2004] and TX2005 [*Simmons et al.*, 2006] place it at depths up to 800 km. In the Ross Sea region (C-D), all models show coherent upper-mid mantle seismically slow region. Fast seismic anomaly in the lower mantle appears to consist of several separate structures, possibly corresponding to different stages of Gondwana subduction. In the zone of Indian Ocean geoid low, all models clearly define fast seismic anomalies in the lower mantle (D), which was previously attributed to Mesozoic Tethyan subduction [*Van der Voo et al.*, 1999]. In the upper-to-mid mantle, TX2005 defines the most coherent slow region in depth range of 300-800 km (D) in the region of local geoid low (10°S to 10°N), while models S20RTS and SB4L18 show no particularly distinctive region of slow velocities (D). Correlation analysis between observed geoid tomography and various component of geoid (E) indicate that negative geoid is correlated with low-velocity tomographic anomalies in upper 1200-1500 km of mantle and high-velocity seismic anomalies in the lower mantle. Positive geoid is correlated with high velocity anomalies in upper 800 km of mantle and negative seismic anomalies in the lower mantle.

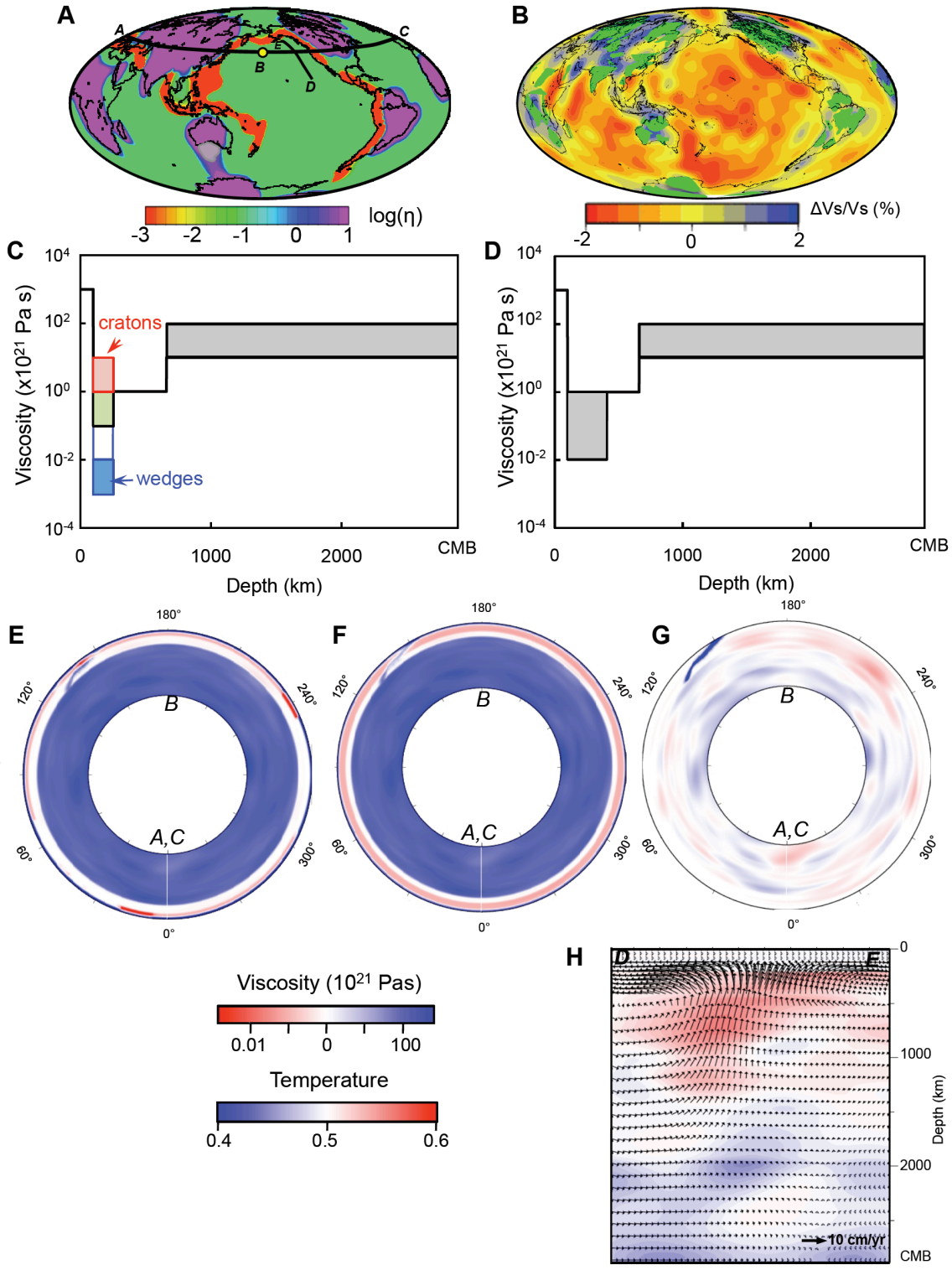

Figure A1.2. Details of viscosity structure. (A) Tectonic regionalization map with high-viscosity cratons, low-viscosity mantle wedges and intermediate-viscosity background regions. (B) S20RTS tomography at 250 km depth with outlines (green) of geologically defined cratons [*Stoddard and Abbott*, 1996]. (C) Radial viscosity

structure for models with tectonic regionalization. (D) Radial viscosity structure for models without tectonic regionalization. (E-F) Viscosity cross-sections for models with (E) and without (F) tectonic regionalization. (G) Global temperature cross-section. (H) Regional cross-section through NE Pacific geoid low with velocity vectors overlay. Position of cross-sections (E-H) is shown with black line on (A); red, green and blue rectangles on (C) show upper mantle range of viscosities for cratons, background and wedges, respectively; grey rectangles on (C-D) show range of viscosities in lower and upper mantle.

Following the experience from previous studies that use scaled tomographic models for geoid and gravity predictions to either define only the best fitting radial viscosity structure [*Forte and Mitrovica*, 2001; *Forte*, 2007; *Simmons et al.*, 2009; *Steinberger*, 2000; *Steinberger and Calderwood*, 2006], without imposing any lateral tectonic viscosity parameterization, or models in which viscosity is not just a function of depth and temperature (seismic velocity), but also have pre-imposed large-scale variations based on upper mantle structure and tectonics [*Cadek and Fleitout*, 2003; *Kaban et al.*, 2007; *Yoshida*, 2004; *Yoshida and Nakakuki*, 2009], we develop two types of models: (1) models with tectonic regionalization in the upper mantle (A-C, E), and (2) models without tectonic regionalization in the upper mantle (D,F). For models with tectonic regionalization, high viscosity cratons are defined simultaneously using seismic tomographic maps [*Masters et al.*, 2000; *Ritsema and van Heijst*, 2000; *Simmons et al.*, 2006] in the depth range 200-250 km and geologically defined cratonic outlines [*Stoddard and Abbott*, 1996] (B), including spatially more extensive area of the two in each particular region. The high viscosity cratons in our models (A) are more extensive than geologically defined cratons (B) and often include several neighboring geologically defined cratonic regions (A), as our models have a wide (~1000 km where possible) regions of interpolations toward the neighboring regions, and merge a number of geologically defined cratonic areas (A). The Australian cratonic region (A) is extended in a way that high-viscosity province also encompasses the Australia-Antarctic discordance zone (AAD), as we were unable to reproduce the correct sign of geoid without AAD having high viscosity in upper mantle. Mantle viscosity wedges are defined as ~1000 km wide zones of lower viscosities that extend from the trench into the backarc region (A), with wider regions defined in the regions of multiple neighboring subduction zones with opposite polarities, such as ones in the SW Pacific (A). We vary viscosity values in depth range 100-250 km in the tectonically regionalized model as it follows: cratons 10^{21}- 10^{22} Pa s, mantle wedges 10^{18}-10^{19} Pa s, background regions 10^{20}- 10^{21} Pas. Viscosity of the mantle in depth range 250-660 km is kept constant (10^{21} Pas), while the lower mantle viscosity is varied between 10^{22} and 10^{23} Pas. For the models without tectonic regionalization, we adopt 4-layer viscosity structure (D,F) that consists of: lithosphere (viscosity 10^{24} Pas), upper mantle (viscosity varied between 10^{19} and 10^{21} Pas), transition zone (viscosity 10^{21} Pas), and lower mantle (viscosity varied between 10^{22} and 10^{23} Pas). Temperature-dependent viscosity is used for both types of viscosity parameterization (E-F).

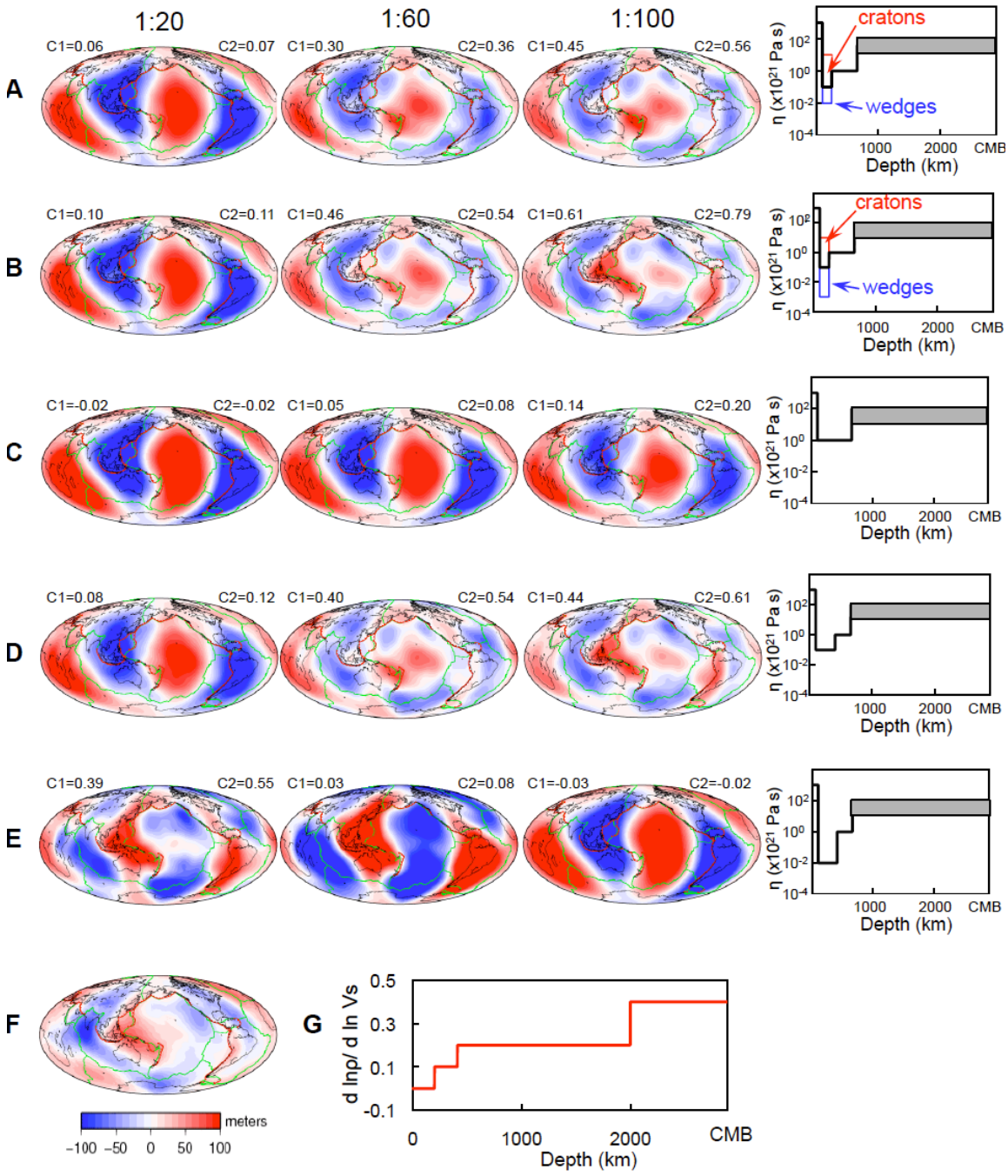

Figure A1.3. Geoid predictions for different viscosity models and a constant seismic velocity-density scaling. (A-B) Models with imposed tectonic regionalization. (C-E) Models without tectonic regionalization. (F) Observed geoid. (G) Seismic velocity-density scaling used for models (A-E). First, second, and third columns show models with viscosity increase between transition zone and lower mantle of 1:20, 1:60 and 1:100, respectively. Fourth column shows details of radial viscosity structure. All buoyancy anomalies are defined from S20RTS tomography [*Ritsema et al.,* 2004]. C1 represents correlation coefficient between observed and predicted geoid for whole

Earth's surface, and C2 indicates average correlation coefficient in the zones of geoid low.

For models with tectonic regionalization (A-B), low viscosity ratio between transition zone and lower mantle (1:20) always results in geoid prediction that is dominated by degree-2 pattern. High viscosity ratios across 660 km discontinuity of 1:60 to 1:100 yield more realistic predictions for the models with imposed tectonic regionalization (A-B). Lower viscosity of mantle wedges (B) of 10^{18} Pa s results in more positive geoid anomaly in the present-day subduction zones, comparing to higher mantle wedge viscosity of 10^{19} Pa s (A), suggesting that the mantle viscosity wedge could be significantly lower that the surrounding regions. For the models without tectonic regionalization, all models with high viscosity of upper mantle (depth range 100-410 km) yield geoid prediction dominated by degree-2 pattern (C), indicating that upper mantle viscosity has to be lower than 10^{21} Pa s. Models with upper mantle viscosity of 10^{20} Pa s and transition zone viscosity of 10^{21} Pa s (D) yield good predictions of geoid for viscosity ratios across 660 km discontinuity larger than 1:60. Finally, if viscosity of the upper mantle is reduced to 10^{19} Pa s (E) predicted geoid patterns are reasonable just for low (1:20 or lower) ratio of transition zone: lower mantle viscosity, but the predicted geoid amplitudes are too high.

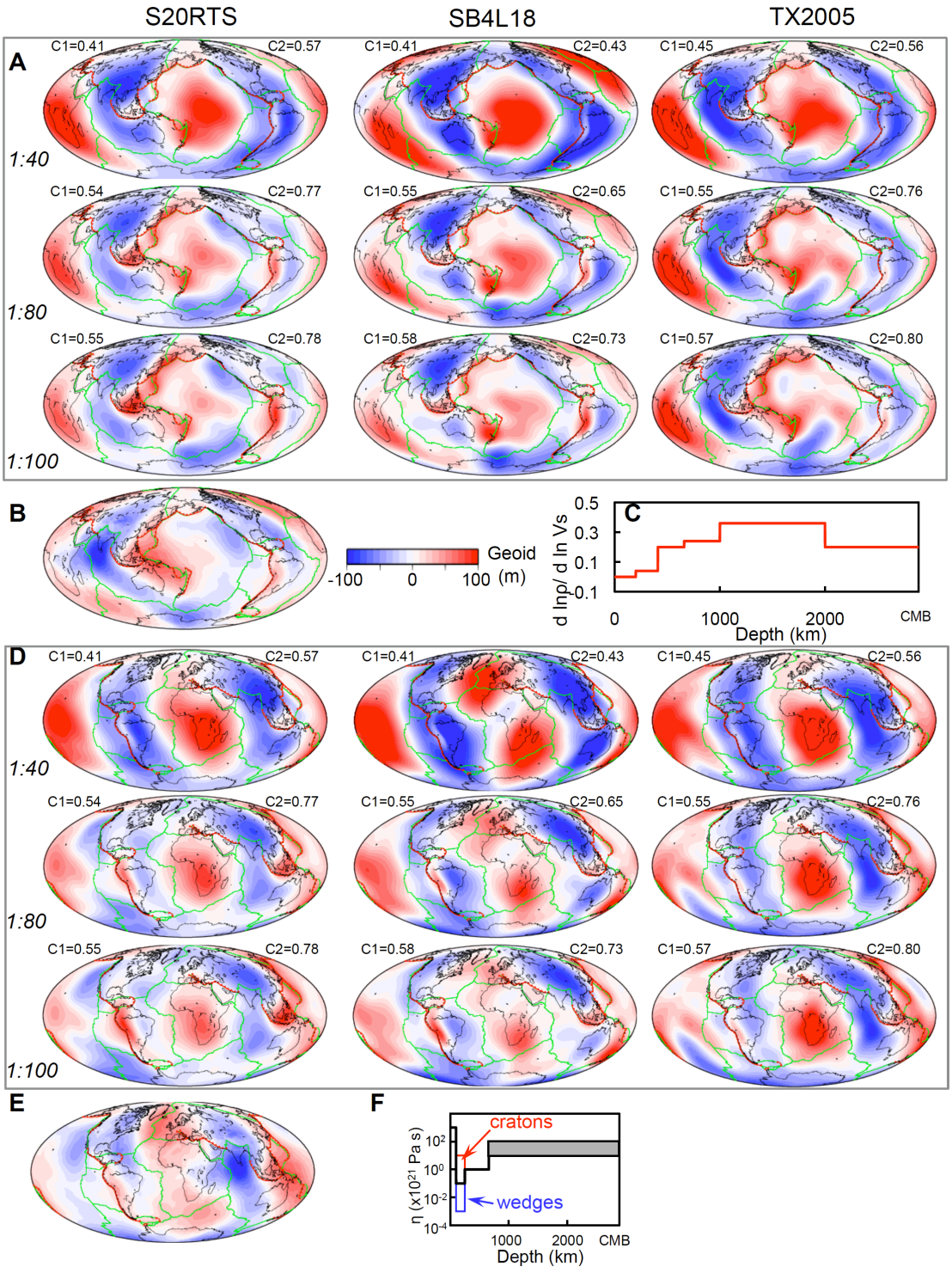

Figure A1.4. Comparison of geoid prediction for models utilizing S20RTS [*Ritsema et al.*, 2004], SB4L18 [*Masters et al.*, 2000] and TX2005 [*Simmons et al.*, 2006] tomography models. (A) Geoid predictions centered on Pacific hemisphere. (B) Observed geoid [*Förste et al.*, 2008] centered on Pacific hemisphere. (C) Seismic

velocity-density scaling. (D) Geoid predictions centered on Atlantic hemisphere. (E) Observed geoid centered on Atlantic hemisphere [*Förste et al.*, 2008]. (F) Radial viscosity profile. Ratios 1:40, 1:80, and 1:100 indicate viscosity increase between transition zone and lower mantle. Negative buoyancy in upper mantle is defined based on RUM model [*Gudmundsson and Sambridge*, 1998], while other buoyancy anomalies are defined using seismic velocity-density scaling shown on (C). C1 represents correlation coefficient between observed and predicted geoid for whole Earth's surface, and C2 indicates average correlation coefficient in the zones of geoid low.

For all models, the preferred viscosity ratio across 660 km has to be higher than 1:40, as models with this viscosity ratio have geoid predictions mostly dominated by degree-2 pattern (A,D). For the Pacific and circum-Pacific region, three models yield rather different geoid predictions (A). Models SB4L18 [*Masters et al.*, 2000] and TX2005 [*Simmons et al.*, 2006] have more strongly defined central Pacific geoid highs, which relates to stronger tomographic anomaly from the Pacific superplume in the lower mantle (A). Model S20RTS [*Ritsema et al.*, 2004] has geoid high translated toward the western Pacific subduction zones, which is more similar to the observations (B). Models SB4L18 and TX2005 are less successful reproducing NE Pacific geoid low, and we therefore prefer model S20RTS for the Pacific region geoid predictions. In addition, predictions of the Ross sea and South Pacific geoid lows are the best obtained by S20RTS model (A). On other hand, S20RTS and SB4L18 models fail reproducing amplitudes of geoid low in the belt extending from Siberia to the Indian Ocean, while TX2005 is more successful in the geoid low prediction in this region. In the region of Atlantic-Africa geoid highs (D), the SB4L18 model seems to be most successful in predicting geoid trends, with two highs centralized in South Africa (presumably related to the African superplume) and Mediterranean–North Atlantic regions (presumably related to Mediterranean subduction and Iceland hotspot). Model S20RTS is less successful reproducing geoid highs in North Atlantic, and South Africa geoid high predicted further north in the central Africa than observed. Model TX2005 on other hand relatively successfully predicts South Africa geoid high, but it fails to adequately reproduce North Atlantic high (d). Since we are mostly interested in the circum-Pacific belt of geoid lows, we utilized S20RTS model for most of the results shown in the main manuscript.

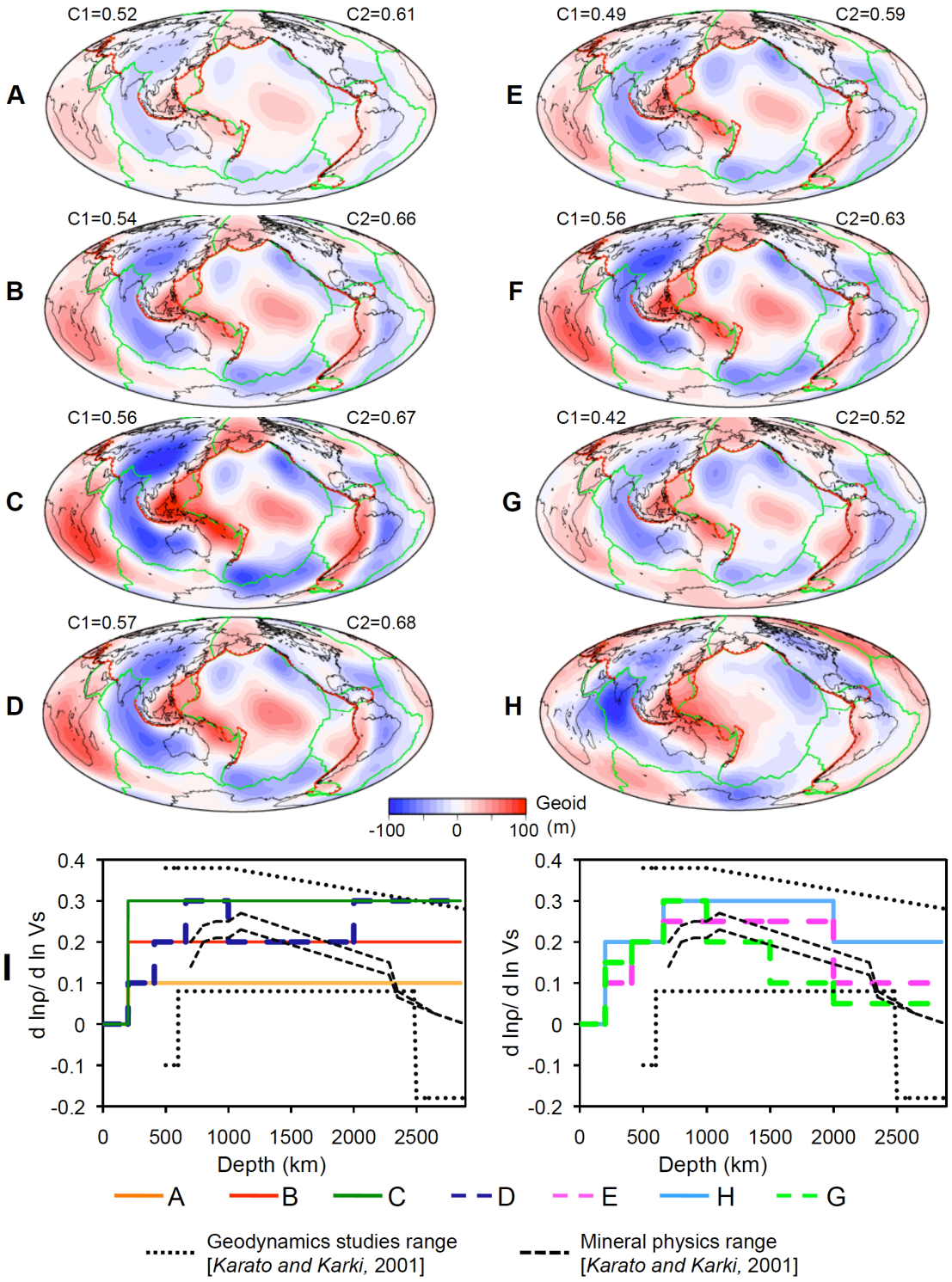

Figure A1.5. Geoid predictions (A-G) for models with different tomography-density scaling functions (I). Observed geoid is shown on (H), colored lines on (I) show scaling functions. Dotted and dashed black lines show range of scaling values suggested by geodynamic (dotted) and mineral physics studies (dashed), based on

[*Karato and Karki*, 2001]. All buoyancy anomalies are defined from S20RTS tomography[*Ritsema et al.*, 2004]. C1 represents correlation coefficient between observed and predicted geoid for whole Earth's surface, and C2 indicates average correlation coefficient in the zones of geoid low.

Although we significantly vary depth-dependent seismic velocity-density scaling, difference in the geoid prediction is smaller than when viscosity model (Fig. A1. 3) or seismic model (Fig. A1.4) are varied. For example, the model with constant scaling of 0.2 (B) yields similarly well-predicted geoid as some of more complex scaling functions (e.g., D, F).

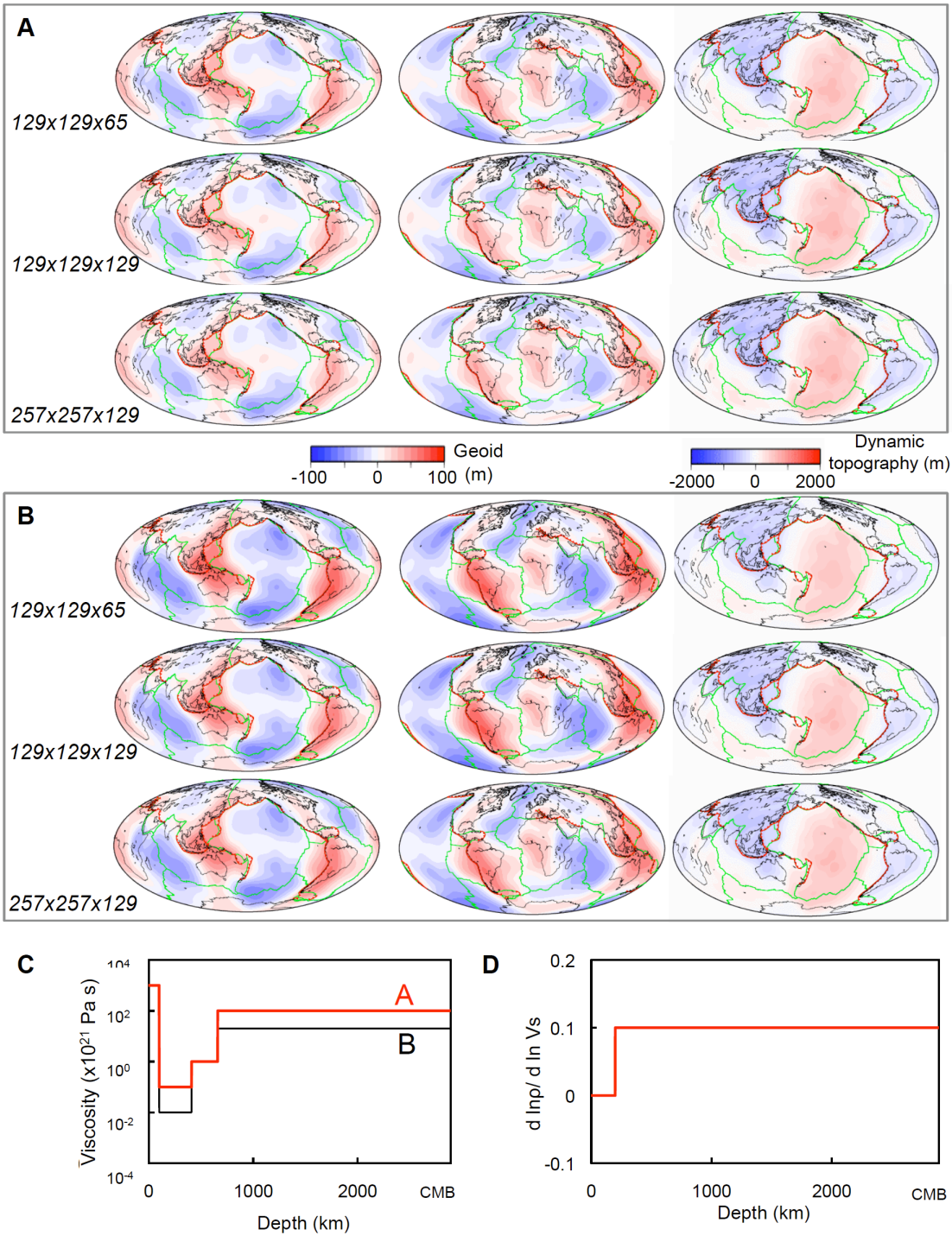

Figure A1.6. Impact of lateral and vertical resolution on geoid prediction for two models without tectonic regionalization (A-B) having different radial viscosity structure (C) and same seismic velocity- density scaling (D). First and second column show geoid predictions centered on Pacific and African hemisphere,

respectively. Third column shows predicted dynamic topography. CitcomS global models use 12 caps for the whole globe, and the resolution is defined for each cap. We test two different lateral resolutions: 129x129 (approximately 50 km) and 257x257 (approximately 25 km). In the radial directions we test two resolutions: 65 nodes (approximately 44 km) and 129 nodes in the whole mantle (approximately 22 km), with nodes uniformly distributed in the radial direction. All buoyancy anomalies are defined from S20RTS tomography [*Ritsema et al.*, 2004].

We find a slight difference (A-B) in geoid predictions between models that have different vertical resolution (129x129x65 vs. 129x129x129), while there seems to be no difference in geoid prediction between models that have 22 km vertical resolution and different lateral resolution (129x129x129 vs. 257x257x129). However, all patterns and trends of geoid predictions are essentially the same for all resolutions we tested. We attribute the difference in the geoid prediction between models having 44 km and 22 km resolution to the slightly different density/temperature models used as input data. Namely, the higher radial resolution models essentially sample tomography at two times denser interval, therefore introducing slightly different additional content in the density field, which is reflected in the geoid prediction.

Table A1.1. Comparison of observed and model geoid minima.

	Northeast Pacific			West Atlantic			Indian Ocean			Ross Sea		
	Lon. ° E	Lat. ° N	Amp. m	Lon. ° E	Lat. ° N	Amp. m	Lon. ° E	Lat. ° N	Amp. m	Lon. ° E	Lat. ° N	Amp. m
Observed*	239	22	-46	295	23	-52	78	3	-102	188	-72	-63
							107	-32	-38			
Model A	224	41	-69	310	23	-47	96	-22	-75	186	-58	-75
										252	-49	-52
Model B	224	45	-45	307	22	-45	95	-19	-65	180	-58	-48
										225	-69	-42
										261	-50	-43
Model C	265	11	-26	306	22	-29	88	-7	-63	170	-59	-28
				311	-11	-32				264	-58	-39

*Filtered to remove features <1000 km in size.

Note: The Hudson Bay anomaly is not compared due to its partial glacial rebound origin.

Table A1.1 shows amplitudes of observed and model geoid minima for the preferred model (Fig. 3.2), obtained for viscosity structure shown on Fig. A1.3B (viscosity ratio at 660 km is 1:100) and seismic velocity-to-density scaling shown on Fig. A1.3G. Model A corresponds to the best-fitting model shown on Fig. 3.2A, while models B and C correspond to the models shown on Figs. 3.2B-C, having upwellings removed from the best-fitting model from depths 0-660 km (B) and 0-1000 km (C). Amplitudes of geoid minima are evaluated at the several locations for observed and predicted models, with the coordinates shown in the table and general location of the zones of localized geoid lows shown on Fig. 3.2A-D. There is a good agreement between observed and predicted geoid amplitudes for the best-fitting model (Model A; Fig. 3.2A). Once the upwellings are removed from the upper mantle (Model B, Fig. 3.2B) and 0-1000 km depth (Model C, Fig. 3.2C), the amplitude fit becomes worse.

Table A1.2. Model parameters held constant in our runs.

Parameter	Symbol	Value
Ambient mantle density	ρ_m	3340 kg/m^3
Reference viscosity	η_o	1x10^{21} Pa s
Thermal diffusivity	κ	10^{-6} m^2/s
Coefficient of thermal expansion	α	3x10^{-5} 1/K
Gravitational acceleration	g	9.81 m/s^2
Earth's radius	R	6371 km
Rayleigh number	Ra	7.5x10^7

References

Cadek, O., and L. Fleitout (2003), Effect of lateral viscosity variations in the top 300 km on the geoid and dynamic topography, *Geophysical Journal International*, *152*(3), 566–580.

Förste, C., R. Schmidt, R. Stubenvoll, F. Flechtner, U. Meyer, R. Konig, H. Neumayer, R. Biancale, J. M. Lemoine, S. Bruinsma, S. Loyer, F. Barthelmes, and S. Esselborn (2008), The GeoForschungsZentrum Potsdam/Groupe de Recherche de Geodesie Spatiale satellite-only and combined gravity field models: EIGEN-GL04S1 and EIGEN-GL04C, *Journal of Geodesy*, *82*(6), 331–346.

Forte, A. M., and J. X. Mitrovica (2001), Deep-mantle high-viscosity flow and thermochemical structure inferred from seismic and geodynamic data, *Nature*, *410*(6832), 1049–1056.

Forte, A. M. (2007), Constraints on seismic models from other disciplines: Implications for mantle dynamics and composition, in *Treatise of Geophysics*, edited by B. Romanowicz and A. M. Dziewonski, 805–854.

Gudmundsson, O., and M. Sambridge (1998), A regionalized upper mantle (RUM) seismic model, *Journal of Geophysical Research*, *103*(B4), 7121–7136.

Kaban, M. K., I. Rogozhina, and V. Trubitsyn (2007), Importance of lateral viscosity variations in the whole mantle for modelling of the dynamic geoid and surface velocities, *Journal of Geodynamics*, *43*(2), 262–273.

Karato, S., and B. B. Karki (2001), Origin of lateral variation of seismic wave velocities and density in the deep mantle, *Journal of Geophysical Research, 106*(B10), 21771–21783.

Long, M. (2009), Complex anisotropy in D beneath the eastern Pacific from SKSñSKKS splitting discrepancies, *Earth and Planetary Science Letters*, *283*(1-4), 181–189.

Masters, G., G. Laske, H. Bolton, and A. Dziewonski (2000), The relative behavior of shear velocity, bulk sound speed, and compressional velocity in the mantle: Implications for chemical and thermal structure, in *Geophysical Monograph Series*, edited by S. Karato, et al., 63–88, American Geophysical Union, Washington DC.

Ritsema, J., and H. J. van Heijst (2000), Seismic imaging of structural heterogeneity in Earth's mantle: Evidence for large-scale mantle flow, *Science Progress*, *83*, 243–259.

Ritsema, J., H. J. van Heijst, and J. H. Woodhouse (2004), Global transition zone tomography, *Journal of Geophysical Research 109*, B02302, doi: 10.1029/2003jb002610.

Simmons, N. A., A. M. Forte, and S. P. Grand (2006), Constraining mantle flow with seismic and geodynamic data: A joint approach, *Earth and Planetary Science Letters*, *246*(1–2), 109–124.

Simmons, N. A., A. M. Forte, and S. P. Grand (2009), Joint seismic, geodynamic and mineral physical constraints on three-dimensional mantle heterogeneity: Implications for the relative importance of thermal versus compositional heterogeneity, *Geophysical Journal International*, *177*(3), 1284–1304.

Steinberger, B. (2000), Slabs in the lower mantle - results of dynamic modelling compared with tomographic images and the geoid, *Physics of Earth and Planetary Interiors*, *118*(3–4), 241–257.

Steinberger, B., and A. R. Calderwood (2006), Models of large-scale viscous flow in the Earth's mantle with constraints from mineral physics and surface observations, *Geophysical Journal International*, *167*(3), 1461–1481.

Stoddard, P. R., and D. Abbott (1996), Influence of the tectosphere upon plate motion, *Journal of Geophysical Research*, *101*(B3), 5425–5433.

Tan, E., E. Choi, P. Thoutireddy, M. Gurnis, and M. Aivazis (2006), GeoFramework: Coupling multiple models of mantle convection within a computational framework, *Geochemistry Geophysics Geosystems*, *7*(Q06001).

Van der Voo, R., W. Spakman, and H. Bijwaard (1999), Tethyan subducted slabs under India, *Earth and Planetary Science Letters*, *171*(1), 7–20.

Yoshida, M. (2004), Possible effects of lateral viscosity variations induced by plate-tectonic mechanism on geoid inferred from numerical models of mantle convection, *Physics of Earth and Planetary Interiors*, *147*(1), 67–85.

Yoshida, M., and T. Nakakuki (2009), Effects on the long-wavelength geoid anomaly of lateral viscosity variations caused by stiff subducting slabs, weak plate margins and lower mantle rheology, *Physics of Earth and Planetary Interiors*, *172*(3–4), 278–288.

Appendix 2

Supplementary material for Chapter 6

A2.1. Additional equations and parameters

The effective viscosity is defined as:

$$\eta = \eta_0 \exp\left[\frac{E^*}{T + T_o} - \frac{E^*}{0.5 + T_o}\right] \quad (1)$$

where η is effective viscosity, η_0 is reference viscosity (Table A2.1), E^* is activation energy divided by the product of the gas constant R (8.314 $\mathrm{J\,K^{-1}\,mol^{-1}}$) and temperature scaling T_S (3000 K), T is non-dimensional temperature, and T_0 is a temperature offset. We use values of E^*=10-30 and T_0 =0.5-1.0 for both upper and lower mantle. Important parameters of hybrid models are given in Table A2.1.

The resolution is about 50 km with the 129x129 nodes per CitcomS cap in map view and 65 nodes in the radial direction with refinement in the upper mantle and lithosphere. Resolution testing with several different spatial and radial resolutions showed that this resolution was sufficient [*Spasojevic et al.*, 2010].

Table A2.1. Parameters of hybrid models.

Parameter	Symbol	Value
Ambient mantle density	ρ_m	3340 kg/m^3
Water density	ρ_w	1000 kg/m^3
Reference viscosity	η_o	1x10^{21} Pa s
Thermal diffusivity	κ	10^{-6} m^2/s
Coefficient of thermal expansion	α	3x10^{-5} 1/K
Gravitational acceleration	g	9.81 m/s^2
Earth's radius	R	6371 km

Ocean bathymetry for half-space model [*Parsons and Sclater*, 1977] with flattening after 70 Ma is defined as:

$$d = 2500m + 350m\sqrt{t} \qquad t \le 70\ Ma \qquad (2)$$

$$d = 6400m + 3200m\exp(-t/62.8) \qquad t > 70\ Ma \qquad (3)$$

where d is depth of ocean floor in meters, t is age of sea-floor in million of years. For plate model GDH1 [*Stein and Stein*, 1992], the ocean bathymetry is defined as:

$$d = 2600m + 365m\sqrt{t} \qquad t = 0\text{-}20\ Ma \qquad (4)$$

$$d = 5651m - 2473m\exp(-0.0278t) \qquad t > 20\ Ma \qquad (5)$$

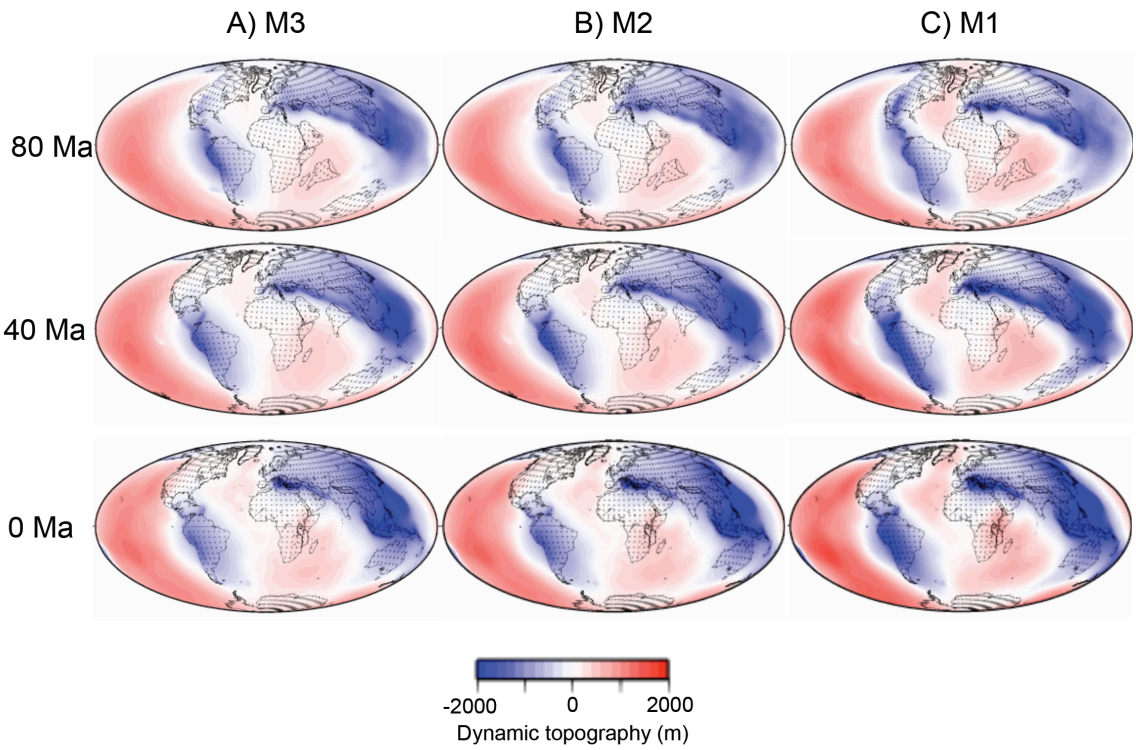

Figure A2.1. Predicted dynamic topography for 80 Ma, 40 Ma, 0 Ma for models M3(A), M2(B) and M1(C). Red lines with triangles indicate position of subduction zones, while green lines represent position of ridges and transform plate boundaries, based on GPlates reconstructions [*Gurnis et al.,* 2010].

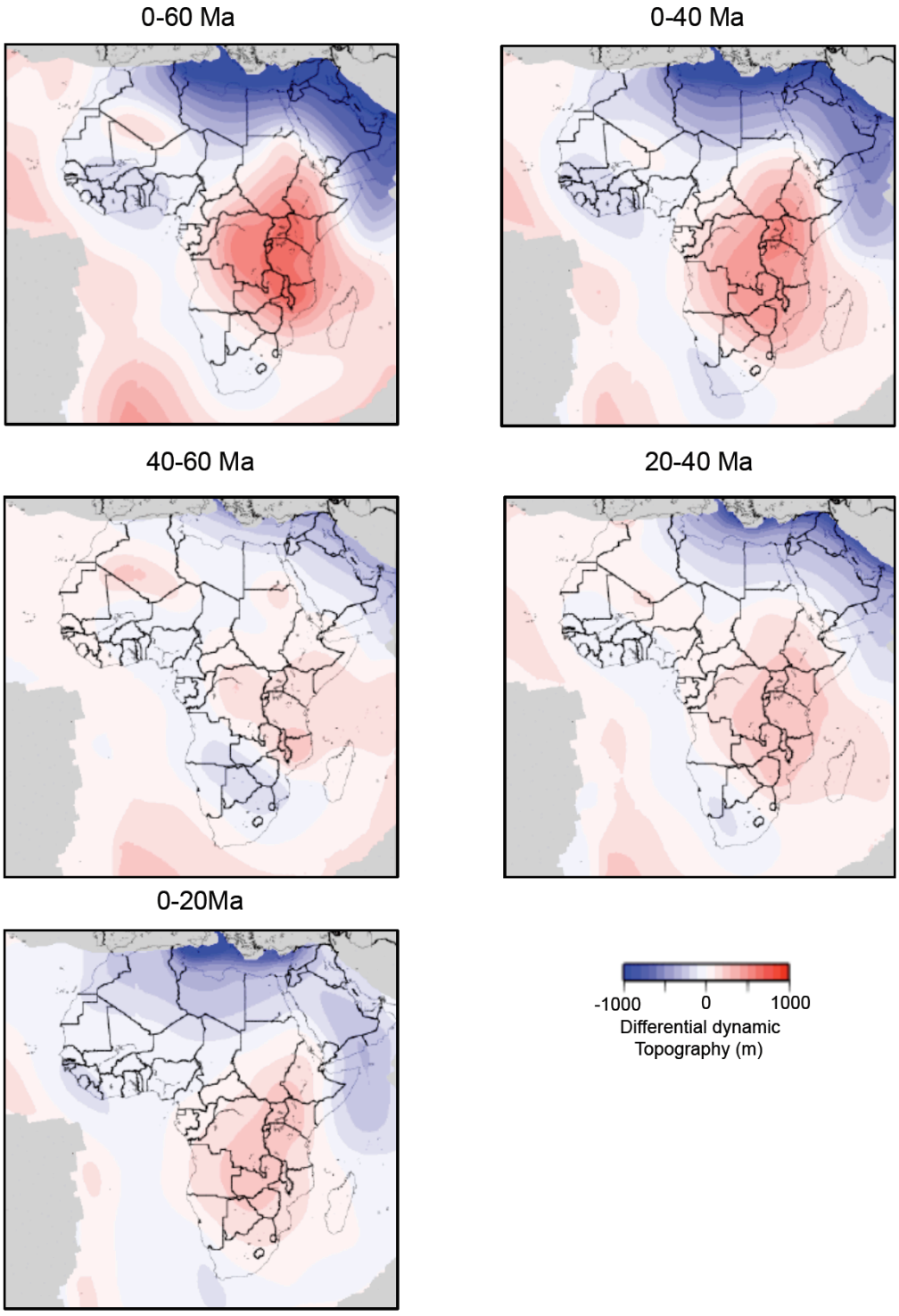

Figure A2.2. Differential dynamic topography in Africa during different time intervals in the Cenozoic for model M1.

References

Gurnis, M., M. Turner, S. Zahirovic, L. DiCaprio, S. Spasojevic, R. D. Müller, J. Boyden, M. Seton, V. C. Manea, and D. V. Bower (2009), Global Plate Reconstructions with Continuously Closing Plates, *Computers and Geosciences*, in review.

Parsons, B., and J. G. Sclater (1977), Analysis of variation of ocean-flow bathymetry and heat-flow with age, *Journal of Geophysical Research*, *82*(5), 803–827.

Spasojevic, S., M. Gurnis, and R. Sutherland (2010), Mantle upwellings above slab graveyards linked to the global geoid lows, *Nature Geoscience, 3,* 435–438, doi:10.1038/ngeo855.

Stein, C., and S. Stein (1992), A model for the global variation in oceanic depth and heat flow with lithospheric age, *Nature*, *359*(6391), 123–129.